Surface Chemical Reactions of Mesoporous Metal Oxides for Environmental and Energy Systems

July 2013

Mohamed Khairy Mohamed ABOELALLA

Surface Chemical Reactions of Mesoporous Metal Oxides for Environmental and Energy Systems

July 2013

Waseda University
Graduate School of
Advanced Science and Engineering
Department of Nanoscience and Nanoengineering
Research on Nano-device

Mohamed Khairy Mohamed ABOELALLA

MEMBERS OF THE DISSERTATION JURY

1- Professor Hiroshi Kawarada

Professor Nano-Science & Nano-engineering, Waseda University

2- Professor Shuichi Shoji

Professor Nano-Science & Nano-engineering, Waseda University

3- Professor Takanobu Watanabe

Professor Nano-Science & Nano-engineering, Waseda University

4- Professor Sherif A. El-Safty

Professor Nano-Science & Nano-engineering, Waseda University

ACKNOWLEDGEMENT

Sincere gratitude is expressed to my supervisor, ***Professor Sherif A. El Safty,*** *for his professional guidance and continuous encouragement throughout my thesis work. His dedication and enthusiasm for scientific research is unsurpassed, and his vast knowledge and incisive insight have been inspiring. I sincerely thank my supervisor for his support in both research work and other aspects.*

At the same time, I wish to express my thanks to Dr. Mohamed Ismael and Dr. Mohamed A. Shenashen, for their assistance during the experiments and helpful discussions. In addition, I would like to thank my colleagues, Ms. Ryoko Onizawa for here great assistance.

Finally, I would like to express my gratitude to the National Institute for Materials Science for providing me a research scholarship to pursue this degree.

Before all, thanks to Allah for finishing this important step in all my life

Mohamed Khairy

LIST OF ABBREVIATIONS

A

AAM	Anodic alumina membrane
ALD	Atomic Layer Deposition
APTMS	3-Aminopropyltrimethoxysilane
APMS	Amino propyl trimethoxy silane
o-AP	o-Aminophenol
o-ATP	o-Aminothiophenol
α-Amy	α-Amylase

C

CVD	Chemical Vapor Deposition
CytC	Cytochrome C
CTAB	Cetyltrimethyl ammonium bromide
CHES	2-(Cyclohexylamino) ethane sulfonic acid
CAPS	*N*-cyclohexyl-3-aminopropane sulfonic acid

D

DSAHMP	4,5-Diamino-6-hydroxy-2-mercaptopyrimidine
DZ	Diphenylthiocarbazone
CS-DAT	*N*-Dodecyl-*N,N*-dimethyl-1-dodecanaminium bromide
DTA	Differential thermal analyses

E

EG	Ethylene glycol
Kc	Equilibrium constant

ΔH	Enthalpy
EDS	Energy-dispersive X-ray spectroscopy
G	
ΔG	Gibbs Free energy
H	
k	Heterogeneous catalytic reaction
HMDS	Hexamethyldisilazane
Hb	Hemoglobin
HEPES	*N*-2-Hydroxyethylpiperazine-*N*-2-ethanesulfonic acid
I	
Ins	Insulin
M	
MPTMS	3-Mercaptopropyltrimethoxysilane
Mb	Myoglobin
My	Myosin
MOPS	3-Morpholinopropane sulfonic acid
P	
PEO	Polyethylene oxide
P123	Pluronic
PEI	Polyethyleneimine
Brij 98	polyoxyethylene(20) oleyl ether
S	
NaAc	Sodium acetate
SEM	Scanning electron microscopy

SAXS	Small angle X-ray scattering
STEM	Scanning transmission electron microscopy
T	
TEOS	Tetraethyl-orthosilicate
TMOS	Tetramethyl-orthosilicat
TEM	Transmission electron microscopy
TGA	Thermogravimetric analysis
W	
WXRD	Wide angle X-ray diffraction
X	
XPS	X-ray photoelectron spectroscopy

TABLE OF CONTENTS

CHAPTER 2

EXPERIMENTAL SECTION

CHAPTER 4

CHAPTER 5

CHAPTER 1

GENERAL INTRODUCTION

1. GENERAL INTRODUCTION

The research in the field of porous materials has a great importance for fundamental research and potential applications ranging from catalysis, adsorption, separation, sensing, energy and biotechnology. The presence of voids of controllable dimensions at the atomic, molecular or nanometer scale makes them of high scientific and technological importance. The International Union of Pure and Applied Chemistry (IUPAC) classifies porous materials according to their pore sizes as: (i) microporous, with pores less than 2 nm; (ii) mesoporous, with pores from 2 to 50 nm; and (iii) macroporous, with pores between 50 and 1000 nm.[1] The pore size controls the accessibility to the pore volume, while the capacity is determined by the ratio between the skeleton and the empty space. A consequence of *porous organization* is the high specific surface area of porous materials, which can vary from several hundred to several thousand square meters per gram of solid. Another important characteristic that determines the properties of porous materials is their *structural organization*. Based on this last criterion, porous solids are divided into two major groups, that is, crystalline and amorphous. It is important to note that the properties of porous materials depend on their chemical nature. Thus, the combination of pore characteristics, structural organization and chemical composition determines the overall properties of a porous material and its possible areas of application.

Porous materials were already known by the ancient Egyptians. Since 1756, zeolites are crystalline inorganic materials commonly used as commercial adsorbents mainly consisting of alumina silicates, with well-defined microporous structures.[2] They still form a field of very intense research on academic and industrial level and recently, unique zeolites frameworks have been identified. The exciting discovery of the novel family of ordered mesoporous silicas (e.g., MCM-41 and SBA-15), was reported by the researchers at Mobil Research and Development Corporation in 1990; through combination of sol–gel chemistry with surfactant liquid crystal micelles.[3,4] A worldwide explosion of research efforts turned towards mesoporous materials. As a result, the researchers now finally had the ability to synthesize materials with well defined pores with the same size as most pharmaceuticals or biochemical molecules, opening a whole range in different domains such as catalysis, separation, adsorption, sensor technology, gas storage, nanocasting, chromatography, medicine…. etc. Due to outstanding surface properties, including high surface areas, periodically arranged mono-dispersed mesopore

space, tunable pore sizes, alternative pore shapes, uniform nanosized frameworks, large particle sizes, and abundant compositions.

Among mesoporous materials, mesoporous metal oxides are particularly important because they possess a nanosized walls, active internal surfaces, and connected pore networks. With these attributes, they exhibit a great utility in different domains. Since the number of their potential applications has continued to grow in those different applications during the last two decades, there has been an increasing need to develop more environmental sustainable procedures for the manufacture of mesoporous metal oxides taking into consideration the increasing concern for environmental protection. Indeed, governments and environmental groups keep on pushing for the development of processes and products with a minimal impact on the environment (EuP (Energy using product) 2005/32/CE and REACH). Since 2006, the REACH European Union Regulation ((EC) No. 1907/2006) has been addressing the production and use of chemical substances, and their potential impacts on both human health and the environment. Considerable efforts have therefore been undertaken to propose greener synthesis routes with sustainable applications, which take into account the whole lifecycle of mesoporous materials from raw material extraction to disposal at the end of their lifetime and consider environmental criteria such as consumption of raw materials, water and energy, emissions in water and air, waste...etc.

Although numerous methods have been developed to prepare metal oxide mesostructures particularly silica oxide, the fabrication of non-silica mesoporous materials is more challenging. Whilst the hydrolysis and condensation of silica precursors can be well controlled, and the resulting silicas are thermally stable during calcination, the hydrolysis and condensation of non-silica precursors (e.g., metal alkoxides) are generally difficult to control precisely.[5] Recently, considerable progress in the preparation of non-silica mesoporous materials has been reported. The obtained metal oxides usually exhibit very poor structural ordering and low thermal stability after the removal of the surfactant templates. Thus, this dissertation research work summarized the fabrication approaches of various mesoporous metal oxides targeting environmental remediation based monitoring, sensing, and decontamination, in addition to possible applications in the energy systems.

1.1.Preparation of porous metal oxides

Synthesis using a nanostructured template is one of the most effective strategies towards achieving high degrees of synthetic control. There are two types of synthetic approaches used; hard and soft templates. In general, route for templated synthesis of nanostructured porous materials includes the following steps:

I. Template preparation,
II. Directed synthesis of target materials using the template,
III. Template removal (if necessary).

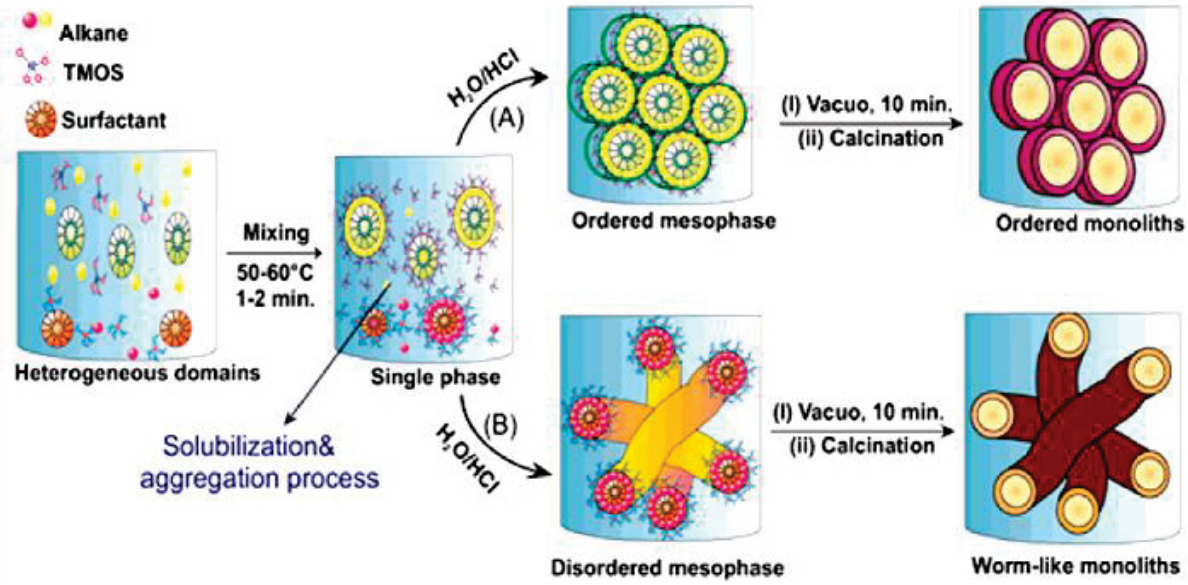

Figure1.1: Systematic formation of ordered (path A) and disordered (path B) mesoporous silica monoliths (HOM type) by adopting the instant direct-templating method of microemulsion liquid crystal phases of nonionic surfactants.

1.1.1. Preparation of porous metal oxides using soft template

Several templating agents have been used since the discovery of mesoporous materials. Classical surfactants, well known for their ability to form lyotropic liquid crystalline phases, were first used. Cationic alkylammonium surfactants were the first to be reported, and then structuring agents were quickly extended to nonionic amine surfactants and neutral amphiphilic block copolymers based on polyethylene oxide. Silica based mesoporous materials with different mesostructures have been synthesized usually using silica precursors such as tetraethyl-orthosilicate or tetramethyl-orthosilicate (TEOS or

TMOS) as the hydrolysable silica building block, and long chain ammonium surfactants, amines or triblock copolymers as templating agents via directed self-assembly as shown in Figure 1.1. Some of the well known materials are MCM-41 (*p6mm*), MCM-48 (*Ia3d*) (MCM = Mobil Composition of Matter), HMS and MSU (wormlike), KIT-6 (*Ia3d*), SBA-1 and SBA-6 (*Pm3n*), SBA-2 and SBA-12 (*P63*/*mmc*), SBA-15(*p6mm*) and SBA-16 (*Im3m*) (SBA = Santa Barbara Amorphous).[6] Besides the mesoscale structures, there are great efforts in controlling the materials in different morphologies by changing the fabrication process conditions. Various forms including thin films, fibers, monoliths, particles and other interesting shapes have been obtained (Figure 1.2).[7-11].

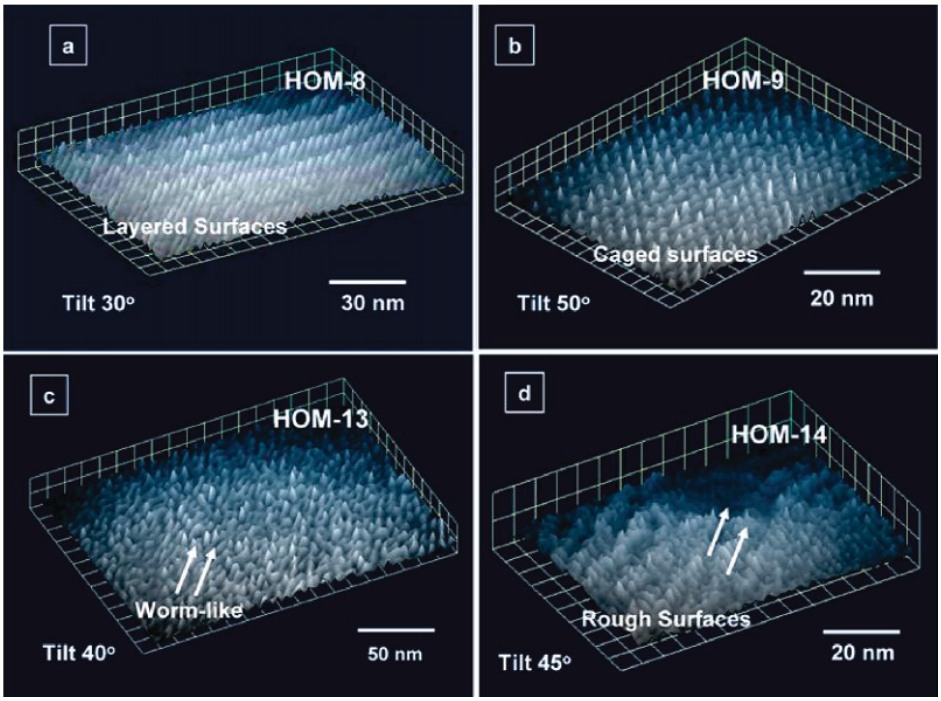

Figure 1.2: Representative 3D TEM surface micrographs of ordered and disordered silica monoliths (HOM) fabricated by using an instant direct-templating method of lyotropic and microemulsion phases of nonionic surfactants: (a) hexagonal/lamellar mesophase (HOM-8) monoliths synthesized by using Brij 97 phase domains at a Brij 97:TMOS ratio of 75 wt %, (b) ordered cubic *Pm3n* (HOM-9) monoliths synthesized by using Brij 56 phase domains at a Brij 56:TMOS ratio of 50 wt %, (c) 3D wormlike (HOM-13) monoliths synthesized by using Brij 35 phase domains at a Brij 35:TMOS ratio of 50 wt %, (d) 2D disordered (HOM-14) monoliths synthesized by using Triton X-100 phase domains at a Triton X-100:TMOS ratio of 50 wt %. Note: Arrows indicate the orientationally distorted domains or wormlike pore surfaces of HOM framework networks.

In general, the self-assembly is mainly driven by non-covalent weak interactions between their polar group and the hydrolyzed metal precursors such as hydrogen bonding, van-der Waals forces, and electrostatic interaction between the surfactants or their supermolecular structures and the building blocks. Cationic surfactants are efficient directing agents owing to the strong ionic interactions between their cationic head-group and the negatively charged silica precursors under basic conditions (synthetic route S^+I^- where S^+ = surfactant cations and I^- = inorganic precursor anions). In this case, the synthesis mechanism relies on the formation of H-bonds between primary amines and neutral inorganic species (synthetic route S^0I^0, where S^0= nonionic surfactants and I^0 = neutral silica species). Stabilization of the hybrid interface is also possible via the formation of H-bonds between the silicic acid and the ether oxygens of a PEO chain of nonionic surfactants (synthetic route S^0I^0 or $S^0H^+X^-I^+$ under strong acidic conditions, where X^- = inorganic counter ions such as Cl^-, Br^-, I^-, SO_4^{2-} or NO_3^-). The higher molecular weight and the wide variability in size and composition of this family of surfactants (that includes the commercial oligomeric acid alkyl–PEO, alkyl–phenol–PEO, sorbitan ester and PEO-based block copolymers) considerably extend the range of accessible pore size as well as the diversity of mesopore structures attainable. A last synthetic route consists in using surfactants with an anionic polar head under basic conditions. The charge matching effect is ensured by the addition of cationic amino groups of organoalkoxysilanes to the reaction mixture (synthetic route $S^-N^+–I^-$, where S^-= anionic surfactants, I^-= silicate species and N^+ = cationic amino groups).[12]

The advantages of the soft templating method are that the templates can be of low cost, the synthesis is relatively easy and can be carried out under mild conditions, and a variety of mesoporous structures are possible depending on the template and the composition of the solution. The main disadvantages are that their syntheses are based on complicated sol–gel processes, and the hydrolysis and polymerization of transitional metal ions are difficult to control. Their products usually have amorphous or semi-crystalline walls and poor thermal stability, as well as the synthesis is generally sensitive to the environment. [18] In order to, overcome the amorphous or semi-crystalline walls, Kondo and Domen [19] suggested that, the mesopores are first filled with a carbon percursor (e.g. sucrose), followed by calcination in an inert atmosphere for crystallization, and the formed carbon can stabilize the mesostructure. Then the filled carbon is removed by calcination in air.

Recently, it was found that the incorporation of aluminum into the silica framework provides materials with acidic active sites. These aluminosilica materials were reported to show an exciting range of catalytic applications, despite the existence of the structural disorder that is being similar to those amorphous alumina and aluminosilicas. The acidity of these solid materials produced from cationic Brønsted or Lewis acid sites of tetrahedrally coordinated aluminum species (AlO_4^-) in the aluminosilica frameworks. Significant key factors controlled the extent of acidity such as the fabrication strategy of aluminosilicas, and the nature and amount of incorporated aluminum in the framework matrices. In principle, the acidity of aluminosilicas results from the charge imbalance created by substitution of a Si^{4+} atom by an Al^{3+} atom in the silica-rich host lattice. The generated AlO_4^- units localize a negative charge, which could be compensated by a proton or a cation. Thus, the aluminosilicas acquire acidic and ion exchange properties (Figure1.3). It is reasonably believed that the high aluminum contents in frameworks led to increase the acidity of the resultant solid acid aluminosilica materials, but the ordering and hydrothermal stability of these materials were drastically decreased with low Si/Al ratio. Therefore, control over the local aluminum structure, structural integrity, and thermal/hydrothermal stability of aluminosilica frameworks, particularly with low Si/Al ratio, remains a significant challenge.[13] In order to introduce aluminum into mesoporous silica frameworks; there are two common pathways as follows;

I. Direct synthesis in which an aluminum precursor was mixed to the sol–gel prior to the hydrothermal synthesis.

This approach was used to control the structural ordering and to produce tetrahedral aluminum coordination in the framework, particularly at low aluminum contents. In addition, the resultant aluminosilicas exhibited homogenous wall, and moderate acidity.

II. Post grafting/incorporation of aluminum onto the mesoporous silica molecular sieves via isomorphous substitution.

This pathway provided aluminosilica materials with higher Brønsted acidity and better hydrothermal stability than that of materials synthesized via direct synthesis route.

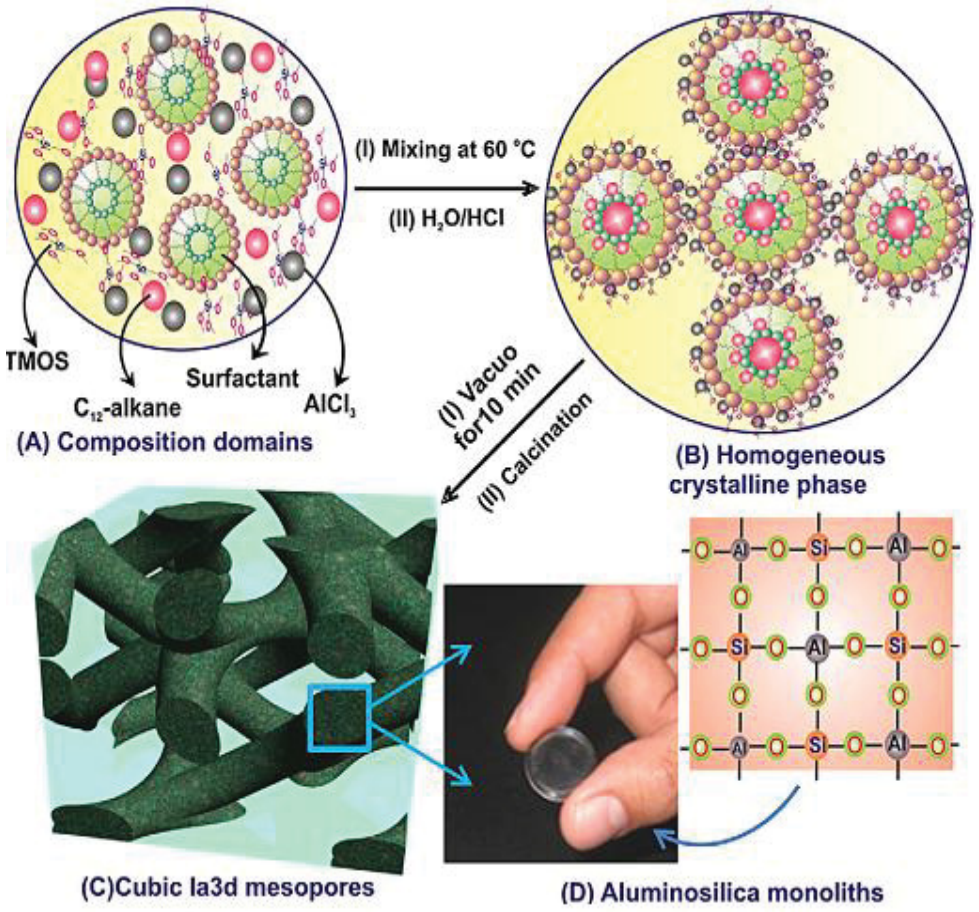

Figure1.3: Simple design of instant, one-pot synthesis in microemulsion systems (A and B) of cubic Ia3d structures (C) with aluminosilica monoliths (D)

The preparation of non-silica mesostructured metal oxides (NiO, WO_3, Sb_2O_5, Fe_2O_3,…. etc.) using soft templates such as cationic and anionic surfactants was first reported in 1994. Two general synthetic pathways have been explored: direct co-condensation with surfactants of opposite charges and indirect co-condensation of similarly charged species mediated by the intercalation of counter ions (Na^+ and K^+) at the surfactant–inorganic interface. However, the mesostructures collapsed when the surfactant was removed by calcination.[14]

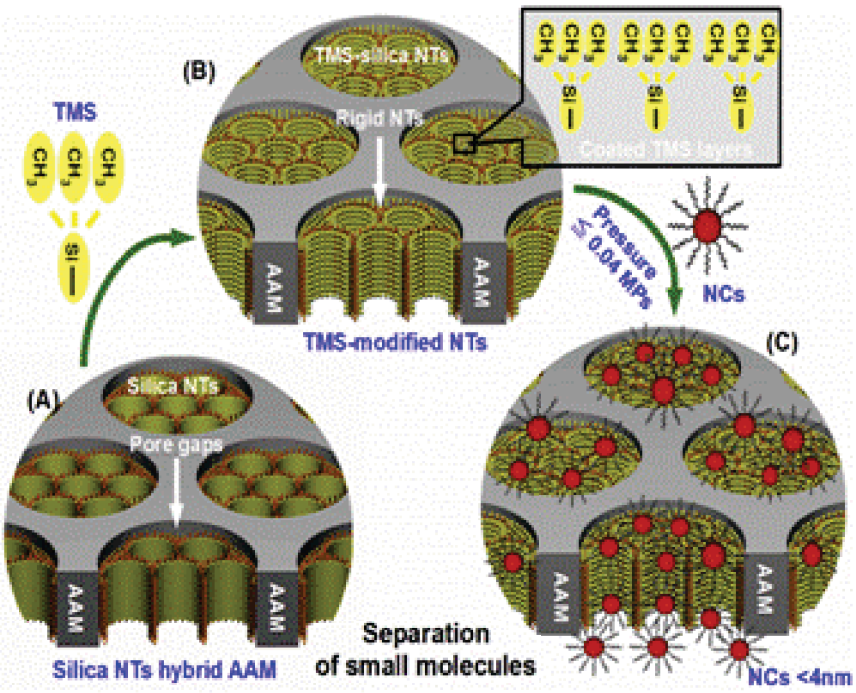

Figure 1.4: Schematic design of ultrafine separation of nanoparticles (C) based on the coating of silica nanotubes (NTs) (A) by trimethylchlorosilane (TMS) groups to form a TMS–silica NTs filter (B).

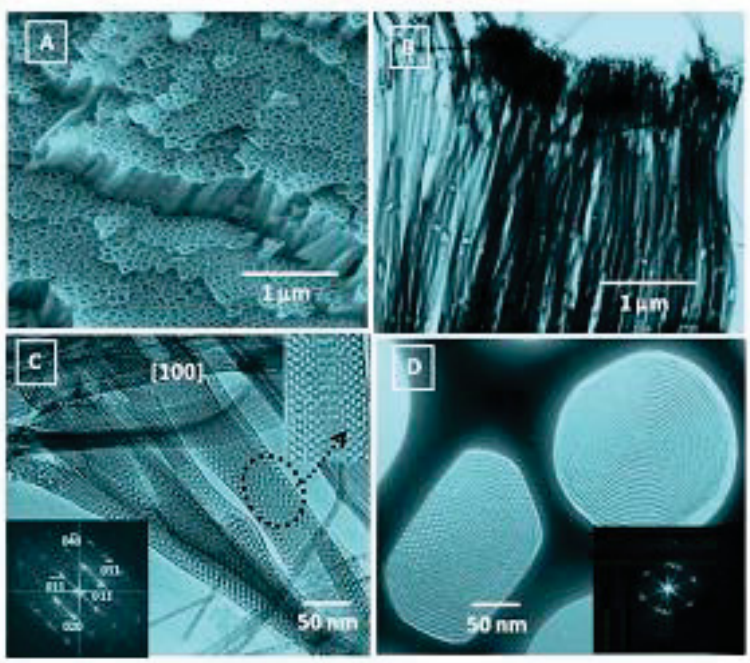

Figure 1.5: FE-SEM cross section (A) and HR-TEM (B, C, D) micrographs of nanofilters after removing the AAM using 5% H_3PO_4 for 600 min. The HR-TEM and FTD patterns (C) recorded along the [100] direction. D) TEM image recorded on the top-view of mosaic cage silica NTs hybrid AAM, and the FTD pattern (inset).

1.1.2. Preparation of porous metal oxides using hard template

The use of hard templates to synthesize mesoporous materials has brought new possibilities for the preparation of novel mesostructured materials. The hard templating method is also called nanocasting, exotemplating, or the repeated templating method. Porous Al_2O_3 membranes prepared by anodic oxidation (AAO) were used initially as a mold to prepare carbons, metals, or other nanostructures by electrodeposition, Chemical Vapor Deposition (CVD), or Atomic Layer Deposition (ALD). The pore sizes of the resulting materials are typically between 15 and 150 nm. Based on this methodology, Direct and simple synthesis of the hexagonal mesoporous silica nanotubes,[15] and 3D mesocage[16] structures through vertically aligned inside AAM by means of direct templating method of microemulsion phases with cationic dilauryldimethylammonium bromide or cetyltrimethylammonium bromide and Pluronic F108 surfactants is reported recently by us. Penetration of the precursor solution into the membrane was achieved by means of vacuum at a starting pressure of ≤ 0.04 MPa, thus allowing control of the silica-NTs inside the membrane pores as shown in Figures 1.4 and 1.5.

Mesoporous silicas with different pore architectures (e.g., MCM-41, MCM-48, SBA-15, SBA-16, KIT-6, FDU-12) or mesoporous carbons (CMK-1, CMK-3) have been used as hard templates. [17] In fact, it is possible to obtain mesoporous metal oxides via hard template however; it is not easy to fill the mesoporous silica template completely, because there are complex interactions between the silica and filtrated metal ion precursor: hydrogen bonding, Coulombic interactions, coordinating interaction, and van-der Waals interaction. Therefore, different methods have been developed to improve the impregnation and minimize the loading outside pores as follows;

I. The functionalization (post synthesis grafting or one-pot preparation) of the mesoporous templates by certain organic groups ($–NH_2$, $–CH=CH_2$).

II. Without surface functionalization

II.1. Two-solvent method;

A suspension of mesoporous silica in dry hexane is mixed with a concentrated aqueous solution of metal nitrate. Generally, the solution volume is equal to the silica pore volume to maximize the impregnation quantity and prevent the growth of metal oxides out of the pores. The precursor ions will be ‘‘pushed into’’ pores as much as possible by the hexane.

II.2. Solvent evaporation method;

Involves fully mixing the mesoporous silica with a selected metal nitrate in ethanol. The nitrate precursor is expected to migrate into the pores by capillary condensation during the slow evaporation of ethanol.

II.3. Solid–liquid method;

A metal nitrate is ground with a mesoporous silica template, and is expected to move into the pores of silica after melting when the mixed solid is heated to a temperature above the melting point of the precursor.

The method is limited to precursors (e.g., $Ce(NO_3)_3.H_2O$, $Cr(NO_3)_3.9H_2O$, $Co(NO_3)_2.6H_2O$, $Ni(NO_3)_2.6H_2O$) with melting points lower than their decomposition temperatures.

II.4. Impregnation–precipitation–calcination method;

Employs low cost metal chlorides as the starting materials. First, mesoporous silica is impregnated with a metal chloride and dried, treated with NH_3 (gas or solution) to convert the chloride into hydroxide, and then calcined to form the corresponding metal oxide. The whole process is generally repeated several times and a mesoporous metal oxide is obtained after removing the silica template. That method was first developed to prepare mesoporous CeO_2 and

The hard templating procedure offers some advantages. The mesostructures of the target materials can be controlled by choosing hard templates with desired structures. In addition, mesoporous metal oxides with highly crystalline walls may be obtained because the hard templates usually are stable to suffering high temperature to allow many metal oxides to crystallize. However, the hard templating method also has disadvantages. The targeting mesoporous metal oxides must be stable to NaOH or HF solutions used to remove the mesoporous silica template. Despite, mesoporous carbon can be used as a hard template and it can be easily removed by calcinations. It has a poor wetting of the pore walls by the aqueous precursor solution.[20]

It is important to note that, after fabrication of mesoporous metal oxides, it is possible to synthesis a series of mesoporous materials have a different oxidation states. For instance, mesoporous Fe_3O_4 was prepared by reducing mesoporous α-Fe_2O_3 in 5% H_2 (balanced with 95% Ar) at 350 ^oC for 1 h.[21]

1.1.3. Nanoparticle self-assembly

The self-assembly processing is based on monodisperse nanoparticles, the process will be less sensitive to the variable reaction conditions.[22] Such a method has four steps:

I. Formation of monodisperse metal oxide nanoparticles;
II. Mixing of the template and nanoparticles;
III. Assembly of nanoparticles into ordered mesoporous metal oxides;
IV. Removal of the template by calcination, etc.

The self-assembly of 5 nm CeO_2 nanoparticles using Pluronic P123 as a template to prepare ordered mesoporous CeO_2 with high surface area is reported (Figure 1.6).[23] Moreover, mesostructured materials using CeO_2, ZrO_2, and CeO_2–$Al(OH)_3$ nanoparticles functionalized by di-functional amino acid species as building blocks. Alternatively, CeO_2 and SnO_2 nanoparticles without surface functionalization were self-assembled into ordered crystalline mesoporous metal oxides.[24]

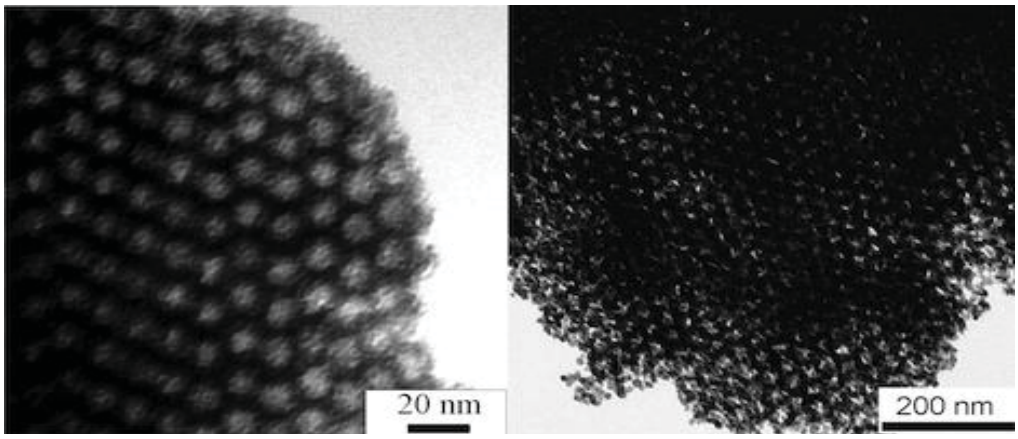

Figure 1.6: The self-assembly of 5 nm CeO_2 nanoparticles using Pluronic P123 as a template to prepare ordered mesoporous CeO_2 .

1.1.4. Template-free methods

In fact, the template methods are arguably the most effective and certainly the most common means of synthesizing porous metal oxides, However, the removal of the hard templates by either thermal (sintering) or chemical (etching) means is very complicated and energy-consuming in addition to poorly controlled morphology and size due to the deformability of the soft template. Recently, template-free approach has been proposed for fabrication of porous metal oxide nanostructures via the hydrothermal decomposition

of a metal-source precursor with room-temperature water stability under the effect of high temperature and high pressure. The growth of some porous metal oxides nanostructures with complex morphologies (especially hollow nanostructures) formed via the organic additive- and template-free hydrothermal synthetic routes can also be given a reasonable explanation by Ostwald ripening. [25] Ostwald ripening process is that the larger crystals grow from those of smaller size, which have higher solubility than the larger ones. When the crystals grow in solution, the concentration of growth units varies across the mother solution, due to the size difference of resultant nanocrystals. With the driving force of the minimization of surface energy, metastable nanoparticle aggregates occur first due to the reduction of super-saturation in solution. Once the particles with different sizes are attached to each other, the large particles begin to grow, drawing from smaller ones. Voids gradually form and grow in the cores of large aggregates, and the shell thickness increases owing to the outward diffusion of solutes through the permeable shell. The inside-out Ostwald ripening mechanism has been used to synthesize hollow spheres of a wide range of materials, such as, Fe_3O_4,[26] SnO_2,[27] Co,[28] Sb_2S_3,[29] Bi_2WO_6,[30] TiO_2,[31] NiO and other materials.[32]

1.2.Application of porous metal oxides

The mesoporous nanomaterials have shown great potentials in various fields. A large number of reaction/interaction sites are related with the high surface area, which benefit for the interface related processes regarding to environmental clean-up systems. This dissertation highlighted on the applications of mesoporous metal oxides in catalysis, sorption, separation, sensing, and electrochemistry application. The uniform and tunable large pores afford enough mono-dispersed void spaces for large molecules and hence break through the size restriction of conventional microporous materials, showing advantages in large molecule involved catalysis, adsorption, separation, drug and DNA delivery, etc. The uniform nano-sized framework structures bring nano-effects (surface and quantum effects), which endow the materials good performance in sensors, Li-ion batteries and nanodevices. In general, the entire particle sizes of mesoporous materials are in the micrometer range, favoring industrial processes, for example adsorption and filtration separation, but without losing their nanoscale advantages. The diversified pore wall compositions lead to wide applications in luminance, photovoltaic, and electronic devices.

1.2.1. Catalysis

In recent years, environmental and economic factors have spurred a strong interest in redesigning commercially important chemical or petrochemical processes so that the use of harmful substances and/or the generation of toxic waste could be avoided. For this reason, heterogeneous catalysts, which do not generate or require harmful or disposable waste materials, are of particular interest. The use of mesoporous supports is advanced to minimize diffusion limitation commonly observed for microporous materials. Significant enhancements in in-pore accessibility can be achieved via the use of 3D interconnected mesopore architectures over 2D ones, for example by stabilizing high active site dispersion, or enhancing reagent diffusion during catalytic reactions when bulky substrates are employed.[33]

The incorporation of macropores into mesoporous architectures offers an alternative strategy to minimize diffusion barriers, and potentially enhance the distribution of active sites during catalyst preparation. Simulations suggest that in the Knudsen diffusion regime, where reactants/products are able to enter/exit mesopores but experience attendant diffusion, such bi-modal pore structures can significantly improve active site accessibility. The first hierarchical macroporous–mesoporous material was report in 1998 by Yanget al.,[34] although only recently has their application in catalytic processes been exploited. Degradation of organic dye molecules in aqueous solutions, such as rhodamine B, methylene blue, and sulforhodamine B, is widely used to evaluate the photocatalytic performance of the porous metal oxides. The catalyst creates electron–hole pairs under light radiation, which in aqueous media generates free radicals (hydroxyl radicals: $OH^{\cdot}$) able to undergo secondary reactions. Photoelectrolysis of water (water splitting) for the production of H_2 and O_2 by semi-conductor metal oxides (e.g., TiO_2, Ta_2O_5, WO_3, $BiVO_4$) has been intensively studied.[35] A micro-meso-macroporous titanium silicate has shown excellent activity in the chemically demanding oxidation of saturated hydrocarbons to alcohol and ketones,[36] with conversions five-times that of mesoporous analogues, and twice that of micro-porous equivalents.

Amino-functionalized silica exhibiting sea urchin morphology,[37] having mesoporosity and limited macroporosity, has been used to support Au nanoparticles via deposition–precipitation. This catalyst can reduce 2-nitroaniline, and is superior to Au

deposited on amino-functionalized SBA-15 and MCM-41, possibly due to the sea urchin superstructure facilitating more efficient diffusion. Ordered mesoporous chromium (III) oxide–phosphotungstic acid nanocomposite structures with controllable composition (17 to 49 wt% in PWA) have been successfully prepared via an ultrasound-assisted nanocasting route, using mesoporous SBA-15 silica as a rigid mold.[38] The integration of regular porosity, large internal surface area, and Cr_2O_3–PWA composition makes these materials highly promising for applications in oxidation catalysis of selected secondary benzyl alcohols, giving good-to-high yields within a short reaction time. The mesoporous CeO_2, Co_3O_4, Cr_2O_3, CuO, Fe_2O_3, ß-MnO_2, Mn_2O_3, Mn_3O_4, NiO, and $NiCoMnO_4$ were investigated as catalysts for CO oxidation.[39]Among them, mesoporous Co_3O_4, ß-MnO_2, and NiO showed appreciable CO conversions. El-Safty, et al,[40] reports NiO-supported cage silica monoliths as effective catalysts toward the oxidation of phenolic pollutants. The NiO nanoparticles with irregular sizes might be embedded, to some extent, into the pore cavity (**Chapter 2)**

1.2.2. Adsorption and separation

Porous materials used as stationary phases in high performance liquid chromatography [41] or as adsorbents for heavy metals, anions, organic pollutants, and gases. Adsorption by solid adsorbents shows promising and efficient methods for environmental remediation, purification and separation of contaminants. Commonly activated carbon used as adsorbents for dyes due to its immense active surface area. For example, a highly mesoporous activated carbon fiber (Y-ACF) has been used to adsorb various types of dyes such as acid dyes (acid blue 9, acid blue 74, acid orange 10, and acid orange 51), direct dyes (direct black 19, direct yellow 11, and direct yellow 50), and basic dyes (basic brown 1 and basic violet 3). Then, silica-based materials employed to adsorb dyes due to their high specific surface. The modification of the silica surface by a cationic polyelectrolyte (chitosan) enabled to produce composed materials, which may be capable of adsorbing both cationic (rhodamine B) and anionic (tectilon blue) dyes. In addition, mesoporous aluminosilicate investigated to adsorb dyes based on colorimetric adsorption methods, in which the monitoring process of the dye removal could be easily controlled through the colorimetric recognition.[42]

Ferrihydrite prepared by using silica gel as a hard template is an excellent sorbent for the removal of heavy metals from waste streams.[43] Various organo-functionalized

mesoporous materials such as thiol, thioether, and amino groups have been reported for metal-ion removal and dye adsorption, and the adsorption capacity and selectivity are good. If these functionalized hybrid materials possessed magnetic properties, the composite adsorbents would be easily separated from aqueous systems by an external magnetic field, and lower operational costs in absorbent separation and the recycling of adsorbent materials could easily be achieved. [44] Through a vacuum nanocasting route, Shi and coworkers synthesized a kind of thioether functionalized mesoporous aluminosilicate hollow spheres with magnetic cores. These nanocomposites exhibited highly selective adsorption for Hg^{2+} and natural magnetic separation.[45]

The NO adsorption and release behavior of various mesoporous metal oxides was investigated. Mesoporous α-Fe_2O_3, β-MnO_2, Mn_2O_3, Mn_3O_4, and NiO exhibited little or no adsorption of NO. Mesoporous Cr_2O_3 and Co_3O_4 demonstrated modest adsorption capacities (0.12 and 0.58 mmol/g, respectively). On the other hand, the adsorption capacities of mesoporous Cu–Cu_2O and CuO were much higher (0.97 and 1.25 mmol/g, respectively). CO adsorption on mesoporous CuO was also investigated between 30 and 120 ^oC. These copper oxides particles containing porous network are active for CO adsorption and have potential medical applications.[14]

The pore size and pore uniformity of mesoporous materials may make them suitable for the separation of macromolecules. Recently, El Safty et al., suggested a size – selective encapsulation approach of proteins with different shapes, sizes, and functions using mesocage alumina[46] or mesocylindrical aluminosilica.[47] The unique physical properties and surface functionality of the mesocaptors enhanced protein adsorption characteristics in terms of loading capacity and quantity of the sample. These tunable pore cavities ensuring a higher concentration of adsorbed proteins, interior pore diffusivity, and encapsulation in a short period. on the other hand, super-paramagnetic silica/iron oxide nanocomposites with mesostructured porosity have been used for immobilization and separation of biomolecules such as lysozyme, cytochrome C.[48] Hyeon et al., found the exposed NiO NPs possess selective adsorption towards Histidine tagged (His-tagged) protein from the mixed-protein solution, as well as Escherichia coli (E. coli) lysate, and the magnetic core allows the particles to be separated from the solution by applying an external magnetic field (**Chapter 3)**.[49]

1.2.3. Sensing applications

1.2.3.1.Gas sensor

The capacitive sensor approaches used for gases with high permittivity values, such as water vapour or ammonia, but not so much for, e.g., methane (CH_4). Therefore, humidity sensing is the main application of mesoporous materials within the field of capacitive sensing. The main advantage of using mesoporous silica for capacitive humidity sensing instead of the commonly used organic polymers lies in its stability at high temperature (>200^{o}C). These features allow the fabrication of humidity sensors capable of controlling industrial processes under harsh conditions, such as in textile drying.[50] In a resistive gas sensor the sensitive layer, most frequently a semiconducting metal oxide, changes its electronic (or ionic) resistance upon interaction with the respective target gas. This is the most common type of gas sensor due to the simple and robust function and low-cost of manufacturing; first devices were introduced as early as 1962. The impact of the target gas on the overall electronic resistance of the sensing material is a complex process. Starting from pure mesoporous silica, the next-simplest synthesis strategy to create a resistive sensor is to incorporate semiconducting metal oxide particles inside the silica pores. These need to be in sufficient contact with each other while at the same time leaving a substantial pore volume unoccupied. Such systems have been reported to exhibit promising gas sensing properties. For example, a (non-ordered) porous silica material with palladium-doped SnO_2 nanoparticles inside its pores showed good sensitivity to CO. Recently, El Safty and co workers[51] suggested highly sensitive and selective volatile organic compound (acetone, benzene, and ethanol) gas sensors based on mesoporous silica nanocomposite monoliths. Monoliths with various loadings of semiconducting metal oxides (SnO_2, ZnO, NiO, CuO, and Fe_2O_3) were prepared through instant direct-templating method. Moreover, the sensor response was not only dependent on the specific surface area, but also on the geometries and crystal size of materials. In Optical gas sensor, the mesoporous silica materials with their optical transparency are ideally suited as host matrices for embedding dye molecules in order to create optical sensors. For example, a very efficient oxygen sensor was fabricated by embedding a Pt-porphyrin system in the pores of mesoporous MCM-41 silica; strong sensitivity to oxygen in low concentrations as well as fast response and recovery were observed (Figure 1.7)

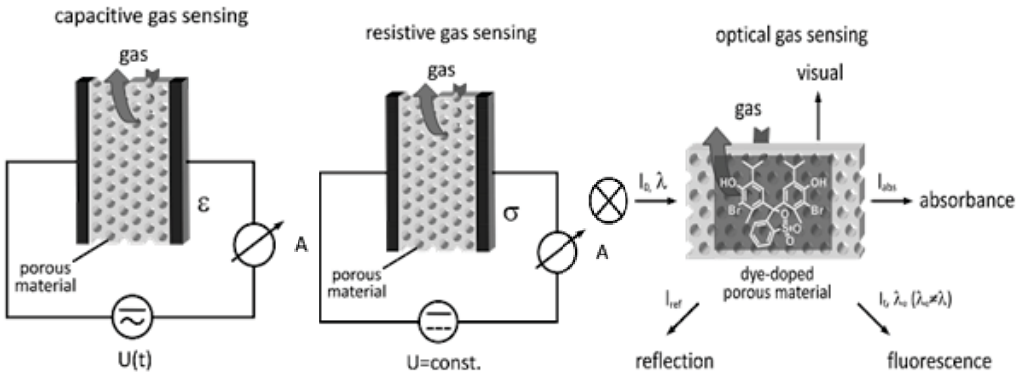

Figure 1.7: Schematic setup of (A) capacitive sensor, B) resistive sensor, and C) optical gas sensnors.

1.2.3.2.Chemosensor

Environmental pollution is a constant problem, since it affects human health and the sustainable development of both society and the economy. The selective sensing of cyanide anions in water by using a hybrid biomaterial composed of a mesoporous TiO_2 film of crystalline nanoparticles and the protein hemoglobin has also been reported. Low levels of cyanide (0.2 ppm) can be detected by monitoring the absorption changes of the hybrid biomolecular films upon cyanide binding to the hemegroups.[52] Owing to the stability, selectivity, high density of binding sites and ease of modification, mesoporous organosilicas are suitable candidates to be employed as optical indicators of target binding. The mesoporous organosilicas containing porphyrins showed extremely sensitive to TNT(2,4,6-trinitrotoluene), RDX (cyclotrimethylenetrinitramine), p-nitrophenol and p-cresol, with selective adsorption of TNT over the other analytes.[53]

In order to monitor metal ions in environment, a simple, inexpensive, rapid responsive and portable sensors or collectors should be developed. Selective optical sensing is attracting strong interest due to the use of "low-tech" spectroscopic instrumentation to detect relevant toxic chemical species in biological and environmental processes. Various rational strategies for developing the optical sensors based different types of reagents such as chromogenic, fluorescent and ionophoric compounds. A highly sensitive, low cost, simple nanosensor designs were successfully developed by the immobilization of hydrophobic and hydrophilic chromophore molecules into spherically nanosized pore cavities and surfaces. These new classes of optical mesoporous sensors exhibited long-term stability of signaling and recognition functionalities that in general provided extraordinary sensitivity, selectivity, reusability, and fast kinetic detection and

quantification of various metal ions in our environment and biological samples. Generally, the binding sites for the metal ions interaction with selected receptor were incorporated either through non-covalent bonding, such as hydrogen bonding, metal coordination, hydrophobic forces, van der Waals forces, π-π interactions, and electrostatic and/or electromagnetic effects. Figure 1.7 shows the fabrication routs for the optical sensors, which involved direct-grafting approach, Dispersion approach, post-grafting approach, and building-block approach. The general fabrication design of optical sensors can be concluded in three steps as follows;[54]

1.2.3.2.1. Fabrication of solid mesoporous carrier.

The fabrication strategies have been described briefly in the previous section 1.1.1.

1.2.3.2.2. Surface activation;

The mesoporous silica has been activated through many routes via cationic or anionic surfactant in order to design hybrid mesoporous silica. Silanol groups at the surfaces of mesoporous silicas can be grafted with organosilanes, common examples of which are 3-aminopropyltrimethoxysilane (APTMS), 3-mercaptopropyltrimethoxysilane (MPTMS), and hexamethyldisilazane (HMDS).

1.2.3.2.3. Optical sensing

Successful design of chemical sensors, in principle, requires controlled assessment processes, which involve evaluation of intrinsic properties of the sensors (i.e. sensitivity, selectivity, reversibility and stability) and their fabrication and operating cost. Recent developments illustrate the capability of several grafting strategies that use hard or soft modifier coupling agents of carriers in developing optical mesoporous sensors for metal ions in environmental systems as follows (Figure 1.8);

1. Direct grafting approach
2. Dispersion approach
3. Building-block approach
4. Post - grafting approach

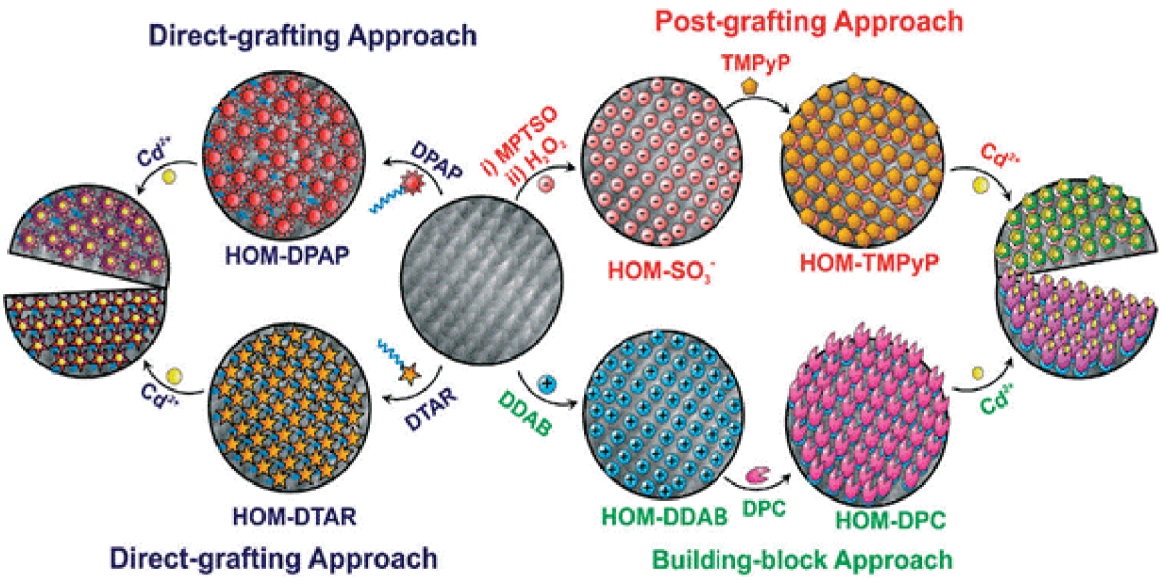

Figure 1.8: Systematic design of nanosensors 1–4 by various synthesis protocols based on the immobilization of TMPyP, DPAP, DTAR, and DPC probes into the 3D cubic Fm3mcage monoliths (HOM-C10). The 3D TEM surface micrograph of cubic Fm3m carriers (HOM-C10) recorded along the [110] zone axis with 45° tilt.

Facile and reliable synthetic designs for mesoporous optical sensors can be achieved through these pathways, namely, the covalent functionalization approach and Incorporation of indicator molecules into inorganic scaffolding by electrostatic and hydrogen bonding interactions. The later has a clear advantage, i.e., it can dispense with the tedious synthesis of a reactive silylated probe derivative. Among all the techniques for nanosensor synthesis, the linker approach is ideal for constructing sensing systems with high loading capacity and controllable flexibility of electron acceptor/donor strength of probes on the pore surfaces. This approach enables the formation of pool-on-surface sensing systems, in which a high flux and rapid diffusion of metal ions was achieved, particularly at trace-analyte levels (Figure 1.9).[55]

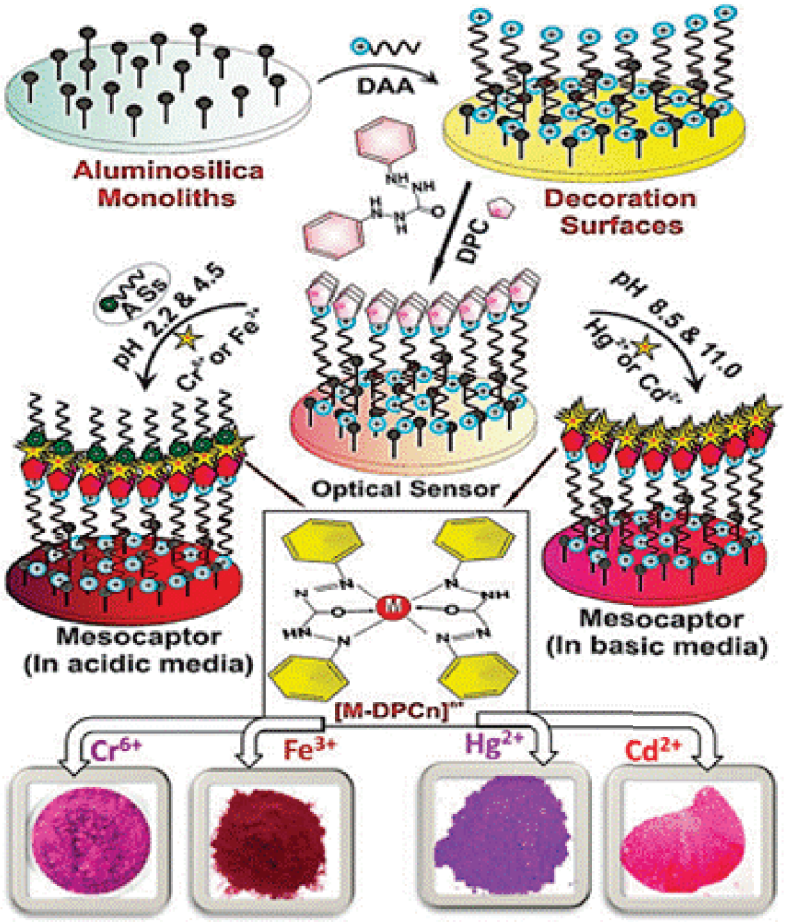

Figure 1.9: Schematic model of hybrid mesocaptor ensembles via the functionalization of the aluminosilica scaffolds with (DDAB and DPC) organic moieties for a wide range of binding site–guest (Hg^{2+},Cd^{2+},Cr^{6+}, and Fe^{3+}) stability during the sensing or capture of metals in acidic or basic media, as evidenced from the color profiles.

1.2.3.2.4. Advantage of optical mesoporous sensor

El-Safty et al., [56] used the synthesized nanostructured cage monolith as an optical sensor for the highly sensitive and selective detection and removal of sub-nanomolar concentrations of toxic metal ions, including Cd(II), Hg (II), Zn (II), Cu (II), Co (II), Sr (II), Cr(III),… etc . This quantitative and qualitative detection method is based on the color changes of probe sensors. In general, optical nanosensors based on mesoporous silica monoliths have numerous advantages and significant features, which are summarized as follows:

1) Simple synthesis of microsized mesoporous monoliths, which result in low operating costs and easy-to-use optical sensors with different morphologies, such as rings or discs.
2) Optical sensors with multidirectional mesopore cavities as platforms enable the development of pool- or sink-like sensing assays through the easy accessibility of toxic ions and rapid ligand-metal binding events.
3) High surface area as well as large, open, cylindrical cage pores, which result in high loading and accommodation of activated surface agents and organic moieties and lead to the detection and removal of low metal ion concentrations.
4) Precise modification of the nanoscale-pore surfaces of mesoporous monoliths with organic moieties in well-defined, homogenous, and dense-patterned organization arrays, which leads to the efficient detection and removal of a wide range of concentrations of target speciesvwithout the need for any pre-concentration process.
5) Surface functionality and good adsorption characteristics of monoliths, which enable the high flux of metal analytes across the probe molecules without significant kinetic hindrance. The resultant mesosensors lead to a facile generation and transduction of optical color signals as a response to probe-metal binding events.
6) Chemical and mechanical stability of mesostructured sensors with sensing/removal assays; two key factors affect the efficient sensing functionality of the nanosensors for metal ions.

   ✧ The strong electrostatic interactions (Coulombic type) of the probes such as molecules with charged carriers lead to an increased stability of probe-based nanosensors for signal response of receptor–metal binding events.
   ✧ The ability to create highly accessible, flexible, and fine-tuned surface probes might lead to retention of the specific activity of the electron acceptor/donor strength of the probe functional group, as evidenced by the facile generation and transduction of an optical color signal as a response to complex binding events after long-term storage (on the order of months).

7) Long-term stability under storage without care for several years. No significant change in the sensing/removal efficiency and mesostructured properties has been observed;
8) High sensitivity and simple workability with fast response time and high flux of metal analytes across the probe molecules. In such mesosensor systems, the sensing signal
9) Applicability of optical nanosensors for the selective discrimination of trace levels of toxic ions from environmental samples and waste disposal systems; Thus, the efficient metal ion-selective mesosensors offer the following features:

- high tolerance level for interfering matrix concentrations, indicating the specificity of the strips to metal target at ultra-trace concentrations;
- high response speed and confidence during the detection of analytes from samples containing chemically-complex matrices;
- The calibration plot of the analytes in the presence of matrix species shows evidence of a significant correlation of the determination and precise sensing procedure of metal ions by the fabricated mesosensor strips with that of the metal ion-sensing data obtained in the presence of a high concentration of active multi-ion matrix species; and,
- Conspicuous divergence in the behavior of the probe-decorated monolith mesosensors to the metal analyte and its matrix environments from their solution chemistry.

10) Reversibility through the use of a simple chemical treatment to strip the toxic ions (Figure 1.9). Hence, these sensors are practical and inexpensive, particularly in waste water management**;**
11) Fully controlled assessment processes, sensitive quantization with high-level precision (i.e., standard calibration curves), and simple recognition and detection of a broad range of toxic metal ions through color changes or fluorescence signals at the frequency utilized by human eyes. Sophisticated methodologies or techniques are generally not required for detection, and sample clean-up procedures that minimize sample matrix interferences during the removal of metal ions are not necessary;

12) Simple separation and visual detection over a wide, adjustable range, as well as sensitive quantification, selective discrimination, reversibility, and fast-response signaling of ions at trace levels. These characteristics offer real-time applications, such as in the recycling of metals from urban mining, water treatment, and high-grade environmental chemistry.

13) pH-dependent signaling response

The development of chemosensors for the colorimetric recognition of different transition metal ions using chemically responsive dyes exhibit signaling ‘‘color changes’’ with the addition of metal ions at controlled pH solutions.[57] At specific pH values, the flexibility of the electron-acceptor/donor strength of the molecular probes on the membrane discs for a specific activity can lead to easy generation and transduction of optical color signals in response to probe-metal analyte-binding events (**Chapter 4).**

1.2.4. Electrochemical applications

1.2.4.1. Electrochemical sensors

Mesoporous materials have attracted increasing interest from the electrochemists community due to their plenty of unique properties and functionalities that can be effectively exploited in electrochemical devices. The three main intersection areas are:

I. The development/use of electrochemical methods to characterize the properties of mesoporous materials (i.e., charge and mass transfer processes);
II. The generation of mesostructured solids by electro-assisted deposition using appropriate templates; and
III. The application of these novel materials for electrochemical purposes.

The straightforward detection scheme is the direct detection of target analytes at mesoporous materials modified electrodes. One can basically distinguish between the electronically conductive materials (mesoporous metals and carbons) and the nonconductive metal oxides (mainly mesoporous silica), which can be used as such or functionalized with appropriate catalysts. In this regard, mesoporous metal oxides have taken much interest. The mesoporous $Ni(OH)_2$ /NiO or Fe_3O_4/Fe_2O_3 exhibiting electrocatalytic properties towards H_2O_2[58] The immobilization of redox protein

(hemeproteins) on the mesoporous metal oxides (TiO_2 and Nb_2O_5) was investigated as biosensor for hydrogen peroxide.

Mesoporous silica-based materials were used to host mediators and deposited as thin films on electrodes or dispersed in carbon paste electrodes for electrocatalytic purposes. Zinc phthalocyanine adsorbed on Ag/Au NPs anchored onto thiol-functionalized MCM-4, which exhibited synergistic effects for the electrocatalytic reduction of molecular oxygen. A 12-tungstophosphoric heteropolyacid anions (in FSM-16) and 1:12-phosphomolybdic anions (in MCM-41) have been used as charge-transfer co-factors for the amperometric detection of NO_2^- and ClO_3^-/BrO_3^- respectively.[59] On the other hand, Several analytes have been detected using electrodes modified with mesoporous organic–inorganic hybrid materials,[60] such as Ag(I), Cu(II), Cd(II), Hg(II), Pb(II), Eu(III), U(VI). The preconcentration step was enhanced using organo-functional groups such as quaternary ammonium, sulfonate, glycinylurea, salicylamide, carnosine, acetamide phosphonic acid, benzothiazolethiol, acetylacetone, cyclam derivatives, β-cyclodextrin, 5-mercapto-1-methyltetrazole, or ionic liquids.

1.2.4.2.Electrochemical Energy storage devices

Finding innovative electrode mesoporous materials with architecturally tailored nanostructures was triggered by the need for systems (batteries, supercapacitors, fuel cells, dye-sensitized solar cells) exhibiting always better performance (extraordinarily high energy densities, high rate capabilities, high yields). Batteries and supercapacitors are two kinds of typical electrochemical energy storage devices, both of which store electricity in electrochemical processes. A rechargeable battery is usually composed of an anode, a cathode, a separator, and an electrolyte. During discharge, electrochemical reactions occur at the electrodes, generating electrons that flow through an external circuit; during charge, an external voltage across the electrodes was applied, driving the movements of electrons and reactions at the electrodes. The principles of supercapacitors include an electrical double layer and pseudo-capacitive charge-storage modes. The former is based on the separation of charges at the interface between a solid electrode and an electrolyte and the latter is a fast faradaic process involving electrochemical redox reactions.

Among the various alternative energy storage technologies, electrochemical energy storage shows advantages of high efficiency, versatility, and flexibility. Li-ion batteries

are the most important and widely used rechargeable battery with advantages of high voltage, low self-discharge, long cycling life, low toxicity, and high reliability. Supercapacitors have attracted increasing interest because of their high power storage capability, which is highly desirable for applications in electric vehicles and hybrid electric vehicles. The performance of Li-ion batteries and supercapacitors is intimately related to the electrode materials used. With the development of materials design strategies, synthesis techniques, and characterization methodologies, electrode materials and consequently the performance of batteries and supercapacitors have been progressing rapidly. Dealing with EDLCs, ordered mesoporous carbons with controlled pore sizes are promising materials to further improve the power and energy densities of capacitors as they meet two important requirements:

I. they are likely to ensure good dynamic charge propagation by facilitating fast ion and electron transportation;
II. they can be manufactured with micropores which have been recently reported to be of major importance for efficient electrical double layer formation (the pore size should ideally match the size of the ions)

As mentioned above recently, pseudo-capacitors based on mesoporous transition metal oxides have taken particular interest. Attempting to go one-step further, recent efforts have been directed to the preparation of ordered mesoporous carbon–metal oxide composites as electrode materials for supercapacitors. Examples are available for mesoporous carbon modified with ruthenium oxide, bismuth oxide, lead oxide, molybdenum oxide, cobalt oxide, or mixed metal oxides (e.g., cobalt and vanadium oxides). Following the same strategy, nanoporous metal–metal oxide hybrid electrodes have been prepared as electrochemical supercapacitors, giving rise to additional double layers and pseudo-capacitive behaviors. The interest in using pseudocapacitor-based materials for electrochemical capacitors is to overcome the limited energy densities usually obtained with EDLCs (10–20mFcm^{-2}) by exploiting faradaic reactions that are characterized by much higher energy density (~100mFcm^{-2}). Various successful examples are available, including, e.g., electrogenerated mesoporous cobalt hydroxide or nickel oxide films, mesoporous TiO_2 films obtained by Evaporation-Induced Self-Assembly (EISA), a mesoporous film of iso-orienteda-MnO_3, ordered mesoporous β-MnO_2 or Co_3O_4 prepared by nanocasting, and CeO_2 films. In conclusion, the key requirements to

maximize power and energy densities of supercapacitors are configuring redox-active materials in specific architectures that:

I. Maximize electrolyte–electrode contact area,
II. Minimize transport distances for both electrons and charge compensating species,
III. Minimize transport barriers (**Chapter 5).**

1.2.4.3.Energy conversion.

The two main devices for electrochemical energy conversion are fuel cells and solar cells. Fuel cells are electrochemical devices that convert the chemical energy of a fuel (e.g. hydrogen, methanol, etc.) and an oxidant (air or pure oxygen) in the presence of a catalyst into electricity, heat and water. Solar cells are usually divided into two categories: photovoltaics in which light is directly transformed into electricity, and dye-sensitized solar cells that utilize a light adsorbing dye (usually accommodated onto a semiconductor) with electron transfer to a counter electrode through an electrochemical reaction involving an electron transfer mediator, thus sending out a current. For fuel cells, mesoporous binary metal oxides with supported metal nanoparticles (Pt on yttria supported zirconia,Au on CeO_2/TiO_2-ZrO_2,or Ni–Fe on CeO_2-ZrO_2) were also of interest for improving the performance of fuel cell electrodes recently. On the other hand, dye-sensitized solar cells (DSSCs) are photoelectrochemical solar cells functioning based on photoinduced charge separation at a dye-sensitized interface between a nanocrystalline, porous metal oxide electrode and a redox electrolyte. Most DSSCs consist of mesoporous TiO_2 electrodes sensitized with organic dyes such as ruthenium dyes, Pt counter-electrodes, and I^-/I_3^- redox electrolytes. The role of TiO_2 is adsorption of dye molecules and transport of photo-excited electrons from the dye to the transparent conductive oxide electrode.

1.3.References

[1] J. Rouquerol, D. Avnir, C. W. Fairbridge, D. H. Everett, J. M. Haynes, N. Pernicone, J. D. F. Ramsay, K. S. W. Sing, K. K. Unger, Pure & Appl. Chem. 66, 1994, 1739–1758.

[2] International Zeolite Association, Database of Zeolite Structures "http://www.iza-structure.org/databases/".

[3] T. Yanagisawa, S. Tsuneo, T. Shimizu, K. Kuroda, C. Kato, Bull. Chem. Soc. JP., 63, 1990, 988–992; C. T. Kresge, M. E. Leonowicz, W. J. Roth, J. C. Vartuli, J. S. Beck, Nature, 359, 1992, 710–712.

[4] D. Y. Zhao, J. L. Feng, Q. S. Huo, N. Melosh, G. H. Fredrickson, B. F. Chmelka, G. D. Stucky, Science, 279, 1998, 548–552.

[5] F. Schüth, Chem. Mater., 13, 2001, 3184–3195.

[6] S. A. El-Safty, F. Mizukami,T. Hanaoka, J. Phys. Chem. B, 109, 2005, 9255-9264; S.A. El-Safty, Y. Kiyozumi, T. Hanaoka, F. Mizukami, J. Phys. Chem. C, 112, 2008,5476-5489.

[7] D. Zhao, P. Yang, D. I. Margolese, B. F. Chmelka, G. D. Stucky, Chem. Commun., 1998, 2499–2500; M. Ogawa, Chem. Commun., 1996, 1149–1150; R. Ryoo, C. H. Ko, S. J. Cho, J. M. Kim, J. Phys. Chem. B, 101, 1997, 10610–10613; H. Yang, N. Coombs, I. Sokolov, G. A. Ozin, Nature, 381, 1996, 589–592; H. Yang, A. Kuperman, N. Coombs, S. Mamicheafara, G. A. Ozin, Nature, 379, 1996, 703–705.

[8] Q. Huo, D. Zhao, J. Feng, K. Weston, S. K. Buratto, G. D. Stucky, S. Schacht, F. Schüth, Adv. Mater., 9, 1997, 974–978; F. Marlow, M. D. McGehee, D. Zhao, B. F. Chmelka, G. D. Stucky, Adv. Mater., 11,1999, 632–636; P. J. Bruinsma, A. Y. Kim, J. Liu, S. Baskaran, Chem. Mater., 9,1997, 2507–2512; P. Yang, D. Zhao, B. F. Chmelka, G. D. Stucky, Chem. Mater., 10, 1998, 2033–2036.

[9] N. A. Melosh, P. Lipic, F. S. Bates, F. Wudl, G. D. Stucky, G. H. Fredrickson, B. F. Chmelka, Macromolecules, 32,1999, 4332–4342; G. S. Attard, J. C. Glyde, C. G. Göltner, Nature, 378,1995, 366–368; P. Feng, X. Bu, G. D. Stucky, D. J. Pine, J. Am. Chem. Soc., 122, 2000, 994–995. S.A. El-Safty, Y. Kiyozumi, T. Hanaoka, F. Mizukami, Mater. Lett. 62, 2008, 2950–2953.

[10] S. Schacht, Q. Huo, I. G. Voigt-Martin, G. D. Stucky and F. Schüth, Science, 273,1996, 768–771; Q. Huo, J. Feng, F. Schüth, G. D. Stucky, Chem. Mater.,

9,1997, 14–17; Y. Lu, H. Fan, A. Stump, T. L. Ward, T. Rieker, C. J. Brinker, Nature, 398,1999, 223–226.

[11] I. Sokolov, H. Yang, G. A. Ozin, C. T. Kresge, Adv. Mater., 11,1999, 636–642; S. M. Yang, I. Sokolov, N. Coombs, C. T. Kresge, G. A. Ozin, Adv. Mater., 11,1999, 1427–1431.

[12] C. Gérardin, J. Reboul, M. Bonneb, B. Lebeau, Chem. Soc. Rev., 42, 2013, 4217—4255.

[13] S. A. El-Safty, A. Shahat, K. Ogawa, T. Hanaoka, Microporous and Mesoporous Mater. 138, 2011, 51–62.

[14] Y. Ren, Z. Ma, P. G. Bruce, Chem. Soc. Rev., 41, 2012, 4909–4927.

[15] S. A El-Safty, A. Shahat, M. Mekawy, H. Nguyen, W. Warkocki, M. Ohnuma, Nanotechnology, 21, 2010, 375603.

[16] S. El-Safty, A. Shahat, Md. R. Awual, M. Mekawy, J. Mater. Chem., 21, 2011, 5593.

[17] H. Liu, G. Wang, J. Liu, S. Qiao, H. Ahn, J. Mater. Chem., 21, 2011, 3046.

[18] F. Jiao, A. Harrison, J. C. Jumas, A. V. Chadwick, W. Kockelmann, P. G. Bruce, J. Am. Chem. Soc., 128, 2006, 5468–5474; L. Ye, S. H. Xie, B. Yue, L. P. Qian, S. J. Feng, S. C. Tsang, Y. C. Li, H. Y. He, Cryst. Eng. Comm., 12, 2010, 344–347; D. L. Li, H. S. Zhou, I. Honma, Nat. Mater., 3, 2004, 65–72; B. Smarsly, D. Grosso, T. Brezesinski, N. Pinna, C. Boissie`re, M. Antonietti, C. Sanchez, Chem. Mater., 16, 2004, 2948–2952.T. Brezesinski, C. Erpen, K. Limura, B. Smarsly, Chem.Mater., 17, 2005, 1683–1690; M. Kuemmel, D. Grosso, C. Boissie`re, B. Smarsly, T. Brezesinski, P. A. Albouy, H. Amenitsch, C. Sanchez, Angew. Chem., Int. Ed., 44, 2005, 4589–4592.

[19] J. N. Kondo, K. Domen, Chem. Mater., 20, 2008, 835–847.

[20] K. T. Ranjit, K. J. Klabunde,Chem. Mater., 17, 2005, 65–73; Q. Liu, A. Q. Wang, X. D. Wang, T. Zhang,Chem. Mater., 18, 2006, 5153–5155; J. Roggenbuck, G. Koch, M. Tiemann,Chem. Mater., 18, 2006, 4151–4156; T. Waitz, M. Tiemann, P. J. Klar, J. Sann, J. Stehr, B. K. Meyer, Appl. Phys. Lett., 90, 2007, 123108.

[21] F. Jiao, J. C. Jumas, M. Womes, A. V. Chadwick, A. Harrison, P. G. Bruce,J. Am. Chem. Soc., 128, 2006, 12905–12909.

[22] S. C. Warren, L. C. Messina, L. S. Slaughter, M. Kamperman, Q. Zhou, S. M. Gruner, F. J. DiSalvo, U. Wiesner, Science, 320, 1748-1752.

[23] A. Corma, P. Atienzar, H. Garcia, J. Y. Chane-Ching, Nat. Mater., 3, 2004, 394–397.

[24] J. Y. Chane-Ching, F. Cobo, D. Aubert, H. G. Harvey, M. Airiau, A. Corma, Chem. Eur. J., 11, 2005, 979–987; J. H. Ba, J. Polleux, M. Antonietti, M. Niederberger, Adv. Mater., 17, 2005, 2509–2512

[25] J. Hu, M. Chen, X. Fang, L. Wu, Chem. Soc. Rev., 40, 2011, 5472–5491.

[26] L. Zhu, H. Xiao, W. Zhang, G. Yang, S. Fu,Cryst. Growth Des., 8, 2008, 957.

[27] W. Cheng, K. Tang, Y. Qi, J. Sheng, Z. Liu,J. Mater. Chem., 20, 2010, 1799

[28] X. Wang, F. Yuan, P. Hu, L. Yu, L. Bai,J. Phys. Chem. C, 112, 2008, 8773.

[29] X. Cao, L. Gu, L. Zhuge, W. J. Gao, W. Wang, S. Wu, Adv.Funct. Mater., 16, 2006, 896.

[30] X. Dai, Y. Luo, W. Zhang, S. Fu, Dalton Trans., 39, 2010, 3426.

[31] C. Guo, Y. Cao, S. Xie, W. Dai, K. N. Fan, Chem. Commun., 2003, 700.

[32] M. Khairy, S. A. El-Safty, M. Ismael, Chem. Commun., 48, 2012, 10832-10834 ; M. Khairy, S. A. El-Safty, M. Ismael, H. Kawarada, Appl. Cat. B,127, 2012, 1– 10

[33] C. M. A. Parlett, K. Wilson, A. F. Lee, Chem. Soc. Rev., 42, 2013, 3876

[34] P. Yang, T. Deng, D. Zhao, P. Feng, D. Pine, B. F. Chmelka, G. M. Whitesides, G. D. Stucky, Science, 282,1998, 2244–2246.

[35] B. D. Alexander, P. J. Kulesza, L. Rutkowska, R. Solarska, J. Augustynski,J. Mater. Chem., 18, 2008, 2298–2303

[36] R. H. P. R. Poladi, C. C. Landry, Microporous Mesoporous Mater., 52, 2002, 11–18.

[37] X. Du, J. He, Nanoscale, 4, 2012, 852–859.

[38] I. Tamiolakis, I. N. Lykakis, A. P. Katsoulidis, C. D. Malliakas, G. S. Armatas, J. Mater. Chem., 22, 2012, 6919.

[39] Y. Ren, Z. Ma, L. P. Qian, S. Dai, H. Y. He, P. G. Bruce, Catal. Lett., 131, 2009,146–154.

[40] S.A. El-Safty, Y. Kiyozumi, T. Hanaoka, F. Mizukami, Appl. Cat. B, 82, 2008, 169–179.

[41] K. K. Unger, D. Kumar, M. Grun, G. Buchel, S. Ludtke, T. Adam, K. Schumacher, S. Renker, J. Chromatogr., A, 892, 2000, 47–55; C. Boissiere, M. Kummel, M. Persin, A. Larbot, E. Prouzet, Adv. Funct. Mater., 11, 2001, 129–135; J. W. Zhao, F. Gao, Y. L. Fu, W. Jin, P. Y. Yang, D. Y. Zhao, Chem. Commun., 2002, 752–

753; Y. R. Ma, L. M. Qi, J. M. Ma, Y. Q. Wu, O. Liu, H. M. Cheng, Colloid Surf., A, 229, 2003, 1–8.

[42] S.A. El-Safty, A. Shahat, Md. R. Awual, J.Colloid. Interf. Sci.359 , 2011, 9–18.

[43] A. B. Fuertes, J. Phys. Chem. Solids, 66, 2005, 741–747.

[44] J. Liu, S. Z. Qiao, Q. H. Hu, G. Q. Lu, small 7, 2011, 425–443.

[45] L. M. Guo, J. T. Li, L. X. Zhang, J. B. Li, Y. S. Li, C. C. Yu, J. L. Shi, M. L. Ruan, J. W. Feng , J. Mater. Chem. 18, 2008, 2733.

[46] S. A. El-Safty, M. A. Shenashen, M. Ismael, M. Khairy, Chem. Commun., 48, 2012, 6708–6710.

[47] S. A. El-Safty, M. A. Shenashen, M. Ismael, M. Khairy, Adv. Funct. Mater. 22, 2012, 3013–3021.

[48] X. Liong , J. Lu , M. Kovochich, T. Xia, S. G. Ruehm, A. E. Nel, F. Tamanoi, J. I. Zink, ACS Nano, 2, 2008, 889 .

[49] J. Kim, Y. Piao, N. Lee, Y. Park, I. H. Lee, J. H. Lee, S. R. Paik ,T. Hyeon , Adv. Mater. 22, 2010, 57.

[50] T. Wagner, S. Haffer, C. Weinberger, D. Klaus, M. Tiemann, Chem. Soc. Rev. 42, 2013, 4036-4053.

[51] N. D. Hoa, S. A. El-Safty, Anal. Methods, 3, 2011, 1948-1956; N. D. Hoa, S. A. El-Safty, Chem. Eur. J. 17, 2011, 12896 – 12901; N. D. Hoa, S. A. El Safty, Nanotechnology 22, 2011, 485503.

[52] K. Poland, E. Topoglidis, J. R. Durrant and E. Palomares, Inorg. Chem. Commun., 9, 2006, 1239.

[53] P.V.D. Voort, C. Vercaemst, D. Schaubroeck, F. Verpoort, Phys. Chem. Chem. Phys., 10, 2008, 347–360.

[54] S. A. El-Safty, D. Prabhakaran, Y. Kiyozumi, F. Mizukami, Adv. Funct. Mater. 18, 2008, 1739; S. A. El-Safty, D. Prabhakaran, A. A. Ismail, H. Matsunaga, F. Mizukami, Adv. Funct. Mater. 17, 2007, 3731.

[55] S. A. El-Safty, M. A. Shenashen, M. Khairy, Talanta *98,* 2012, 69; S. A. El-Safty, M. A. Shenashen, M. Ismael, M. Khairy, Md. R. Awual, Microporous Mesoporous Mater. 166, 2012, 195-205; S. A. El-Safty, M. Khairy, M. Ismeal, Sens. Act. B. Chemical, 66, 2012, 253.

[56] S. A. El-Safty, T. Hanaoka, F. Mizukami, Acta Mater. 54, 2006*,* 899; S. A. El-Safty, J. Porous Mater. 15, 2008, 369; S. A. El-Safty, T. Hanaoka, Adv. Mater. 15*,* 2008, 1893; S. A. El-Safty, D. Prabhakaran, A. A. Ismail, H. Matsunaga, F.

Mizukam, Adv. Funct. Mater. 17, 2007, 3731; S. A. El-Safty, M. A. Shenashen, TrAC, 38, 2012, 98; T. Balaji, S. A. El-Safty, H. Matsunaga, T. Hanaoka, F. Mizukami, Angew. Chem. Int. Ed. 45, 2006, 7202.

[57] S. A. El-Safty, M. A. Shenashen, A. A. Ismail, Chem. Commun., 48, 2012, 9652.

[58] B. Lu, J. Bai, X. Bo, L. Zhu L. Guo, Electrochim. Acta, 55, 2010, 8724; X. Bo, J. Bai, L. Wang, L. Guo, Talanta, 81, 2010, 339; J. C. Ndamanisha, Y. Hou, J. Bai, L. Guo, Electrochim. Acta, 54, 2009, 3935.

[59] W. Li, L. Li, Z. Wang, A. Cui, C. Sun, J. Zhao, Mater. Lett., 49, 2001, 228; L. Li, W. Li, C. Sun, L. Li, Electroanalysis, 14, 2002, 368.

[60] A. Walcarius, Chem. Soc. Rev., 42, 2013, 4098 – 4140.

CHAPTER 2

EXPERIMENTAL SECTION

2.1.Materials

All materials were of analytical grade and used without further purification. Anhydrous nickel chloride, ammonium hydroxide, o-aminophenol (o-AP), sodium acetate (NaAc), Ethylene glycol (EG), and o-aminothiophenol (o-ATP) were purchased from Japan Tokyo Chemical Industry Company Ltd. (Japan). o-AP and o-ATP solutions (0.015 mol L^{-1}) were prepared in water with 3% ethanol content at a phenol concentration of 5×10^{-4} mol L^{-1} during the oxidation process.

The ferric chloride, ferrous chloride and oleic acid were obtained from Wako Company Ltd. Osaka, Japan. Polyethyleneimine, Insulin (Ins, 5.73 kDa, 2.4 nm), Cytochrome C (CytC, 12.33 kDa, 3.0 nm), Myoglobin (Mb, 16.9 kDa, 4.0 nm), α-Amylase (α-Amy, ~54 kDa, 6.8 nm), Hemoglobin (Hb, 68.0 kDa, 7.0 nm), and Myosin (My, 200-500 kDa, ~14–19 nm) were obtained from Sigma-Adrich Company Ltd., USA.

In addition, Tetramethylorthosilicate (TMOS), dodecane (C_{12}-alkane), aluminum nitrate enneahydrate ($Al(NO_3)_3.9H_2O$), $C_{18}H_{35}(OCH_2CH_2)_{10}OH$, polyoxyethylene(20) oleyl ether (Brij 98) surfactant were obtained from Sigma–Aldrich Company Ltd., USA. 4,5-diamino-6-hydroxy-2-mercaptopyrimidine (DSAHMP) and diphenylthiocarbazone (DZ) were obtained from Wako Company Ltd. (Osaka, Japan).

As well as, Cetyltrimethyl ammonium bromide (CTAB), amino propyl trimethoxy silane (APMS), *N*-lauroyl sarcosine sodium surfactants, and tetraethylorthosilicate (TEOS) were obtained from Sigma-Aldrich Company USA. Inorganic $PbCl_2$ and other salts used in buffers for the preparation of PBS was purchased from Wako Company (Osaka, Japan). *N*-2-Hydroxyethylpiperazine-*N*-2-ethanesulfonic acid (HEPES) and cationic surfactant *N*-dodecyl-*N,N*-dimethyl-1-dodecanaminium bromide (CS-DAT) were purchased from Tokyo Chemical Co. (Tokyo, Japan). Buffer solutions of either 0.01 M sulfuric acid or 0.2 M KCl-HCl and CH_3COOH-CH_3COONa were used to adjust the pH in the 1 to 6 range. A mixture of 2-(cyclohexylamino) ethane sulfonic acid (CHES), 3-morpholinopropane sulfonic acid (MOPS), and *N*-cyclohexyl-3-aminopropane sulfonic acid (CAPS) was used to adjust the pH in the 7 to 12 range by using 0.2 M NaOH. MOPS and CAPS were purchased from Dojindo Chemicals (Kumamoto, Japan).

2.2.Fabrication of mesoporous metal oxides and control experiment

2.2.1. Mesoporous nickel oxides with hexagonal nanoplatelet mosaics.

Multidirectional micro-, meso-, and macropore NiO platelet mosaic catalysts were fabricated via a one pot and eco-friendly method. In a typical procedure, 2.58 g anhydrous nickel chloride was dissolved in 60 mL of distilled water and 20 mL of ethylene glycol (EG). The pH of the solution was adjusted to 10 via drop-wise addition of ammonia solution (28%). Then, the solution was loaded into the Teflon liner of a stainless steel autoclave with a volume of 100 mL. The autoclave was sealed and maintained at 160 °C for 6 h, and then the solution was allowed to cool to room temperature. Finally, the precipitate was obtained and washed several times with distilled water and ethanol to remove remaining agents. The precipitate collected by filtration, dried at 45 °C overnight and carefully calcined in air by heating at 2 C°/min from room temperature up to 300 °C. The product was maintained for 2 h to obtain the NiO nanoplatelet-like morphology. The porous NiO nanocatalyst was formed through the thermal decomposition of $Ni(OH)_2$. The generation of mesopores within the NiO nanoplatelet samples was attributed to the dehydroxylation of $Ni(OH)_2$ and growth of NiO NCs at high-temperature treatments without changes in the nanoplatelet morphology.

2.2.2. Mesoporous nickel oxides with flower-like morphology.

The NiO NFs were synthesized using a one-pot hydrothermal method in the presence of EG and NaAc. During typical synthesis, 20 mmol of anhydrous nickel chloride precursor was dissolved in 40 mL of EG, followed by 40 mmol of anhydrous NaAc, which were then combined through sonication. The solution was loaded into a 100 mL Teflon-lined, stainless steel autoclave at 180 °C for 6h. The solution was then allowed to cool to room temperature. Finally, the precipitate was collected and washed ten times with distilled water and ethanol to remove the remaining agents, after which it was dried at 60 °C.

2.2.3. Mesoporous nickel oxides with sphere-like morphology.

A combination of 1.47 g nickel chloride precursor and 4.5 g of anhydrous NaAc were dissolved in 25 mL Triethanol amine diluted in a 50 mL deionized H_2O plus 2.0 g polyethyleneimine. The solution was transferred to a 100 mL Teflon-lined, stainless steel autoclave, which was sealed and maintained at 200 °C for 8 h and then cooled to room

temperature. The precipitate was collected and washed ten times with distilled water and ethanol to remove the remaining agents and was then dried at 45 °C. Finally, NiO powder was calcined at 270 °C for 30 min with a heating of 2 °C/min.

2.2.4. Mesoporous nickel oxides with rectangular nanoplatelet.

Approximately 2.58 g of nickel chloride hexahydrate precursor and 3.2 g of anhydrous NaAc were dissolved in a mixture of 40 mL of EG and 10 mL de-ionized water. The solution was loaded in a 100 mL Teflon-lined, stainless steel autoclave, which was then sealed and maintained at 200 °C for 6 h. Subsequently, the solution was allowed to cool at room temperature. The precipitate was then collected and washed several times with distilled water and ethanol to remove the remaining agents, and was dried at 45 °C. The NiO powder was calcined at 270 °C for 2 h with a heating rate of 2 °C/min.

2.2.5. Mesoporous Fe_3O_4 nanoparticles

Approximately 9.6 g of ferric chloride hexahydrate and 4 g of ferrous chloride tetrahydrate were dissolved in 30 mL H_2O, followed by the addition of 1.7 mL Oleic acid. The solution was then heated at 90 °C, and then 40 mL NH_4OH (14%) was added. Subsequently, the temperature was maintained at 90 °C for 5 h. The precipitate was then collected and washed several times with distilled water and ethanol to remove the remaining agents, and dried at 45 °C overnight.

2.2.6. Mesoporous nickel oxides with rose-like morphology (NRs)

The NiO NRs were synthesized using a one-pot hydrothermal method in the presence of The NiO NFs were synthesized using a one-pot hydrothermal method in the presence of EG and NaAc. During typical synthesis, 20 mmol of anhydrous nickel chloride precursor was dissolved in 80 mL of EG, followed by 40 mmol of anhydrous NaAc, which were then combined through sonication. The solution was loaded into a 100 mL Teflon-lined, stainless steel autoclave at 200 °C for 8 h. The solution was then allowed to cool to room temperature. Finally, the precipitate was collected and washed ten times with distilled water and ethanol to remove the remaining agents, after which it was dried at 60 °C.

2.2.7. Microwave -assisted synthesis of NiO nanoflakes.

NiO NFs were fabricated through a microwave-assisted strategy in the presence of EG and sodium acetate (NaAc). During typical synthesis, 2.5 g of anhydrous nickel chloride precursor was dissolved in 50 mL of EG, followed by 3.32 g of anhydrous NaAc, which were then mixed through sonication. The solution was loaded into a 75 mL Teflon-lined autoclave. The autoclave was sealed and maintained at 200 °C for 3 h; the solution was allowed to cool to room temperature. The precipitate was collected and washed several times with a mixed solution of water and ethanol to remove the remaining agents, and then dried at 60 °C. NiO was obtained after calcination at 300 °C for 30 h.

2.2.8. Microwave -assisted synthesis of hexagonal NiO nanoplatelets.

In a typical procedure, 2.0 g of anhydrous nickel chloride and 0.5 g of SO were dissolved in 50 mL of distilled water. The pH of the solution was adjusted to 10 through the dropwise addition of ammonia solution (28%). The solution was subsequently loaded into the Teflon-lined autoclave with a volume of 75 mL. The autoclave was sealed and maintained at 160 °C for 1 h; the solution was allowed to cool to room temperature. Finally, the precipitate was collected, washed, and dried at 45 °C overnight and carefully calcined at 300 °C (the heating rate 2 °C/min) for 3 h under an oxygen flow.

2.2.9. Microwave -assisted synthesis of rectangular NiO nanoslices.

Up to 2.5 g of anhydrous nickel chloride was dissolved in 50 mL of distilled water. The pH of the solution was adjusted to 10 through the dropwise addition of ammonia solution (28%). The mixture was then loaded into a Teflon-lined autoclave with a volume of 75 mL. The autoclave was sealed and maintained at 160 °C for 2 h; the solution was allowed to cool to room temperature. Finally, the precipitate was collected, washed, and dried at 45 °C overnight and carefully calcined at 300 °C (the heating rate 2 °C/min) for 3 h under an oxygen flow.

2.2.10. Synthesis of mesoporous aluminosilica mesocages and optical sensor

Mesocage cubic aluminosilica monoliths were fabricated by using direct templating method of microemulsion liquid crystalline phase of Brij 98 as template. Based on the previous report, the liquid crystalline phases formed at definite Brij 98/ TMOS/$Al(NO_3)_3$.

$9H_2O$ concentration ratios to form the quaternary system (Brij 98/ TMOS: $Al(NO_3)_3.9H_2O$ / C_{12}-alkane /HCl(aq), pH 1.3). To obtain samples with aluminum contents at Si/Al ratio of 19, 4, 2.3 and 1, the composition of $Al(NO_3)_3.9H_2O$ was varied. For example, in the direct synthesis of aluminosilica monoliths at Si/Al mole ratio of 4 and at Brij98 /TMOS mass ratio of 0.5 (w/w), the precursor solution (0.45 g of Brij 98 surfactant, 0.225 g of C_{12}-alkane, 0.9 g of TMOS, 0.256 g of $Al(NO_3)_3.9H_2O$, and 1.125 g of H_2O-HCl (pH 1.3)) was used. Homogeneous sol-gel synthesis was achieved by mixing Brij98/TMOS/ $Al(NO_3)_3$ in a 100-cm^3 beaker and then shaking at 50◦C for 2 min until homogeneous. The exothermic hydrolysis and condensation occurred rapidly by addition of acidified aqueous solution of HCl (at pH 1.3) to this homogeneous solution. The resultant surfactant/ aluminosilica solid was gently dried at room temperature for 3 h and allowed to stand in a sealed container at 25 ◦C for 1 day to complete the drying process. The organic moieties were then removed by calcination at 550 ◦C for 7 h.

Mesoporous cubic aluminosilica mesocaptors were fabricated through the direct immobilization of ethanol solution/10 mg DSAHMP and DZ ligands into 0.5 g monolith carriers. The impregnation procedure was performed under vacuum at 25 °C until probe saturation was achieved. The ethanol was removed using a gentle vacuum connected to a rotary evaporator at room temperature, leading to the direct contact of the dye probe into the mesoporous aluminosilica. The immobilization process was repeated several times until the equilibrium adsorption capacity of the DSAHMP and DZ probes reached saturation. The resulting mesoporous aluminosilica sensor was thoroughly washed with deionized water until no elution of DSAHMP and DZ colors were observed. The sensors were dried at 60 °C for 2 h.

2.2.11. Optical detection/recovery of Cu(II) and Zn(II) ions

The Cu(II) and Zn(II) analytes were removed, determined, and visually detected from drinking water using DSAHMP and DZ receptor-doped mesoporous aluminosilicas. To check the optical removal efficiency, we assayed the mesocaptor at various pH solutions by adjusting the pH level to approximately 2 (using 0.2 M of KCl/HCl/H_2SO_4), 4and 6 (using 0.2 M of CH_3COOH/CH_3-COONa with 0.1 M NaOH), and 7 (using 0.2 M of 3-morpholinopropane sulfonic acid, MOPS) in specific amounts (10 mg to 20 mg) of cubic aluminosilica captors at constant volume (20 cm^3) with shaking. After completing the Cu(II) and Zn(II) ions-removal process from the solution, the solid captors were collected

through suction and using a 25-mm-diameter cellulose acetate filter paper (Sibata filter holder). Given the changes in the captor color with Cu(II) and Zn(II) ions adsorption, the naked-eye and solid-state UV–vis spectrophotometer can be used for the qualitative and quantitative estimation of Cu(II) and Zn(II) ions. The aluminosilica monolith captors were ground to fine powder disks to achieve homogeneity in the reflectance spectra. Our previous studies revealed that the ground monolith-based sensor did not lose its utility or functionality in terms of fast response time and sensitivity. The concentration of Cu(II) and Zn(II) ions was also analyzed using a Seiko SPS-1500 inductively coupled plasma atomic emission spectrometer (ICP-AES) before and after detection. To ensure accuracy and precision of the analyte ion sensing system, we conducted successive measurements using wide-range concentrations of the standard "well-known" solutions of analyte ions.

2.2.12. Synthesis of mesoporous core/double silica

Typically, three consecutive steps were used to fabricate mesoporous core/double-shell. First, in a beaker, 1.75 mL NH_4OH, 23 mL absolute ethanol, and 4 g deionized water (DIW) were mixed at 30 °C; then 3 g tetraethylorthosilicate (TEOS) was added, and the resulting solution was stirred for 30 min. The highly dense inner core of the silica nanoparticles was used as a template for the assembly of the double mesoporous shells. Second, the inner shell was formed by using a second beaker in which 3 g DIW, 0.5 mL amino propyl trimethoxy silane (APMS), 1 g cetyltrimethyl ammonium bromide (CTAB) and 4 mL HCl (pH 1.3) were stirred for 10 min; then 1 g sodium laurate (or 2.5 mL of *N*-lauroyl sarcosine sodium) dissolved in a solution of HCl:DIW (1:5, v:v) at pH 1.3 was added. Third, to enhance the formation of the stable outer shell, the addition of anionic surfactant sodium laurate was followed by the addition of TEOS at the mass ratio of 1:4. The reaction with TEOS was conducted at 50 °C for 6 h. The as-made, solid sample was collected and dried at 60-80 ^{o}C for 6h in sealed condition. The solid double core-shell sample was thoroughly washed with EtOH under stirring for 6 h at 50 ºC. The solid sample was collected, and then dried at 100 ºC before use as a scaffold for the synthesis of the sensor.

2.2.13. Synthesis of 4-dodecyl-6-(2-pyridylazo) phenol (AC-LHT)

Sodium ethylate solution was obtained by dissolving metallic sodium (1.2 g) in dehydrated ethanol (18.5 mL). To this, 2-amino pyridine (5 g, 0.053mol) was dissolved in the minimum quantity of ethanol (5 mL), and isoamyl nitrite (6 g), was added drop-wise. The mixture was refluxed gently for 2-2.5 h, the diazotate forming as a brown solid. Coupling reaction with an equimolar ratio of 4-dodecylphenol (13.9 g, 0.053 mol)

dissolved in absolute alcohol (20 mL) was carried out directly, without isolation of the very unstable diazotate, cooled in an ice-bath. The product was obtained as a viscous brownish- red semi-solid, which was purified by water washings, followed by chloroform extraction and elimination of solvent in vacuum. The purity of the product was analyzed by CHNS elemental analyses, ^{1}H and ^{13}C NMR spectroscopy. The data were as follows:

^{1}H NMR (400 MHz, $CDCl_3$): 0.86 (t, *J* = 7.0 Hz, 3H, CH_3), 1.19-1.53 (m, 16H, 8xCH_2), 1.86 (p, *J* = 7.2 Hz, 2H, CH_2), 2.73 (t, *J* = 7.6 Hz, 2H, CH_2), 8.96 (d, J = 8.8 Hz, 1H, PyH), 8.32 (d, 1H, PyH), 7.88 (d, 1H, PyH), 8.08 (d, 1H, PyH), 7.21 (d, 1H, ArH), 7.33 (d, 1H, ArH), 6.61 (d, 1H, ArH), 5.39 (s, 1H, OH) ; **^{13}C NMR** (100 MHz, $CDCl_3$): □ 14.8 (CH_3), 22.7 (CH_2), 29.2 (CH_2), 29.4 (CH_2), 29.5 (CH_2), 29.6 (CH_2), 29.6 (CH_2), 29.7 (CH_2), 29.7 (CH_2), 29.7 (CH_2), 29.8 (CH_2), 32.1 (CH_2), 160.1 (Py, C), 143.7 (Py, CH), 139.1 (Py, CH), 122.1 (Py, CH), 119.1 (Py, CH), 106.1 (C), 121.1 (CH), 134.2 (CH), 132.3 (C), 138.1 (CH), 170.2 (C-OH); **CHN**: Calcd (%):**C,** 75.2; **H**, 8.99; **N,** 11.44, as consistent with $\mathbf{C_{23}H_{33}ON_3}$ molecular formula, which required **C**, 75.62; **H**, 9.07; **N,** 11.21; **UV-Vis** (Medium: 50% EtOH): λ_{max} - 402 nm, ε = 1.21 x10^4 dm^3 $mol^{-1}cm^{-1}$. (Py denotes pyridine).

2.2.14. Synthesis of the hierarchically organic–inorganic multi-shelled sphere sensor

The mesoporous multi-shelled sensor design through four consecutive steps was undertaken. The first step was the formation of the silica core composed of mesopores through the excessive condensation of alkoxysilane under mild basic conditions. The highly dense inner core of the silica nanoparticles was used as a template for the assembly of the double mesoporous shells. In the second and third steps of the synthesis, the direct and stepwise addition of a precursor solution containing aminopropyl trimethoxysilane (APMS)/cetyltrimethyl ammonium bromide / sodium laurate / tetraethylorthosilicate (TEOS) caused a simultaneous interaction between the interior and exterior silica cores of the sphere particles. Third, the further condensation of silica species in the sodium laurate/TEOS composition domains led to the formation of double mesoporous core-shell silica. The fourth step of the synthesis resulted in the formation of a hierarchically multi-shelled sphere sensor. The consequent decorations of the mesoporous core/double-shell silica nanosphere through the chemically responsive azo–chromophores with long hydrophobic tail AC–LHT, such as 4-n-dodecyl-6-(2-pyridylazo)-phenol, enabled us to create a unique hierarchical multi-shelled sensor. The adsorption of the probe was 40

mg/g of the sensor.

2.2.15. Preparation of NiO supercapacitor electrodes

A three-electrode cell system was used to evaluate the electrochemical performance through cyclic voltammetry (CV), galvanostatic charge–discharge techniques, and electrochemical impedance spectroscopy (EIS) on a Zennium/ZAHNER-Elektrik GmbH & Co. KG controlled by Thales Z 2.0 Software at room temperature. A 3 mm glassy carbon electrode from BAS, Inc. was used as a substrate for the mesoporous NiO material. The glassy carbon electrode was polished with a 1 μm coarse diamond polish followed by a 0.05 μm alumina suspension to provide a mirror finish. Typically, 5 mg of NiO was mixed with 100 μL polytetrafluoroethylene and dispersed in 50 mL of deionized water through sonication for 30 min. Up to 10 μL of this sample was then dropped onto the glassy carbon electrode and dried for 12 h at 45 ^{o}C in the oven before the electrochemical test. The electrochemical performance of synthesized mesoporous NiO nanostructures was evaluated using CV, galvanostatic charge–discharge, and electrochemical impedance spectroscopy in a three-electrode cell containing 2 M NaOH solution at room temperature. A platinum wire and Ag/AgCl/3M NaCl electrode were used as counter and reference electrodes, respectively. The EIS measurements were carried out at room temperature, the excitation voltage applied to the cell was 5 mV, and the frequency range was from 100 kHz to 10 Hz.

2.3.Characterization of porous metal oxides

2.3.1. Scanning electron microscopy

The morphologies of the metal oxide samples were investigated by field emission scanning electron microscopy (FESEM, JEOL model 6500). Before insertion into the chamber, the metal oxide powders were grinded and fixed to a specimen stub using a double-sided carbon tape. Then, a 10 nm Pt film was coated by anion sputtering (HitachiE-1030) at room temperature to obtain high resolution micrographs. Before sputtering deposition, the Pt target (4 in diameter, purity 99.95%) was sputter cleaned in pure Ar. The sputtering deposition system used for the experiments consists of a stainless steel chamber, evacuated down to 8×10^{-5} Pa with a turbo molecular pump backed up by a rotary pump. The Ar working pressure (2.8×10^{-1}Pa), the power supply (100 W) and the deposition rate were kept constant throughout these investigations. Moreover, to better record the SEM images of the metal oxide samples, the scanning electron microscope were operated at 15 keV.

2.3.2. Transmission electron microscopy

High-resolution transmission electron microscopy (HRTEM), electron diffraction (ED), scanning transmission electron microscopy (STEM), and energy dispersive X-ray spectroscopy for elemental mapping (STEM-EDS) were performed using a JEOL JEM model 2100F microscope. HRTEM was conducted at an acceleration voltage of 200 kV to obtain a lattice resolution of 0.1 nm. The HRTEM images were recorded using a CCD camera. STEM and STEM-EDS were carried out at a camera length of 80 cm and a spot size of 1 nm. In the HRTEM, ED, STEM, and STEM-EDS characterization, the metal oxide samples were dispersed in ethanol solution using an ultrasonic cleaner, and then dropped on a copper grid. Prior to inserting the samples in the HRTEM column, the grid was vacuum dried for 20 min.

2.3.3. X-ray analysis

Small angle X-ray scattering (SAXS) experiments were performed at room temperature. A two-dimensional (2D) confocal mirror (Rigaku Nanoviewer) and a pinhole collimator were used to obtain a focused high flux/high transmission; a monochromatic X-ray beam of CuKα radiation (λ = 1.54 Å) was also used. The 2D SAXS patterns were recorded

using a 2D detector (Bruker Hi-Star) covering a range of momentum transfer $q = (4\pi/\lambda) \sin(2\theta/2)$, from 0.2 to 10 cm^{-1}, where is the wavelength of the incident X-ray beam and 2 is the scattering angle. The value of inter-particle distance (center to center) was calculated from $d = 2\pi / q_{max}$. Wide angle powder X-ray diffraction (XRD) patterns were measured using an 18 kW diffractometer (Bruker D8 Advance) with monochromated CuKα radiation. The sample measurement was repeated three times under rotation at various angles (15◦, 30◦, and 45◦). The diffraction data were analyzed using the DIFRAC plus Evaluation Package (EVA) software with PDF-2 Release 2009 databases provided by Bruker AXS. The standard diffraction data were identified according to the databases of the International Centre for Diffraction Data (ICDD). For poor quality diffraction data, the TOPAS package program provided by Bruker AXS 2009 for profile and structure analysis was applied to integrate various types of X-ray diffraction analyses by supporting all profile fit methods currently employed in powder diffractometry.

2.5.3. N_2 adsorption/desorption isotherm

The textural surface properties and pore size distribution were determined by N_2 adsorption/desorption isotherms at 77 K with a BELSORP36 analyzer (JP. BEL Co., Ltd.). Prior to the adsorption/desorption process, all the samples were pre-treated at 200◦C for 4h under vacuum until the pressure was equilibrated to10^{-3}Torr. The specific surface area (S_{BET}) was calculated using the Brunauer–Emmett–Teller (BET) method with multipoint adsorption data from the linear segment of the N_2 adsorption isotherm. The pore size distribution was determined using nonlocal density functional theory (NLDFT).

2.3.4. ^{27}Al MAS NMR

^{27}Al Magic-angle spinning nuclear magnetic spectroscopy (^{27}Al MAS NMR) was also recorded using a Bruker AMX-500 spectrometer. ^{27}Al NMR spectra were measured at a frequency of 125.78 MHz with a 90^o pulse length of 4.7 μs. For all samples, the repetition delay was 64 s with a rotor spinning at 4 kHz for ^{27}Al NMR. The chemical shift scale was externally adjusted to be zero for ^{27}Al signal by using aqueous solution (0.33 $mol.dm^{-3}$) of $Al(NO_3)_3$. To investigate the acidic properties of aluminosilica samples, NH_3 temperature-programmed desorption (NH_3-TPD) was measured by using a BEL-Japan TPD-1S system with a quadrupole mass spectrometer.

2.5.6. X-ray photoelectron spectroscopy

X-ray photoelectron spectroscopy (XPS) was conducted using a PHI Quantera SXM (ULVAC-PHI) (Perkin–Elmer Co., USA) with monochromated Al K radiation (1.5×0.1 mm, 15 kV, 50 W).

2.5.7. Thermogravimetric and differential thermal analyses

Thermogravimetric and differential thermal analyses (TG and DTA, respectively) were measured using a simultaneous DTA-TG Apparatus TG-60 (Shimadzu, Japan).

2.5.8. Spectral analysis

The absorbance spectrum of the heterogeneous catalytic reactions was recorded using a UV-Vis spectrophotometer (Shimadzu 3150, Japan).

2.6. Mathematical equations

2.6.1. Heterogeneous catalytic reactions

The first-order rate equation

$$\ln\left(\frac{A_\infty}{A_\infty - A_t}\right) = kmt \quad (1)$$

The second-order rate equation

$$\frac{1}{A_f - A_t} = \frac{1}{A_f} + k_2 t \quad (2)$$

The activation energy E_a of the phenolic pollutants was deduced from an Arrhenius plot

$$k = \mathrm{A}\ e^{-Ea/\mathrm{RT}} \quad (3)$$

where k is the heterogeneous rate constant per gram of catalyst, R is the gas constant, and A is the frequency factor).

The other activation parameters of the free energy of activation $\Delta G^{\#}$ (the enthalpy of activation $\Delta H^{\#}$ and the entropy of activation $\Delta S^{\#}$) were calculated using Eyring's equation

$$k = \frac{h}{k_B T} e^{-\Delta \mathrm{G}^{\#}/RT} \quad (4)$$

where h is the Blank's constant and k_B is the Boltzmann constant.

2.6.2. Adsorption of pollutants or pathogens

The percentage of adsorbed amounts (X) of toxin or protein at steady state was calculated by the following equation (3):

$$\%X = (q_f/q_o) \times 100 \quad (5)$$

Where q_f is the adsorbed quantity of the proteins or toxin at steady state, and q_o is the maximum amount of protein when the adsorbed time is equal to affinity

The adsorbed amounts (q_f, mmol. g^{-1}) of the toxin or protein molecules at the steady state (equilibrium step), in which the toxin or protein was covered the particle surfaces, was determined according to the equation (4):

$q_f = (C_o - C_f)\ V/m$ (6)

Where q_f is the adsorbed amount at steady state, V is the solution volume (L), m is the mass of sorbent (g), C_o and C_f are the initial concentration and the concentration at saturation time t, respectively.

The adsorption characteristics of protein toxin molecules onto the adsorbents can be studied through the Langmuir adsorption isotherm equation as follows:

$$\frac{C_e}{q_e} = \frac{1}{K_L q_m} + \left(\frac{1}{q_m}\right) C_e \quad (7)$$

Where q_m (μmol g^{-1}) is the amount of protein or toxin molecules adsorbed to form a monolayer coverage, and K_L is Langmuir adsorption equilibrium constants. From the plot of C_e/q_e against C_e, q_m, and K_L can be determined from the slope and the intercept.

The intra-particle diffusion of proteins or toxin into particles can be determined by;

$$q_t = kt^{0.5} + C \quad (8)$$

Where k is the intra-particle diffusion rate constant and C is the intercept which indicates the boundary layers thickness. q_t is the adsorbed quantity of molecules at time (t).

The batch adsorption of proteins or toxins into the particles was analyzed by applying Lagergren's equation:

$$\frac{dq}{dt} = k_t(q_e - q_t) \quad (9)$$

By applying the initial conditions $q_t = 0$ at $t = 0$, the linear integration form of pseudo first order model can be expressed as:

$$\mathrm{Ln}\left({}^{q_e - q_t}/_{q_e}\right) = K_t t \quad (10)$$

where k_t is the rate constant (per gram adsorbent, pga) of the first-order kinetics. The free energy of the activation ($\Delta G^{\#}$), the enthalpy of activation ($\Delta H^{\#}$) and the entropy of activation ($\Delta S^{\#}$) were calculated from Eyring's equation:

$$k_t = \frac{KT}{h} e^{-\Delta G^{\#}/RT} \quad (11)$$

$$\Delta H^{\#} = E - RT \quad (12)$$

$$\Delta G^{\#} = \Delta H^{\#} - T\Delta S^{\#} \quad (13)$$

$$\mathrm{Ln}\, {k_t h}/{KT} = -{\Delta H}/{RT} + {\Delta S}/{R} \quad (14)$$

Where k is Boltzmann's constant, h is Planck's constants and T is absolute temperature. The thermodynamic equilibrium constant, K_c which is dependent upon the fractional attainment of equilibrium (f_e) of the protein or toxin adsorbed molecules deduced from the following equation:

$$K_c = {q_f}/{(1 - q_f)} \quad (15)$$

Where q_f is the ratio of the amount of molecule adsorbed at a time (q_t) to that adsorbed at infinity (q_∞), (i.e. $q_f = q_t / q_\infty$).

From the value of K_c, the Gibbs free energy change, ∆G, can be derived. The plot of ln K_c vs. 1/T, gives the numerical values of ∆H of the adsorption of protein adsorption; ∆G and ∆S using the following relations:

$$\Delta G = -RT\mathrm{Ln}K_c \quad (16)$$

$$\mathrm{Ln}\, K_c = -{\Delta H}/{RT} + {\Delta S}/{R} \quad (17)$$

Where ∆H, ∆S, ∆G, and T are the change in enthalpy, the change in entropy, the change in Gibbs free energy and temperature in kelvin, respectively. R is the gas constant and K_c is equilibrium constant.

2.6.3. Analytical quantifications of sensor

The stability constant was estimated, according to the following equation:

$$\log K_s = [ML]_S / \{[L]_S * [M]\} \quad (18)$$

where [M] refers to the concentration of metal ions in solution that have not reacted with the chelating agents, [L] represents not only the concentration of free probe ligand but also all concentrations of probes not bound to the metal ion, and the subscript S refers to the total concentration and the species in the solid phase.

The optical limit of detection (LOD) of metal ions using the capturing sensors was estimated according to the equation

$$LOD = kS_b/m, \quad (19)$$

where k = 3, S_b is the standard deviation for the blank, and m is the slope of the calibration graph in the linear range.

2.6.4. Evaluation of pseudocapacitors

The specific capacitance (C_s) was derived from CV measurements using the following equation;

$$C_s = \frac{Q}{m\,(\Delta V)} \quad (20)$$

The energy density (E_d) and power density (P_d) of the NiO pseudocapacitor were derived from CV analysis at the scan rates 1, 2, 5, 10, 20 mVs^{-1}. The energy density was calculated using the following equation:

$$E_d = \frac{1}{2} C_s (\Delta V)^2 . \quad (21)$$

The specific power density can be calculated using the following equation:

$$P_d = \frac{I\,\Delta V}{m} \quad (22)$$

where C_s is the specific capacitance in Fg^{-1}, ν is the voltammetric sweep rate in Vs^{-1}, ΔV(V) is the potential window in V, and m is the weight of NiO samples in grams.

The specific capacitance was also calculated from charge/ discharge curves using the following equation:

$$C_s = \frac{I \, x \, \Delta t}{m \, x \, \Delta V} \tag{23}$$

where C_s is the specific capacitance in Fg^{-1}, m is the mass of the active materials in grams, V is the potential drop during the discharge in V, I is the applied discharge current in A, and Δt is the discharge time in seconds.

CHAPTER 3

CATALYTIC HAND-SAFE CHEMICAL TRANSFORMATION OF ORGANIC CONTAMINANTS

1. **M. Khairy**, S. A. El-Safty, M. Ismael, H. Kawarada, *Applied Catalysis B: Environmental* 127, 2012, 1– 10.
2. S. A. El-Safty**, M. Khairy**, M. Ismael, H. Kawarada, *Applied Catalysis B: Environmental* 123– 124, 2012, 162 – 173.
3. **M. Khairy**, S. A. EL-Safty, *Current Catalysis*, 2 (2013) 17-26.
4. **M. Khairy**, S. A. El-Safty, M. Ismael, M. A. Shenashen, *Recent Research in Nanotechnology* (2012) 215-219. (Published at Cambridge, UK).

3.1. Introduction

Environmental problems, such as organic and toxic water pollutants, provide the impetus for fundamental and applied research in catalytic processes for detoxifying the pollutants. Such challenges result in the need for greener chemical products and the transformation of hazardous chemicals.[1-19] In addition, petrochemical, chemical, and pharmaceutical industries produce wastewater containing high concentrations of organic materials, which may be difficult to oxidize biologically and are extremely toxic to aquatic life.[20-24] Considering the increasing concern for public health and environmental quality, the complete removal of organic pollutants from the environment, particularly wastewater, is imperative and presents a great challenge to water suppliers.[25] Recently, different strategies to remove organic pollutants from aqueous water including adsorption,[26-27] ion exchange,[28] membrane filtration,[7-8,29] and chemical oxidation[30] have been used. A more efficient and cost-effective method of removing organic pollutants from water is needed. The chemical transformation or chemical oxidation of these pollutants is one of the most commonly adopted methods in refinery techniques to produce safe compounds. Phenolic compounds, such as aminophenols (APs),[31-32] have a variety of uses as reducing agents, intermediates in chemical synthesis, bleaching and hair dyes, and materials for photography. In addition, APs are highly important in producing phenoxazone compounds, including questiomycin A, which is related to the natural antineoplastic agent actinomycin *D*. The latter is used clinically for the treatment of certain types of cancer. APs are one of the most common organic pollutants, and their toxicity depends on relative position of the amino and hydroxyl groups, in which the toxicity of *o*-aminophenols (*o*-AP) is stronger than that of *m*-aminophenols (*m*-AP) and *p*-aminophenols (*p*-AP). According to the Natural Skincare Authority report, *o*-AP is a suspected teratogen, which has immunotoxicity, endocrine toxicity, and skin or sense organ toxicity. Meanwhile, *o*-aminothiophenol (*o*-ATP) is used as an antinematodal agent and converts oxyhemoglobin to methemoglobin; it is also used in the study of toxicity levels in human red blood cells.[33]

The design of porous metal oxide catalysts has attracted extensive attention because such materials have potential for environmental applications.[34-35] To satisfy the requirements of these applications, large-scale production, low-cost manufacturing, and efficient transformation reactions are needed. The practical design of nanocatalysts

requires controlled assessment processes, which involve high-performance molecular transport and adsorption of pollutant molecules into the pore networks. Hence, the preparation of porous NiO-based catalysts that are simple, easy to use, and have appropriate dynamic working ranges still remains a challenge. In the present study, a simple and reproducible fabrication method of porous NiO NPs with hexagonal nanoplatelets (NPLs), nanflowers (NFs) and nanospheres (NSs) were reported. The NiO NPLs exhibit multidirectional pore cavities however, the NiO NFs and NSs present large mesocage cavities. The significant key point of this study is the NiO NPLs show controlled size and shape of hexagonal platelets in condensed orientation sequence "tesserae blocks," leading to the formation of a mosaic-like morphology. The mosaic features of NiO NPLs induce higher catalytic activity toward transformation of phenolic pollutants to safe substances than that of NiO NFs and NiO NSs (Figure 3.1). However, the NiO NFs are capable of the high-gradient magnetic separation of organic contaminants from aquatic life, which may help in wastewater management and supply. Moreover, NiO platelet mosaic catalysts significantly offer highly stable catalytic activity more than NFs and NSs even after several reuse cycles. To understand the proposed chemical transformation mechanism of pollutants, the energy profiles and the charge distribution of the reactants, intermediates, transition states, and products were calculated through the density function theory (DFT) method.[36]

In these sections focused on the transformation of phenolic pollutants onto mesoporous NiO NPLs, NiO NFs and NiO NSs fabricated via simple hydrothermal methods.

3.2.Multi-directional porous NiO nanoplatelets as catalyst for green chemical transformations

A simple and reproducible fabrication method of hierarchical NiO NCs with hexagonal nanoplatelets and micro-, meso-, and macropore cavities is reported. The proposed approach shows evidence of controlled size and shape of hexagonal NiO platelets in condensed orientation sequence "tesserae blocks," leading to the formation of a mosaic-like morphology. The porous NiO nanocatalyst was formed through the thermal decomposition of $Ni(OH_2)$ [Figure 3.1]. The generation of mesopores within the NiO nanoplatelet samples was attributed to the dehydroxylation of $Ni(OH)_2$ and growth of NiO NCs at high-temperature treatments without changes in the nanoplatelet morphology.

The mosaic features of NiO NCs induce high catalytic activity that enables the chemical transformation of phenolic pollutants into safe substances (Figure 3.2). NiO platelet mosaic catalysts significantly offer highly stable catalytic activity even after several reuse cycles.

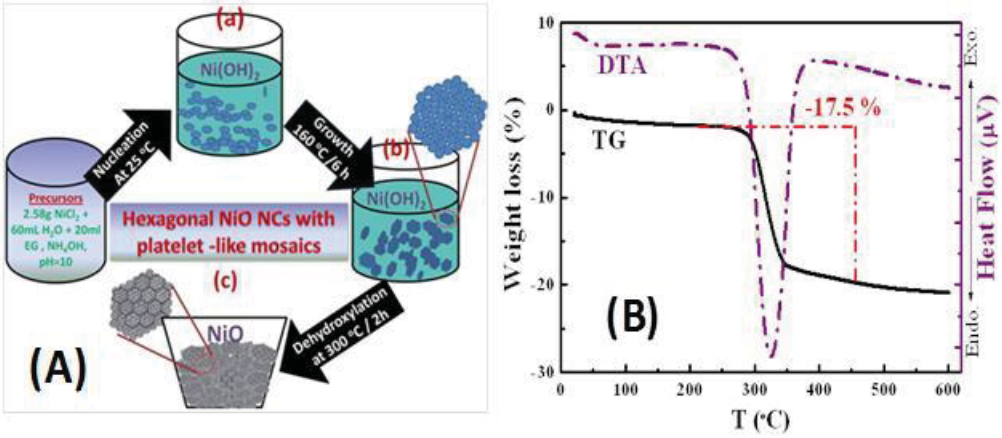

Figure 3.1: A) The formation mechanism route of nickel oxide platelet mosaics (a) formation of $Ni(OH)_2$ particles, (b) hydrothermal products of $Ni(OH)_2$ nanoplatelets, and (c) hexagonal NiO nanoplatelet mosaics formed during the thermal treatment of $Ni(OH)_2$ at 300 °C for 2 h (B)

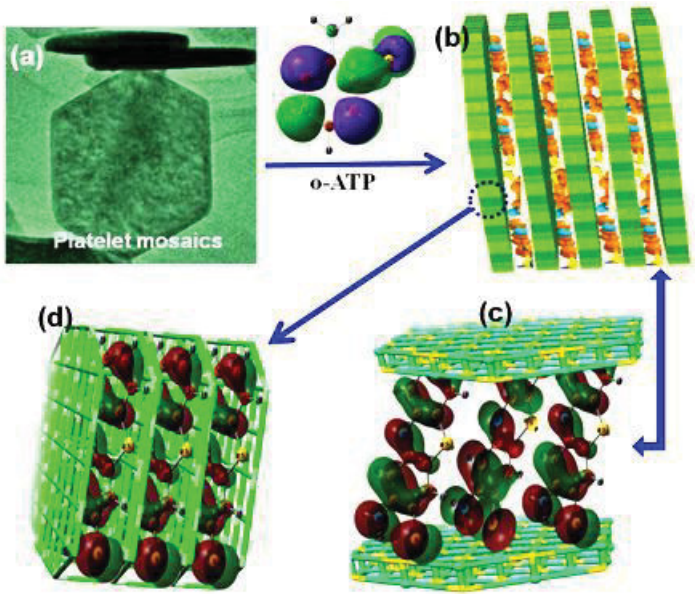

Figure 3.2: Schematic of the chemical transformation of *o*-aminothiophenol over the NiO nanoplatelet-like mosaics; (a) HRTEM micrograph of NiO NCs with platelet-like morphology; (b) *o*-ATP molecules penetrating the nanoplatelet; (c) formation of 3-aminophenothiozine-3-thizone between platelets; (d) formation of 3-aminophenothiozine-3-thizone inside the pores of the platelets

3.2.1. Formation of porous NiO nanoplatelet catalysts

The possible mechanism behind the formation of the NiO nanoplatelets (Figure 3.1) involved three stages: nucleation, growth, and dehydroxylation. Nucleation, that is, the precipitation of Ni^{2+} in pH 10 as $Ni(OH)_2$, proceeded too rapidly to generate nuclei. Second, the $Ni(OH)_2$ nanoplatelets were formed via a hydrothermal technique. The addition of EG to the synthesized composition was key to the controlled hexagonal morphology with dense and condensed orientation during the growth of the NCs. The controlled size and shape of the hexagonal NiO platelets in the condensed orientation sequence "tesserae blocks" significantly led to the formation of mosaic-like structures. Third, the dehydroxylation of $Ni(OH)_2$ under mild thermal treatment led to the generation of micro-, meso-, macroporous NiO with hexagonal platelet-like mosaics. The thermal decomposition of $Ni(OH)_2$ moieties was studied using thermogravimetry-differential thermal analysis (TG-DTA) techniques. The TG profile (Figure 3.1B) revealed the decrease in the mass of $Ni(OH)_2$ decreased at around 270 °C to 340 °C. This decrease was accompanied by an endothermic peak in the corresponding DTA curve, indicating the dehydroxylation of $Ni(OH)_2$. The weight loss from the decomposition of $Ni(OH)_2$ was 17.45 wt%, which is consistent with that in previous reports.[37]

3.2.2. Design of multidirectional micro-, meso-, and macroporous NiO nanoplatelet mosaic catalysts.

Control over the particle morphology of $Ni(OH)_2$ and NiO was evident (Figure 3.3). Field emission-scanning electron microscopy (FE-SEM) micrographs revealed that $Ni(OH)_2$ and NiO had nanosized tesserae block (mosaics) particles with an average diameter of 150 nm to 250 nm and a thickness of about 20 nm. These mosaic particles were arranged in hexagonal platelets with smooth fine surfaces, according to the conditions of the synthesis. Furthermore, these results [Figure 3.3 (c and e)] indicated the retention of hexagonal nanoplatelets during the formation of NiO under temperature treatment at 300 °C. SEM images showed significant evidence of shape- and size-controlled NiO platelets in condensed orientation sequences, indicating the versatility of this method over the real control of the NiO mosaic geometry [Figure 3.3 (c and d)].

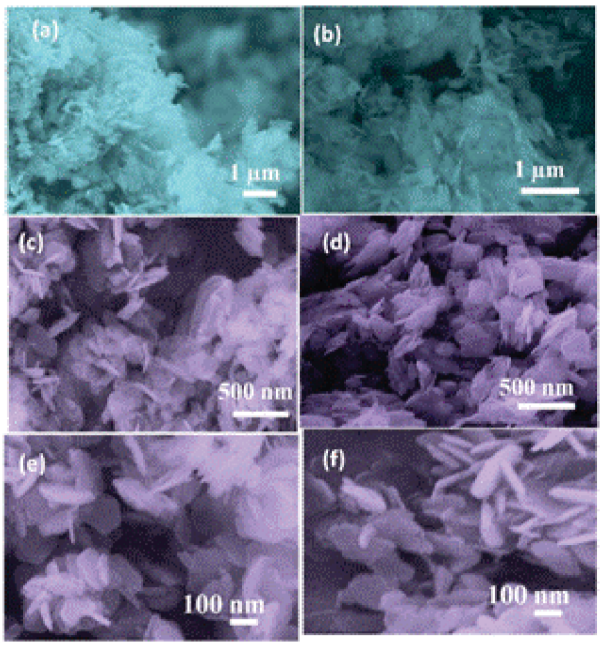

Figure 3.3: FE-SEM micrograph of the NiO nanocatalyst, (a to b) *β*-$Ni(OH)_2$ phase, (c to f) calcined products of hexagonal NiO nanoplatelets.

High-resolution transmission electron microscopy (HRTEM) images of the NiO samples clearly revealed the formation of regular and condensed hexagonal platelet mosaics with an average size of 250 nm [Figure 3.4 (a - d)]. The nanoplatelets were very thin; the thickness was less than 20 nm, as shown in Figure 3.4 (a). In addition, the adjacent edge angle was approximately 120°, as shown in Figure 3.4 (b). The local structure of the nanoplatelets showed variable sizes of hexagonal morphology, indicating the formation of mosaic networks, despite the symmetric deviation with inter-planar angles from 60°. TEM micrographs (Figure 3.4 (a-d)) showed the formation of disordered (wormlike) mesopores (around 3.5 nm), based on scanning transmission electron microscopy (STEM), small angle X-ray scattering (SAXS), and N_2 isothermal profiles [Figures 3.5 - 3.7]. The representative electron diffraction (ED) image (Figure 3.4e) showed well-defined orientations of bright-dot incidences, indicating the formation of large-scale NC domains. The distance between two lattice fringes was 0.24 nm (Figure 3.4e), which is consistent with the interplanar space of the (111) plane of the cubic NiO symmetry (Figure 3.4f). Enlarged HRTEM images of selected areas (Figure 3.4 (g and h)) showed further evidence of the formation of a cubic Fm3m NiO NCs. The images revealed well-organized lattice arrays over a large area with distances of 0.2 nm and 0.149 nm, respectively, which feature the d-spacings of the (200) and (220) planes (Figure 3.6).

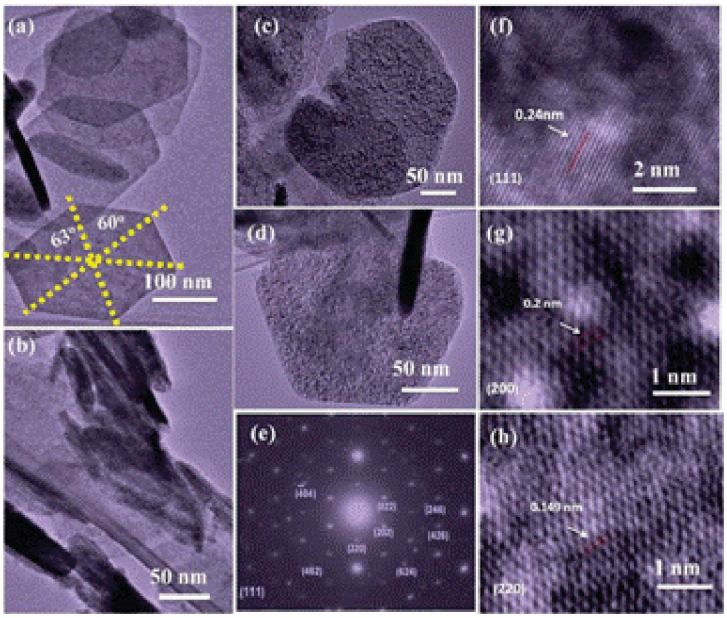

Figure 3.4: Typical HRTEM images of multidirectional pores NiO nanoplatelets with an average size of 250 nm, nanoplatelet thickness of about 20 nm (a, b), magnified view of the acicular branch (c, d), and corresponding ED pattern of selected area (e). The HRTEM and ED patterns reveal the high crystallinity of the nanoplatelets.

STEM image and EDS mapping (Figure 3.5) further prove the control of the formation of hexagonal platelet-like mosaics of NiO NCs. Dark-field STEM images confirmed the formation of porous NiO platelets with an average diameter of 250 nm and a thickness of less than 20 nm. STEM micrographs (insets) showed dense micro- and mesopore surface voids (open holes). STEM-EDS mapping and X-ray photoelectron spectroscopy (XPS) analysis were performed to characterize the surface composition and atomic distribution of the NiO NCs. Figure 3.5 shows the STEM-EDS mapping of the surface distribution of Ni, O, and C. The contribution of Ni and O was mainly in the formation of NiO NCs with hexagonal platelet-like mosaic; however, C was originally observed from the TEM grid. The STEM-EDS mapping indicated that Ni and O were uniformly distributed on the surface of the platelet. In addition, the intensity of Ni and O did not show co-incident regions of high or low intensity as would be expected if they occurred in a 1:1 atomic ratio of Ni:O as in NiO structures. Thus, significant differences in the atomic distribution of Ni and O were observed, as described in the XPS data (Figure 3.8). The elemental analysis of the NiO platelet using EDS (Figure 3.5(b)) indicated the presence of Ni, O, C, and Pt. The existence of Pt and C peaks was attributed to the TEM grid. In addition, O and Ni were originally found in the NiO NCs, which had a [Ni] / [O] ratio of 0.77. The lower value compared with that of the stoichiometric NiO was because of the accession of the O atoms. Thus, the NiO nanoplatelet catalysts were

composed of more O atoms and deficient in Ni atoms on the surface of the NiO, leading to intrinsic advantages in the catalytic transformation of organic species.

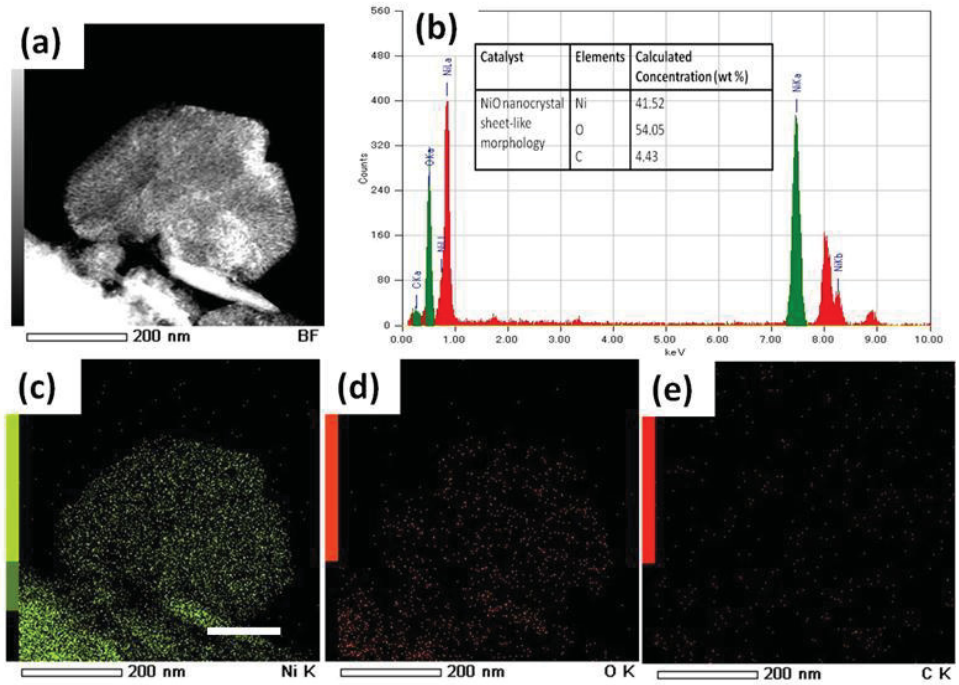

Figure 3.5: STEM image and STEM-EDS mapping, and EDS of the multidirectional pores NiO nanoplatelet; (a) STEM of NiO map, (b) EDS analysis, (c) nickel, (d) oxygen, (e) carbon (inset) calculated values of atomic abundance of Ni and oxygen species present in the solid catalyst.

3.2.3. Structural features of the NiO nanoplatelet-like mosaic catalysts.

Figure 3.6 shows the crystal structure of the as-made $Ni(OH)_2$ and the thermal-treated product of NiO powder, which were characterized via SAXS and wide angle X-ray diffraction (WAXRD). The SAXS profiles of the NiO platelets were subjected to absolute intensity scaling after in-plane diffracted beams with substrate thickness were normalized (Figure 3.6A). The SAXS pattern of the $Ni(OH)_2$ sample did not show any scattering peaks (Figure 3.6A(a)) because of amorphous pore networks within the $Ni(OH)_2$ nanoplatelets. After mild thermal treatment at 300 °C, $Ni(OH)_2$ decomposed to mesoporous NiO platelets (Figure 3.6A(b)). The SAXS pattern of the NiO nanoplatelets showed a broadly resolved scattering peak at approximately q = 1.16 nm^{-1}, corresponding to $d_{spacing}$ = 5.41 nm. Despite the broadening and low resolution in the intense scattering peak, the formation of mesostructures and retention of the mesopore architectures inside the NiO nanoplatelets were evident. This SAXS pattern [Figure 3.6 A(b)] is similar to the hexagonal mesoporous silica nanostrands fabricated using cationic surfactants as soft

templates.[38] In conclusion, the boarding and low resolution peaks indicated the formation of short-range order NiO mesostructures.[39] WAXRD patterns of the β-Ni(OH)$_2$ and NiO platelet-like mosaic are shown in Figure 3.6(B). The WAXRD pattern of the hydrothermal product showed well-resolved and distinct diffraction peaks, indicating the formation of single-phase β-Ni(OH)$_2$ nanoplatelets with crystalline structures, consistent with JCPDS No. 14-0117, a = 3.126 Å. The WAXRD pattern of NiO (Figure 3.6A(a)) showed typical strong diffraction peaks assigned to the (111), (200), (220), (311), and (222) planes with $d_{spacing}$=2.422, 2.08, 1.48, 1.262, and 1.208 Å, respectively. These diffraction peaks coincided with the face-centered cubic Fm3m symmetry with a lattice constant of a = 4.17 Å (JCPDS, No. 04-0835), as confirmed by the TEM profiles (Figure 3.6 (e to h)). Thus, the NiO NCs with platelet-like mosaics were produced from the conversion of β-Ni(OH)$_2$ to NiO during the dehydroxylation process under temperature treatment

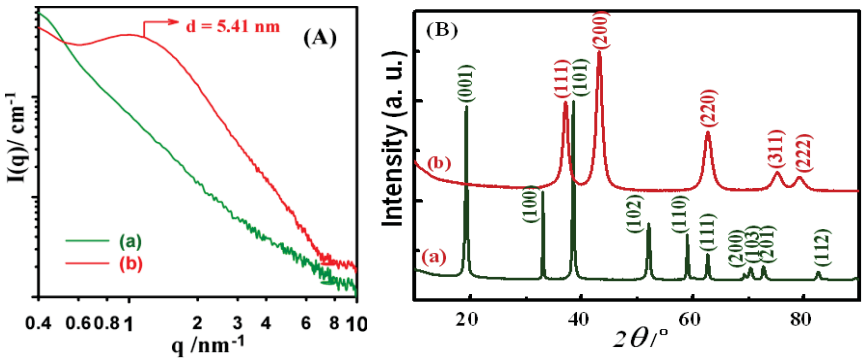

Figure 3.6: (A) Small-angle X-ray scattering pattern, (B) wide-angle X-ray pattern of (a) the nickel oxide nanoplatelet and (b) hydrothermal product of $NiCl_2$ in pH 10, both indicating the formation of β-Ni(OH)$_2$ phase.

The textural properties of the NiO and β-Ni(OH)$_2$ nanoplatelets were further elucidated using N_2 isotherms (Figure 3.7 (A)). According to the IUPAC classification, the NiO nanoplatelets showed a type IV isotherm with a small H_2 hysteresis loop, indicating the formation of the mesoporous NiO.[40] The lower closure point of the hysteresis loop was observed in a very narrow range of relative pressures, which was approximately 0.42 or 0.52 for N_2 at 77 K, indicating the cavitation-induced stepwise desorption in the ink-bottle pores.[41] The desorption branch of the isotherms showed a stepwise behavior and ended at the limiting pressure of the hysteresis closure, implying non-uniformity of the pore openings associated with pore constrictions and/or ink-bottle pores with narrow necks. In turn, the N_2 isotherms of the as-made β-Ni(OH)$_2$

nanoplatelets showed type V isotherms, indicating the formation of micro/macropores.[42] The high-pressure parts of the hysteresis loop ($0.9 < P/P_0 < 1$) may be associated with the textural larger pores that can be formed between the secondary platelet particles in the mosaic structures. The $Ni(OH)_2$ sample showed a low surface area and a low pore volume compared with the NiO nanoplatelets. The specific surface area was S_{BET} = 19 m^2g^{-1} and 145 m^2g^{-1} for $Ni(OH)_2$ and NiO-platelets, respectively. The Horvath-Kawazoe (HK) model was studied (Figure 3.7B, insets) to investigate the microporosity of the platelet-like mosaics. The NiO platelets had multidirectional micro-, meso-, and macropores measuring 0.45, 3.6, and 270 nm, respectively (Figure 3.7(B)). One of the main features of NiO nanoplatelets was the existence of micropores (4 Å to 6 Å) interconnecting the disordered mesopores, leading to a more suitable diffusion of the small molecules of the phenolic pollutants inside the entire micropore structure volumes (Vm= 0.04 cm^3/g to 0.06 cm^3/g). The NiO nanoplatelets had higher surface areas than those of the ordered mesoporous (108 m^2g^{-1}), [43]as well as a microspherical structure[44] and a NiO flower-like morphology that were recently fabricated through sophisticated methods

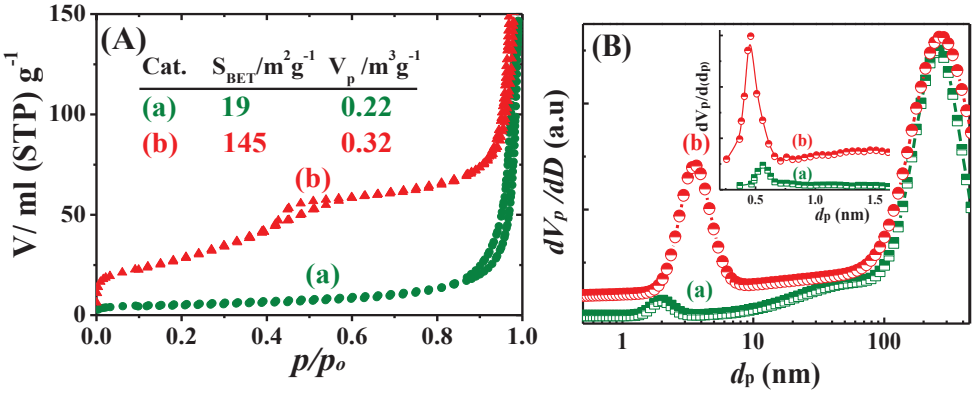

Figure 3.7: (A) N_2 adsorption/desorption isotherms, (B) pore size distribution of (a) the $Ni(OH)_2$ nanoplatelet and (b) NiO nanoplatelets calculated using the NLDFT and HK methods.

XPS technique was employed to elucidate the valence distribution and dispersion of the Ni ions in the NiO particles. The XPS patterns of the Ni 2p spectra (Figure 3.8A) showed two edges of $2p_{1/2}$ (from about 869 eV to 885 eV) and $2p_{3/2}$ (from about 850 eV to 867 eV). A Shirley background was applied across the Ni $2p_{3/2}$ portion of the spectra. The core level spectrum "edge" of the 3*d* transition metal composites was split into two signal peaks. The lowest energy peak at the ground state is called the main peak; however, the signal line at the excited final state is called the satellite peak. The positions of the

peaks were almost the same for $Ni(OH)_2$ and NiO within an experimental error. The $Ni2p_{1/2}$ (872 eV) and $Ni2p_{3/2}$ (853.2 eV) peaks were assigned to the Ni(II) ions in the NiO. The position of the peaks was close to the value of pure NiO (854.2 eV) with a slight shift to a lower binding energy. This shift in binding energy was attributed to the oxygen vacancy on the surface of the catalyst. The peak at 855 eV was ambiguous, which may be attributed to the Ni^{3+} species on the surface.[47] The splitting separation between these two main peaks, namely, 18.8 eV, indicated the well-defined symmetry of Ni(II) ions in oxide form. Figure 3.8A shows two peaks of satellite structures at 860.5 and 864.6 eV. These satellite peaks may be assigned to the existence of the Ni(II) and Ni(III) ions; however, the latter was disregarded because of its low intensity and poor resolution compared with the Ni(II) satellite peak. The XPS results, in general, primarily indicated the dispersion of the dominant Ni(II) ions in intrinsic NiO particles. This finding indicated the contribution of NiO_6 in octahedral symmetry and NiO_5 in pyramidal symmetry containing more than one Ni ion in the core-hole sites. This result agreed with that in a previous report. For the NiO nanoplatelets, many Ni and O atoms were found on the surface because of their porosity and nanosized nature, as shown in STEM-EDS mapping. Figure 3.8B reveals the O1s XPS signal line with a distinct peak at 529.53 eV and a shoulder peak at 531.09 eV. The first peak was assigned to O bonded within a regular oxide crystal (O^{2-}). The second peak, which was a shoulder peak, could correspond to the defective sites within the NiO crystal assigned to O atoms in positions adjacent to Ni vacancies within the oxide structure, adsorbed oxygen, or hydroxide species.[49] The surface atomic content of the NiO nanoplatelet was 40% for $Ni2p_{3/2}$, 48% for O1s, and 10% for C with an atomic ratio of about 0.84, indicating the oxygen overstoichiometry of NiO NCs on the surface.

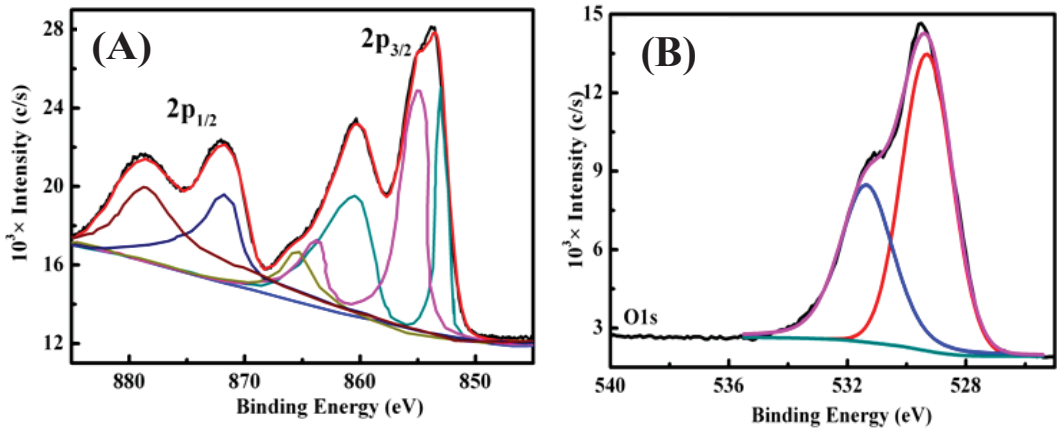

Figure 3.8: XPS pattern of Ni 2p (A) and O 1s (B) spectra of NiO nanocatalyst synthesized via the hydrothermal method.

3.2.4. Catalytic transformations of organic pollutants to hand-safe chemicals

3.2.4.1.Batch chemical transformation method of organic pollutants

The catalytic transformation of phenolic compounds was performed using NiO nanoplatelets as catalysts. The stock solution of phenolic compounds was prepared in water/3% ethanol (v/v) mixture. However the percentage of ethanol is less than 0.15% in reaction vessel. The heterogeneous catalytic reaction was performed at various temperature ranges within 25–40◦C using a thermostated shaker at a constant shaking rate. In a typical kinetic experiment, the catalyst (0.83 g/L) was mixed with 28 mL of deionized water purged with N_2 gas in closed Erlenmeyer-flask. The content was placed in a water shaker thermostat for 10 min at a specific temperature. A standard solution of phenol (2 mL) was added to the mixture with a micropipette and then the time was recorded. The concentration of phenols was 0.5 mM in the reaction vessel. After a set interval of time, an aliquot volume (3 mL) was transferred into the quartz cell to quench the reaction. No filtration or centrifugation system was used for detection of the reaction over NiO nanocatalyst, indicating easy batch contact-time experiments. The heterogeneous catalytic reaction was monitored spectrophotometrically at 435 and 322 nm for 3-APZ and 3-APT, respectively. To reuse the NiO catalyst after the first set of reaction experiments, the solid catalyst was collected and washed by 0.01 M HCl solution for several times and then dried at 200◦C overnight under air to remove the adsorbate product into interior/exterior pore surfaces. Modeling calculations of the cyclization of 3-APZ and 3-APT products were done based on DFT calculations implemented in the Gaussian 03 suite program [36]. All calculations performed using an ordinary B3LYP functional theory, which comprises the hybrid Becke+Hartree–Fock exchange and Lee–Yang–Parr functional correlation with nonlocal corrections, were adopted with the basis set to 6-311++G (d, p). The solvent effects on the models were achieved using the polarized continuum model to obtain more reliable data.

3.2.4.2. Heterogeneous catalytic assay of porous NiO nanoplatelet catalysts

To investigate the catalytic performance of multidirectional micro-, meso-, and macroporous NiO nanoplatelet-like mosaics, *o*-AP and *o*-ATP were used as models for the transformation reactions (Figure 3.9). The physical characteristics of NiO nanocatalyst,

such as multidirectional porosity, surface area, and pore volume, enabled organic pollutants to access the active site of the nanoplatelet mosaics, leading to enhanced oxidation activity to form 3-aminophenoxazone (3-APZ) or 3-aminophenothiozine-3-thizone (3-APT) compounds. Our finding reveals that the heterogeneous catalytic reaction depends on the temperature, solvent, and concentration of APs (Figure 2.9 to Figure 3.12). Furthermore, the transformation reactions were performed in ethanol to study the effect of solvents on the catalytic rate. The conversion rate of *o*-AP to 3-APZ in water was higher than the reaction in ethanol by about 1.8 times. This effect was a result of reactant solubility and their adsorption on the surface of the catalyst, competitive adsorption of solvent, and interaction between the solvent and reactant molecules.[51] To demonstrate the applicability and efficiency of the hexagonal NiO platelet mosaic catalyst in these chemical transformation reactions, the heterogeneous catalytic reaction of o-AP was performed using a variety of NiO nanomaterials previously fabricated in nanoflower and nanoplatelet morphologies.[43-44,52] The results (Table 3.1) revealed the higher catalytic efficiency of NiO platelet mosaics compared with NiO nanoflowers and nanoplatelets. Hence, textural surface parameters (S_{BET}, multidirectional pores, and pore volume), mosaic morphology, and surface composition played significant roles in the high-degree conversion of pollutants to hand-safe chemicals.

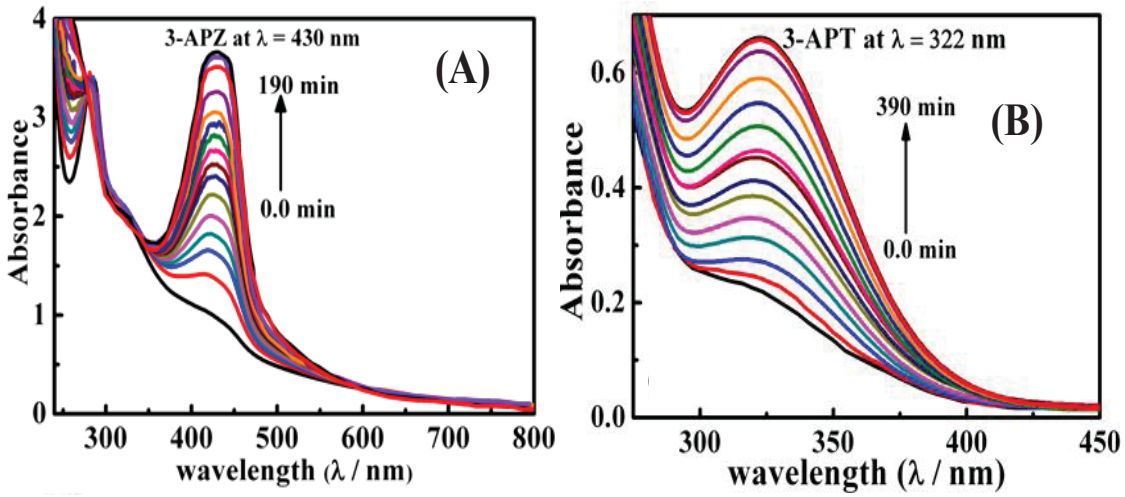

Figure 3.9: UV-vis spectra of 3-APZ and 3-APT solutions in the course of catalytic reaction in the presence of NiO nanoplatelet. {Reaction condition: 0.5 mM 3-APZ/3-APT in water, air atmosphere, NiO 0.83 g/l, and 25^{o}C}.

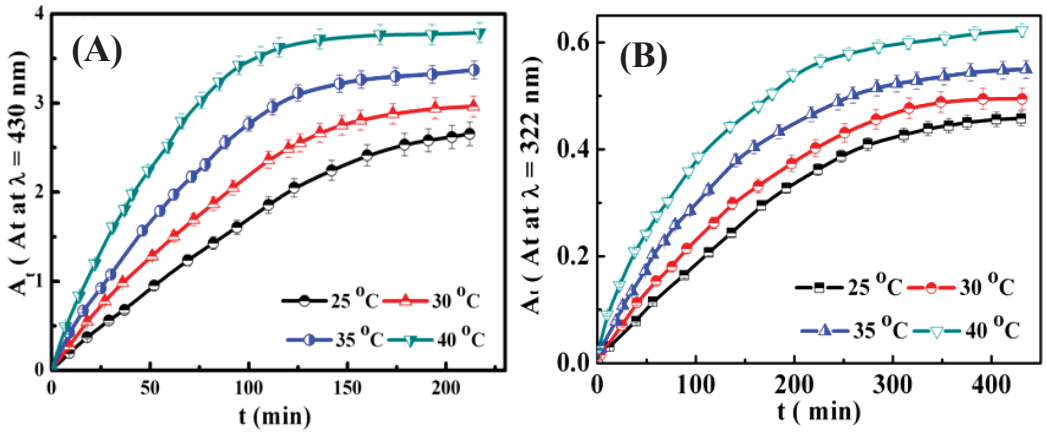

Figure 3.10: Effect of various reaction temperatures on the time-rate dependence of the formation of 3-APZ at 430 nm (A) and 3-APT at 322 nm (B) during catalytic oxidation reactions of [0.5 mM) *o*-AP/ *o*-ATP, respectively, over a NiO nanocatalyst.

Table 3.1: Physical property of NiO nanomaterials for catalytic oxidation of phenolic pollutants including the values of heterogeneous rate constant at 30 °C.

Catalyst	***Morphology***	***Specific surface area (m^2g^{-1})***	***$10^3 \times k / s^{-1}$***
Ni(OH)	Platelet mosaics	18.68	0.83
NiO	Platelet mosaics	145.2	11.36
***NiO** [42]	Nanoflowers	*80.2*	3.34
***NiO** [42]	Nanoflowers	*38.5*	1.5
#NiO [35]	nanoplatelets	75	3.17

**NiO –H flower prepared by the thermal decomposition of $Ni(OH)_2$; NiO-A flower prepared by the thermal decomposition of $Ni(Ac)_2$*
#NiO mesoporous NiO nanoplatelet prepared using nickel oxalate as precursor by the hydrothermal method in the presence of methyleamine

3.2.4.3.Physical studies of chemical transformation of phenolic pollutants

As shown in Figure 3.11 and Table 3.2, the reaction was monitored at various temperatures (25 °C to 40 °C). K_c, and the negativity of ΔG increased with temperature. The purpose of the experiment was to investigate the kinetic and thermodynamic features of the transformation process of phenolic pollutants (*o*-AP and *o*-ATP) on the micro-, meso-, and macropore cavities of NiO platelet-like mosaics. Based on the results, the

transformation reaction was spontaneous and more favorable at high temperatures, which confirmed an endothermic process with a positive value of ΔH. This finding indicated that the increase in reaction temperature facilitated the diffusion through the NiO pores. On the other hand, the transformation reactions between the phenolic pollutants and a known amount of the NiO nanocatalyst followed first-order kinetics with respect to [phenol] (Figure 3.11) according to equation 1(section 2.6.1).

The heterogeneous catalytic reaction *(k)* of the NiO nanoplatelets increased with increasing temperatures. The hexagonal nanoplatelet mosaics provided high accessibility, and the mobility of the small molecules of the phenolic pollutants, such as *o*-AP or o-ATP (about 6 Å), was crucially affected by the degree of porosity. The activation energy E_a of the phenolic pollutants was deduced from an Arrhenius plot equation 3. The other activation parameters of the free energy of activation $\Delta G^{\#}$ (the enthalpy of activation $\Delta H^{\#}$ and the entropy of activation $\Delta S^{\#}$) were calculated using Eyring's equation (4) and are listed in Table 3.2. The $\Delta H^{\#}$ value of activation and the $\Delta G^{\#}$ value were in the range of the chemical reaction control. The transformation reactions were found to be entropy-controlled. Furthermore, a greater $\Delta S^{\#}$ value of the chemical transformation of *o*-AP, compared with o-ATP, corresponded to the greater probability of activated complex formation, as shown in Table 3.2 and Figure 3.12. The thermodynamic and kinetic parameters during the course of chemical transformation indicated the migration on pollutants through the interior of the micro-, meso-, and macropore cavities of NiO platelet mosaics.[54]

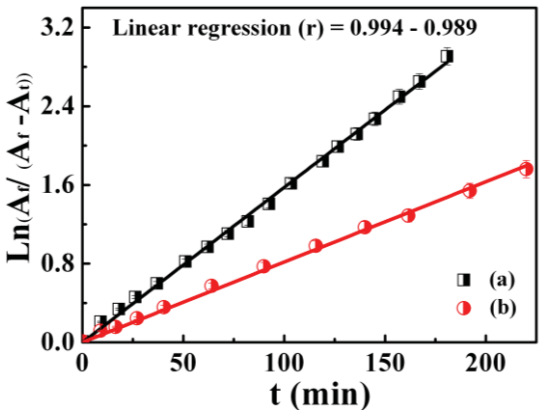

Figure 3.11: Integrated first-order reaction rate of the catalytic transformation of [0.5 mM] *o*-AP (a) and *o*-ATP (b) over the NiO nanoplatelet.

Table 3.2: Kinetic and thermodynamic features; heterogeneous reaction rate constant of the NiO nanocatalyst after recycling during oxidation of [0.5 mM] phenols at different temperatures.

NiO nanoplatelet catalyst				*Kinetic parameters*				*Thermodynamic parameters*		
Pollutants	***T/ °C***	***10^3 × (k/s $^{-1}$)***	***Kc***	***Ea/ kJmol^{-1}***	***$\Delta H^{\#}$/ kJmol^{-1}***	***$\Delta S^{\#}$/ Jmol^{-1}K^{-1}***	***$\Delta G^{\#}$/ kJmol^{-1}***	***ΔH/ kJmol^{-1}***	***ΔS/ Jmol^{-1}K^{-1}***	***ΔG/ kJmol^{-1}***
o-AP	*25*	9.50	0.69	*28.88*	26.31	-161.44	*75.63*	40.11	130.78	0.95
	30	11.37	0.76							0.70
	40	12.68	0.97							0.077
	45	17.05	1.51							-1.046
o-ATP	*25*	4.40	0.28	*21.12*	18.58	-193.67	*77.75*	44.86	139.79	3.23
	30	4.97	0.35							2.66
	40	5.75	0.50							1.76
	45	6.60	0.65							1.09

3.2.4.4. Mechanistic studies of the chemical transformation of *o*-AP and *o*-ATP pollutants

In general, the catalytic oxidation of phenol over the NiO nanocatalyst involved four electrons and four protons in producing 3-APZ and 3-APT, respectively. For *o*-AP, benzo-imine was formed and then reacted with another molecule of *o*-AP to form dimeric oxidation products.[55] The reaction sequence of the expected oxidation products is shown in Figure 3.12. Mass spectrometry was used to determine the molecular weight of the oxidation product of the transformation reaction of pollutants. The results showed that the oxidation product of *o*-AP exhibited a molecular ion consistent with the formation of dimers $[C_{12}H_{11}N_2O_2]^+$. On the basis of the experimental results, two possibilities for the reaction of the *o*-AP molecules on the NiO nanocatalyst can be inferred. *o*-AP may have been present inside the pore or in the interlayer distance between the condensed platelets (Figure 3.2). The textural surface parameters (surface area and pore volumes) with hexagonal nanoplatelet-like mosaics substantially influenced the catalytic functionality of the NiO surfaces. The heterogeneous catalytic transformation mechanism of the reaction between phenol (P) and the metal oxide surface (NiO) occurred as shown in the mechanistic Figure 3.12 and Figure 3.13.

1- Surface physosption process

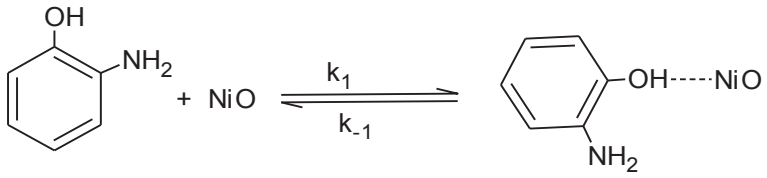

(1)

2- Formation of radical structure (TS1)

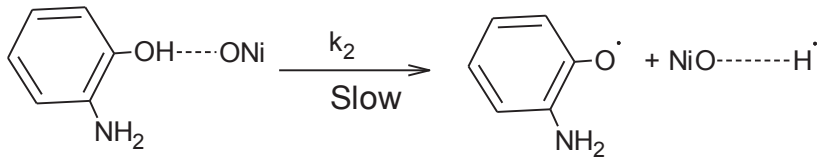

(2)

3- Formation of the metastable structure (IT)

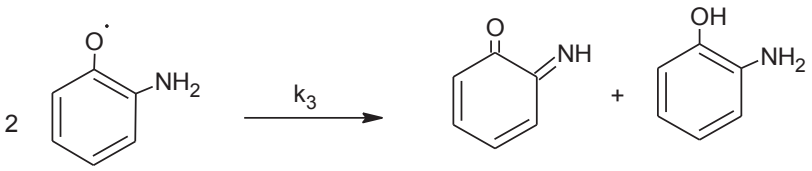

(3)

4- Dimerization process of molecules

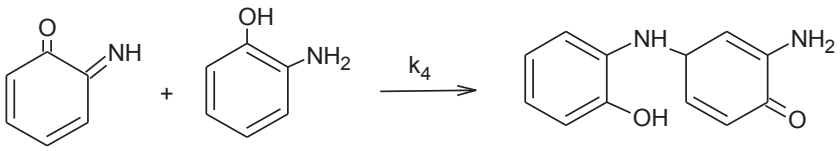

(4)

5- Cyclization process of dimer molecule

The reaction rate;

$$-\frac{dx}{dt} = k_2 [NiO-----P] \quad (5)$$

Applying the steady–state approximation for the intermediate:

$$\frac{d\{[NiO\ ----P]\}}{dt} = k_1 \{NiO\}\ [P]\ - k_{-1}[NiO\ ---P\ ]\ - k_2 \{NiO\ ----P^*\}] = 0 \quad (6)$$

$$\text{Where, } [\text{NiO}\text{---}\text{P}] = \frac{k_1\{\text{NiO}\}[\text{P}]}{k_{-1} + k_2} \quad (7)$$

$$-\frac{\mathrm{dx}}{\mathrm{dt}} = \frac{k_2 k_1\{\mathrm{NiO}\}[\mathrm{P}]}{k_{-1} + k_2} \quad (8)$$

$$-\frac{\mathrm{dx}}{\mathrm{dt}} = \mathrm{k}_{\mathrm{obs}}\{\mathrm{NiO}\}[\mathrm{P}] \quad (9)$$

The experimental results suggested that the oxidation of phenolic pollutant via radical mechanism pathway. According to the kinetic data obtained and Eq. (9), the chemical transformation reaction rate is proportional to {NiO} and pollutant [P]. The reaction rate of phenol transformation followed first-order kinetics, which is consistent with that in previous studies,[55] as shown in Figures 3.11.

3.2.4.5.Theoretical models of the catalytic transformation reactions

The geometrical orientation of the functional groups -NH_2, -SH, and -OH is very important in heterogeneous catalytic transformation reactions. DFT calculations were performed for two reaction models using *o*-AP and *o*-ATP as reactants[36] to understand the proposed mechanism (Equations. 1 to 4). Figure 3.12 shows the energy profiles of the oxidation reaction of pollutant [P] (e.g., *o*-AP molecule, and the charge distribution of the reactants, intermediates, transition states (TS), and products (S4)). The highest electronegative charge was attributed to the -NH_2 group (-0.57), suggesting that oxidation may have been induced by the electron loss from the -NH_2 group. One *o*-AP molecule was adsorbed on the nanoplatelet surface where the adsorption energy was about -15 kcal/mol. During the oxidation reaction, the first transition state (TS1) showed evidence of the formation of the *o*-AP radical on the surface of the platelet [NiO---*o*-AP$^{\bullet}$], as indicated in the proposed mechanism (TS1, Eq. 2). The energy barrier for the produced radical structure (TS1) was about 38 kcal/mol. This highest energy level of the TS1 structure may have enabled the metastable outer-sphere orientation in the structure arrangement on the platelet surfaces {NiO----*o*-AP} with a low energy of 5.8 kcal/mol intermediate (IT, Eq. 3). The metastable structure led to the formation of the dimer throughout the combination to another *o*-AP molecule in the p-position with respect to the -OH group, which was the most electronegative part in the ring (-0.39), (TS2, Eq. 4). The

increase in the energy level (11.8 kcal/mole) of the TS2 dimer structure may be attributed to the rotation of the aromatic ring around the formed C-N bond to release the steric hindrance around the -OH group. Following the TS2 state formation, the cyclization step for the formation of the 3-APZ product spontaneously occurred via the reaction with oxygen of the lowest energy level at -29 kcal/mol. Furthermore, the cyclization reaction of *o*-ATP on the NiO platelet mosaics is presented in Figure 3.13. The analysis of the orbital energies of the *o*-ATP and *o*-AP models showed the behavior of the intermediates for further cyclization (Table 3.3). The electronic structure of the intermediates and products showed that the highest occupied molecular orbital-lowest unoccupied molecular orbital (HOMO-LUMO) band gap of both the *o*-ATP and *o*-AP molecules are very small. As the difference is insignificant, the phenol molecules may have the tendency for further polymerization.

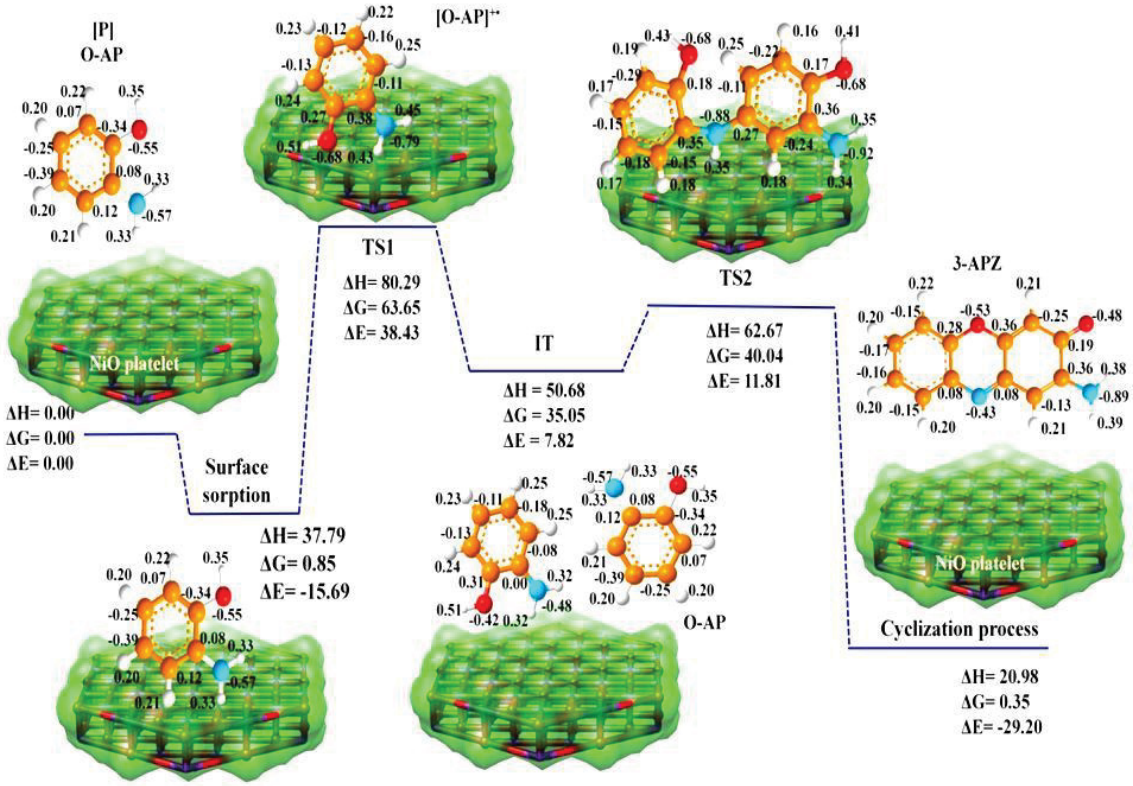

Figure 3.12: Theoretical models of the chemical transformation mechanism of *o*-AP onto NiO platelet mosaics. The energy profiles and the charge distribution of reactants, intermediates, transition states, and products were calculated using the DFT method. The atom colors of carbon, nitrogen, oxygen, and hydrogen are orange, blue, red, and gray, respectively. The NiO platelets are presented as electron-density surfaces. The unit of the energy profiles is kcal/mol.

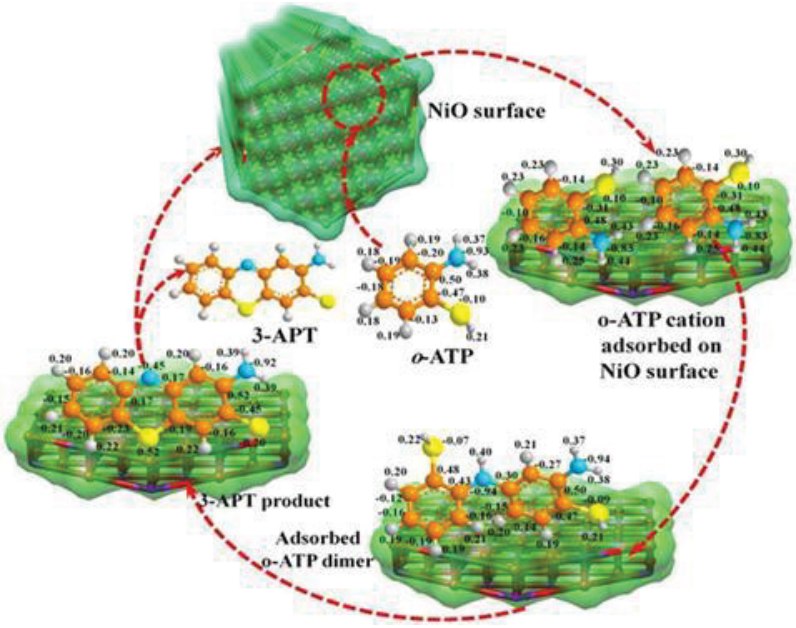

Figure 3.13: Catalytic transformation mechanism of *o*-ATP to benzothione-imine and 3-aminophenoxazine-3-thiol over hexagonal NiO platelets.

Table 3.3: HOMO-LUMO and band gap energies of the reactants, intermediates, and products models.

Model	**HOMO** (electron Volt)	**LUMO** (electron Volt)	**Energy gap** (electron Volt)
o-aminophenol	-0.205	-0.014	0.191
o-aminophenol dimmer	-0.178	-0.008	0.170
3-aminophenoxazone	-0.200	-0.071	0.129
o-aminothiophenol	-0.205	-0.014	0.191
o-aminothiophenol dimmer	-0.197	-0.022	0.175
3-aminophenothizine-3-thiozone	-0.215	-0.1375	0.77

3.2.4.6.Efficiency and Reusability of NiO nanoplatelet catalysts

A major advantage of nanostructured catalysts is that they can maintain their activity toward the reaction media. Furthermore, the reusable catalyst should be safe, inexpensive, easy to handle and dispose, and environmentally benign. Many of these methodologies suffer from the drawback of green chemistry and have been associated with several

shortcomings, such as long reaction periods, expensive reagents, low product yields, and difficulty in catalyst recovery and reusability. Developing recyclable catalysts is important for industrial applications to solve these problems. After several regeneration / reuse cycles of the NiO catalysts, catalytic experiments showed no significant changes in the textural properties and catalytic efficiency of the oxidation of the phenol molecules (0.5 mM). Figure 3.14 shows the catalytic efficiency of the NiO catalyst in each cycle. The NiO nanoplatelet catalysts lost about 5% of their original efficiency after six regenerations/reuse cycles without a change in structure or textural properties, as confirmed by the N_2 isotherms, SEM, and STEM profiles. These findings indicated that the binding of organic moieties (reactant and product) onto the NiO catalyst does not lead to the deformation of the internal/external ordered and porous surface sites, despite the extended reuse cycles. In general, NiO platelet mosaics showed better catalytic transformation of organic pollutants than mesoporous NiO-supported silica composites. However, the development of nanomagnet based-catalyst for transformation of organic pollutants might help in wastewater management and supply as shown in section 2.3.

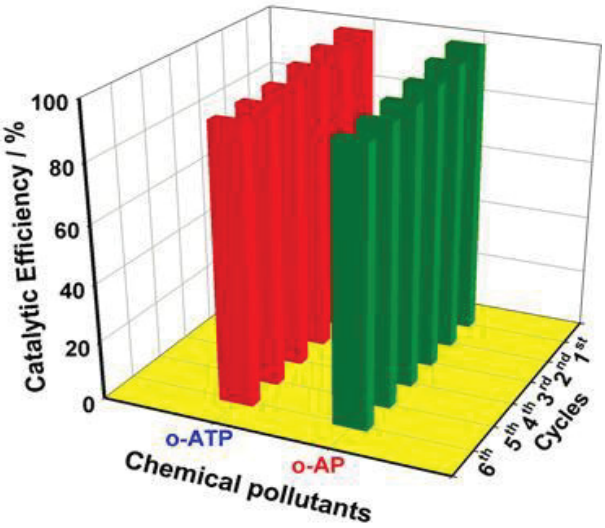

Figure 3.14: Reproducibility and catalytic efficiency of the hexagonal NiO platelet mosaics after multiple cycles of heterogeneous catalytic transformation of [5×10^{-4} M] *o*-AP at 30 °C. The efficiency of the hexagonal NiO platelet mosaics (E) was calculated from the % ratio of the reaction rate constant (k/s^{-1}) per reuse cycle (No.) and the initial reaction rate constant obtained from the initial use of the catalysts.

3.3.Mesoporous NiO nanomagnets as catalysts and separators of chemical agents

Nanoscale magnetic materials are considered to be potential adsorbents because of their large surface area and unique features of easy separation when subjected to external magnetic fields. These properties facilitate a wider range of applications, such as the purification of bio-molecules, magnetic refrigeration, magnetic resonance imaging enhancement, information storage, magneto-optical devices, solid devices, targeted drug delivery, cell separation, and environmental capture.[56-69] Magnetic nanoparticles (NPs) features enable the easy recovery of catalysts in a liquid-phase reaction compared with cross-flow filtration and centrifugation, particularly when the catalysts are in the nanometer-size range and have high surface area that enables the creation of numerous catalytic sites for high activity levels.[70-79] Recently, we developed a simple control for hierarchal mesoporous nickel oxide (NiO) nanomagnets with flower- and sphere-like morphology and large mesocage cavities. Our findings shows that the NiO NPs with flower-like morphology (NFs) has higher catalytic activity toward the oxidation of organic contaminates than that of nanospheres (NS) or even other magnetic NPs such as Fe_3O_4 NPs. Furthermore, the NiO NFs are capable of the high-gradient magnetic separation of organic contaminants from aquatic life with excellent reusability even after several cycles, which may help in wastewater management and supply (Figure 3.15).

Figures 3.15: Catalytic transformation and removal of organic pollutants (3–APZ) using mesoporous NiO NPs.

3.3.1. Design of mesoporous NiO nanomagnets (NMs)

Control over the particle morphology of NiO NPs was clearly made evident using one-pot, simple hydrothermal synthesis (Figure 3.16). Field emission scanning electron microscopy (FE-SEM) micrographs revealed that NiO had a nanosized particle with an average diameter of ~300 and 500 nm for NiO NFs and NiO NSs, respectively. Generally, in the initial reaction period, acetate groups might coordinate with nickel to form nickel acetate precursors. The hydrolysis and/or alcoholysis of nickel acetate then occurred to form NiO nanomaterials. The possible formation mechanism of mesoporous NiO NMs with flower-like morphology involves two consecutive reactions, followed by orientation attachment and local Oswald ripening. Figures 3.16 (a and b) reveal that the crystal particles of NiO were aggregated in a petal-like manner and had smooth and fine surfaces aligned according to the flower morphology. On the other hand, the NiO NMs with sphere-like morphology was generated from the aggregation of NiO NPs [Figure 3.16 (c and d)]. The magnified FE-SEM image of the NiO NMs showed that the morphological particles were either of shape- or size-controlled geometry, indicating the versatility of this method compared with the real control of the morphological and geometrical 3D NiO nanostructures.

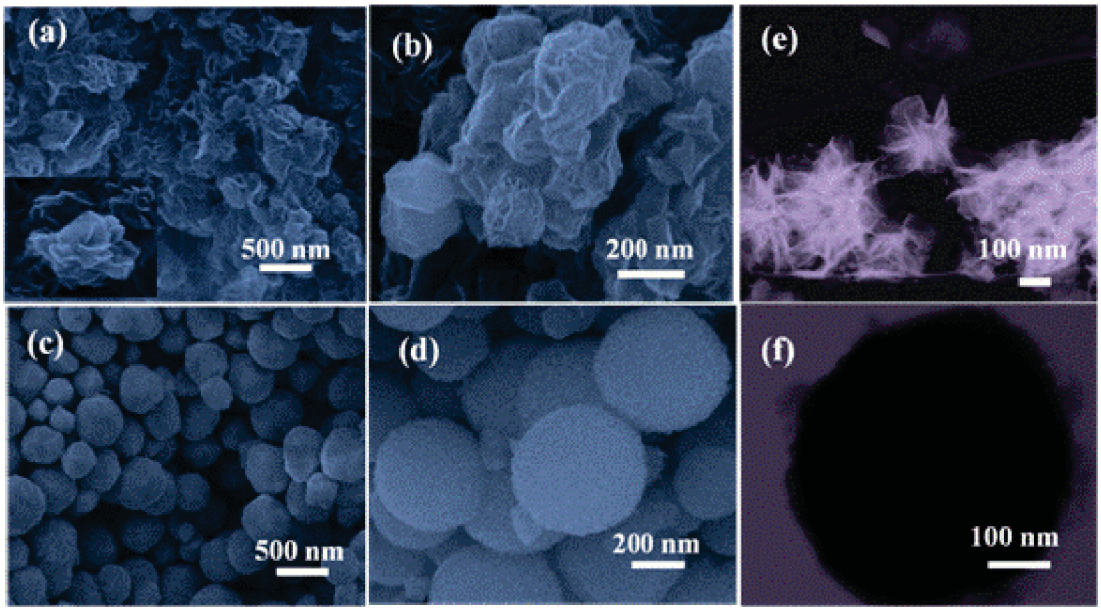

Figure 3.16: FE-SEM and STEM images of NiO NMs (a, b, and e); mesoporous NiO NFs (c, d, and f); and mesoporous NiO NSs revealing the controlled size and shape of NiO NMs

Furthermore, evidence of the control formation of NiO NMs was revealed from the STEM image. The STEM image confirms the formation of the NiO NMs with an average size of 300 and 500 nm for NiO NFs and NiO NSs, respectively. The STEM-EDS mapping revealed the surface distribution of Ni and O (Figure 3.17). The STEM-EDS mapping indicates that Ni and O are uniformly distributed in the NF and NS surfaces. However, significant differences in the atomic distribution of Ni and O were evident. The elemental analysis of the NiO NMs by STEM-EDS indicates the presence of Ni, O, and C atoms. The O and Ni atoms were originally found in the NiO NCs, which had an [O] / [Ni] ratio of 0.79 and 0.71 for NFs and NSs, respectively. To estimate the surface composition of NiO NPs, X-ray photoelectron spectroscopy (XPS) was performed. The surface atomic content of the NiO NFs was 50% for Ni2p3/2, 45% for O1s, and 5% for C with an atomic ratio of ~0.9, indicating the nickel overstoichiometry of NiO NPs on the surface. The results showed that the NMs comprised more nickel atoms and were deficient in oxygen atoms on the surface of NiO NPs. These values are consistent with STEM-EDS mapping analysis and are lower than the stoichiometric NiO because of the accession of Ni atoms. The characteristics of NiO NM surface architectures enhance the catalytic oxidation of organic contaminates or chemical agents. In addition, the altering of the surface composition for NiO NCs attributed to synthetic methodology is one of key factors to employ the uncompensated magnet moments, as previously reported by the Nẽel models.[71.]

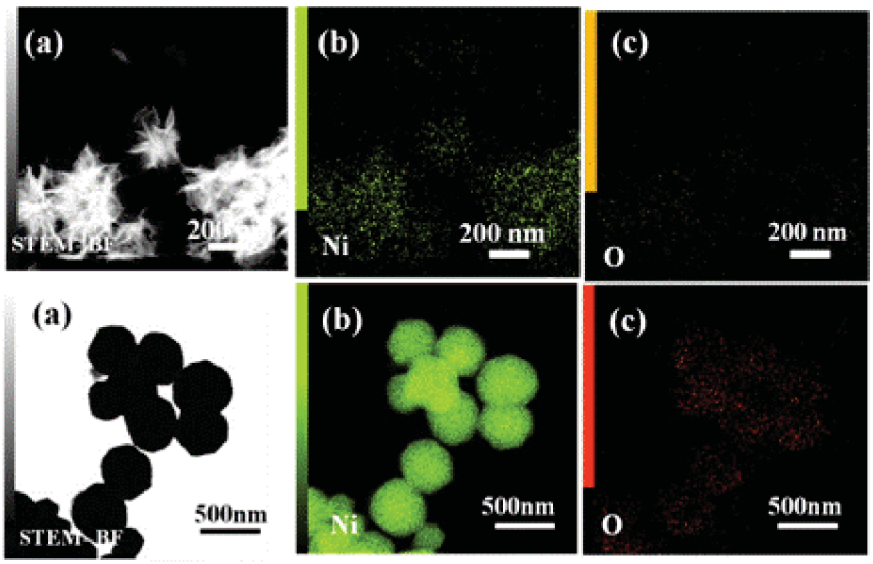

Figure 3.17: STEM-EDS mapping of the mesoporous NiO NCs with flower- and sphere-like morphology; STEM images (a), Nickel (b), and Oxygen (c).

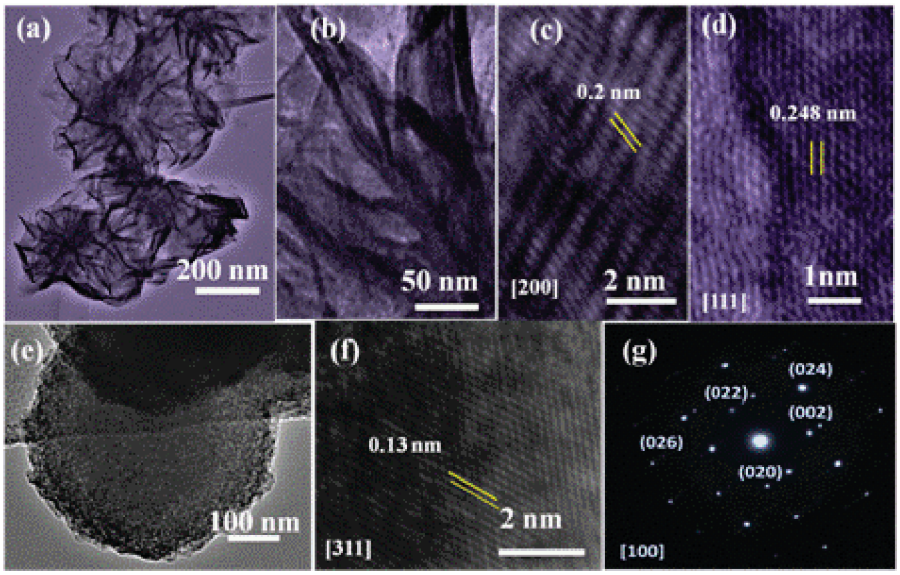

Figure 3.18: Typical HRTEM images of NiO nanomagnet: (a) Flower-like morphology with an average size of 300 nm, nanopetals at ~10 nm thick; (b, c, and d) magnified view of the acicular branch; (e) HRTEM image NiO NS and magnified view of the crystal fringes; (f and g) corresponding ED pattern of selected areas revealing the high crystallinity of the NM

The high-resolution transmission electron microscopy (HRTEM) images [Figure 3.18] clearly indicate the controlling morphology of the NiO NMs (NFs and NSs) with an average size of ~300 and 500 nm, as well as disordered mesopore structures. These HRTEM images of the NiO NFs [Figure 3.18 (a, and b)] show the formation of assembled petals with disordered pore surfaces. First, the NiO petals assembled to form NiO crystals with flower-like morphology. According to the distinct color contrast of TEM images associated with the flower structure, the nanopetals in the core region were observed to be more compact than those in the exterior. In addition, the aggregated petals are very thin; the thickness is less than 10 nm, as shown in Figure 3.18 (a). The most prominent feature was that the NFs showed uniform arrangements and continuous ordering of lattice fringes over large-scale regions without distortion. Large-scale NC domains along the incidences are characteristic of an NiO cubic lattice. The TEM micrographs [Figure 3.18 (c and d)] generally revealed well-organized lattice fringe arrays over a large area, with a distance between two lattice fringes being 0.2 and 0.248 nm featuring the interplanar space of (200) and (111) planes of cubic Fm3m crystal lattices. Figure 3.18 (e) shows the HRTEM image of the NS at 500 nm. The surface was not smooth because the spheres were formed

from aggregated NCs. A higher magnification HRTEM image [Figure 3.18 (f)] shows that the lattice fringes had an interspacing of 0.13 nm, which corresponds to the distance between (311) planes of the cubic Fm3m NiO (JCPDS, No. 04-0835). The representative ED image [Figure 3.18 (g)] oriented with the preferable [100] incidence provided direct evidence of the formation of large-scale NC domains with cubic Fm3m symmetry. These results are consistent with the XRD results (see below).

3.3.2. Structural features of magnetic mesoporous NiO (NM) catalyst

The small-angle X-ray scattering (SAXS) [Figure 3.19 (a)] profiles of the NiO NMs were subjected to absolute intensity scaling after normalizing the in-plane diffracted beams with substrate thickness. The scattering intensity and peak resolution were in the range of $1.3 < q < 2.2$, corresponding to $d_{(100)} = 3.6$ nm. Despite the broadening and low resolution in the intense scattering peak, the formation of mesostructures and the retention of the mesopore architectures inside the NiO NMs were evident.[80] Moreover, the wide angle XRD [inset Figure 3.19 (a)] pattern exhibits typical diffraction peaks of cubic NiO phase (JCPDS, No. 04-0835).

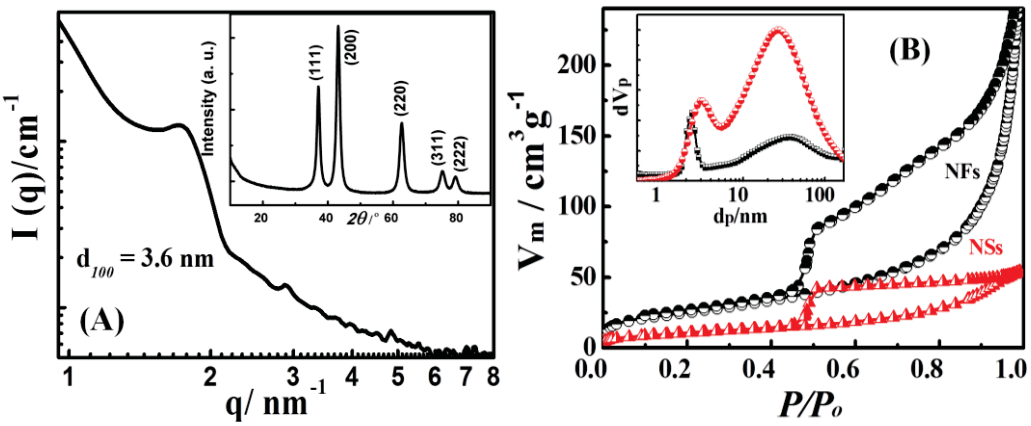

Figure 3.19:(a) SAXS (inset; wide angle X-ray patterns) and (b) N_2 adsorption isotherm (inset: pore size distribution calculated by the NLDFT model of NiO nanomagnet with flower- and sphere-like morphology

The N_2 isotherms of the NiO NMs feature type IV isotherms with a H_2-type hysteresis loop for typical mesocage materials with large pore cavities (10 nm to 30 nm) [Figure 3.19 (b)].[81] This finding demonstrates that our synthesis protocol enables effective control over the size and shape of the cage opening and cavity pores. Notably,

the mesoporous NiO nanocatalysts featured a specific surface area of S_{BET} = 119 and 60.1 m^2g^{-1} for NiO NFs and NSs, respectively. The pore size distribution of NiO NMs was calculated according to the non-local DFT (NLDFT) model [inset Figure 3.19 (b)]. Moreover, the NiO crystals with flower-like morphology exhibited a macroporous regime with an average value of 400 nm. The formation of the mesopore type is probably related to the pores present inside the nanopetals, which were formed between primary crystallites. In turn, the broad band and macroporous type may be related to the assembly of secondary petals to form flower architectures. Our findings showed that the NiO NFs had higher surface area than NiO NSs and that the NiO flowers were fabricated under sophisticated methods. This result indicated that our method yields a high degree of mesopore orientation in the NiO NMs with high surface area and pore volume, which may enable the organic pollutant molecules to penetrate and be easily adsorbed onto the pore network matrices. Moreover, the magnetic characteristic of NiO NMs (Figures 3.19 and 3.20) offers a large exposed surface area without the use of porous materials, which are often plagued by high mass transfer resistances.[82]

3.3.3. Magnetic characteristics mesoporous NiO (NPs)

The magnetic hysteresis loop (M-H loop) of NiO NMs with flower- and sphere-like morphology measured at 300 K indicates magnetic properties, including saturation magnetization M_s and coercivity H. Although the NiO is an anti-ferromagnetic system, the fabrication of NiO nanostructures with large-scale NC domains and well-shaped morphologies exhibited new physical phenomena, such as weak ferromagnetism and paramagnetism. Such magnetic properties of NiO NF- and NS-like morphology might be attributed to the complicated spin configuration. This phenomenon is attributed to the permanent magnetic moment due to uncompensated spins in the two sublattices as suggested by Nĕel in 1961. The number of uncompensated spins (q) depends on the crystal structure and particle morphology; three different models have been considered. If the uncompensated spins are randomly distributed in the particle, $q \alpha n_S^{1/2}$ (where n_S is the total number of spins) is expected. However, if they are arranged parallel to each other in an odd number of layers stacked in a cube, then $q \alpha n_S^{2/3}$. Finally, if the core of the particles has no defects and the uncompensated moments are randomly distributed at the surface, then $q \alpha n_S^{1/3}$. Figure 3.20 shows that the M_s values for the NiO NMs are 12.5 and 6.8 $emu.g^{-1}$ for NiO NFs and NSs, respectively. The results showed that the NiO NFs

have higher paramagnetism than NiO NSs and other NiO nanomaterials reported previously.[83-84] The STEM (Fig. 3.17) results revealed that this paramagnetic behavior of NiO NFs and NSs might be attributed to the uncompensated Ni ions, which are most likely located at or close to the particle surfaces. The design of the NiO nanomagnetic catalysts facilitates the catalytic transformation and separation of chemical pollutants from the environment.

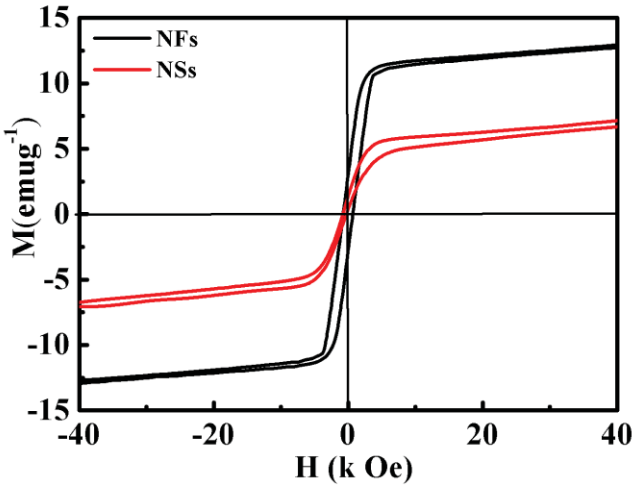

Figure 3.20: Magnetic hysteresis loops of NiO-nanomagnet with flowers- and sphere-like morphology measured at 300 K.

3.3.4. NiO nanomagnetic catalysts

To investigate the magnetization, efficiency, and applicability of NiO NMs in the catalytic conversion and removal of organic contaminates using an external magnet, *o*-AP was used as a phenolic contaminate. The oxidation of *o*-AP was studied and monitored using UV-vis spectroscopy at λ = 430 nm in batch-contact experiments at a temperature range from 25 °C to 40 °C (Figure 3.21).[79] To support our work, the heterogeneous catalytic transformation reaction was conducted using a variety of magnetic materials, such as NiO and iron oxide nanoparticles. Our findings reveal that the transformation of *o*-AP in aquatic systems led to formation of nontoxic compounds (3-APZ). The results showed that the *o*-AP oxidation product exhibited a molecular ion consistent with the formation of dimers ($C_{12}H_{11}N_2O_2$). These dimer ions are consistent with the protonated forms of the oxidation products of the *o*-AP, as shown in Figures 3.12 and 3.13.

The physical characteristics of NiO nanomagnetic catalysts, such as particle morphology, large surface area, mesocage porosity, and magnetic properties, enabled the phenolic contaminates to access the active site of the NiO NMs. These unique characteristic of the NiO NMs enhanced not only the catalytic oxidation of organic pollutants to nontoxic chemical compounds, but also the removal of pollutants, as shown in Figure 3.15. These results suggest that the magnetic feature did not have a significant effect on the catalytic reaction pathway and on the resultant product despite the significant recovery effect of chemical agents.

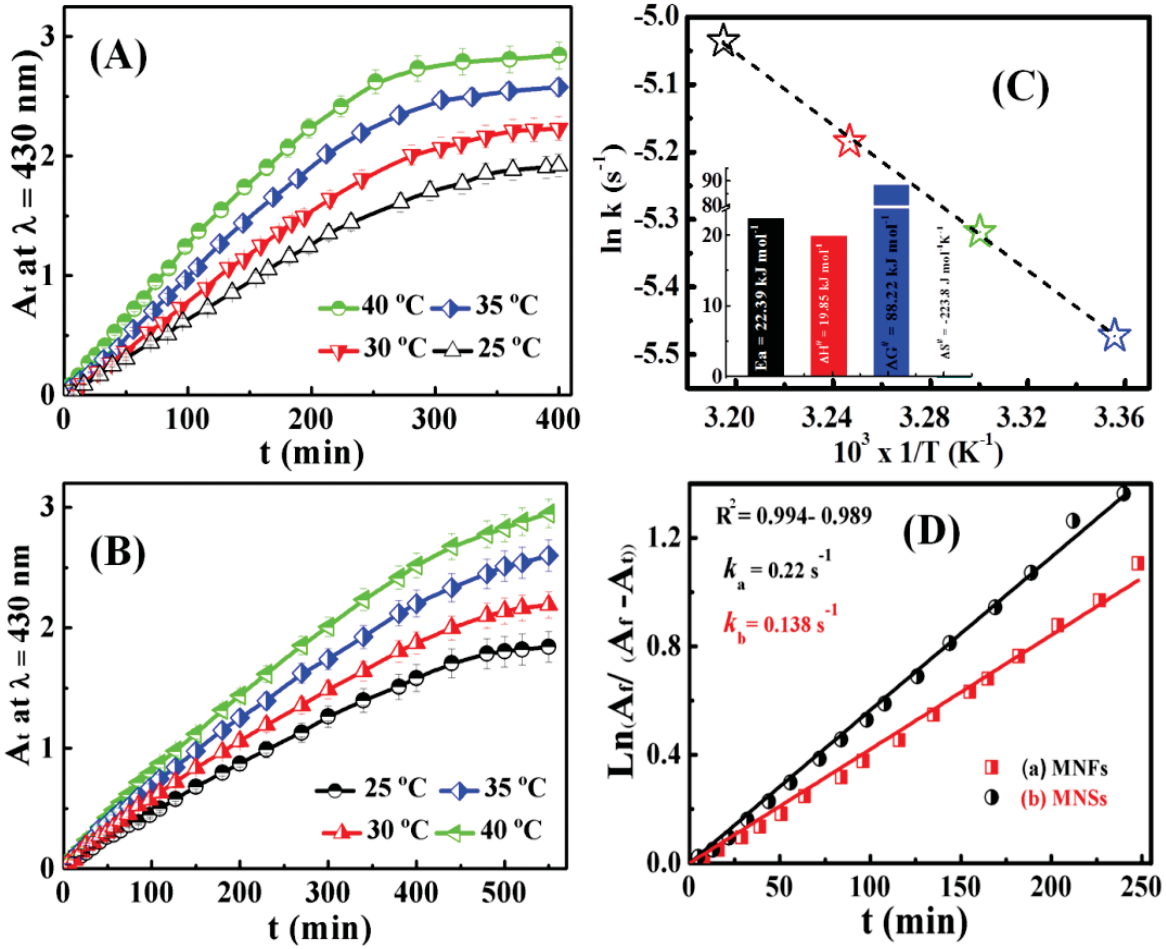

Figure 3.21: A) Effect of various reaction temperatures on the time-rate dependence of the formation of 3-APZ at 430 nm over NiO NFs (A) and NSs (B). C) The calculated kinetic parameters during the transformation reaction of 5×10^{-4} M *o*-AP over NiO NFs. (D) the integrated first-order reaction rate in the formation of 5×10^{-4} M *o*-AP to 3-APZ at NiO NMs at 25 °C.

Table 3.4: Kinetic and thermodynamic features; heterogeneous reaction rate constant of the NiO nanomagnet during oxidation of [5 × 10^{-4}M] o-APs at different temperatures. (Note: Ea, ΔH, ΔS *and* ΔG are the energy of activation, enthalpy, entropy and free Energy, respectively).

NiO nanomagnet flower-like catalyst				***Kinetic parameters***				***Thermodynamic parameters***		
Pollutant	***T/ °C***	***10^3 × (k/s $^{-1}$)***	***Kc***	***Ea/ kJmol^{-1}***	***$\Delta H^{\#}$/ kJmol^{-1}***	***$\Delta S^{\#}$/ Jmol^{-1}K^{-1}***	***$\Delta G^{\#}$/ kJmol^{-1}***	***ΔH/ kJmol^{-1}***	***ΔS/ Jmol^{-1}K^{-1}***	***ΔG/ kJmol^{-1}***
o-AP	*25*	4.2	0.97	*22.39*	19.85	-223.8	*86.54*	23.9	79.7	0.157
	30	4.9	1.03							-0.241
	35	5.6	1.31				*87.66*			-0.64
	40	6.5	1.50				*88.78*			-1.039
							89.89			

3.3.5. Kinetic and thermodynamic studies of magnetic catalysts

To understand the characteristics of the phenolic pollutant conversion process, the kinetics and thermodynamic parameters over NiO NMs were examined at varying temperature (25 °C to 40 °C) (Table 3.4). First-order and pseudo-second-order models were applied. Our findings indicate that the transformation of *o*-AP over NiO NMs was controlled by the first-order kinetics with respect to [phenol] molecules [Figure 3.21 (d)].[81-82] The heterogeneous rate constant (k) of the transformation reaction increased with increasing temperatures [Figure 3.21(d)]. The key achievement in this catalytic NM study is that the NiO NFs catalysts significantly showed doubled catalytic efficiency in terms of the rate constant and degree of conversion compared with NiO NS catalysts. This finding indicates the unique characteristics of NiO NF catalysts, such as morphology, large surface area, and high porosity, which serve as a key parameter in enhancing the accessibility of the active sites to the phenolic contaminates. From the value of the heterogeneous rate constant, the Gibbs free energy change, $E_a^{\#}$, $\Delta G^{\#}$, $\Delta H^{\#}$, *and* $\Delta S^{\#}$ values can be derived using the Arrhenius and Eyring equations. The $\Delta H^{\#}$ activation value and the $\Delta G^{\#}$ values were in the range of the chemical reaction control.

Despite the magnetization effect of NiO catalysts, the transformation reaction of *o*-AP was spontaneous and more favorable at high temperatures, resulting in an endothermic process with a positive value of ΔH, as reported in NiO nanoplatelet catalysts. This finding indicated that the increase in reaction temperature facilitated the diffusion through the NiO NM pores [Table 3.4, and Figure 2.21 (c)]. Furthermore, the NiO NFs provided high accessibility. The mobility of the small molecules of the phenolic pollutants, such as *o*-AP (approximately 6 Å) was significantly affected by the degree of porosity and exposed surface area. The thermodynamic and kinetic parameters (Table 3.4) during the course of chemical transformation generally indicated the migration and effective transformation of pollutants through the interior of mesoporous cavities of the NiO NM.

3.3.6. NiO NM catalysts for separation of chemical agents.

Magnetic NPs with good stability have unique properties that are of great interest in catalysis, mainly in biotechnology and biomedicine applications. To demonstrate the applicability of mesoporous NiO NMs in the efficient chemical oxidation and separation of organic contaminates, the heterogeneous catalytic reaction of *o*-AP was performed using a variety of non-magnetic materials that were previously fabricated. The results revealed that mesoporous NiO NFs have higher catalytic efficiency of chemical agents than NiO NSs and small NiO NPs or even super-paramagnetic Fe_3O_4 NPs. The morphology, surface composition, and parameters (high S_{BET} and pore volume uniform porosity) of the mesoporous NiO NFs play a role in achieving not only a high degree of pollutant conversion into nontoxic chemicals, but also a high-gradient magnetic separation of organic contaminants.[83-86]

3.3.7. Applicability and structural features of NiO nanomagnet after recycling.

A major advantage of NiO NM catalysts is their retained texture, morphology, and magnetic characteristics in terms of reactivity with fast chemical transformation even after multiple cycles. Although the improvement in the reducibility and reversibility of the catalyst is a challenge, NiO NMs can extend the control of the oxidative transformation and separation of phenolic pollutants from wastewater even after several cycles [Figure 3.22 (a)]. However, after the first set of reaction experiments, the NiO nanocatalysts were collected and washed several times with a mixed solution of HCl (1 mM) and ethanol in air to remove the adsorbance product on the surfaces and were

then dried overnight at 100 °C. The results showed that the NiO NF catalysts lost approximately 6% of their original efficiency after the fourth cycle. This finding indicates that the binding of organic moieties (reactant and product) onto the NiO catalyst did not result in the deformation of the internal- and external-ordered mesoporous surface sites [Figure 3.22 (b and d)]. Such long-term reversibility renders the mesoporous NiO NMs catalyst applicable for further oxidative transformation and removal processes.[85]

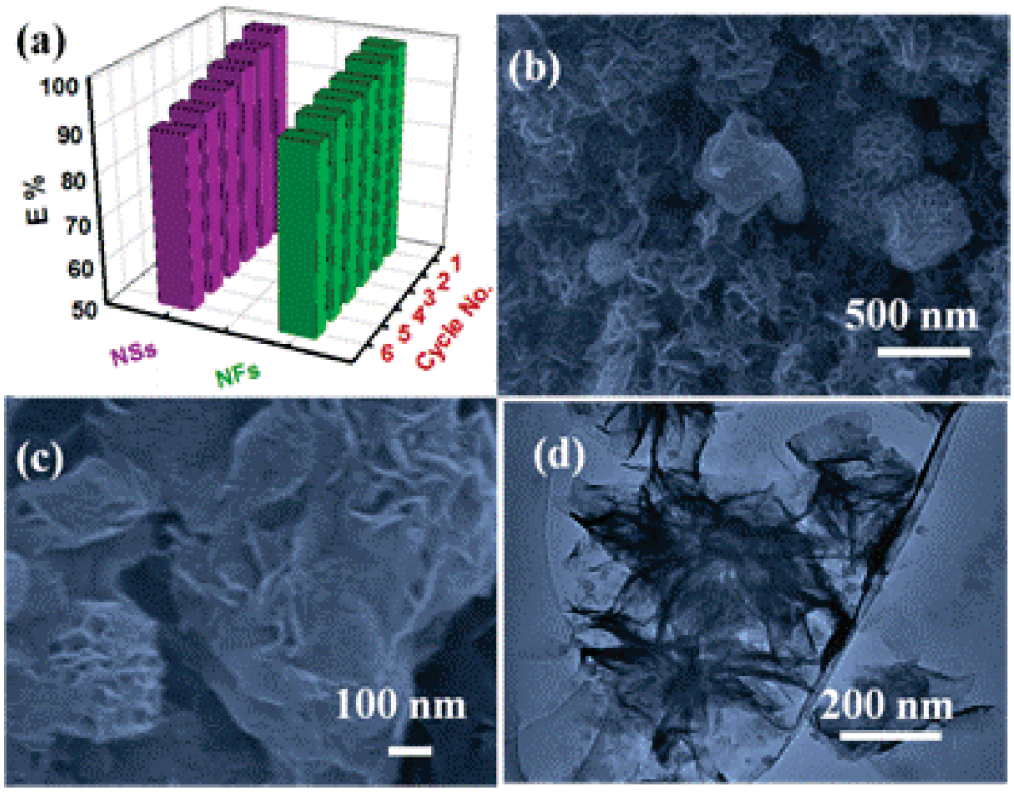

Figure 3.22: (a) Catalytic efficiency (E%) of the NiO NMs after multiple cycles at 25 °C, [E% of the NiO NMs was calculated from the % ratio of the reaction rate constant (k/s^{-1}) per recycle (No.) and the rate constant obtained from the initial use of the catalysts; the FE-SEM (b–c) and TEM (d) micrographs of mesoporous NiO NM after the third cycle

3.4.References

[1] T. Balaji, S. A. El-Safty, H. Matsunaga, T. Hanaoka, F. Mizukami, Angew. Chem. Int. Ed. 45, 2006, 7202.

[2] S. A. El-Safty, A. A. Ismail, H. Matsunaga, T. Hanaoka, F. Mizukami, Adv. Funct. Mater. 18, 2008, 1485.

[3] Y. Jin, C. Jia, S.W. Huang, M. O. Donnell, X. Gao, Nat. Commun. 1, 2010, 4.

[4] D. K. Kirui, D. A. Rey, C. A. Batt, Nanotechnology 21, 2010, 105; Y. Ren, P. G. Bruce, Z. Ma, J. Mater. Chem. 21, 2011, 9312.

[5] A. J. Gellman, N. Shukla, Nat. Mater. 8 , 2009, 87.

[6] H. P. Liang, H. M. Zhang, J. S. Hu, Y.G. Guo, L. J. Wan, C. L. Bai, Angew. Chem. Int. Ed. 43, 2004, 1540.

[7] S. A. El-Safty, A. Shahat, W. Warkocki, M. Ohnuma, small 7, 2011, 62

[8] S. A. El-Safty, Trend Anal. Chem. 30 , 2011, 447.

[9] A. Chen, P. Holt-Hindle, Chem. Rev. 110, 2010, 3767.

[10] A. S. Zuruzi, N. C. MacDonald, M. Moskovits, , A. Kolmakov, Angew. Chem. Int. Ed., 46, 2007, 4298.

[11] P. Yang, D. Zhao, D. I. Margolese, B. F. Chmelka, G. D. Stucky, Nature, 396, 1998,152.

[12] T. L. Lai, C. C. Lee, G. L. Huang Y. Y. Shu, C. B. Wang, Appl. Catal., B: Environmental 78, 2008, 151.

[13] Y. Li, B.C. Zhang, X.W. Xie, J. L. Liu, Y. D. Xu, W. J. Shen, J. Catal. 238, 2006, 412.

[14] P. Poizot, S. Laruelle, S. Grugeon, L. Dupont, J. M. Tarascon, Nature 407,2000, 496.

[15] G. Mattei, P. Mazzoldi, M. L. Post, D. Buso, M. Guglielmi, A. Martucci, Ad. Mater. 19 , 2007, 561

[16] A. Nattestad, M. Ferguson, R. Kerr, Y. B. Cheng, U. Bach, Nanotechnology, 19, 2008, 295304

[17] P. Jeevanandam, Y. Koltypin, A. Gedanken, Nano Lett. 10 , 2001, 263.

[18] N. Cordente, M. Respaud, F. Senocq, M. J. Casanove, C. Amiens, B. Chaudre, Nano Lett. 1, 2001, 565

[19] H. Liu, G. Wang, J. Liu, S. Qiao, H. Ahn, J. Mater. Chem. 21, 2011, 3046.

[20] N. M. Carneiro, W. C. Nunes, R. P. Borges, M. Godinho, L. E. Fernandez-Outon, W. A. A.Macedo, I. O. Mazali, J. Phys. Chem. C 114 , 2010, 18773.

[21] D. B. Kuang, B. X. Lei, Y. P. Pan, X. Y. Yu, C. Y. Su, J. Phys. Chem. C. 113, 2009, 5508.

[22] J. Hu, K. Zhu, L. Chen, H. Yang, Z. Li, A. Suchopar, R. Richards, Adv. Mater. 20, 2008, 267.

[23] N. D. Hoa, S. A. El-Safty, Nanotechnology 22, 2011, 485503.

[24] A. Sadana, J. R. Katrer, Ind. Eng. Chem. Fundam. 13, 1974, 2.

[25] World Health Organization and UNICEF.: Water for Life: Making it Happen ISBN 9241562935, 2005.

[26] A. Walcarius, L. Mercier, J. Mater. Chem. 20, 2010, 4478

[27] S. A. El-Safty, A. Shahat, Md. R. Awual, J. Colloid Interface Sci. 359, 2011, 9.

[28] A. A. Zagorodni, Ion Exchange Materials, Properties and Applications, Elsevier, Amsterdam, 2006.

[29] B. V. Bruggen, C. Vandecasteele, Environ. Pollut. 122, 2003, 435.

[30] L. K. Posey, M. G., Viegas, A. J. Boucher, C. Wang, , K. R. Stambaugh, M. M. Smith, B. G. Carpenter, B. L. Bridges, S. E. Baker, D. A. Perry, J. Phys. Chem. C 111, 2007, 12352.

[31] U. Hollstien, Chem. Rev. 74 (1974) 625; b) E. Frei, Cancer Chemother. Rep. 58, 1974, 49.

[32] C. Oishi, Bull. Univ. Osaka Pref. Ser., B 22, 1970, 49.

[33] P. Amrolia, S. G. A. Sullivan, Stern, R. Munday, J. Appl. Toxicol, 9, 1989, 113.

[34] Y. H. Hu, E. Ruckenstein, Langmuir 13, 1997, 2055, J. Li, R. Yan, B. Xiao, D. T. Liang, L. Du, Environ. Sci. Technol. 42, 2008, 6224

[35] N. D. Hoa, S. A. El-Safty, Chem. Eur. J. 17, 2011, 12896.

[36] M. J. Frisch, et al., Gaussian 03, Revision D.01, Gaussian, Inc., Wallingford, CT, 2004.

[37] Z. H. Liang, Y. J. Zhu, X. L. Hu, J. Phys. Chem., B 108, 2004, 3488.

[38] S. A. El-Safty, M. Mekawy, A. Yamaguchi, A. Shahat, K. Ogawa, N. Teramae, Chem. Commun. 46, 2010, 3917.

[39] K. S. Napolskii, I. V. Roslyakov, A. A. Eliseev, A. V. Petukhov, D. V. Byelov, N. A. Grigoryeva, W. G. Bouwman, A. V. Lukashin, K. O. Kvashnina, A. P. Chumakov, S. V. Grigoriev, J. Appl. Cryst., 43, 2010, 531.

[40] S. A. El-Safty, A. Shahat, M. Mekawy, H. Nguyen, W. Warkocki, M. Ohnuma, Nanotechnology, 21, 2010, 603.

[41] M. Kruk, V. Antochshuk, J. R. Matos, L. P. Mercuri, M. Jaroniec, J. Am. Chem. Soc. 124, 2002, 768.

[42] W. Q. Cai, J. G. Yu, B. Cheng, B. L. Su, M. Jaroniec, J. Phys. Chem. C. 113, 2009, 14739.

[43] F. Jiao, A. H. Hill, A. Harrison, A. Berko, A. V. Chadwick, P. G. Bruce, J. Am. Chem. Soc. 130, 2008, 5262.

[44] X. Song, L. Gao, J. Phys. Chem. C. 112, 2008, 15299.

[45] B. Zhao, X. K. Ke, J. H. Bao, C. L. Wang, L. Dong, Y. W. Chen, H. L. Chen, J. Phys. Chem. C 113, 2009, 14440.

[46] Y. Hattori, T. Konishi, K. Kaneko, Chem. Phys. Lett. 355, 2002, 37.

[47] M. J. Tomellini, J. Electron Spectrosc. Relat. Phenom. 58, 1992, 75.

[48] M. C. Biesinger, Payne B. P., W. M. L. Lau, A. Gerson, R. S. C. Smart, Surf. Interface Anal. 41, 2009, 324.

[49] a) H. A. E. Hagelin–Weaver, J. F. Weaver, G. B. Hoflund, G. N. Salaita, J. Electron Spectrosc. Relat. Phenom. 134, 2004, 139.

[50] R. Moreno-Tost, J. Santamaría-González, P. Maireles-Torres, E. Rodrguez-Castellón, A. Jiménez-López, J. Mater. Chem. 12, 2002, 3331.

[51] M. K. Moghaddam, A. Yangjeh, M. Reza Gholami, J. Mol. Catal. A: Chem. 306, 2009, 11.

[52] X. Wang, L. Li, Y. Zhang, S. Wang, Z. Zhang, L. Fei, Y. Qian, Cryst. Growth Des. 6, 2006, 9.

[53] A. B. Zaki, M. Y. El-Sheikh, J. Evans, S. A. El-Safty, Polyhedron 19, 2000, 1317.

[54] Y. Zhu, , J. Li , Z. Liu, G. Cheng, S. Dong, E. Wang, J. Mol. Catal., B Enzymatic 4, 1998, 33.

[55] J. Kaizer, R. Csonka, G. Speier, J. Mol. Catal. A 180, 2002, 91.

[56] T. Bell, Science. 299, 2003, 1688-1690

[57] Y. Wang, A. Zhu, Y. Zhang, C.T. Au, X. Yang, Appl. Catal. B 81, 2008, 141–149.

[58] H.J. Gallon, X. Tu, M.V. Twigg, J.C. Whitehead, App. Catal. B 106, 2011, 616–620

[59] A. Chen, P. Holt-Hindle, Chem. Rev. 110, 2010, 3767–3804

[60] A. N. Shipway, E. Katz, I. Willner, Chem. Phys. Chem. 1, 2000, 18; S. A. El-Safty, M. Khairy, M. Ismael, Sens. Actuators, B, 166, 2012, 253-263; S.A. El-Safty, M. A. Shenashen, M. Khairy, M. Ismeal, Chem. Commun., 48, 2012,

6708–6710; c) S.A. El-Safty, M. A. Shenashen, M. Khairy, M. Ismeal, Adv. Funct. Mater.22, 2012, 3013–3021

[61] Y. H. Lin, X. L. Cui, C. Yen, C. M. Wai, J. Phys. Chem. B 109, 2005, 14410-14415.

[62] S. Nakade, Y.Saito, W. Kubo, T. Kitamura,Y.Wada, S. I. Yanagida, J. Phys. Chem. B. 107, 2003, 8607–8611

[63] N. Liu, M. Tang, M. Hentschel, H. Giessen, A. P. Alivisatos, Nat. Mater. 10, 2011, 31-636.

[64] R. Narayanan, M. A.El-Sayed, J. Am. Chem. Soc. 126, 2004, 7194-7195

[65] K. Butter, K. Kassapidou, G. J.Vroege, A. P. Philipse, J. Colloid Interf. Sci. 287, 2005, 485-495.

[66] Y. Kobayashi, M. Horie, M. Konno, B. R. Gonzälez, M. L. Liz-Marzañ, J. Phys. Chem., B 107, 2003, 7420- 7425.

[67] M. Mikhaylova, D. Kim, N. Bobrysheva, M. Osmolowsky, V. Semenov, T. Tsakalakos, M. Muhammed, Langmuir, 20, 2004, 2472.

[68] Z. L. Liu, X. Wang, G. H. Du, Q. H. Lu, Z. H. Ding, J. Tao, J. Mater. Sci. 39, 2004, 2633

[69] S. Xuan, F. Wang, X. Gong, S. K. Kong, J. C. Yua, K. C- F. Leung, Chem. Commun. 47 , 2011, 2514–2516.

[70] M.C.A. Fantini, F.F. Ferreira, A. Gorenstein, Solid State Ionics. 152, 2002,867–872

[71] S. D. Tiwari, K. P. Rajeev, Thin Solid Films 505, 2006, 113.

[72] J. G. Cook, F. P. Koffyberg, Solar Energy Materials, 10 , 1984, 55-67.

[73] X. Zhang, W. Shi, J. Zhu, W. Zhao, J. Ma, S. Mhaisalkar, T. L. Maria, Y. Yang, H. Zhang, H. H. Hang, Q. Yan, Nano Res. 3, 2010, 643–652.

[74] J. Liang, Y. D. Li, Chem. Lett. 32, 2003, 1126.

[75] Z. Y. Wu, C. M. Liu, L. Guo, R. Hu, M. I. Abbas, T. D. Hu, H. B. Xu, J. Phys. Chem. B 109, 2005, 2512.

[76] G. Malandrino, L. M. S. Perdicaro, I. L. Fragala, R. L. Nigro, M. Losurdo, G. Bruno, J. Phys. Chem. C 111, 2007, 3211.

[77] X. B. Chen, S. S. Mao, Chem. Res. 107, 2007, 2891.

[78] M. Khairy, S. A. El-Safty, M. Ismael, H. Kawarada, Appl. Catal., B 123, 2012, 162-173

[79] N. D. Hoa, S. A. El-Safty, Nanotechnology 22, 2011, 485503.

[80] K. S. W. Sing, D. H. Everett, R. A. W.Haul, L. Moscou, R. A. Pierotti, J. Rouquerol, T. Siemieniewska, Pure Appl. Chem. 57, 1985, 603–19; S.A. El-Safty, Y. Kiyozumi, T. Hanaoka, F. Mizukami, Appl. Catal. B 82, 2008, 169–179; S. A. El-Safty, Y. Kiyozumi, T. Hanaoka, F. Mizukami, Appl. Catal., A, 337, 2008, 121-129.

[81] G. D. Moeser, K. A. Roach, W. H. Green, T. A. Hatton, P. E. Laibinis, AIChE J. 50, 2004, 2835- 2848.

[82] M.Y.Ge, L. Y. Han, U. Wiedwald, X. B. Xu, C. Wang, K. Kuepper, P. Ziemann, J. Z. Jiang, Nanotechnology 21, 2010, 425702; S. A. El-Safty, A. Shahat, Md. R. Awual, J. Colloid Interface Sci., 359, 2011, 9-18.

[83] M. P. Proenca, C. T. Sousa, A. M. Pereira, P. B. Tavares, J. Ventura, M. Vazquez, J. P. Araujo, Phys. Chem. Chem. Phys. 13 , 2011, 9561–9567.

[84] X. Chen, L. Li, X. Sun, Y. Liu, B. Luo, C. Wang, Y. Bao, H. Xu, H. Peng, Angew. Chem. Int. Ed. 50, 2011, 1–5.

[85] N. Nasuha, B.H. Hameed, Chem. Eng. J. 166, 2011, 783-786.

CHAPTER 4

NANOMAGNET SELECTIVE ADSORPTION AND REMOVAL OF BIOLOGICAL MOLECULES

1- **Mohamed Khairy**, Sherif A. El-Safty and Mohamed Ismael, *Chemical Communications,* 2012, 48, 10832-10834.

2- **Mohamed Khairy**, Sherif A. El-Safty, *Colloids and Surfaces B: Biointerfaces*, COLSUB-D-13-00089R1, 2013, in Press.

3- Sherif A. El-Safty, Mohamed A. Shenashen, **Mohamed Khairy**, *Colloids and Surfaces B: Biointerfaces,* 2013, 103, 1 288-297.

4- Sherif A. El-Safty, Mohamed A. Shenashen, Mohamed Ismael, **Mohamed Khairy**, *Chemical Communications,*2012, 48, 6708-6710.

5- Sherif A. El-Safty, Mohamed A. Shenashen, Mohamed Ismael, **Mohamed Khairy,** *Advanced Functional Materials*. 2012, 22(14) 3013–3021.

4.1.Introduction

The adsorption and separation of the target protein from a complex solution on a solid surface has a critical function in different disciplines ranging from gene biology, biotechnology, biochemical engineering, biomedicine, and environmental processes.[1–13] Therefore, special attention should be exerted in understanding the fundamental factors that control protein-surface interactions. These factors are imperative in improving the ability to design biocompatible materials and biotechnological devices.[14, 15] Protein loading on solid surfaces is a complex process because it involves numerous binding events, such as conformational changes, hydrogen bonding, and/or hydrophobic and electrostatic interactions.[4–6, 16, 17] Surface characteristics, protein properties, and chemical environments influence these interactions. In the last few decades, proteins have been separated and purified from tissues after expression in bacteria or yeast by different classical techniques including chromatography, gel electrophoresis, ultrafiltration, microfluidics, and multi-lane channel methods.[7] Among all these techniques, the chromatographic method is one of the most important; however, it is not suitable in the early stages of the isolation/purification process due to the suspended solid and fouling components. Furthermore, the use of polymeric membrane materials with large pores and heterogeneous matrices leads to low protein adsorption capacities and increased separation times.[8] Therefore, the development of improved adsorption and separation techniques is necessary. These techniques should be capable of treating solutions with wide range of protein concentrations in large-scale processes, even in the presence of particulate mixtures.

Successful strategies for adsorption, separation, and manipulation of protein based on porosity and functionality of nanomaterials have been established.[18–22] Significant progress in cancer diagnosis, protein separation, and detection has been achieved based on well-synthesized and functionalized iron oxide nanoparticles.[22–28] These nanoparticles have the following key features:

I. Have the ability to interact with biological molecules in different ways due to their magnetic features.

II. Offer a large exposed surface area without using porous materials, which are often plagued by high mass transfer resistances.

III. Introduced a wide variety of surface functionalizations that can serve as versatile platforms for effective manipulation of various bimolecular reactions, which is an important factor in proteomics.

IV. Required simple separation of the target compound, support full automation, and provide precise results.[9,10] However, the key factor and main drawback is the alteration of the chemical surface characteristics that need extensive surface processing. This process involves multiple steps, entails difficulty in scale-up fabrication, and requires a longer span of time. Therefore, the development of a new strategy in the production of synthetically constructed nanomagnet materials is highly desirable for the selective and efficient separation of macromolecules.

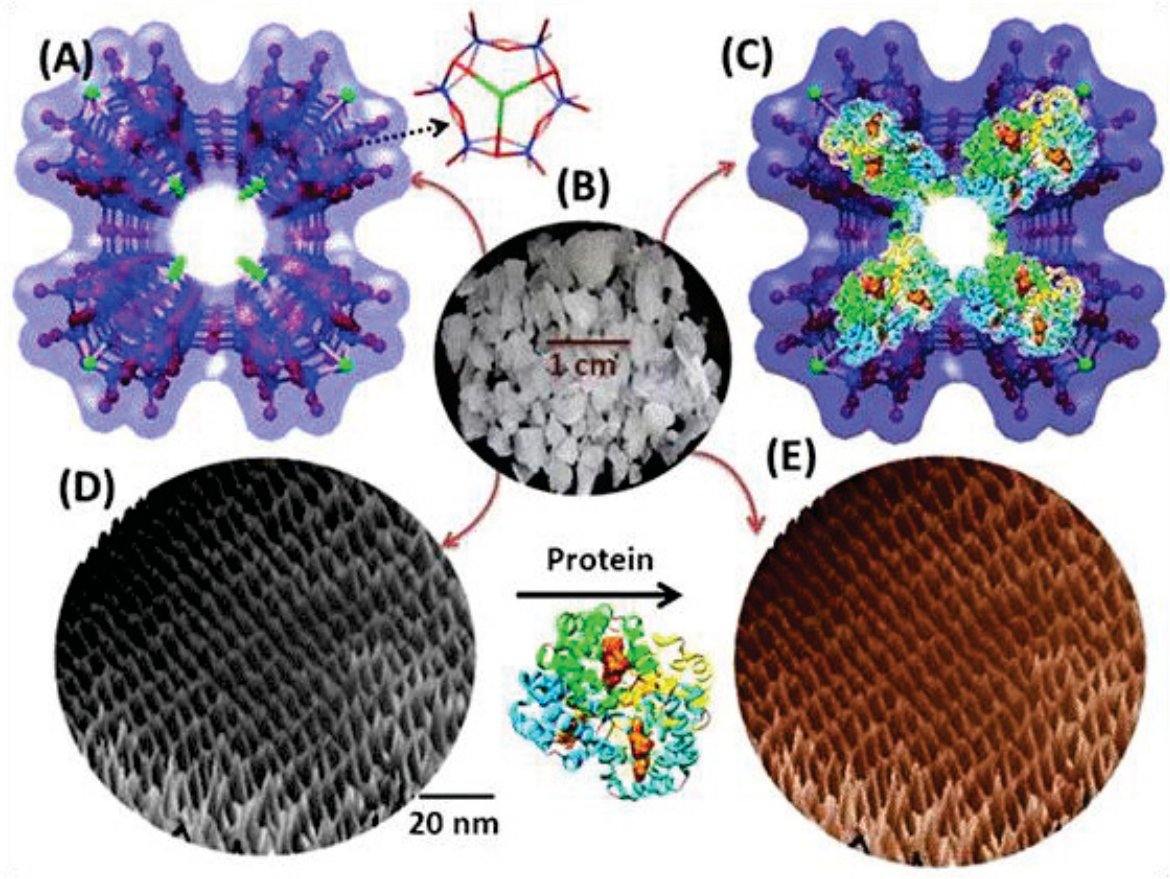

Figure 4.1: 3D Geometrical models (A, C) and pore surfaces (D, E) of mesobiocaptors based on cubic *Pm3n* mesostructures with aluminosilica cylindrical pore monoliths (B). The design indicates the feasibility of the protein adsorption interior mesopores (C) and inside pore surfaces (E) of 3D cubic *Pm3n* aluminosilica structures with Si/Al ratio of 4. The colors of the atoms in the truncated aluminosilica cluster (A) are as follows: Al (green), Si (Blue), and oxygen (red), respectively.

The size-selective adsorption and separation process of virtual macromolecules (i.e., proteins) with different shapes, sizes, functions, and properties into mesocaptor aluminosilica monoliths and mesocage alumina (Figure 4.1) was recently reported.[6] The unique physical properties and the active-site surface functionality of aluminosilicas and alumina enhance size-selective adsorption of low-molecular-weight proteins in terms of loading capacity and sample quantity, ensuring a higher concentration of adsorbed proteins, interior pore diffusivity, and encapsulation in a short period. However, the clogging of pores with large-molecular-weight proteins, particularly at high feed concentration during size-selective encapsulation assays (i.e., dead-term adsorption) still remains a challenge. The fabrication of selective protein supercaptors that 1) are not impeded by the physical shape and 3-D hydrodynamic dimensions of the protein; 2) exhibits minimal clogging effect with high retention of the protein; and 3) has uniformly sized adsorbent pores is a key requirement in successful protein encapsulation and uptake.

Large-scale production, as well as low-cost and simple fabrication strategies for mesoporous metal oxide nanomagnet-selective supercaptors of hemoproteins (iron-porphyrin prosthetic group) from mammalian cells, such as hemoglobin (Hb), myoglobin (Mb) and cytochrome C (CytC) as shown in this chapter. Hemoglobin is a quaternary protein that occurs in red blood cells, whereas myoglobin and cytochrome C are tertiary proteins found in muscle cells and liver cells of mammals, respectively. In this adsorption and separation model, the morphology, crystal sizes and shapes, magnetic properties, heme-group distributions, and protein-carrier binding energy have a key function in broadening the controlled adsorption affinity and selectivity of hemoproteins.

4.2. Selective encapsulation of heme-proteins using mesoporous metal oxide nanoparticles.

4.2.1. Formation mechanism of mesoporous metal oxides

A recent approach for the morphology-controlled synthesis of materials without a template is based on formation and decomposition of metal–organic precursors. The organic part serves as a linker that affords a wide variety of linking sites with tuned binding strength and directionality, as shown in Figure 4.2. The formed supermolecular structures under hydrothermal synthesis form anisotropic crystals.29, 30 Upon heating conditions, the acetate groups (organic linker) might coordinate with nickel to form nickel acetate complex. Then, hydrolysis and/or alcoholysis of nickel complexes were took place to form NiO nanomaterials.

As example, the possible formation mechanism of mesoporous NiO NFs with rose-like morphology involves two consecutive reactions followed by orientation attachment followed by local Oswald ripening to form magnetic NiO nanocrystal with rose-like morphology. Figure 4.2b reveals the crystal particles of NiO were aggregated petal-like with smooth fine surfaces that were aligned according to the rose morphology. To form the mesoporosity inside the NPs, the calcinations are performed at an appropriate temperature. The thermal decomposition of nickel samples reveals that the solid sample decreased in mass at around 270 °C to 340 °C. This decrease was accompanied by an endothermic peak in the corresponding DTA curve, indicating the decomposition of the inorganic–organic moieties. The weight loss from the decomposition process was 25.8, 27.5, and 28.447 wt% for NRs, NPLs, and NSs, respectively (Figure 4.3). The thermal decomposition of Fe_3O_4 NPs showed two consecutive derivative peaks with exothermic peaks in the corresponding DTA curve. These peaks are related to the decomposition of the weakly bound oleic acid and covalently bonded oleic acid molecules (23%). Oleic acid is very important in fabricating nanoparticles with the desired magnetic properties and in protecting the magnetite particles from oxidation and agglomeration.

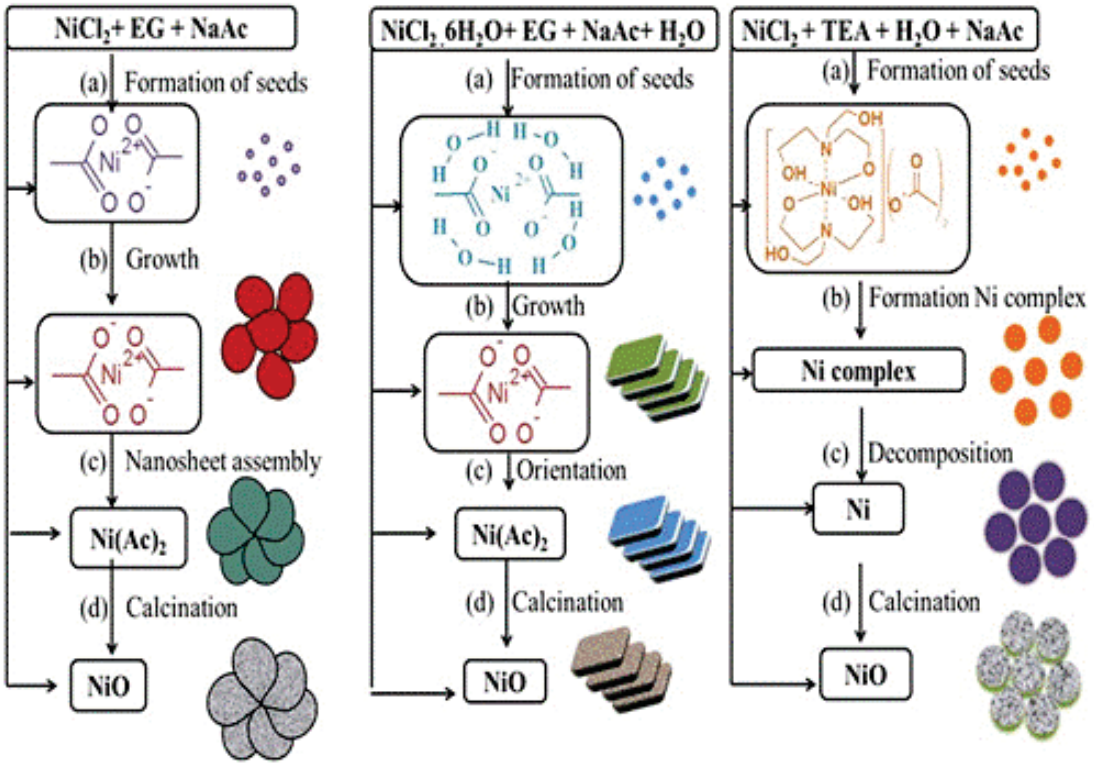

Figure 4.2. Formation mechanism of NiO nanoparticles via hydrothermal treatment [Not that, NaAc is sodium acetate, EG is ethylene glycol, and TEA is triethanol amine].

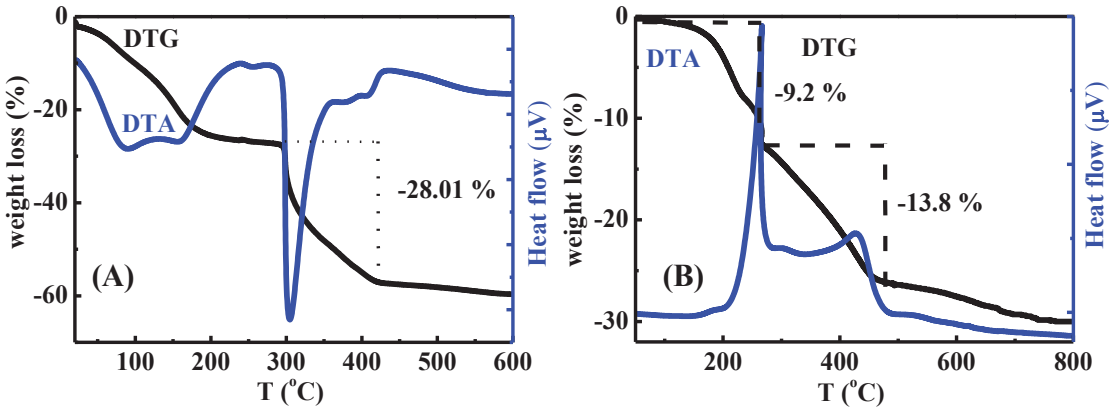

Figure 4.3: DTG and DTA profiles of NiO nanorose and Fe_3O_4 nanoparticles.

4.2.2. Textural and physicochemical features of metal oxide NPs

The small-angle X-ray scattering (SAXS) profiles of NiO and Fe_3O_4 NPs were subjected to absolute intensity scaling after normalizing the in-plane diffracted beams with substrate thickness (Figure 4.4). The scattering intensity and peak resolution in the range of $1.3 < q < 2.2$ strongly suggest that mesostructures with worm-like pore cavities could be formed within NiO NPs. The typical wide angle X-ray diffraction patterns of the NiO NPs (Figures 4.6 and 4.19) are consistent with the face-centered cubic (*Fm3m)* symmetry with a lattice constant a = 4.194 Å (JCPDS, No. 01-089-7130). The particle size of the NiO NPs was calculated by using the Scherrer equation, and the estimated particle size varied from 12.1 nm to 12.7 nm.

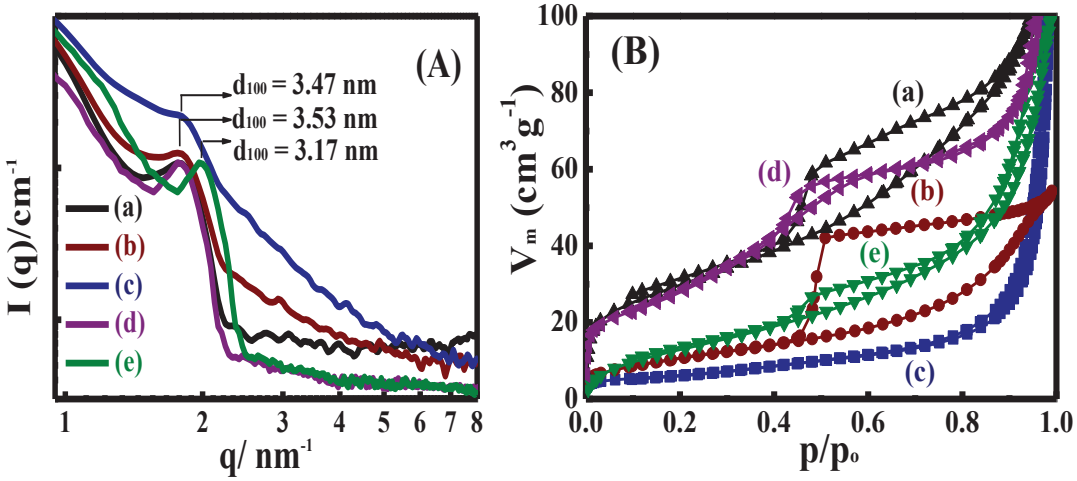

Figure 4.4: A) SAXS pattern (A) and N_2 adsorption/desorption isotherms of mesoporous NiO and Fe_3O_4 NPs: a) NiO nanoroses, b) NiO nanospheres, c) rectangular NiO nanoplatelets, d) hexagonal NiO nanoplatelets, and e) Fe_3O_4 nanoparticles.

The textural properties of the NiO NPs were investigated using N_2 isotherms (Figure 4.4). N_2 isotherms of NiO NFs, NiO NSs, and NiO H-NPLs featured type IV isotherms. NiO NFs showed H_3-type hysteresis loops due to flaky structures. These flaky structures and factors such as inter-particle spacing are the apparent reasons for the bimodal pore size distribution (2.1 and 10 nm) [25, 26]. NiO NSs and NiO H-NPLs present H_2-type hysteresis loop for typical mesocage materials with bimodal pore cavities 3 nm to 27 nm and 3.6 nm to 268 nm. The macroporous cavity of H-NPLs is attributed to the pores between the nanoplatelets. NiO R-NPLs did not show any hysteresis and demonstrated type II isotherm with bimodal pore sizes of 31 and 280 nm (Figure 4.5). The desorption branch of the isotherms shows a stepwise behavior and ends at the limiting pressure of the hysteresis closure, implying non-uniformity of pore openings associated with pore constrictions and/or ink-bottle pores with narrow necks. This finding demonstrates that the synthesis protocol could provide control over the size and shape of cage opening and cavity pores. The specific surface areas were S_{BET} = 171, 60, 160, and 45 m^2g^{-1} for NiO NRs, NSs, H-NPLs, and R-NPLs, respectively. Generally, the formation of mesopore type is related to the pores inside the NiO NPs, which formed between primary crystallites. The N_2 adsorption/desorption isotherm of Fe_3O_4 NPs reveals type IV isotherm with H_3 hysteresis loops and high specific surface area (S_{BET} = 52 m^2g^{-1}) with bimodal pore size (5.8 nm to 55 nm). This mesoporosity would create more convenient channels for proteins to diffuse into the 3D pore network matrices.

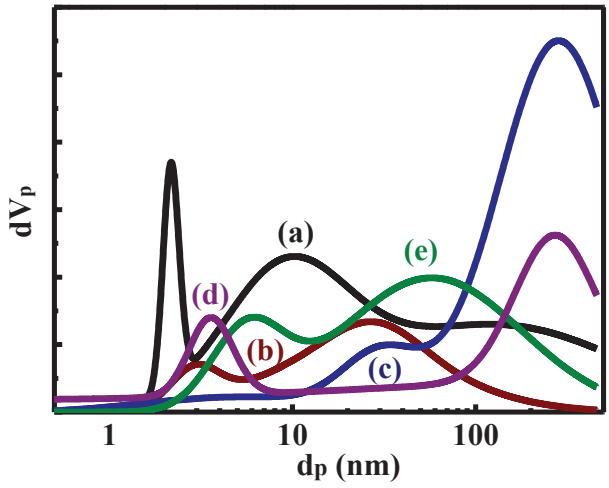

Figure 4.5: NLDFT profile of the pore size distribution of mesoporous NiO and Fe_3O_4 NPs, a) NiO nanoroses, b) NiO nanospheres, and c) rectangular NiO nanoplatelets, d) hexagonal NiO nanoplatelets and e) Fe_3O_4 NPs.

Meanwhile, the magnetic properties of mesoporous metal oxide nanoparticles were studied using a superconducting quantum interference device (SQUID) magnetometer at 300 K. When the dimensions of anti-ferromagnetic oxides were decreased to a nanoscale, a variety of new physical phenomena were exhibited, including weak ferromagnetism and para-magnetism arising from the surface and finite size effects or net magnetic moment coming from uncompensated spins. This surface effect was studied by Nĕel in 1961, from which he suggested that small particles of an anti-ferromagnetic oxide exhibit paramagnetism and weak ferromagnetism. This phenomenon is attributed to the permanent magnetic moment due to uncompensated spins in the two sublattices. The number of uncompensated spins (q) depends on the crystal structure and particle morphology; three different models have been considered. If the uncompensated spins are randomly distributed in the particle, $q \alpha n_S^{1/2}$ (where n_S is the total number of spins) is expected. However, if they are arranged parallel to each other in an odd number of layers stacked in a cube, then $q \alpha n_S^{2/3}$. Finally, if the core of the particles has no defects and the uncompensated moments are randomly distributed at the surface, then $q \alpha n_S^{1/3}$. The unexpected magnetic behavior of NiO NPs largely depends on their synthetic methods. The magnetic hysteresis loop (M-H loop) of NiO and Fe_3O_4 was measured (Fig. 4.6). The saturation magnetization (M_s) of NiO NPs follows the order NRs > NSs > NPLs (rectangular). This magnetic moment may be due to the uncompensated spins, which are mainly dependent on synthetic composition, particle size, and morphology.[31] Under exposure to external magnetic field, NiO NPs were easily separated from the solution in a short period of time (i.e., in minutes).

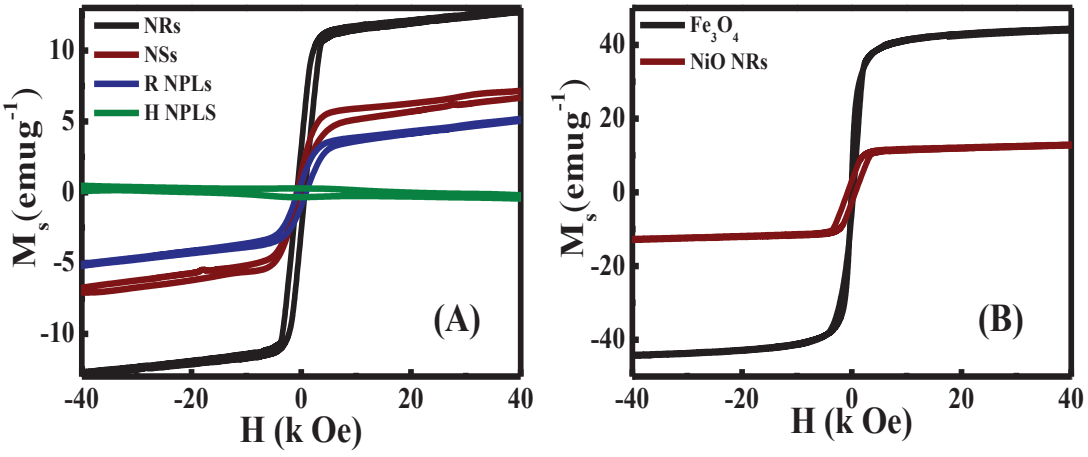

Figure 4.6: Magnetization curves of mesoporous NiO and Fe_3O_4 nanoparticles.

4.2.3. Structural geometry and particle morphology of metal oxides

Figure 4.7 reveals that various synthetic conditions could control the sizes and morphology of NiO NPs, which is a key trend in nanotechnology and biotechnology [32, 33]. The FE-SEM micrograph (Figure 4.7a) indicates the formation of rose-like hierarchical structures with an average particle diameter of ~250 nm. Moreover, close inspection of these images revealed that the material possesses lightly packed irregular sheets similar to petals or rose clefts interwoven together to form a rose shape with an open porous structure (Figure 4.7a). These nanopetals exhibited a curved shape with a thickness of ~15 nm. The spheres and rectangular platelets of NiO NPs with average sizes of ~550 and 200 nm are illustrated in Figure 4.7 (b and c). The surface of the spheres was not smooth, which was possibly due to the formation of aggregated NiO NPs. Figure 4.7c shows the formation of NiO platelets with average size of ~200 nm and thickness of ~20 nm. By contrast, Figure 4.7d shows the formation of hexagonal NiO with an average diameter of 250 nm and a thickness of 20 nm. Moreover, Fe_3O_4 NPs have sphere morphology with rough surfaces, which can be attributed to the formation of aggregated Fe_3O_4 NPs (Figure. 4.7 (e and f)).

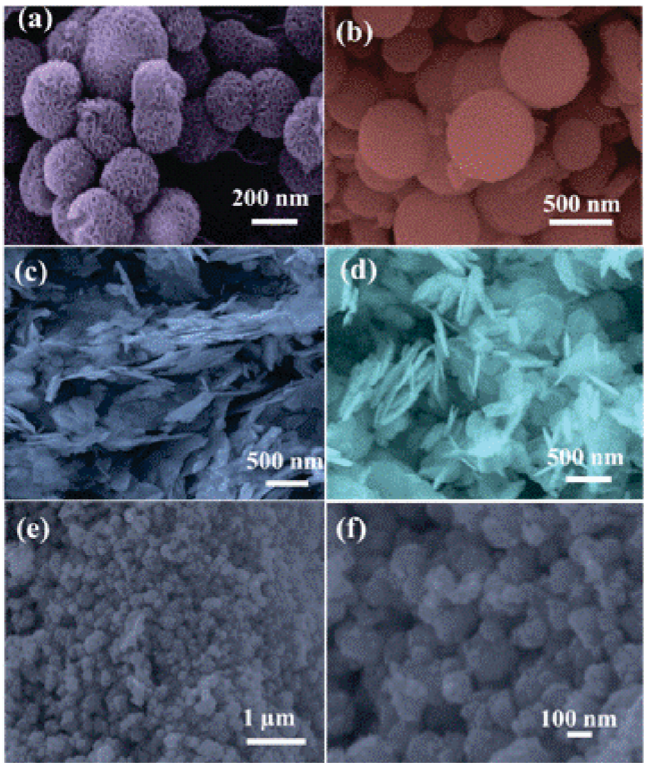

Figure 4.7: FE-SEM images of mesoporous NiO and Fe_3O_4 NPs: a) NiO rose, b) NiO sphere, c) rectangular NiO nanoplatelet, d) hexagonal NiO nanoplatelet-like morphology, and e, f) Fe_3O_4 NPs.

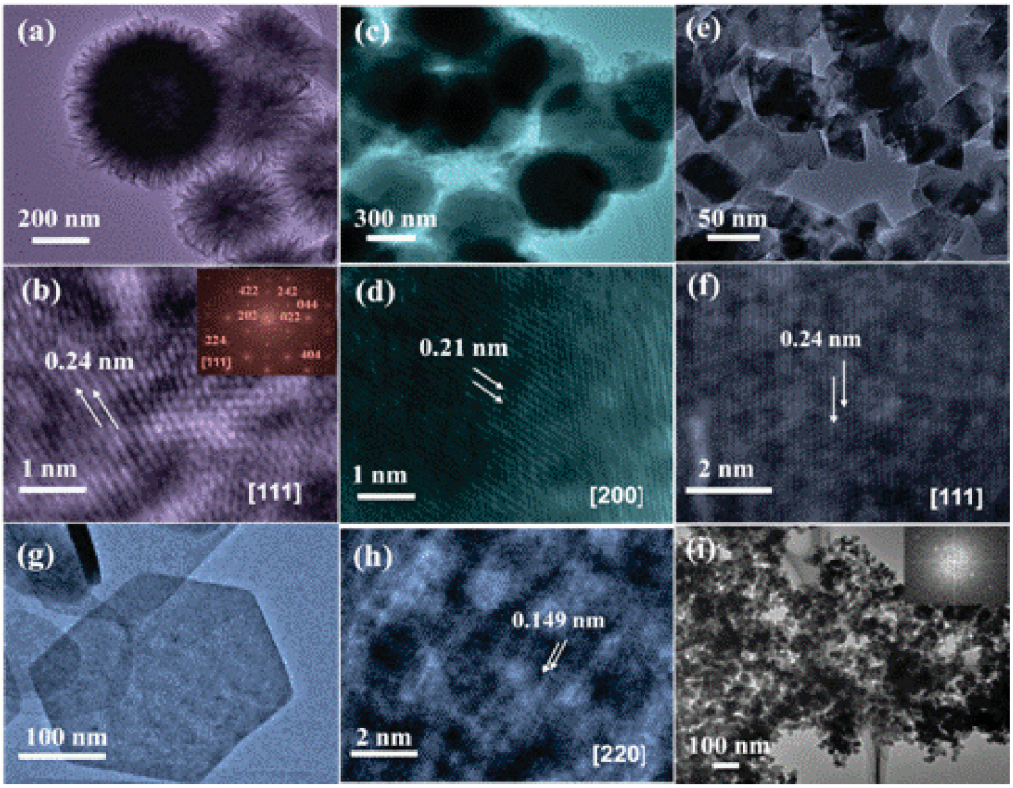

Figure 4.8: HR-TEM micrographs of mesoporous NiO and Fe_3O_4 NPs. HR-TEM and high-magnification HR-TEM patterns of nanorose (a and b), nanosphere (c and d), rectangular nanoplatelets, (e and f) and hexagonal nanoplatelets (g and h) [Inset (b) the ED pattern of NiO NCs along [111] direction, i) the HR-TEM images and FTD pattern of Fe_3O_4 NPs.

The HR-TEM micrographs clearly demonstrated the controlled shapes of NiO NPs in nanorose, nanosphere, and nanoplatelet-like morphology depending on the synthetic conditions. Figure 4.8a shows the rose formation of condensed clefts with an average size of ~250 nm. The petals were very thin, with a thickness of less than 15 nm. The HRTEM images showed well-ordered lattice fringes of NiO crystals, indicating the high crystallinity of the sample (Figure 4.8b). The distance between two lattice fringes is 0.24 nm, which is consistent with the inter-planar space of the (111) plane of cubic *Fm3m* NiO symmetry (JCPDS, No. 01-089-7130). The representative ED image [inset Figure 4.8b] showed well-defined orientations of bright dot incidences, indicating the formation of large-scale NCs domains of the (111) plane with cubic NiO symmetry. Figure 4.8c reveals the controlled formation of mesoporous NiO NSs and rectangular NPLs with an average size of 550 and 50 nm, respectively. The higher-magnification HRTEM images showed the lattice fringes with an interspacing of 0.21 and 0.24 nm, corresponding to the distance

between the (200) and (111) planes of cubic *Fm3m*. Figure 4.8g clearly reveals the formation of irregular hexagonal nanoplatelets with an average size of 250 nm, a thickness of less than 20 nm, and an adjacent edge angle of approximately 120°. Generally, the TEM micrograph of NiO NPs showed the formation of disordered (wormlike) mesopores, as indicated by the SAXS and N_2 adsorption isothermal profiles. Notably, FE-SEM and HRTEM showed the shape- and size-controlled NiO NPs in different morphologies based on the synthetic conditions. This evidence indicates the versatility of the current method in the control of NiO NPs geometry. By contrast, the TEM micrograph of Fe_3O_4 (Figure 4.8i) demonstrated nanosized particles of Fe_3O_4 with an average diameter of 40 nm; the arrangement of the specific lattice fringes in the Fourier transform diffractogram (FTD) patterns were also recorded. The FTD image of Fe_3O_4 indicates that the high crystallinity nanoparticles with *Fd3m* space group.

4.2.4. The Batch adsorption method of proteins over nanoscale porous metal oxides

The biosorbent based on NiO and Fe_3O_4 mesostructured materials were used for the separation of proteins such as hemoglobin (Hb), myoglobin (Mb) and cytochrome c (CytC), insulin (Ins), α-amylase (Amy), and myosin (My) respectively. In such a batch adsorption experiment, 25 mg of NiO and Fe_3O_4 nonmaterials were performed in an aqueous solution (30 ml deionized water) under constant stirring conditions and at different temperatures (20 °C to 35 °C, ± 0.1 °C range). The initial concentration used of proteins was in the range of 3.5 x 10^{-6} mol. dm^{-3} to 6.01 x 10^{-5} mol.dm^{-3}. The aliquot protein was collected and monitored as a function of adsorption time. The concentration of Hb, Mb, CytC, Ins, Amy, and My proteins were studied using UV–vis spectroscopy (a Shimadzu 3700 model solid-state) at λ of 277, 409, 408, 405, 252 and 267 nm, respectively. The decrease of the UV-vis spectra of all proteins at specific wavelengths indicated the adsorbed amount of proteins within these adsorption processes.

The Molecular weight and size of proteins:

Protein	M.wt (g/mol)	Size (nm)
Insulin	5733	2.4
α-Amylase	58000	6.8 nm
Myosin	220000	14nm
Cytochrome c	12327	2.5 x 2.5 x 3.7 nm
myoglobin	16950	2.5 × 3.5 ×4.5 nm
hemoglobin	68000	7.0 nm

4.2.5. Key components in the adsorption assay

In this study, the adsorption assay of proteins was performed using mesoporous metal oxides such as NiO and Fe_3O_4 NPs, as shown in Figure 4.9. The results indicate that the supercaptor design-based NiO NRs have high loading capacity, efficiency, and selectivity for adsorption of hemoproteins, among all other proteins. The adsorption amount is in the following order: Hb >> Mb > CytC, and was found to be 85.2%: 23.5%: 12.6% from its initial concentration (3.5×10^{-6} mol. dm^{-3}) after 20 min. The features of mesoporous magnetic metal oxides introduced an extra surface area that induced high diffusion of hemoproteins into the mesopore cavities. To investigate the effective protein adsorption onto mesoporous metal oxide NPs, the adsorption assays were performed on hexagonal anti-ferromagnetic NiO NPLs and superparamagnetic Fe_3O_4 NPs (Figure 4.9B).[34, 35] these findings prove that morphological feature is one of the most significant factors affecting the selective adsorption of hemoproteins. For instance, the adsorption of Hb shows the following sequence: NRs >> NSs > R-NPLs > H-NPLs >> Fe_3O_4 (Figure 4.9B). Another important factor is the high adsorption efficiency and selectivity for high-concentration Hb of mesoporous NiO NRs.

Notably, the adsorption efficiency of Hb showed that NiO NRs >>> Fe_3O_4 NPs despite the high magnetization of Fe_3O_4 NPs compared with that of mesoporous NiO NPs. In turn, the mesopore size of Fe_3O_4 may prevent Hb from penetrating the interior pore; thus, the adsorption of hemoproteins onto Fe_3O_4 was subsequently studied (Figure 4.9D). Interestingly, the adsorption affinity follows the order CytC > Mb> Hb, although Mb and CytC have almost the same size. These results are unexpected and are supported by theoretical binding calculations over NiO and Fe_3O_4 surfaces as shown in Figure 4.11.

To investigate the adsorption isothermal assays, adsorption of the protein molecules was studied following the Langmuir isotherm (Figure 4.10). The homogeneous hemoprotein structures have key functions based on the Langmuir equation, which proposes that empirical symmetry exists in all adsorbent–adsorbate sites and energy. The Langmuir adsorption isotherms (Figure 4.10 (A, B, and C)) of the adsorption of hemoproteins onto mesoporous surfaces of NiO and Fe_3O_4 NPs show real evidence on the selective adsorption, encapsulation, and separation of hemoproteins based on NiO NPs. Moreover, the linear adsorption curves indicate that a wide range of biomolecule concentrations can be removed in a one-step treatment. Figure 4.10 D further shows that

Fe_3O_4 NPs generally reveal low adsorption affinity of hemoproteins compared with mesoporous NiO NRs. The q_m values of Fe_3O_4 adsorbents follow the order CytC > Mb > Hb, which is inconsistent with the sequence of the NiO NPs assays.

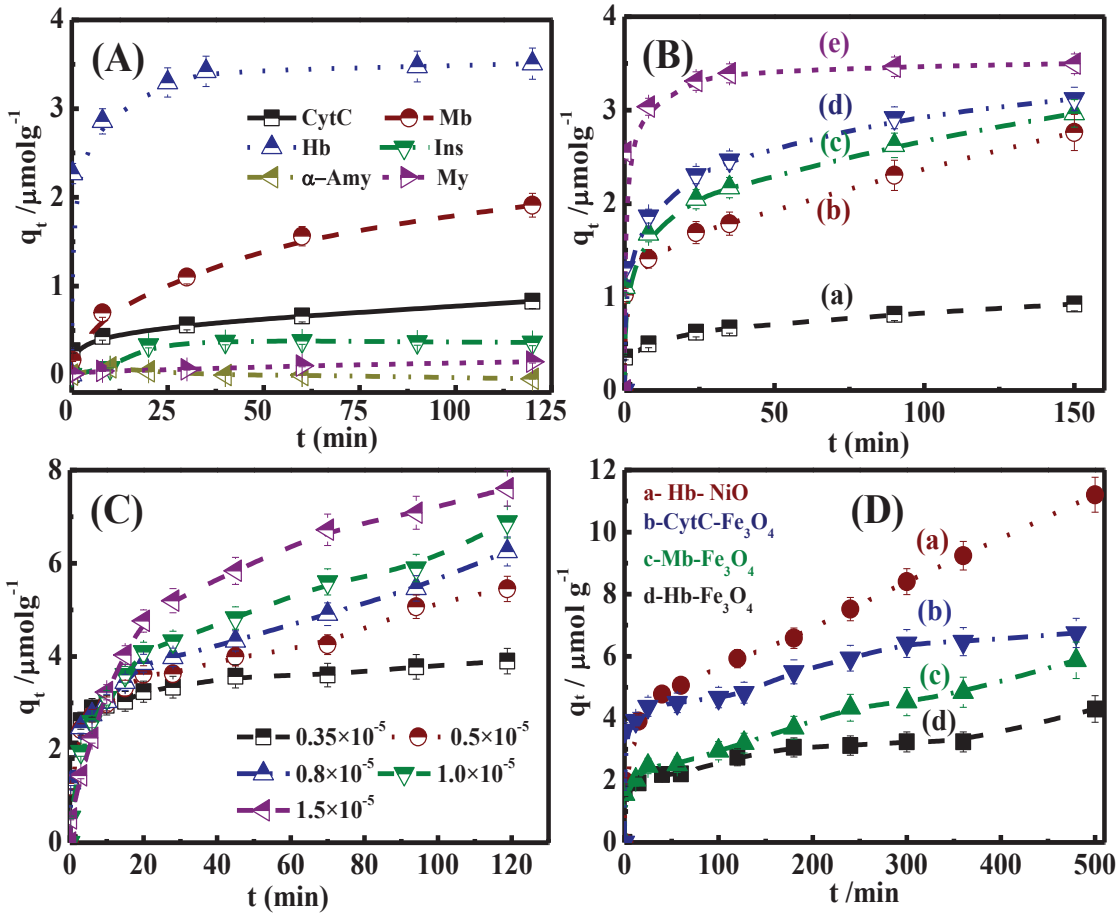

Figure 4.9: A) Time dependence of the adsorption amount of 3.5 × 10^{-6} M proteins on mesoporous NiO NRs. B) Effect of chemical composition and morphology of nanobiosorbent on the adsorption of 3.5× 10^{-6} M hemoglobin: a) Fe_3O_4 NPs, b) NiO NPLs (hexagonal), c) NiO NPLs (rectangular), d) NiO NSs, and e) NiO NR-like morphology. C) Effect of hemoglobin concentration on the adsorption assays over 0.025 g NiO NRs. D) Adsorption affinity of (1 × 10^{-5} M) heme-protein at Fe_3O_4 NPs compared with NiO NRs. The presented data are the mean values ± SD, for analytical data of three replicate analyses.

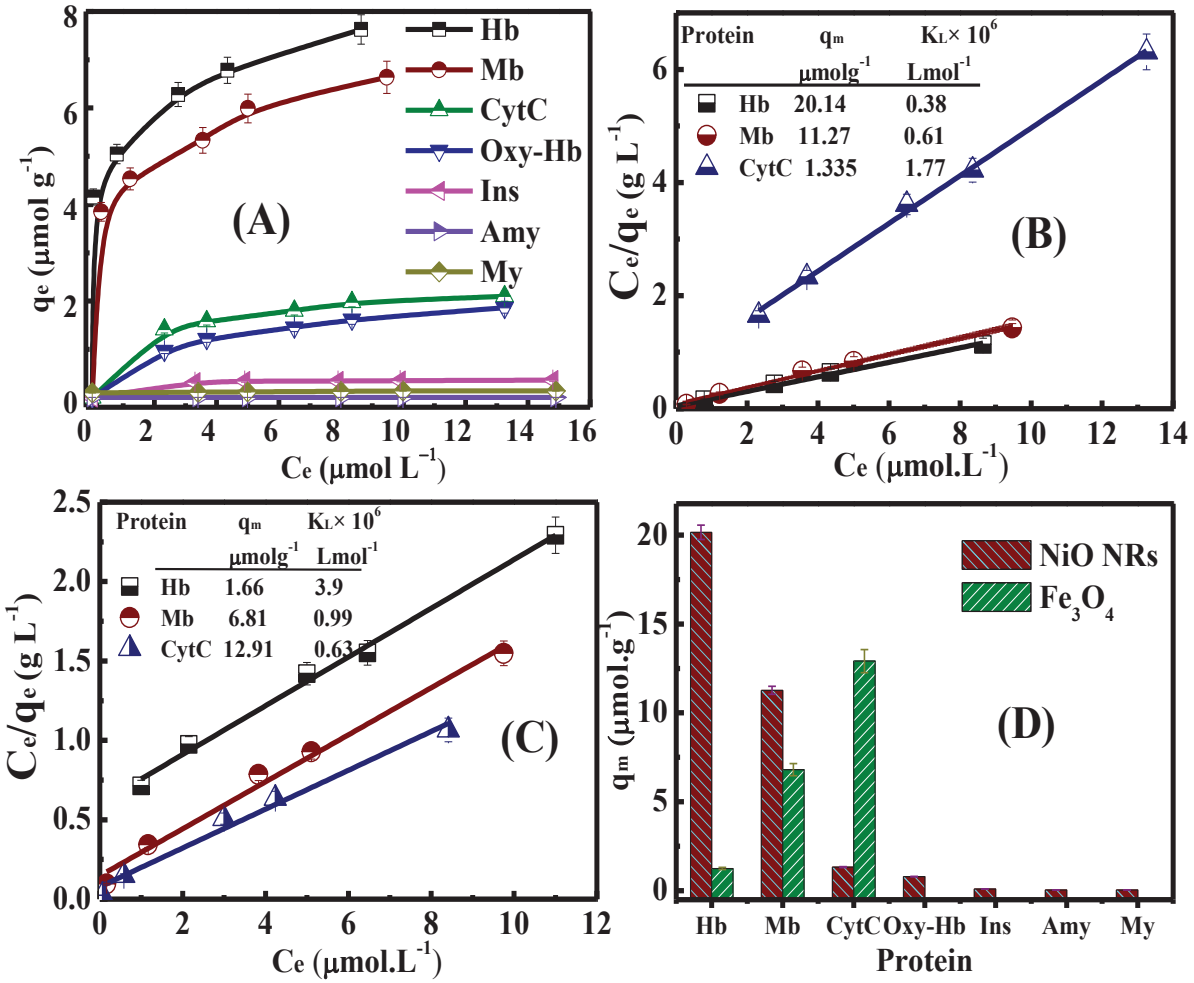

Figure 4.10: A) Concentration-dependent adsorption amount of different proteins over NiO NRs. (B) Langmuir adsorption isotherms for adsorption of hemoproteins into 0.83 g/L NiO NRs and (C) 0.83 g/L Fe_3O_4 NPs. (D) Adsorption assay of proteins over mesoporous NiO and Fe_3O_4 NPs. The error bar indicates the mean ± SD for analytical data of three replicate analyses.

The orientation and distribution of heme-moiety in the molecular shape of protein have significant functions in the magnetic flux and adsorption affinity of mesoporous NiO and Fe_3O_4 NP adsorption assays. For instance, Hb contains four heme-moieties that are directed to the protein surface compared with that of Mb (with one heme-group on the surface) and CytC (with one-heme group in the center). By contrast, the weak adsorption of Hb on Fe_3O_4 NP surfaces is due to anti-bonding orbital affinity, which possibly originated from the parallel, unpaired spins of both Fe_3O_4 and heme groups. This anti-bonding orbital affinity increases as the number of heme groups increases in the following order: Hb > Mb > CytC. To provide an obvious proof of successful purification of hemoprotein despite the strength of protein magnetic forces, we carried out the adsorption

of oxyhemoglobin onto NiO supercaptors. Due to the diamagnetic character of oxyhemoglobin, the supercaptors show negligible adsorption capacity, as shown in Figure 4.10**.**

4.2.6. Theoretical modeling of hemoprotein adsorption onto metal oxides

To understand the chemical behavior of the molecular adsorption characteristics of hemoproteins on NiO and Fe_3O_4 NPs, a soft docking algorithm was implemented on an SYBYL-X suite program (Figure 4.11).[36] With respect to the NiO and Fe_3O_4 nanomagnets, the docking studies performed energy function calculations along the axial orientation of the interacting molecules in space. The energy function is represented in the form of a force field that describes the bond, angle, and dihedral angle potentials. The molecular activity of surfaces was estimated from the orbital occupation point of view of NPs. Figure 4.11 shows that the highest occupied molecular orbital (HOMO) is localized for both models of NiO and Fe_3O_4 NPs; it consists of pre-constructed solid cross-section surface of NiO and Fe_3O_4 nanoparticles. These models were constructed based on previously reported space groups *Fm3m* and *Fd3m* for NiO and Fe_3O_4, respectively. In addition, two protein models CytC and Hb were used for docking. All atoms of the surfaces were constrained through the docking processes, preventing them from moving.

Adsorption free energy (ΔE_{ads}) was calculated from the equation ($\Delta E_{ads} = E_{comp} - (E_P + E_{Sur})$) to evaluate the stability of the existing complex model, where E_{comp}, E_P, and E_{Sur} are the energies of solid–protein complex, protein, and solid, respectively. Docking calculations show that the adsorption energies for Hb and CytC adsorption on the NiO surface are -211.45 and -119.41 kcal/mol, respectively. For the adsorption on the Fe_3O_4 surface, the adsorption energies for Hb and CytC are -113.48 and -156.41 kcal/mol, respectively. In general, the results show that the geometrical NiO NPs occupied by parallel, unpaired spin electrons are concentrated in the lattice center. In turn, the geometrical Fe_3O_4 NPs occupied by unpaired spin electrons are localized in the lattice terminals. These spin orientations of NPs may be responsible for surface magnetization. Moreover, protein–NiO complex interactions afforded high adsorption/immobilization stability (i.e., high negative value of adsorption free energy, E_{ads}) compared with Fe_3O_4 NM surface adsorption. These results reveal that the selective adsorption affinity of hemoproteins, particularly Hb, is more favorable with NiO than with Fe_3O_4 NPs.

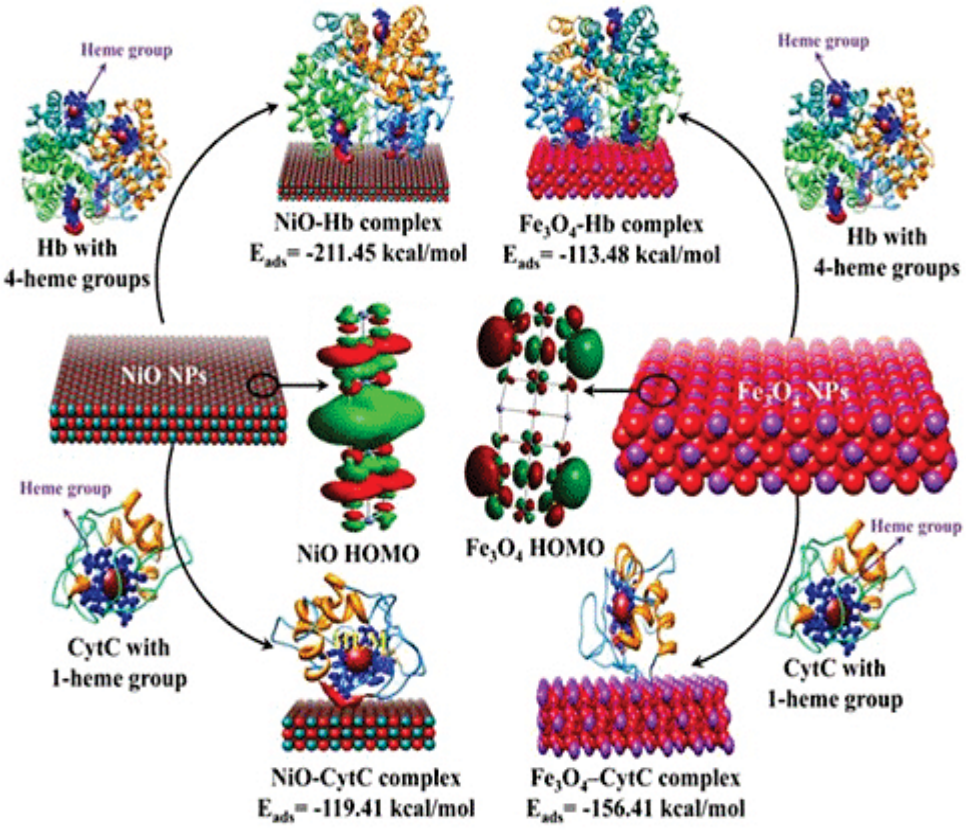

Figure 4.11: Theoretical design of hemoprotein adsorption over NiO and Fe_3O_4 nanomaterials.

4.2.7. Diffusion, kinetic and thermodynamic parameters of hemoproteins.

During the adsorption of proteins, the protein is probably transformed from a bulk solution to hierarchical mesoporous metal oxides through intra-particle diffusion (D), which considered as the rate-limiting step in most of adsorption processes. Based on the intra-particle diffusion theory, the uptake of adsorbate onto mesoporous NiO NRs is proportional to the square root of contact time in the course of adsorption (Fig. 4.12 A). The relation of q_t versus $t^{0.5}$ does not pass the origin, indicating that the diffusion in boundary layers involves mass diffusion at the external surface of the particles through the hypothetical boundary layers surrounding the particles due to particle morphology. Furthermore, the large intercept suggests that the process largely involves external surface adsorption. To study the stability and efficiency of the adsorption model, the adsorption of Hb was carried out in different temperatures ranging from 20 °C to 40 °C (Fig. 4.12-B). Results show that the loading affinity of protein increased with increasing temperatures. In addition, the kinetics

and thermodynamic parameters of the adsorption assay were depicted (Figs 4.12- C and D). Furthermore, "pseudo-first-order" was used to describe adsorption in solid–liquid systems based on the adsorption capacity of mesoporous NiO nanomagnet solids to investigate the adsorption mechanism. The adsorption rate was in the following sequence Hb >>> Mb > CytC. The thermodynamic equilibrium constant K_c increased with increasing temperature, whereas the absolute value of ΔG decreased with increasing temperature (Figure 4.12-Table 4.1). These results indicate that adsorption is spontaneous and more favourable at high temperature, confirming an endothermic adsorption process of protein immobilization.

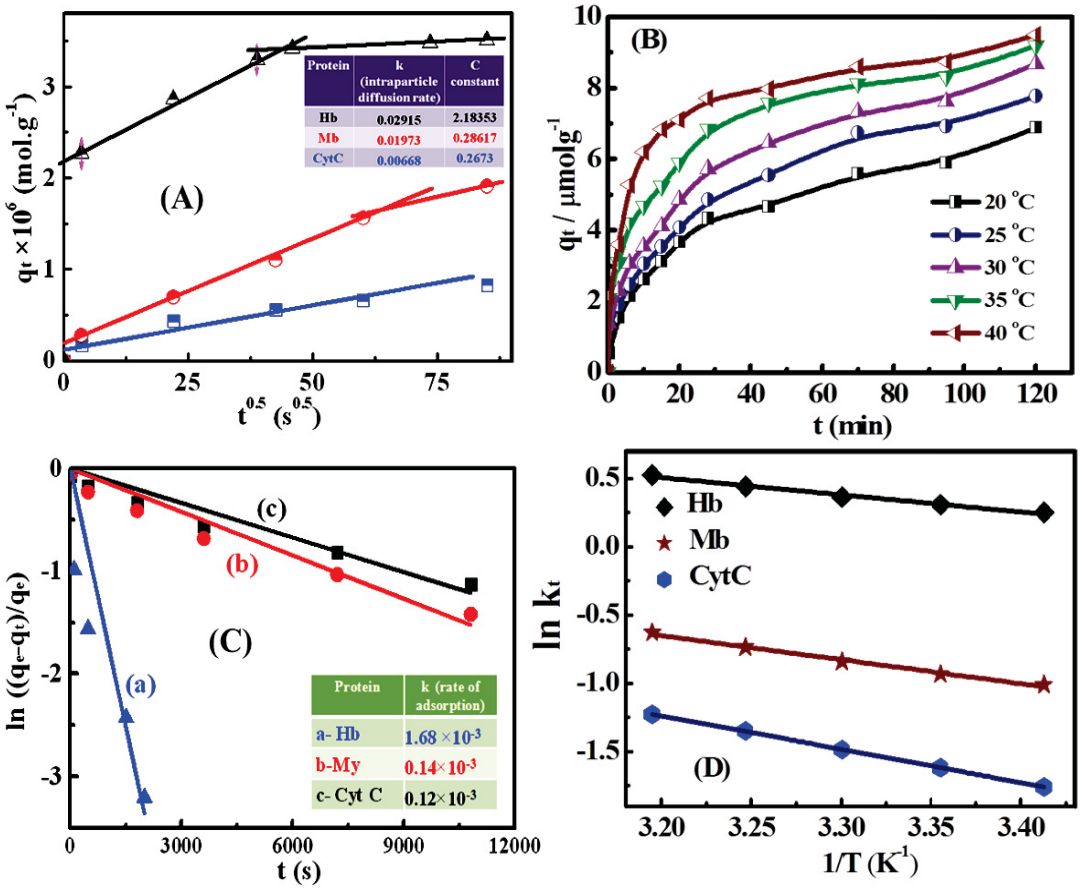

Figure 4.12: A) Intra-particle diffusion of hemo-protein adsorption on mesoporous NiO NRs, B) The Temperature effect of 1× 10^{-5} M hemoglobin adsorption at NiO NRs structured, C) Integrated first order adsorption of heme-proteins over NiO NRs (inset the values of adsorption rate constant) and D) Effect of temperture on the adsorption rate constant of heme-proteins at NiO NRs.

Table 4.1: Thermoynamic and kinetic parameters of the adsorption of hemo-proteins at NiO NRs.

Protein	T/K	k_t / s^{-1}	Kc	Ea/kJ mol^{-1}	$\Delta H^{\#}$/kJ mol^{-1}	$\Delta S^{\#}$/ J $mol^{-1}K^{-1}$	$\Delta G^{\#}$/kJ mol^{-1}	ΔH/kJ mol^{-1}	ΔS/J $mol^{-1}K^{-1}$	ΔG/kJ mol^{-1}
Hb	20	0.032	1.147253				63.00			-0.335
	25	0.0339	1.188046				64.08			-0.427
	30	0.0359	1.337016	10.48	7.959	-215	65.15	-18.47	63.74	-0.732
	35	0.0389	1.554665				66.23			-1.13
	40	0.0423	1.842494				67.30			-1.59
Mb	20	0.0091	0.400877				61.84			2.227
	25	0.0098	0.469527				62.89			1.873
	30	0.0108	0.582649	14.62	12.099	-211	63.95	-28.97	91.11	1.361
	35	0.0119	0.680355				65.00			0.986
	40	0.0133	0.861966				66.06			0.387
CytC	20	0.0043	0.07945				58.03			6.169
	25	0.0049	0.091867				59.02			5.915
	30	0.0057	0.106965	20.34	17.818	-198	60.01	-33.31	92.08	5.631
	35	0.0065	0.138711				61.00			5.058
	40	0.0074	0.193534				61.99			4.274

4.2.8. Real applicability of NiO NPs in adsorption and separation of hemeprotein*s*

In the adsorption experiment of hemoprotein on mesoporous NiO NPs, the adsorption of high-concentration Hb (6.06×10^{-4} M) onto 0.833 g/L mesoporous NiO NRs at 20 °C was carried out. Our finding reveals that the mesoporous NiO NRs have impressive ability to capture all Hb in 15 h (Figure 4.13A). The concentration of Hb that is in equilibrium with mesoporous NiO NRs was calculated from the calibration plot. The adsorption of ~50 g Hb required 1 g of NiO NRs. To assess the practical utility of the nanomagnet-selective Hb from blood, the quantification of 150 µL/30 mL H_2O of sterilized human blood sample was tested individually with magnetic NiO NRs (Figure 4.13B). The decrease in the UV–visible spectra of Hb protein at specific wavelengths indicated that a 99% adsorbed amount of Hb was achieved in the human blood on NiO NPs within hours. The time-dependent spectral analyses indicated that the Hb protein can be removed from human blood with high adsorption efficiency of 96% to 99% using a simple and effective

one-step separation technique based on NiO NPs (inset Fig. 4.13B). These results demonstrate a practical method of hemoprotein separation without intensive design and experimental conditions. These results also indicate that mesoporous NiO NPs with specific morphology such as NRs can be engineered for selective applications, including enrichment and separation of proteins, as well as drug delivery.

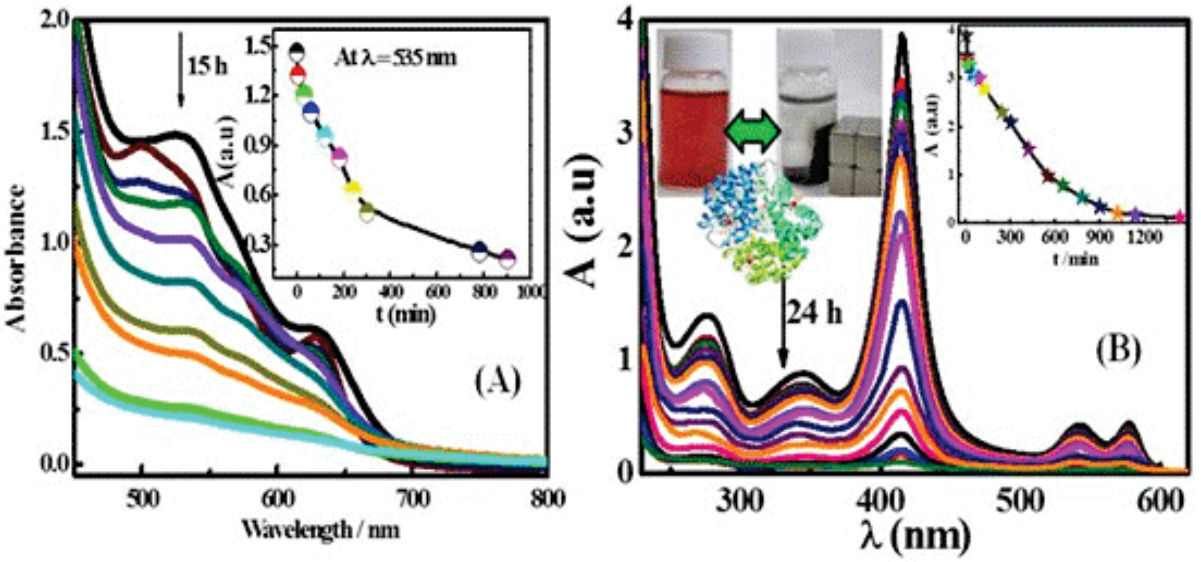

Figure 4.13: (A) UV–vis spectrum of 6.06 × 10^{-4} M Hb adsorption onto (0.833 g/L) mesoporous NiO NRs at 20 °C. (B) Adsorption of sterilized human blood sample (150 µL in 30 mL H_2O) over (0.025 g) NiO NRs [Inset: time dependence of the adsorption amount of hemoprotein onto mesoporous NiO NRs].

4.2.9. Visual assessment of adsorbed Hb onto NiO NRS

The visual assessment of the selective adsorption of Hb uptake from blood on mesoporous NiO NRs surfaces was performed using fluorescence microscopy. The collected solid NiO NRs following adsorption of Hb from the human blood were dispersed on the glass plate with the addition of pyranine reagent (green florescence 520 nm to 560 nm), as seen in Figure 4.14. The results showed remarkable fluorescence response when pyranine was added to mesoporous NiO NRs in the Hb-free sample assays. The phenomenal quenching behavior of Hb ensured excellent separation of Hb using mesoporous NiO NRs, as indicated by the identical fluorescence response of Hb–NiO NRs adsorbent.

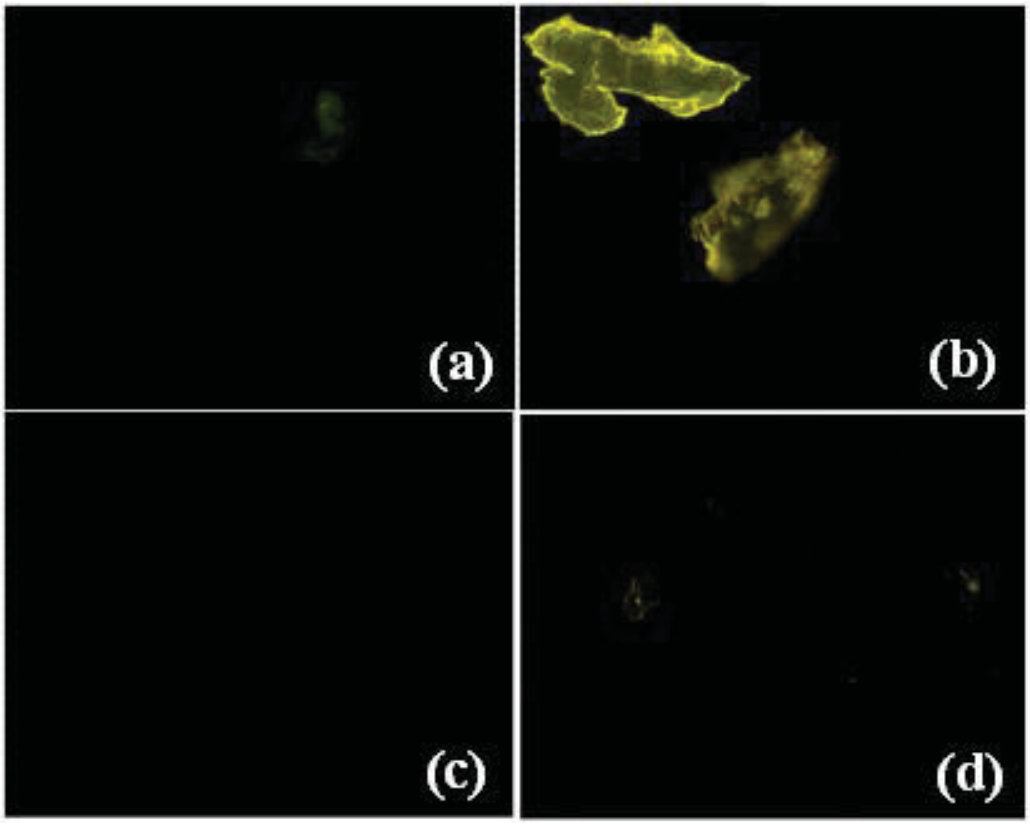

Figure 4.14: Fluorescence microscopic imaging for visual assessment of the mesoporous NiO nanomagnet-selective (rose-like morphology) adsorption of Hb human blood cells.

4.2.10. Workability and stability of the adsorption system

After the first set of reaction experiments, a simple chemical treatment of acidified solution (HCl/NaCl) was used to effectively remove the trapped proteins adsorbed on NiO NPs without significant damage to the morphology and physical properties of the nanostructures. Moreover, the protein functional active groups were unchanged following this chemical treatment, which can be observed from the protein spectrum (Figure 4.15). The precipitate was collected and dried overnight at 60 °C. One of the key issues in the workability of mesoporous NiO NPs is the reversibility after multiple cycles of adsorption of Hb from human blood. Although the adsorption efficiency slightly decreased with the cycling number, the reused NiO NPs remained effective up to a high level even after five recycles. This study shows that the NiO NPs can serve as potential candidates for selective hemoprotein adsorption, particularly for Hb, and laboratory assays can be alternative tools for currently effective adsorption methods.

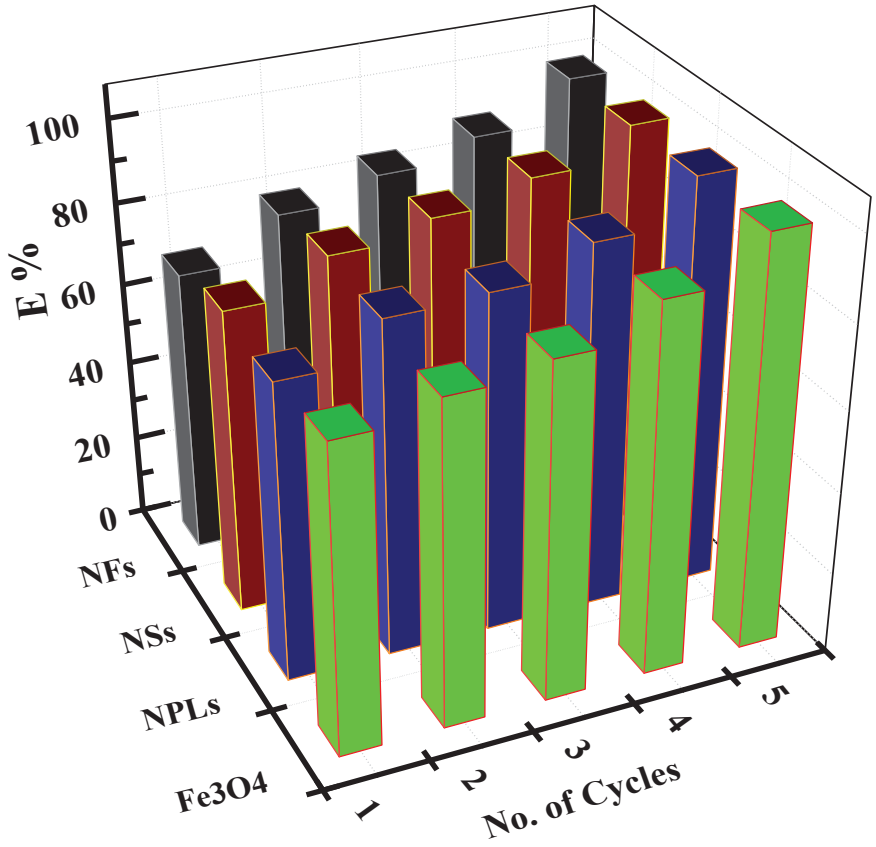

Figure 4.15: Reusability study of mesoporous NiO and Fe_3O_4 NPs during the adsorption of Hb from human blood up to five times. The efficiency of the adsorption system (E) was calculated from the % ratio of adsorbed amount (X_C) per reuse cycle (No.) and the initial adsorbed amount (X) obtained from the initial use of the NPs biosorbent.

4.3. References

[1] C.-H. Lee, T.-S. Lin, C.-Y. Mou, Nanotoday 4, 2009, 165—179.

[2] D. Li, H. Zhou, I. Honma, Nat. Mater. 3, 2004, 65 – 72.

[3] D. Mao, J. Yao, X. Lai, M. Yang, J. Du, D. Wang, Small 7, 2011, 578 – 582.

[4] S. A. El-Safty, TrAC Trends Anal. Chem. 30, 2011, 447-458

[5] S. A. El-Safty, M. A. Shenashen, Analytica Chimica Acta. 694, 2011, 151–161.

[6] S. A. El-Safty, M. A. Shenashen, M. Ismael, M. Khairy, Adv. Funct. Mater. 22, 2012, 3013–3021; S. A. El-Safty, M. A. Shenashen, M. Khairy, Colloids Surf. B: Biointerfaces 103, 2013, 288– 297.

[7] S. A. El-Safty, A. Shahat, W. Warkocki, M. Ohnuma, Small. 7, 2011, 62–65

[8] S. M. Safarikova, Biomagn. Res. Technol. 2, 2004, 2-7

[9] H. Chen, C. Deng, X. Zhang, Angew. Chem. Int. Ed. 49, 2010, 607 –611; J. Zhang, X. Li, J. M. Rosenholm, H.-C. Gu, J. Colloid Interf. Sci. 361, 2011, 16–24.

[10] J. Liu, S. Z. Qiao, Q. H. Hu, G. Q. Lu, Small. 7, 2011, 425–443; F. Ozel, H. Kockar, S. Beyaz, O. Karaagac, J Mater Sci: Mater Electron., 2013, DOI 10.1007/s10854-013-1213-3

[11] T. Tanrisever, S. Fexby, L. Bulow, Trends Biotechnol. 22, 2004, 511-516.

[12] C. R. So, Tamerler, M. Sarikaya, Angew. Chem. Int. Ed. 48, 2009, 5174 –5177.

[13] K. Riehemann, S. W. Schneider, T. A. Luger, B. Godin, M. Ferrari, H. Fuchs, Angew. Chem. Int. Ed. 48, 2009, 872 – 897.

[14] S. H. Huang, R. S. Juang, J. Nanopart. Res. 13, 2011, 4411–4430.

[15] J. Satulovsky, M. A. Carignano, I. Szleifer, PNAS. 97, 2000, 9037–9041.

[16] F. Fang, I. Szleifer, Biophys. J. 80, 2001, 2568 –2589.

[17] F. Fang, J. Satulovsky, I. Szleifer, Biophys. J. 89, 2005, 1516–1533.

[18] S. Xuan, F. Wang, X. Gong, S. Kong, J. C. Yua, K. Cham-Fai Leung, Chem. Commun. 47, 2011, 2514–2516.

[19] J. Bao, W. Chen, T. Liu, Y. Zhu, P. Jin, L. Wang, J. Liu, Y. Wei, Y. Li, ACS Nano. 1, 2007, 293–298.

[20] R. Hao, R. Xing, Z. Xu, Y. Hou, S. Gao, S. Sun, Adv. Mater. 22, 2010, 2729–2742.

[21] J. Kim, Y. Piao, N. Lee, Y. Park, I. H. Lee, J. H. Lee, S. R. Paik, T. Hyeon, Adv. Mater. 22, 2010, 57–60.

[22] J. Won, M. Kim, Y.W. Yi, Y. H. Kim, N. Jung, T.K. Kim, Science 309, 2005,121–125.

[23] Y. W. Jun, Y. M. Huh, J. S. Choi, J. H. Lee, H.T. Song, S. Kim, S. Yoon, K. S. Kim, J. S. Shin, J. S. Suh, J. Cheon, J. Am. Chem. Soc. 127, 2005, 5732–5733.

[24] C. J. Xu, K. M. Xu, H.W. Gu, R.K. Zheng, H. Liu, X. X. Zhang, Z. H. Guo, B. Xu, J. Am. Chem. Soc. 126, 2004, 9938–9939.

[25] S. A. El-Safty, M. A. Shenashen, M. Ismael, M. Khairy, Chem. Commun. 48, 2012, 6708-6710.

[26] E.J. Woo, K. M. Ponvel, I. S. Ahn, C. H. Lee, J. Mater. Chem. 20, 2010, 1511-1515.

[27] L. Zhang, S. Z. Qiao, Y. G. Jin, Z. G. Chen, H. C. Gu, G. Q. Lu, Adv. Mater. 20, 2008, 805-809.

[28] J. Liu, S. Z. Qiao, S. B. Hartono, G. Q. Lu, Angew. Chem. Int. Ed. 49, 2010, 4981 – 4985.

[29] K. Judai, J. Nishijo, N. Nishi, Ad .Mater. 18, 2006, 2842–2846.

[30] C.-Y. Su, A. M. Goforth, M. D. Smith, P. J. Pellechia, H.-C. Loye, J. Am. Chem. Soc. 126, 2004, 3576–3586.

[31] M. P. Proenca, C. T. Sousa, A. M. Pereira, P. B. Tavares, J. Ventura, M. Vazquezb, J. P. Araujo, Phys. Chem. Chem. Phys. 13, 2011, 9561–9567

[32] S. A. El-Safty, Khairy, M. M. Ismael, H. Kawarada, Appl. Catal., B. 123, 2012, 162– 173.

[33] Y. Zhu, W. Chen, C. Nan, Q. Peng, R. Wang, Y. Li, Cryst. Growth Des. 11, 2011, 4406–4412

[34] R. Fu, X. Jin, J. Liang, W. Zheng, J. Zhuang, W. Yang, J. Mater. Chem. 21, 2011,15352.

[35] S. Mohapatra, N. Panda, P. Pramanik, Mater. Sci. Eng., C. 29, 2009, 2254-2260.

[36] SYBYL-X 1.2, Tripos International, 1699 South Hanley Rd., St. Louis, Missouri, 63144, USA.

CHAPTER 5

SEQUESTERING AND OPTICAL DETECTION OF TOXIC METAL IONS

1. **Mohamed Khairy**, Sherif A. El-Safty, Mohamed Shenashen, Emad elshehy, nanoscale, 2013, In Press.
2. Sherif A. El-Safty, **Mohamed Khairy**, Mohamed Ismael , *Sensors and. Actuators, B*, 2012, 166, 253-263.
3. Sherif A. El-Safty, Mohamed A. Shenashen, **Mohamed Khairy,** *Talanta*, 2012, 98, 69-78.
4. Sherif A. El-Safty, Mohamed A. Shenashen, Mohamed Ismael, **Mohamed Khairy,** Md. R. Awal, *Analyst*, 2012,137, 5278-5290
5. Sherif A. El-Safty, Mohamed A. Shenashen, Mohamed Ismael, **Mohamed Khairy**, Md. R. Awual, *Microporous Mesoporous Materials*, 2013,166, 195-205.
6. Mohamed A. Shenashen, Emad Elshehy, Sherif A. El-Safty, **Mohamed Khairy,** Separation and Purification Technology, 2013, 116, 73-86.

5.1.Introduction

The increased contamination level and heavy metal content in the environment due to industrial development has posed a very serious problem to the global environment because of the heavy metal's toxicity, non-degradability, and persistent threat to human lives and the environment. Therefore, the complete remediation and purification of trace amounts of these toxic analytes is particularly significant in environmental science and technology.[1,2] In the next section demonstrated optical detection and removal of toxic metals from the aquatic life (Section 5.2) as well as removal of lead ions from biological environments (Section 5.3).

5.2.Optical monitoring and removal of ultra-trace concentration of zn(ii) and cu(ii) ions from water.

Copper has a wide range of applications. Many actual or potential sources of copper pollution exist in aqueous waste streams, such as electronic and electrical manufacturing, metal plating, mining, computer heat sink manufacturing, Cu plumbing, smelting, extracting, and finishing processes, and in biostatic surfaces, as a component in ceramic glazing and glass colouring. Cu(II) is a highly toxic element, and excessive intake results in its accumulation in the liver and in gastrointestinal problems such as vomiting, diarrhoea, haemolysis, gastrointestinal disorder, stomach cramps, nausea, and respiratory problems.[3-9] Zinc is a relatively non-toxic element; however, it can be toxic if it consumed in large quantities (>124 ppb). Actually, Zn (II) ion is the second most abundant transition metal ion in the human body after iron. However, a high zinc intake is known to produce copper-deficiency anemia by inducing the intestinal cells to synthesize large amounts of a protein that captures copper in a non-absorbable form.[10] Zinc is an essential factor in many biological processes such as brain function and pathology, gene transcription, immune function, and mammalian reproduction, as well as some pathological processes, such as Alzheimer's disease, epilepsy, ischemic stroke, and infantile diarrhea. Although most Zn(II) is tightly bound to enzymes and proteins, free zinc pools exist in some tissues such as the brain, intestine, pancreas, and retina.[10,11] Therefore, the monitoring and removal of Cu (II) and Zn(II) ions from water is important in biological processes.

Water pollution results in serious health problems, particularly in developing

countries. With the common use of Cu(II) and Zn(II) target ions in various industries and biological treatments, numerous techniques have been developed for Cu(II) ion detection. High concentrations of heavy metal pollutants can be removed from water through several methods such as precipitation, ion exchange, filtration, solvent extraction, and membrane technology.[12,13] However, despite their successes, most of these methods require intensive conditions, well-controlled equipment, and high costs. Moreover, these methods have low efficiency, are inapplicable to a wide range of pollutants, and involve time-consuming assessments, making them unattractive candidates for the significant detection of Cu(II) and Zn(II) analytes.[12,14] Adsorption is one of the most effective methods for removing Cu(II) and Zn(II) ions and other metals from their matrices.[15,16]

Most commonly used treatment methods only find low concentrations of most heavy metals.[17] Hence, a growing worldwide demand for chemical sensors that accurately and rapidly detect/remove and selectively recognize pollutant species exists.[18-21] Engineered nanoscale materials with particular sizes, shapes, compositions, and functions have recently played a leading role in sensor design because of their emerging applications in the optical detection of cations and anions.[22-24] To date, the development of receptors as "indicator dyes" and surface-confinement materials as "carriers" has been a key to broadening the applications of optical chemical sensors to achieve wide-range detection of neutral and ionic analytes.[25] Changes in the absorption spectra in the ultraviolet-to-near infrared regions have been used to trigger analytical signals by modifying suitable receptor ligands into optical sensors of Cu(II) and Zn(II) ions.[26-28] Ordered mesoporous silica monoliths featuring uniform sizes, monodispersed porosities in the range of 2 nm to 20 nm, and large particle sizes are a promising new class of optical sensor materials. In such systematic sensor designs, the anchoring of organic dyes into 3D inorganic networks with well-defined cage cavities enhances the sensitivity of toxic analytes.[29-32] Although successful designs of optical nanosensors have allowed scientists to develop controlled assessment processes for the naked-eye detection of several toxic heavy metal ions up to nanomolar concentrations,[33] the challenges in achieving smart detection and removal of Cu(II) and Zn(II) ions from water in the basic laboratory assays using eco-friendly solid sensors remain.

Since the discovery of a novel class of the M41S family of mesoporous molecular sieves, the incorporation of aluminum into the framework has provided materials with

acidic active sites.[34-36] These aluminosilica materials have been reported to show an exciting range of catalytic applications despite the existence of a structural disorder similar to those in amorphous alumina and aluminosilicas.[35,37] High aluminium contents in frameworks reasonably lead to increases in the acidity of the resultant solid acid aluminosilica materials. However, the ordering and hydrothermal stability of these materials are drastically decreased at low Si/Al ratios.[38, 39] Alumina is one of the most widely used materials in heterogeneous catalysis because of its unique catalytic, adsorption, optical, and electronic properties.[40] Active alumina with mesostructures is an adsorbent material that valuably supports a large number of catalyst-developed framework porosities.[41] Given the advantages above, mesoporous aluminosilica materials have been used for the first time as carriers for design optical captors/sensors.[34,42-45] As example we recently fabricated an optical mesocaptor design based on the direct immobilization of N, N'-disalicylidene-4,5-diamino-6-hydroxy-2-mercaptopyrimidine (DSAHMP) and diphenylthiocarbazone (DZ) chromophores into ordered pore-based aluminosilica monoliths to enable easy generation and transduction of optical colour signals as a response to DSAHMP–Cu(II) and DZ–Zn(II) binding events during the recovery of even ultra-trace concentrations (10^{-9} mol.dm^{-3}) of Cu(II) and Zn(II) ions from drinking water (Figure 5.1).

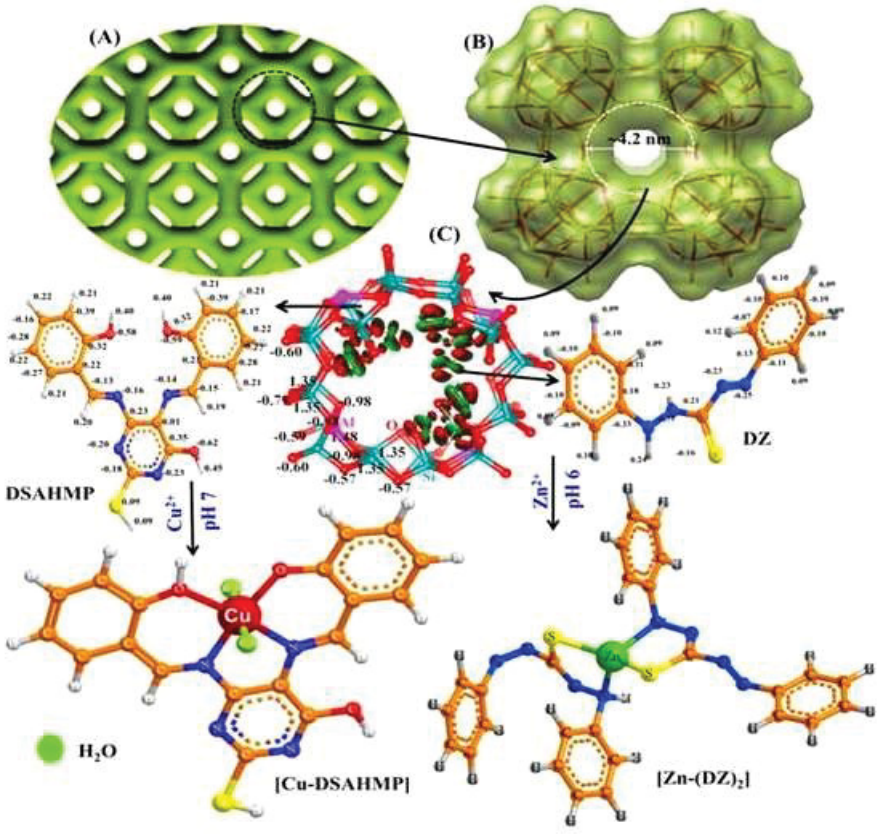

Figure 5.1: Three-dimensional cubic Pm3n geometrical modelling of the meso- and micro-scale structures of the aluminosilica (A, B) and the model of charged cluster aluminosilica monoliths with DZ and DSAHMP chromophores (C). Three-dimensional structure of the DSAHMP molecule (left) and DZ (right) with the atomic charge distribution of each atom and the feasibility of the formation octahedral complexes with Cu(II) and Zn(II) ions.

5.2.1. Fabrication of cubic mesocage aluminosilica carriers.

In the microemulsion mesophase systems, the addition of an alkane with long alkyl chain lengths (C_{12}-alkane) to the (surfactant/TMOS/aluminium salt) composition substantially affected the formation of the 3D mesophase and the enlargement of the pore sizes of the aluminosilica mesostructures. Our findings show (Figure 5.2 and Table 5.1) that the increase in the Al contents increased the unit-cell constants (a Pm3n= $d_{210}\sqrt{5}$) of the cubic Pm3n structures, as evidenced by the shift of all reflection peaks to a low 2θ angle. This increase is mainly the effect of the aluminium salt, which changed the micellar aggregate sizes and volume fractions of the sphere core and corona of the surfactant at specific synthesis compositions.[44] The N_2 adsorption isotherms (Figure 5.2 B) of the aluminosilica monoliths showed a H_2-type hysteresis loop and well-defined steepness of isotherms,

indicating that uniform cage-like pore structures are a characteristic of the cubic aluminosilica monoliths (Figure 5.1 A and B).[47] Generally, the adsorption branches significantly shifted toward a lower relative pressure (P/Po) with increasing aluminium content. With both hexagonal and cubic Pm3n, a decrease in textural parameters was observed. This decrease can be attributed to the structural ordering degradation with the high aluminium content of monoliths. Furthermore, the direct immobilization of DSAHMP receptor into carriers enabled the design of uniform captors without pore blockage that commonly occurs when grafting silane and thiol moieties, as indicated by the XRD images and N_2 isotherms (Figure 5.2, and Table 5.1). The slight decrease in surface parameters of the mesocaptor designs indicated the immobilization of receptor into the inner pores of the aluminosilica carriers.

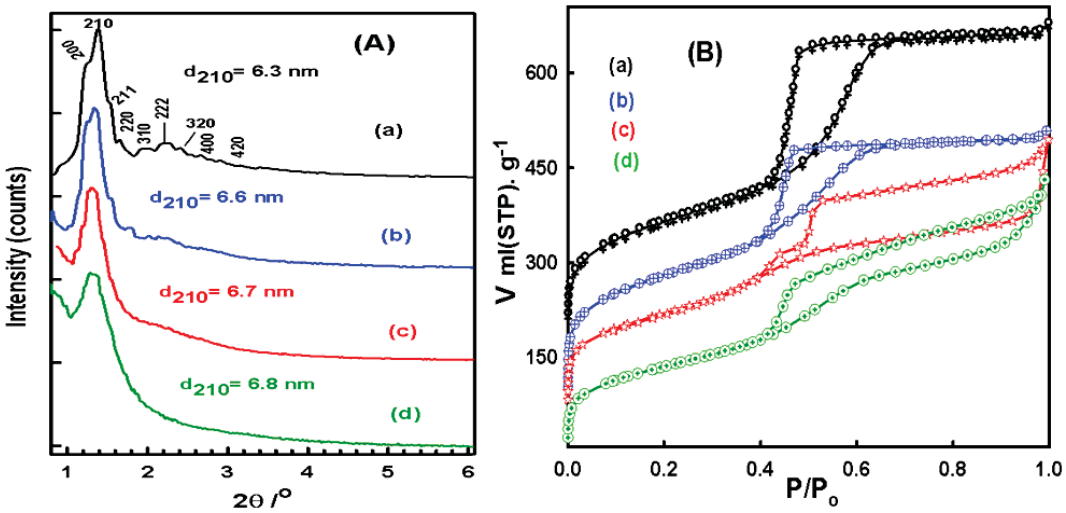

Figure 5.2: XRD patterns (A) and N_2 isotherms (B) of cubic Pm3n aluminosilicate monolith carriers with Si/Al mole ratios of 19 (a), 9 (b), 2.33 (c), and 1 (d).

The cubic *Pm3n* crystal structure defined on the bases of the cluster model of spherical aluminosilicates ($AlSi_4O_{12}$) consists of two types of oxygen linkages (that is, oxygen-bonded to Si or Al and siloxane species, respectively). The first group is responsible mainly for the creation of Brønsted acid sites. Siloxane orientation may contribute to crystal shape formation. This spherical aluminosilicate ($AlSi_4O_{12}$) cluster unit was used for the construction of a nanoscale alumiosilicate model (Figure 5.1). On the other hand, Figure 5.1 B shows the electron density distribution on the structural model of the aluminosilicate. As shown, the atoms oriented at the edges of the cubic Pm3n symmetry can form a micropore cavity with a diameter of 0.7 nm toward the inner side of the mesopore surfaces (~4.2 nm), as shown by the N_2 isotherms (Figure 5.2 and Table 5.1).

Table 5.1: Synthesis conditions and structural and textural parameters of cubic Pm3n aluminosilica membrane carriers fabricated using microemulsion phases of Brij 98 as soft templates with a wide range of Si/Al mole ratios. The unit lattice constant (a_{pm3n}= $d_{210}\sqrt{5}$), BET surface area (S_{BET}), and NLDFT pore size distribution (PSD), and pore volume (V_p) are indicated.

Si/Al	Synthesis conditions			Structure parameters			
	10^2 T/mol	$(10^3)Al(NO_3)_3$ /mol	Brij 98/TMOS w/w	*a* nm	S_{BET} m^2/g	*R* nm	V_p cm^3/g
19	1.31	0.7	0.5	14.1	703	4.3	0.73
4	1.31	3.4	0. 5	14.7	543	4.2	0.70
2.3	1.31	5.8	0.5	14.9	445	4.0	0.68
1.0	1.31	13.6	0. 5	15.2	390	3.9	0.43

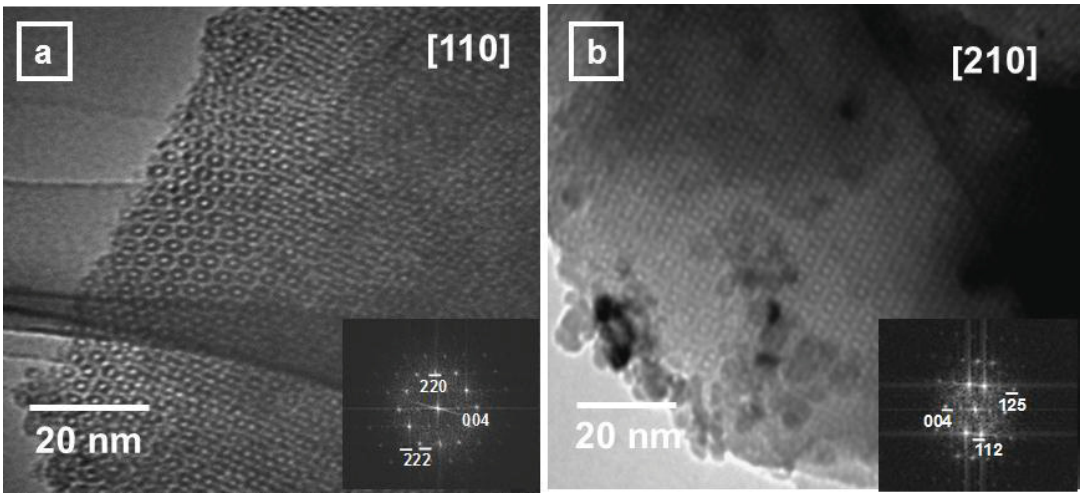

Figure 5.3: Representative HRTEM and FTD (insets) patterns of cubic Pm3n aluminosilica DZ-modified captor monoliths with a Si/Al mole ratio of 4 recorded along the [110] (a) and [210] (b) zone axes.

The transmission electron microscopy (TEM) images (Figure 5.3) show that the 3D mesoscopic qualities of aluminosilica captors still retained their long-range structural ordering over a large area even for samples with Si/Al ratios as high as 4. The overall TEM lattice images and corresponding Fourier transform diffractogram (FTD) patterns (insets) indicate the formation of cubic Pm3n structures. With low silica contents (4 ≤ Si/Al ≤ 1), the representative TEM images reveal a short-range ordering or even wormlike mesopore channels interconnecting in large size domains. These cubic captors

with pore cavities are promising for the removal and detection of Cu(II) and Zn (II) ions from water.

The coordination state of the aluminium species was investigated using ^{27}Al NMR (Figure 5.4). In all the aluminosilica captors ($19 \leq Si/Al \leq 1$), two ^{27}Al peaks were centred at the chemical shift of -1 and 58 ppm, indicating the existence of octahedral (Al^{VI}, AlO_6, extra framework) and tetrahedral (Al^{IV}, AlO_4, framework) aluminium sites, respectively. The tetrahedrally coordinated aluminium sites were significantly increased with increasing aluminium content in the mesoporous monoliths. The surface acidity of the aluminosilica monoliths is evidenced by the two resultant NH_3 desorption peaks at around 200 °C and a small, broad peak at about 200 °C to 500 °C (Figure 5.5). The results clearly indicate that ammonia is desorbed from the weak Lewis and mildly strong Brønsted acid sites of the OH- groups of the aluminosilica carriers.[48] In general, these natural surfaces of acid sites strongly induce H-bonding and dispersive interactions with the DSAHMP and DZ receptors, leading to the formation of stable sensors without receptor leaching during the sensing assays of metal ions.[45,48-51] The electronic structures of the aluminosilica carriers were also calculated to determine the charge distribution in each atom and the effect of Al sites on the immobilization of the receptor into the pore surfaces. The calculated atomic charges of Al, Si, the O-siloxane cross-linked framework, O-bridge Si, and O-bridge Al were 1.48, 1.35, -0.6, -0.57, and -0.99, respectively. Evidently, the oxygen atoms in the Si–O–Al linkages were lesser than the other oxygen atoms in the linkage species, indicating the large number of acid sites in these linkages compared with the other sites in the frameworks (Figure 5.1).

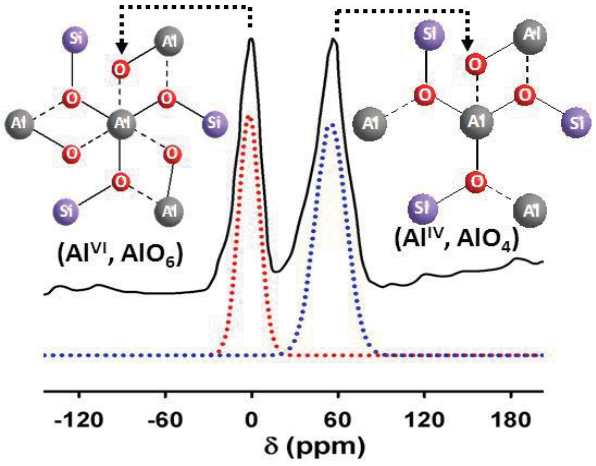

Figure 5.4: ^{27}Al MAS NMR spectra and a deconvolution of each peak of aluminosilica carriers fabricated with a Si/Al ratio of 4.

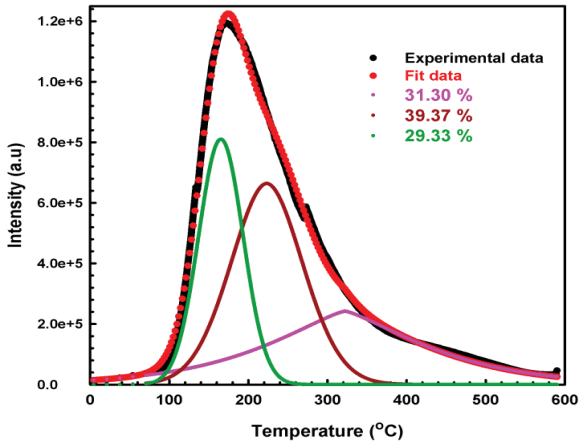

Figure 5.5: NH_3-TPD spectra and a deconvolution of each peak of hexagonal aluminosilica monoliths fabricated with a Si/Al mole ratio of 4. To determine the amount and strength of acid sites of the mesoporous aluminosilica particles quantitatively, we deconvoluted the peaks around 100 °C to 500 °C using a Gaussian function with temperature as the variant.

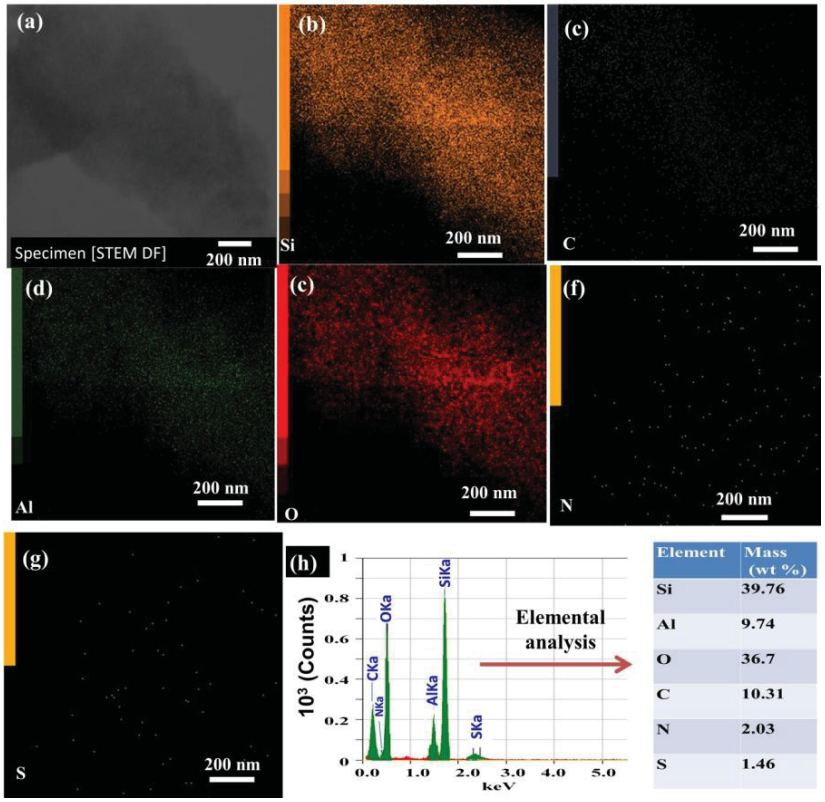

Figure 5.6: STEM image, EDS, and STEM-EDS mapping of the mesoporous aluminosilica DSAHMP captor (with Si/Al ratio of 4). STEM image (a), silicon (b), carbon (c), aluminum (d), oxygen (e), nitrogen (f), sulphur (g), and EDS (h) analyses and the calculated values of atomic distribution of species in the solid captor.

The dark fields in the STEM image (Figure 5.6A) confirm the formation of nanoscale captor particles. The particle morphology and EDS mapping of the mesocaptor were further characterized using STEM and STEM-EDS, as shown in Figure 5.6 (B to F). The STEM-EDS map of the aluminosilica mesostructure sensors shows the presence of Si, Al, O, C, N, and some S (Figure 5.6 (C to F). The O, Si, and Al contributions come mainly from the mesostructure. The STEM-EDS map also indicates that the C, N, and S atoms of the DSAHMP chromophore are uniformly distributed through the mesoporous aluminosilica, thereby allowing the homogenous diffusion of metal ions toward the DSAHMP molecular probe centres.[52]

5.2.2. Batch contact-time experiments of Cu(II) and Zn(II) ion captures

We performed a series of batch contact-time experiments to define and evaluate the suitable conditions of the Cu(II) and Zn(II) ion captures systematically. To define and evaluate suitable pH conditions for the donor–acceptor combinations between solid modified DSAHMP or DZ and metal targets systematically, we carefully monitored the reflectance spectra of the [Cu-DSAHMP] and [Zn-DZ_2] complexes on pore surfaces over a wide range of pH solutions after equilibration and colour response time (C_{RT}) of 12 min and 45 sec respectively (Figure 5.7A). The prominent colour change and signal saturation in the reflectance spectra of mesocaptors after equilibration and the colour response time (C_{RT}) were recorded and considered as a reference signal (Figure 5.7B). The optimum change in the colour intensity of the [Cu-DSAHMP] and [Zn-DZ] complexes was around pH 7 and pH 6 for Cu(II) and Zn(II) ions, respectively. The pH graph suggests that the Cu(II) and Zn(II) ions can bind firmly to solid modified DSAHMP and DZ during the formation of octahedral [Cu-DSAHMP] and tetrahedral [Zn-$(DZ)_2$] complexes at pH 7 and pH 6 respectively.[52-55]

The stoichiometry of the [Cu-DSAHMP] and [Zn-$(DZ)_2$] complexes were determined from a Job's plot, in which changes in the absorbance of the colour complexes in a solution under experimental control conditions were monitored. The Cu: DSAHMP and Zn: DZ stoichiometric ratios of the [Cu-DSAHMP] and [Zn-DZ] complexes were determined as 1:1 and 1:2 respectively during these sensing assays. The stability constant (log K_s) of the formed the [Zn-$(DZ)_2$] and [Cu-DSAHMP] complexes into the solid mesocaptor strips at pH 6 and 7, respectively, was estimated, according to equation 18 (in experimental part).[29-32] The optical limit of detection (LOD) of Cu(II) and Zn(II) ions

using the capturing sensors was estimated from the linear part of the calibration plot[28,40] according to equation 19.

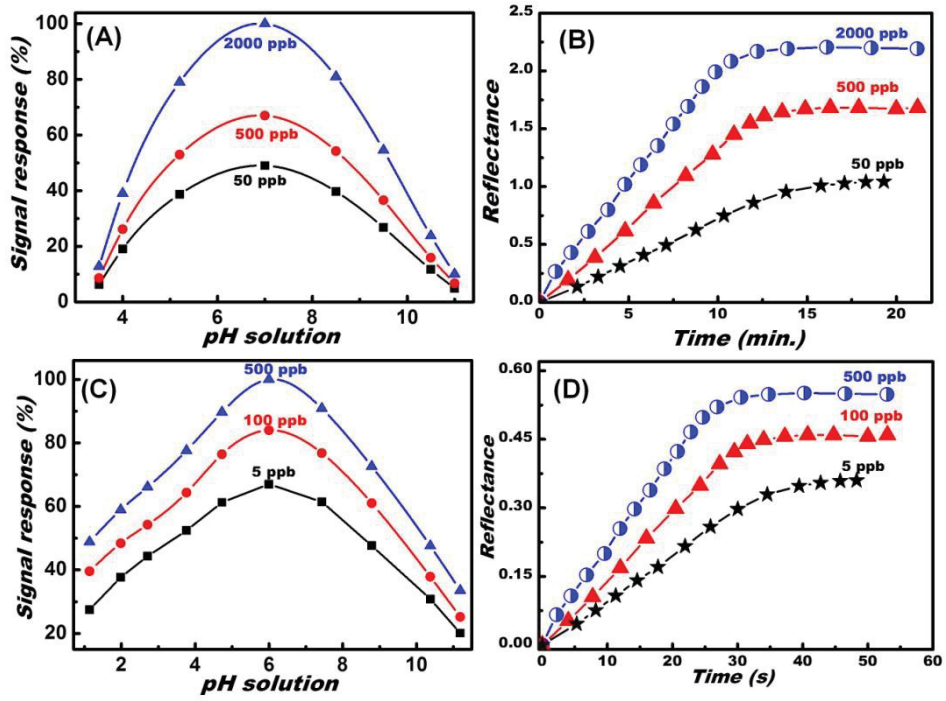

Figure 5.7: Quantitative study of pH (A,C) and time (B,D) responses of nanocaptor fabricated with a Si/Al ratio of 4 during the color signal changes of the $[Cu\text{-}DSAHMP]^{n+}$ (A,B) and $[Zn\text{-}\ DZ]^{n+}$ (C,D) complexes formed by adding different C(II) and Zn(II) ion concentrations at optimal recovery/sensing conditions (amount of 20 mg, volume of 20 mL, and temperature of 25 °C).

Figure 5.1 shows the 3D structure of the DSAHMP and DZ chromophores and its corresponding Cu(II) and Zn(II) complexes. The symmetrical charge distributions in the two phenolic rings allow plane–structure stability. This flat structure is capable of forming highly ordered complexes. Our studies show that the Cu (II) and Zn (II) ions can easily bind to DSAHMP and DZ respectively at neutral solutions, leading to change the intermolecular charge transfer during the formation metal-to-ligand complexes. Our findings indicated that the binding constants of [Cu-DSAHMP] and $[Zn\text{-}(DZ)_2]$ complexes were estimated of log K_s =11.3, and 2.9, respectively.[56] Therefore, the octahedral configuration was achieved using water molecules, indicating that the DSAHMP protonation form can strongly coordinate to the metal ion by releasing the protons to form a stable [Cu-DSAHMP] complex at pH 7. Moreover, two of DZ ligands bind to Zn (II) ions to from stable tetrahedral $[Zn\text{-}(DZ)_2]$ in pH 6.

In such sensing/capture system, three key factors affected the coloremetric Zn(II), Cu(II) ion-sensor/captor assays of these DSAHMP- and DZ-modified aluminosilica mesocaptors as follows;

1. The potential of metal ion binding site to deprotonate the NH, OH or SH fragments of the DSAHMP and DZ ligands at the specific pH value (Figure 5.7).
2. The 3D conformational preorganization of ligands (see 3D structure of ligands, Figure 5.1).
3. The mobility of existed multi-dentate binding sites. Therefore, the delocalization of electrons in the DSAHMP and DZ moieties could promote the deprotonation of the amino or hydroxyl groups during the metal-to-ligand binding events.

5.2.3. Cu(II) and Zn(II) ion-selective captors at neutral conditions

To investigate the selectivity of the mesocaptors in the presence of interfering multiple components that may coexist with Cu(II) and Zn(II) ions in water and the environment. In the experiment Cu(II) ion captor, we studied the effect of adding an equivalent amount (2 ppm) of individual cations on the captor system at pH 7. Whereas, In the experiment Zn(II) ion captor, an equivalent amounts (500ppb) of individual cations were added at pH 6. Figure 5.8 (A and B) shows the colour profiles and UV spectra of the ion captors (blank) after the addition of various foreign cations such as K^{+}, Li^{+}, Ca^{2+}, Mg^{2+}, Cr^{6+}, Al^{3+}, Cu^{2+}, Ni^{2+}, Mn^{2+}, Zn^{2+}, Co^{2+}, Cd^{2+}, Pb^{2+}, Hg^{2+}, Fe^{3+}, Bi^{3+}, Sb^{3+}, Mo^{6+}, and Se^{4+}. Despite the minimal increase in the reflectance spectra of the ion captor at 415 nm with the addition of metal ions such as Co^{2+}, Fe^{3+}, Bi^{3+}, Sb^{3+}, Mo^{6+}, and Se^{4+} as disturbance species, the general results show slight changes in both the colour map and signal intensity. In turn, the addition of Cu(II) and Zn (II) ions to the ion captor resulted in prominent colour changes and enhanced signal intensities (Figure 5.9), indicating the significant ion selectivity of Cu(II) and Zn ions at pH 7 and pH 6 respectively.

Interference studies were also extended by adding these actively interfered surfactants and anions such as tartrate, citrate, oxalate, chloride, acetate, nitrate, sulfate, carbonate, cetyltrimethyl ammonium chloride, tetraamyl ammonium chloride, and tetraethyl ammonium chloride species prior to the [1 ppm] Zn(II) and [2 ppm] Cu(II) analytes to these optical ion-captors (Table 5.1). With this interfering system, results also show the efficient Zn(II) and Cu(II) ion-selective captor with high tolerable limits of interfering matrix concentrations.

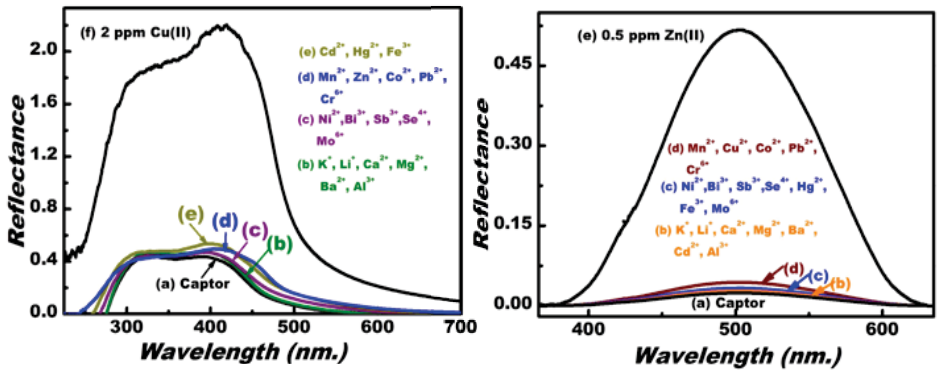

Figure 5.8: Representative selectivity profiles of Cu(II) [upper] and Zn (II) [bottom] ion-nanocaptors (fabricated with a Si/Al ratio of 4) after adding various foreign metal ions of [2 ppm] Cu(II), and [0.5 ppm] Zn(II) ions at optimal pH values of 7 and 6.5, respectively and other capture conditions (amount of 20 mg, volume of 20 mL, and temperature of 25 °C). The interfered cations are the following [listed in order (1 to 19)]: (1) Na^{+}, (2) K^{+}, (3) Ca^{2+}, (4) Mg^{2+}, (5) Cr^{6+}, (6) Al^{3+}, (7) Fe^{2+}, (8) Ni^{2+}, (9) Mn^{2+}, (10) Zn^{2+}, (11) Co^{2+}, (12) Cd^{2+}, (13) Pb^{2+}, (14) Hg^{2+}, (15) Fe^{3+}, (16) Bi^{3+}, (17) Sb^{3+}, (17) Mo^{6+}, and (19) Se^{4+}.

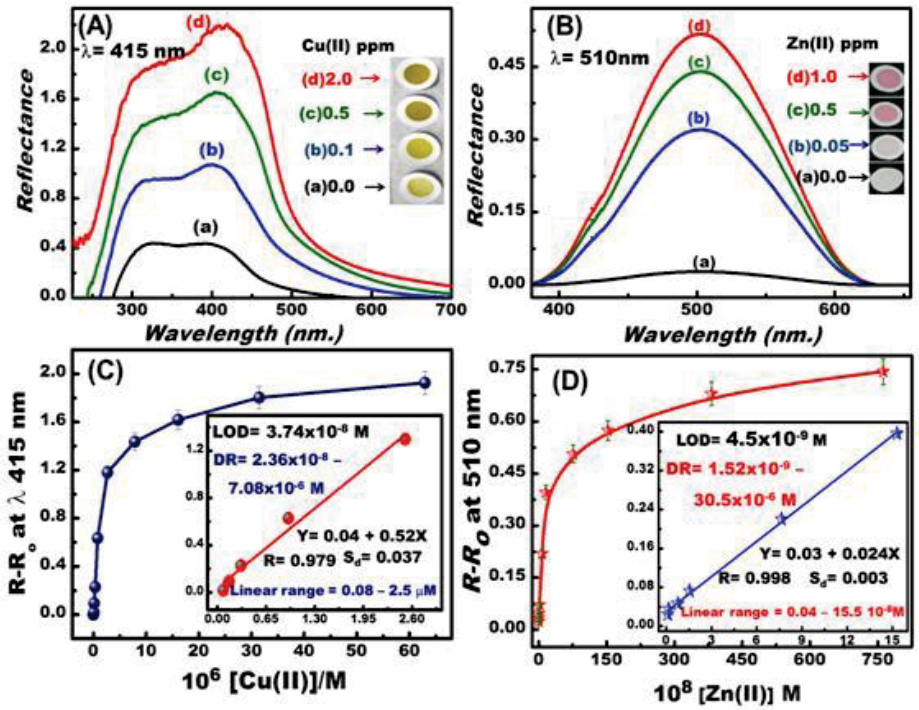

Figure 5.9. Concentration-dependent changes in UV/vis reflectance spectroscopic responses of nanocaptors (fabricated with Si/Al ratio of 4) during the removal/detection of Cu(II) and Zn(II) ions (A,B). Representative calibration curve of Cu(II) and Zn(II) ions at optimal pH values of 7 and 6.5, respectively and other capture conditions (amount of 20 mg, volume of 20 mL, and temperature of 25 °C) (C,D).

Table 5.2: Tolerance limits (TL) for interfering matrix species on the Cu(II) and Zn(II) ion-selective captors during optical sensing/removal of [1 ppm] Zn(II) and [2 ppm] Cu(II) ions.

	Tolerance concentration for interfering metal ions (mg/L) for Zn (II) ion-captor											
Matrix	NaCl	KNO_3	SO_4^{2-}	CO_3^{2-}	NO_2^-	AcO^-	Oxalate	Citrate	Tartrate	CTAC	TAAC	**TEAC**
(TL)	1050	1020	525	30	50	95	6030	4600	7000	700	200	**540**
	Tolerance concentration for common electrolyte species (mg/L) for Cu (II) ion-captor											
Matrix	NaCl	KNO_3	SO_4^{2-}	CO_3^{2-}	NO_2^-	AcO^-	Oxalate	Citrate	Tartrate	CTAC	TAAC	**TEAC**
(TL)	1550	1220	530	20	120	87	6303	5200	6000	650	150	**440**

Abbreviations: CTAC – Cetyltrimethyl ammonium chloride; TAAC –Tetraamyl ammonium chloride; TEAC – Tetraethyl ammonium chloride; Note: data obtained at captor amount of 20 mg, volume of 20 mL, and temperature of 25 °C). *Moreover, there were excellent correlations between the analytical results obtained with the sensors/captors with those obtained using the more traditional laboratory methods such as* ICP-AES *in these interference studies.*

5.2.4. Multiparticulate mesocaptor systems for visual removal and detection of Zn (II) and Cu(II) ions

To check the capability of the DSAHMP and DZ chromophores to visually detect and determine Cu(II) and Zn(II) ions, we conducted experiments for sensing Cu(II) and Zn(II) ions in liquid phase using a DSAHMP and DZ chromophores solution The Cu(II) and Zn(II) quantification experiments were performed in a quartz flask with a total volume of 20 mL. The Cu(II) and Zn(II) aliquots were injected from a 10 mM aqueous stock solution into a flask containing a mixture solution of 30 μM of DSAHMP and 30 μM of DZ at pH 7 and pH 6 respectively. In this sensing assay, naked-eye detection was clearly observed from 0.2 ppm to 1.0 ppm, as indicated by the change in colour from yellow to green or pink after the addition of Cu(II) and Zn (II) ions. Results show that the response time (12 min and 40 s) of the Cu(II) and Zn(II) ion sensors were sufficient to achieve a good colour separation "signal" between the DSAHMP, DZ "blank" and the Cu(II) ion-DSAHMP, Zn(II) ion-DZ sensing, respectively.

In solid-state ion-capture systems, the aluminosilica captor is strongly sensitive in terms of its optical "colour intensity" and signal responses of Cu(II) and Zn(II) in pH 7

and pH 6 respectively, even at low recognition or trace concentration levels of metal ions.[30-33] The use of the design-based aluminosilica DSAHMP and DZ captors not only leads to visual detection over a wide, adjustable concentration range (0.005 ppm to 2.0 ppm) but also offers easy-to-use removal assays with sensitive quantification of Cu(II) and Zn(II) ions at ultra-trace levels (~10^{-9} mol.dm^{-3}). The physical features of the mesocaptors in terms of large surface area-to-volume ratios of functional chromophores and uniform mesocage pores enabled the creation of a multiparticulate capture system for optical separation/extraction and monitoring/detection of metal ions even at ultra-trace concentration levels without a preconcentration process. The colour change in this multiparticulate capture system provides a simple procedure for sensitive and selective detection, removal, and collection of metal ions without the need for sophisticated instruments (Figure 5.9).

Table 5.3: Cu(II) and Zn(II) ion-captor functionalities in terms of accessibility (Q), sensitivity in terms of detection of limit (**LOD**) and range (**DR**), and color response time ($\mathbf{C_{RT}}$)

Si/Al	q [mmol g^{-1}] of DSAHMP	q [mmol g^{-1}] of DZ	Structure parameters				Time response (C_{RT})/min		Cu- captor		Zn- captor	
			a nm	S_{BET} m^2/g	R nm	Vp cm^3/g			LOD × 10^{-8} mol dm^{-3}	DR mol dm^{-3}	LOD × 10^{-9} mol dm^{-3}	DR mol dm^{-3}
19	0.055	0.049	14.1	630	4.0	0.66	12	0.67	2.49	1.57 × 10^{-8} to 7.86 × 10^{-6}	3.59	1.66 × 10^{-8} to 6.86 × 10^{-6}
4	0.074	0.071	14.7	450	3.8	0.62	12	0.67	3.74	2.36 × 10^{-8} to 7.08 × 10^{-6}	4.84	2.46 × 10^{-8} to 6.18 × 10^{-6}
2.3	0.079	0.073	14.9	400	3.7	0.53	12	0.67	4.66	3.14 × 10^{-8} to 6.60 × 10^{-6}	6.60	4.15 × 10^{-8} to 6.60 × 10^{-6}
1	0.082	0.080	15.2	320	3.6	0.4	12	0.67	6.23	3.93 × 10^{-8} to 5.97 × 10^{-5}	8.31	2.94 × 10^{-8} to 5.90 × 10^{-5}

To demonstrate the sensitive removal/detection applicability of optical mesocaptors, we conducted capture assays over a wide concentration range of metal ions. Results revealed that the signalling changes in the reflectance spectra and colour of the mesocaptors were caused by the formation of the octahedral [Cu-DSAHMP] and tetrahedral [Zn-$(DZ)_2$] complexes at $\lambda = 415$ nm and $\lambda = 510$ nm respectively (Figure 5.9). Figures 5.9 (B and D) shows the calibration plot of the optical mesocaptor during the detection of Cu(II) and Zn(II) ions analyte. Several quantification measurements (≥10 times) were performed using a wide range of concentrations (4.69×10^{-9} mol.dm^{-3} to 5.97×10^{-5} mol.dm^{-3}) and (2.2×10^{-8} mol.dm^{-3} to 7.62×10^{-6} mol.dm^{-3}), respectively, from among standard solutions of Cu(II) and Zn(II) ions under specific sensing conditions. The standard deviations for the analysis of Cu(II) and Zn (II) ions were 0.05% to 5%, as shown in the fitting plot of the calibration graphs (Figure 5.9, inset). The linear correlation at low concentration ranges indicated that the Cu(II) and Zn(II) ions can be detected and removed with high sensitivity over a wide range of concentrations (0.08×10^{-6} mol.dm^{-3} to 2.5×10^{-6} mol.dm^{-3}) and (4.0×10^{-10} mol.dm^{-3} to 1.55×10^{-7} mol.dm^{-3}), as also evidenced by the ICP-AES data. However, a nonlinear correlation at the inflection point was evident at the highest concentration of Cu(II) ions (≥ 2.5×10^{-6} mol.dm^{-3}) and Zn(II) ions and (> 1.55×10^{-7} mol.dm^{-3}), indicating that highly efficient removal and sensitivity could be obtained at low concentrations of metal ions. The capability of our capture assays, which is the first to offer sensitive, optical removal of sub-nanomolar concentrations of Cu(II) and Zn (II) ions, is shown by the limit of detection (LOD) values with all mesocaptors fabricated using different Si/Al ratios (Table 5.3).

5.2.5. Effect of captor mesostructures on the optical sensing assays

Considering the effect of Si/Al ratios on the mesocaptors, the different Cu(II) and Zn (II) ion-capture utilities in terms of detection/recovery range were observed (Table 5.3). Although the insertion of large amounts of aluminium into solid carriers leads to the enhanced development of active acid sites at internal mesopore surfaces, the decrease in mesocage pore uniformity and surface area-to-volume ratios could slightly affect the capture functionality in terms of limit of detection (LOD) and range (DR) values. The uniformity of the captor mesostructures (with low aluminium contents) plays a role in achieving flexibility in the specific activity of the electron acceptor/donor strength of a

chemically responsive DSAHMP and DZ molecular probe. Such molecular arrangement and organization of the entrapped DSAHMP and DZ chromophores inside 3D uniform mesocage pores (Figure 5.3) could facilitate the generation and transduction of an optical colour signal as a response to [Cu(II)-DSAHMP] and [Zn(II)-DZ] binding events during the recovery of Cu(II) and Zn(II) ion in aqueous solutions.[31,57,58]

5.2.6. Adsorption performance of the metal ion captures system

In the study of the adsorption performance of Cu(II) and Zn(II) ions removal from an aqueous solution, the Langmuir equilibrium isotherm model has been a widely applied theoretical model for monolayer adsorption. Langmuir adsorption, which is a monolayer adsorption model, depends on the assumption that intermolecular forces decrease rapidly with distance and consequently predicts the existence of the monolayer coverage of mesocaptors. The monolayer coverage and removal characteristics of metal ions on a mesocaptor surface at constant temperature is represented by the Langmuir isotherm (Figure 5-10 (A and C)).[19,20,52,53]

The monolayer coverage can be obtained from a plot of C_e/q_e versus C_e (Figure 5.10 (B and D)), which gives a straight line indicating the formation of the monolayer coverage of the Cu(II) and Zn(II) ions in the interior pore surfaces of mesoporous aluminosilica captors with these removal assays. The practical adsorption capacity q_m and the Langmuir coverage constant K_L were obtained from the slope and intercept of the linear plot. The linear removal curves indicated that a wide range of Cu(II) and Zn (II) ion concentrations can be removed from aqueous water in a one-step treatment with high adsorption efficiency of 96% to 99%. These results indicated that the practical removal of 1 g of metal ions [i.e. Cu(II) and Zn(II)] from an aqueous solution required ~4.07 g and ~ 7.38 g of mesocaptors. Our mesocaptors show significant adsorption functionalities over commercial adsorbents of Zn (II)[11,12] and Cu(II) ions,[13] which showed various limitations as follows:

1) There is no selectivity or specificity for target ions,
2) difficulty to adsorb or remove ultra-trace concentrations of element without preconcentartion process,
3) intensive design and experimental conditions during the adsorption and assessment monitoring analyses, and 4) one single use these absorbents (i.e. no

reversibility). [11-13]

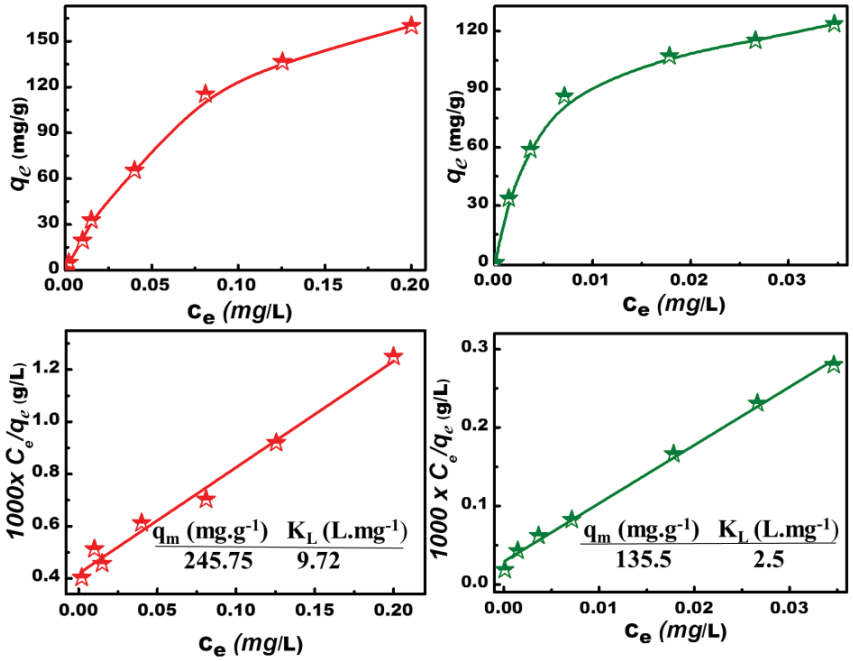

Figure 5.10: Langmuir adsorption isotherms (upper) and linear form of the Langmuir plot (bottom) of the DSAHMP-modified (left) and DZ-modified (right) nanocaptors fabricated with a Si/Al ratio of 4 during the optical removal of Cu(II) and Zn(II) ions at optimal recovery/sensing conditions (recovery time of > 60 min, amount of 30 mg, volume of 1 L, and temperature of 25 °C).

5.2.7. Selective recovery of Cu(II) and Zn(II) ions in real aqueous samples

A major advantage of the DSAHMP and DZ-modified captors is their ability to create selective extracting systems of Cu(II) and Zn(II) ions, thus preventing hindrance from actively interfering components, particularly the competitive element ions (Table 5.4).[11,30,57,58] These interfering components may make the recovery of Zn(II) and Cu(II) target ions from a mixture containing most competitive components difficult. Figure 5.11 shows the systematic consequences of the selective recovery stages of Cu(II) and Zn(II) ions for mixtures as follows; 1) removal of metal targets from solution mixture, 2) separation of metal ions from captor; however, the metal ions have been separated to reinforce metal-free-captor surfaces (i.e., the captor returns to a state before use) and to form a pure Cu(II) or Zn(II) ion-containing liquid, and 3) reusability of the solid captor to be freely reused in another capture assay, as clearly supported by data obtained (see below).

Table 5.4: The evidence of the selective removal of targets without disturbance of other interfered ions using ICP-AES analyses of metal ions. The metal ions was spiked in aqueous samples and measured before and after removal of metal ion target using a nanocaptor. This captor was fabricated with a Si/Al ratio of 4. The analysis was repeated 10 times for high accuracy and precision.

Target	Captor	ICP analysis of the samples	Efficiency[(a)]
Cu (II)	Al/HOM- DSAHMP	**Mixture (1)** (1) 1000 ppm of K^+, (2) 1000 ppm of Li^+, (3) 500.0 ppm of Ca^{2+}, (4) 100 ppm of Mg^{2+}, (5) 4.0 ppm of Cr^{6+}, (6) 4.0 ppm of Al^{3+}, (7) 3.0 ppm of Ba^{2+}, (8) 4.5 ppm of Ni^{2+}, (9) 4.5 ppm of Mn^{2+}, (10) 4.5 ppm of Zn^{2+}, (11) 4.0 ppm of Co^{2+}, (12) 4.0 ppm of Cd^{2+}, (13) 4.0 ppm of Pb^{2+}, (14) 4.0 ppm of Hg^{2+}, (15) 3.5 ppm of Fe^{3+}, (16) 4.0 ppm of Bi^{3+}, (17) 3.5 ppm of Sb^{3+}, (17) 4.0 ppm of Mo^{6+}, and (19) 4.0 ppm of Se^{4+} (20) **2.0 ppm of Cu^{2+}**	
		(A) Removal	98.25 %
		(1) 1000 ppm of K^+, 1000 ppm of Li^+, (3) 500.0 ppm of Ca^{2+}, (4) 100 ppm of Mg^{2+}, (5) 4.0 ppm of Cr^{6+}, (6) 3.98 ppm of Al^{3+}, (7) 2.9 ppm of Ba^{2+}, (8) 4.4 ppm of Ni^{2+}, (9) 4.6 ppm of Mn^{2+}, (10) 4.5 ppm of Zn^{2+}, (11) 4.0 ppm of Co^{2+}, (12) 4.0 ppm of Cd^{2+}, (13) 3.85 ppm of Pb^{2+}, (14) 4.0 ppm of Hg^{2+}, (15) 3.45 ppm of Fe^{3+}, (16) 4.0 ppm of Bi^{3+}, (17) 3.5 ppm of Sb^{3+}, (17) 4.0 ppm of Mo^{6+}, and (19) 3.9 ppm of Se^{4+} (20) **0.035 ppm of Cu^{2+}**	
		(B) Extraction/separation = 1.9 ppm	95.5 %
Zu (II)	Al/HOM- DZ	**Mixture (2)** (1) 1000 ppm of K^+, (2) 1000 ppm of Li^+, (3) 500.0 ppm of Ca^{2+}, (4) 100 ppm of Mg^{2+}, (5) 4.0 ppm of Cr^{6+}, (6) 4.0 ppm of Al^{3+}, (7) 3.0 ppm of Ba^{2+}, (8) 4.5 ppm of Ni^{2+}, (9) 4.5 ppm of Mn^{2+}, (10) 4.5 ppm of Cu^{2+}, (11) 4.0 ppm of Co^{2+}, (12) 4.0 ppm of Cd^{2+}, (13) 4.0 ppm of Pb^{2+}, (14) 4.0 ppm of Hg^{2+}, (15) 3.5 ppm of Fe^{3+}, (16) 4.0 ppm of Bi^{3+}, (17) 3.5 ppm of Sb^{3+}, (17) 4.0 ppm of Mo^{6+}, and (19) 4.0 ppm of Se^{4+} (20)**1.0 ppm of Zn^{2+}**	
		(A) Removal	98.9 %
		(1) 1000 ppm of K^+, 1000 ppm of Li^+, (3) 500.0 ppm of Ca^{2+}, (4) 100 ppm of Mg^{2+}, (5) 3.92 ppm of Cr^{6+}, (6) 3.99 ppm of Al^{3+}, (7) 2.9 ppm of Ba^{2+}, (8) 4.3 ppm of Ni^{2+}, (9) 4.6 ppm of Mn^{2+}, (10) 4.49 ppm of Cu^{2+}, (11) 4.0 ppm of Co^{2+}, (12) 4.0 ppm of Cd^{2+}, (13) 3.85 ppm of Pb^{2+}, (14) 3.89 ppm of Hg^{2+}, (15) 3.5 ppm of Fe^{3+}, (16) 4.0 ppm of Bi^{3+}, (17) 3.48 ppm of Sb^{3+}, (17) 4.0 ppm of Mo^{6+}, and (19) 3.8 ppm of Se^{4+}, **0.011 ppm of Zn^{2+}**	
		(B) Extraction/separation = 0.98 ppm	98.0 %

(a) The efficiency of the nanocaptor was calculated from the % ratio of the metal uptake or extracted concentrations and the initial concentration of metal ions in mixture.

To study the recovery of metals from a real aqueous sample, we mixed 200 mL of a 0.03 M sodium citrate/thiosulfate/tartrate mixture as a masking agent solution with a 400 mL solution containing 2 ppm of Cu(II) or 0.5 ppm of Zn(II) ions and other competitive metal ion concentrations. The solution was then completed to 1.0 L by adding an aqueous solution, as listed in Table 5.4. Then, 30 mg of mesocaptors was added to this mixture and stirred for 2h to ensure the complete removal of Cu(II) and Zn(II) ions. The solid Cu(II) ion-captor (with green color) or Zn(II) ion-captor (with pink color, see Figure 5.12) and filtrate solution were analyzed using UV-vis-NIR spectrometry and ICP-AES, respectively, as shown in Table 5.4. Our data analyses revealed that the Cu(II) and Zn(II) ions can be removed from the aqueous solution with ~98% recovery without disturbance, to a high extent of concentrations of other competitive ions.

To assess the practical utility of the Zn(II), and Cu(II) ion-mesocaptors in terms of the quality and efficiency during the optical recognition and determination of Zn(II), and Cu(II) analytes from the commercial wastes, the quantification of 100 μg dm^{-3} levels of Zn(II), and Cu(II) ions was investigated with pretreated real sample effluents collected from different sources such as food processing, and hospital effluent samples (Table 5.5). The quantitative analyses of the sensor, according to the calibration plot (Fig. 5.9 (C and D)), showed the detectable amounts to be 99.5-100.1 μg dm^{-3} for Zn(II), and Cu(II) ions, with a standard deviation value of ≤ 3-4% for triplicate analyses. These analytical data indicated that the proposed sensing system of optical mesocaptors can serve as a potential candidate for monitoring of Zn(II), and Cu(II) ion from polluted environment.

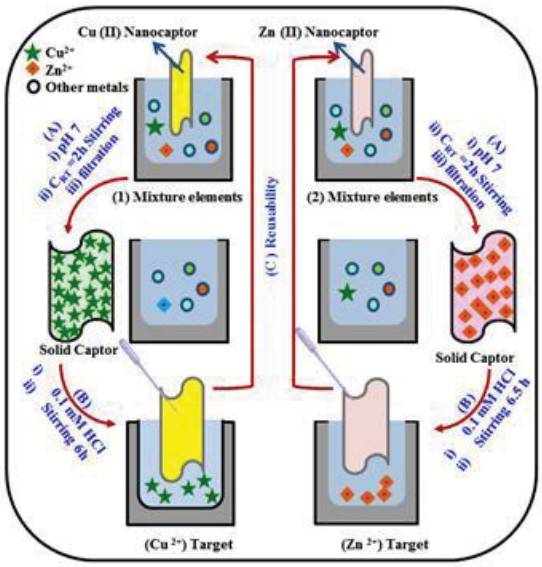

Figure 5.11: Systematic consequences of the selective recovery stages of Cu(II) and Zn(II) ions; A) removal step at proper pH, B) separation of metal ions from captor, and C) reusability of the captor using stripping agent of 0.1 mM HCl.

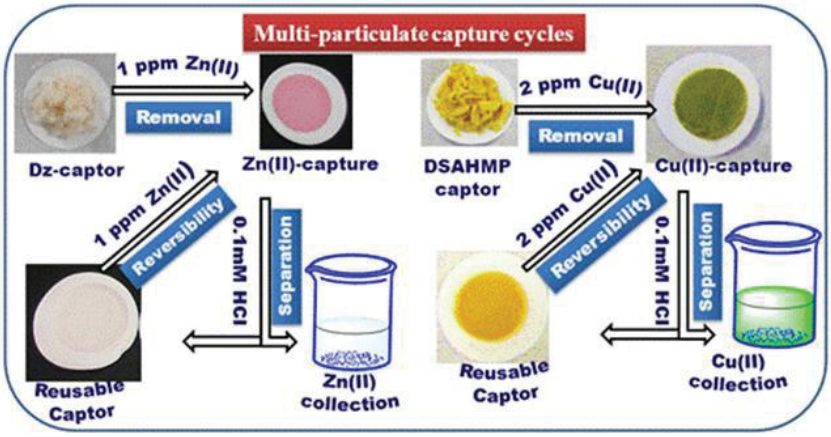

Figure 5.12: Real experimental and color profile of the captor with the recovery system of Cu(II) and Zn(II) ions after several reuse/cycles (No.).

Table 5.5: Analysis of Zn(II), and Cu(II) in spiked environmental samples with optical mesocaptors using amount of 20 mg, volume of 20 mL, and temperature of 25 °C

Sample Source	Sample composition (mg dm^{-3})	Zn^{2+} or Cu^{2+} spiked amount (ppb)	Zn^{2+} analysed amount (ppb) -	Cu^{2+} analysed amount (ppb) -
Food processing	0.005-As^{5+}, 10-Mn^{2+}; 0.2 - Sn^{2+}, Sb^{2+}; 10 - Ca^{2+}, 1.5 - Ni^{2+}, Fe^{2+}; 0.05 - $Cr^{3+/6+}$, Mg^{2+}	100	100.1 ± 3.2	99.7 ± 2.2
Hospital effluent	1.75 - Co^{2+}, Ni^{2+}, Mn^{2+}, Fe^{2+}; 20 - Ca^{2+}, 100 - Na^{+}, K^{+}, Mg^{2+}	100	99.5 ± 4.0*	99.6 ± 3.0*

The Cl^- anion, which was used as the stripping agent at 0.1 $mmol.L^{-1}$ concentration, could effectively be used to remove metal ions to extract and collect Cu(II) and Zn(II) ions onto the solid captor (that is, decomplexation) (Figure 5.12). Stripping experiments were conducted several times via a liquid-exchange process to release the metal ions and obtain "metal ion-free" captor surfaces. After a few minutes, the colour of the metal ion captor changed from initial color, indicating the release of the collecting Cu(II) and Zn(II) ions from the solid captor. The reflectance spectra of the solid captor displayed spectra similar to those of the DSAHMP-modified captor at λ = 415 nm and DZ-modified at λ = 510 nm after decomplexation, indicating the stability of the captor, as evidenced by the XRD and N_2 isothermal profiles (data not shown). The ICP-AES analysis of the collected

Cu(II) solution also indicated that 98.9%- 99.9% of the metal ions can be released using this simple chemical treatment (Figure 5.12).

A major advantage of mesocaptors is their retaining functionality in terms of Cu(II) and Zn(II) ion recovery after multiple reuse cycles.[49-51] To investigate the efficiency of the captor design for the recovery of metal ions after several recovery cycles, we analyzed the ICP-AES results of the Cu(II) and Zn(II) ions solution after completing all stages of the capture assays according to the following: 1) the removal of metal ion from aqueous solution and 2) the release of the metal ion from solid capture (Figure 5.13). In turn, the signal intensity of the captor with each reuse cycle was compared with the signal spectra of the captor prior to the use of the stripping agent (Cl^- anion). Both solid captor and metal ion solution analyses indicated that the captor had well-controlled signalling in the recovery of Cu(II) and Zn(II) ions even after multiple reuse cycles (that is, ≥ 7) (Figure 5.13). This finding indicated that the functional molecular probe onto mesocaptors still attained their electron acceptor/donor strength functionality to offer effective binding and signalling of the metal ion targets despite substantial influence upon cycling.

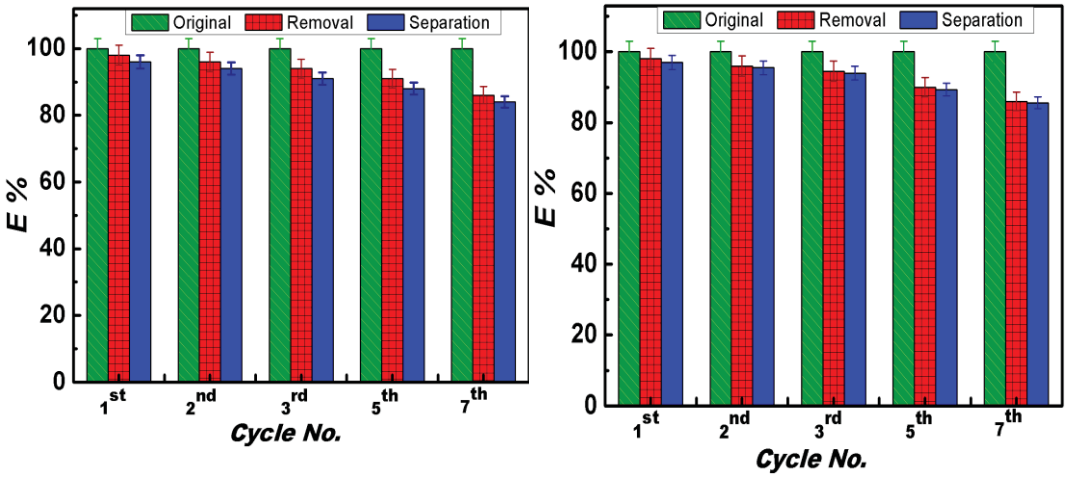

Figure 5.13: ICP-AES analysis of the solution of Cu(II) [upper] and Zn(II) [bottom] ions after completing all stages of the capture assays in terms of the removal and release of Cu(II) and Zn(II) ions within multiple reuse cycles (that is, ≥ 7). E% represents the percentage ratio of the Cu(II) and Zn(II) concentration per reuse cycle (No.) of the initial concentration use [2 ppm and 0.5 pmm for Cu(II) and Zn(II) ions, respectively] at capture condition assays (recovery time of > 60 min, amount of 30 mg, volume of 1 L, and temperature of 25 °C).

5.3. Hierarchically inorganic–organic multi-shelled nanospheres for intervention and treatment of lead-contaminated blood

In order to apply the developed nanosensors in medical applications, a novel optical multi-shell nanosphere sensor is fabricated. This sensor enables selective recognition, unrestrained accessibility, monitoring, and removal of Pb^{2+} ions from human blood (i.e. red blood cells, RBCs). Lead in wastewater mainly originates from industries such as battery manufacturing, printing, painting, and dying. Lead is ubiquitous in the environment and is hazardous at high levels.[59, 60] Lead is also a potent neurotoxin that can interfere with brain development,[61-63] slow down nerve conduction velocity,[64] and trigger behavioral problems[65] once introduced into the body through inhalation, diet or skin contact. Lead toxicity remains the world's most common environment-borne disease, particularly in children,[66] despite efforts in reducing global emissions. Continued evidence of lead toxicity has led to the reduction of the permissible blood lead level to 10 $\mu g \cdot L^{-1}$ (0.483 μmol/L).[67-69]

The adverse effects of lead ions on the environment and living organisms necessitate the periodic monitoring and removal of lead concentrations from human blood and body fluids.[70-73] Various techniques, including chemical precipitation,[74] reverse osmosis,[75] electrochemical treatment techniques,[76] ion exchange,[78,78] and membrane filtration,[70] have been utilized in removing Pb^{2+} ions from aqueous phases. However, these methods remain unsuitable in removing heavy metal from human blood because of their limitations for in vivo use.[80,81] Adsorption is a widely used method because of its simplicity and cost effectiveness. Various adsorbents, such as activated carbon,[82,83] iron oxides,[84] biomaterials,[85] zeolites,[86] manganese oxides,[87] recycled alum sludge,[88] and natural condensed tannin,[89] have been studied. However, the low adsorption capacity, selectivity, and reversibility of these adsorbents limit their applications. Therefore, the development of an inexpensive, simple, and rapid sensor that is safe for in vivo use and is capable of detecting Pb^{2+}can potentially revolutionize the detection and removal of Pb^{2+} from the human body.[59,77,78] The development of optical sensors for the detection of Pb^{2+} has elicited great interest in environmental and biomedical fields.[90-92] Recent efforts have been focused on the development of sensitive metal–oxide-based sensors for the detection and selective removal of Pb^{2+} ions.[93-95] Optical sensors are more flexible, easier to use, have lower operating costs, and are less time consuming in fabrication than sensors

synthesized through previous approaches.[59,70-73,90-95] However, the ability of optical sensors in selectively recognizing and removing the target metal ion from human blood is limited. Designing selective sensors for metal ions has recently become important in many applications, including environmental and security monitoring, waste management, nutrition, and clinical toxicology.[96, 97]

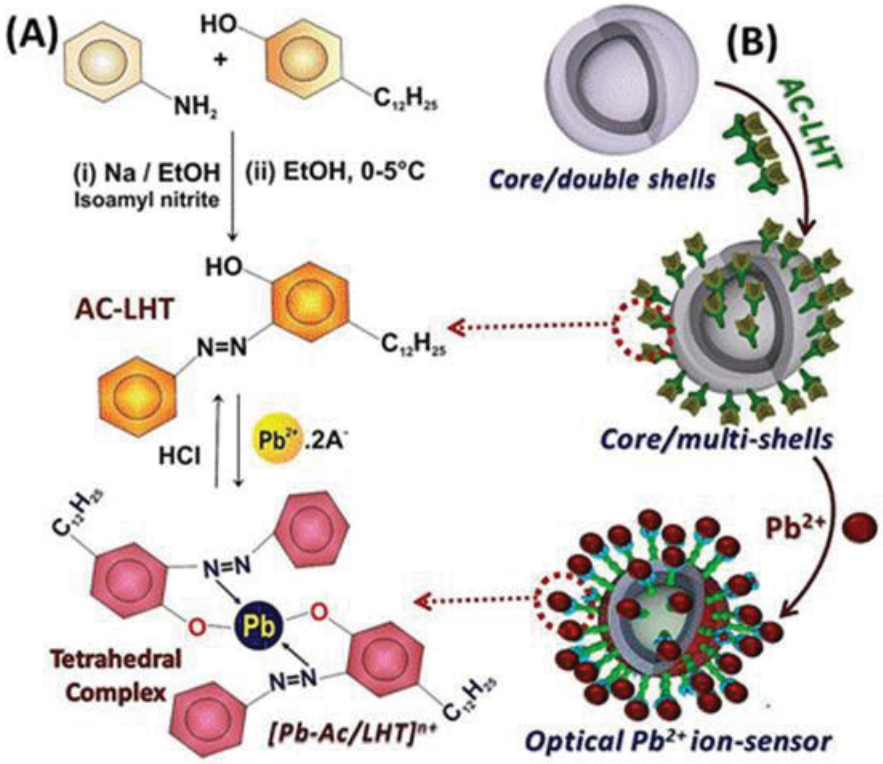

Figure 5.14: The structure of the chemically synthesized AC–LHT, which is a complex formation of $[Pb–AC/LHT]^{n+}$ that occurs during Pb^{2+} ion sensing. The collection of the Pb^{2+} ion from the shell surfaces during the reversible process was performed using HCl stripping agent (A). The systematic design of the multi-shelled Pb^{2+} ion sensor (B) possibly distributed and diffused the AC–LHT onto the inner/outer shell construction during the direct AC–LHT-immobilized synthesis process.

Much attention has also been given to the different types of core-shell structures based on the mesoporous microspheres that enable the encapsulation and transport of guest molecules. The fields that have shown interest in these structures include biomedical and environmental research applications such as biolabeling, imaging, drug delivery, separation processes, and optical sensing because of the biocompatibility and stability of the structures against degradation.[98-100] Iron oxide nanoparticles particularly

provide a basis upon which to explore further applications of magnetic nanoparticles in biomedicine because of the inherent biocompatibility of the iron oxide.[101-103] Several groups have demonstrated the exciting and promising biological applications of magnetic nanoparticles, and have confirmed the superior performance of magnetic nanoparticles to magnetic microparticles in applications such as separation of proteins and detection of pathogens. The design and fabrication of nanoparticle-based chemosensors has generated great interest in a variety of scientific communities ranging from biological and environmental sciences to engineering. The detection of targeted metal ions that typically occur through a controlled binding event is transmitted as a readable signal.[80] Such attributes are required for modern-day analytical schemes as a response to the battlefield detection of biowarfare agents and applications in biomedical diagnostics in economically depressed regions.[98-103] We have developed a colorimetric approach to Pb^{2+} ion recognition and removal using cross-responsive shells containing chemically responsive azo–chromophores with long hydrophobic tail (AC–LHT) dyes because we recognize that humans are visual creatures; moreover, our imaging technology is highly advanced yet inexpensive (Figure 5.14).

5.3.1. Control design of the hieratically multi-shelled sphere sensor

The multi-shelled sensor was fabricated through sufficiently physisorbed interactions (Figure 5.14 B) between the interior/exterior silanol and APMS groups of core/double-shell silica nanospheres and the heteroatoms of AC–LHT. A unique feature of the core/double-shell sensor design is the capacious hollow cage shell structure that can encapsulate numerous different types of functional groups and protect the immobilized probe (III) to maintain electron acceptor and donor strength. The development of a dynamic surface-coating process of AC–LHT with long alkyl tails ($\geq C_{12}H_{35}$) provides the required hydrophobicity in the dense and flexible probe shell around the core/double-shell silica. No elution of the AC–LHT dressing layer from the robustly constructed multi-shell sequences was observed during the recognition of Pb^{2+} ion target. The results indicate the stability of the fabricated silica core/multi-shelled sensor when the incorporated azo-probe had a long chain hydrophobic tails for one year or even longer. The necessity for high-cost silane or thiol coupling agents as surface modifiers during the design of nanosphere sensors was eliminated,[16,17] as proven by scanning electron microscopy (SEM), transmission electron microscopy (TEM), scanning transmission electron

microscopy (STEM), and scanning transmission electron microscopy using energy-dispersive X-ray spectroscopy (STEM–EDS) profiles (Figures. 5.15 and 5.16). The SEM and TEM images revealed the formation of core-shell silica spheres characterized by particle size uniformity (300 nm to 500 nm) (Figure 5.15 (A and B)). The additional layers of AC–LHT showed an extra thin layer covering the external surface of the outer shell, which increased the overall diameter of the spheres as clearly seen from TEM and STEM (Figure 5.15 C and Figure 5.16 C, respectively).

STEM–EDS mapping of the sensor indicated the presence of Si, O, C, and N ((Figure 5.16 (B to E)). The O and Si contributions mainly came from the double core-shell [Figure 5.16 (B and C)], whereas N and C were originally from APMS and AC–LHT [Figure 5.16 (D and E)]. STEM–EDS mapping also indicated that the Si, O, N, and C atoms were uniformly distributed in the double core-shell (Figure 5.16 F).

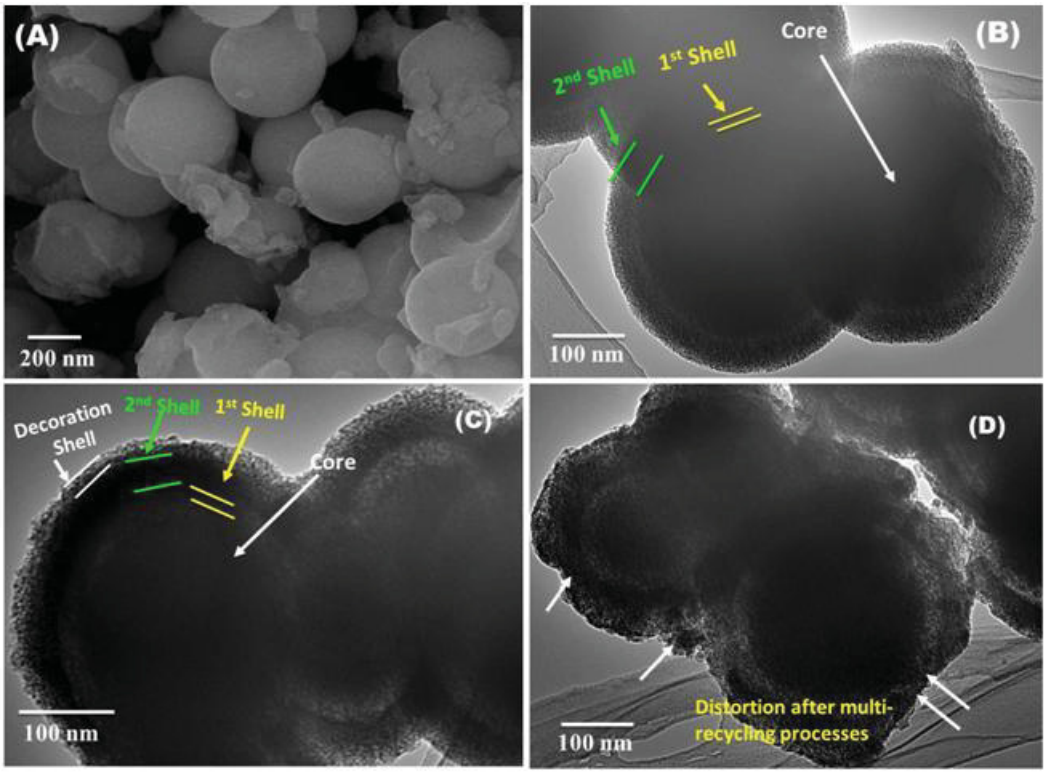

Figure 5.15: SEM image of the mesoporous core/multi-shelled sensor (A). Representative TEM images of the core/double shell structure (B), the core/multi-shelled sensor (C), and the core/multi-shelled sensor after the recycling process (D).

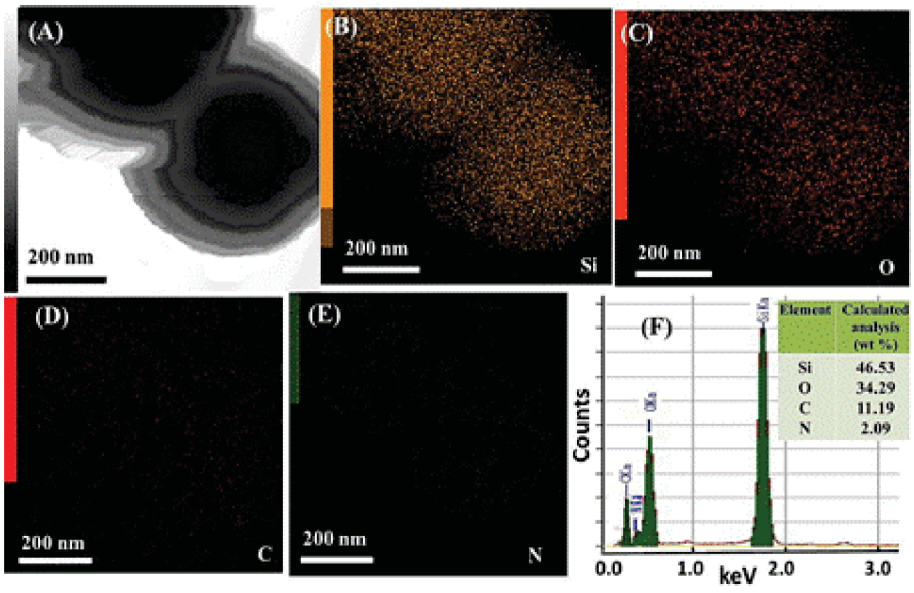

Figure 5.16: STEM–EDS mapping (A–F) of the mesoporous core/multi-shell sensor. (A) STEM images of (B) silicon, (C) oxygen, (D) carbon, (E) nitrogen, and (F) EDS analysis results, and the calculated values of the atomic abundance of the species present in the solid multi-shelled sensor.

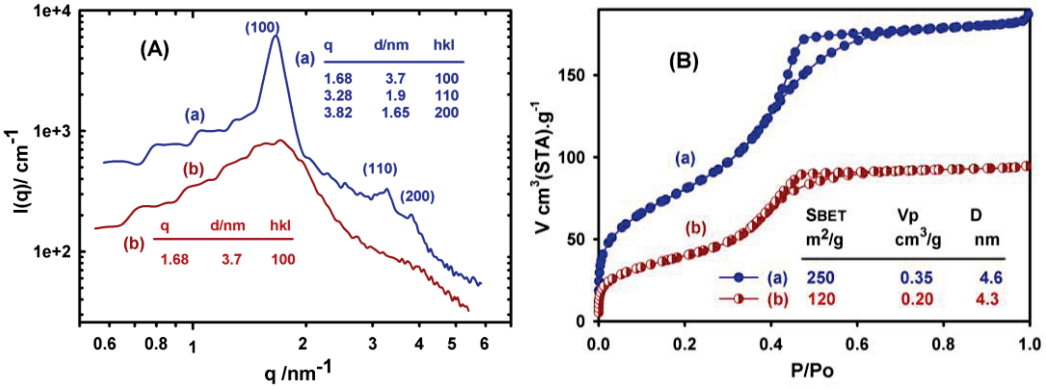

Figure 5.17: (A) SAXS patterns and (B) N_2 adsorption/desorption isotherms of the mesoporous core/multi-shell silica (a) before and (b) after the recycling process. (B) The inset table shows the surface area (S_{BET}), pore size (D), and pore volume (V_p), respectively. (A) The average inter-particle distance d (center to center) can be evaluated from the SAXS peaks using $d = 2\pi / q_{max}$.

SAXS patterns of the core/double-shell scaffold and the multi-shelled sensor show well-resolved and broad scattering peaks that tentatively led to the assignment of the hexagonal P6mm geometries. The N_2 isotherms for the scaffold and sensor (Figure 5.17B) also exhibited well-defined hysteresis loops of type H_1 with sharp capillary

condensation of isotherms with type IV, indicating open cylindrical pores.[105-107] The steepness of the isotherms decreased with the immobilization of the azo dyes into membrane templates. This result indicated the embedding of the AC–LHT into the exterior/interior pore shells, as proven by the decrease of the structural parameters (such as mesopore size and volume and surface area) of the sensor strips (Figure 5.17B, Inset).

5.3.2. Selective, sensitive detection and removal assay of Lead ions.

The pH and kinetic contact time are key control factors in the selective and sensitive detection or removal of Pb^{2+} ions from blood or water using the multi-shelled sensor. The sensitivity of the sensor based on optical color intensities and signal responses to Pb^{2+} ions was revealed at pH 7, as shown in Figure 5.18. The specific color intensity and signal response of Pb^{2+}-to-AC–LHT complexes onto the shell sensor at pH 7 and at response time R_t > 10 min indicated the thermodynamic stability of the geometrical "tetrahedral" coordination of this AC–LHT–Pb^{2+} ion complexation reaction (Figure 5.14 & Figure 5.18). A deficiency in the *d*-orbital of the metal ion centers in the optimized metal complexes firmly bound the metal to the AC/LHT donor and formed five member rings in the symmetrical complexes, as shown in Figure 5.14.[70-71] The results also suggest that the elevated temperature enhanced Pb^{2+} ion diffusion across the aqueous diffusive boundary layer at the shell–water interface.[108,109] The increase of the internal energy of the Pb^{2+} ion aqueous phase may also have affected Pb^{2+} ion transfer to the AC/LHT binding sites, as proven by the change of the R_t value (4 min ≤ R_t ≤ 10 min, 20 °C to 40 °C), which over-shadowed the hindrance effect of the hydrophobic tails of AC–LHT in the outer decoration shell.

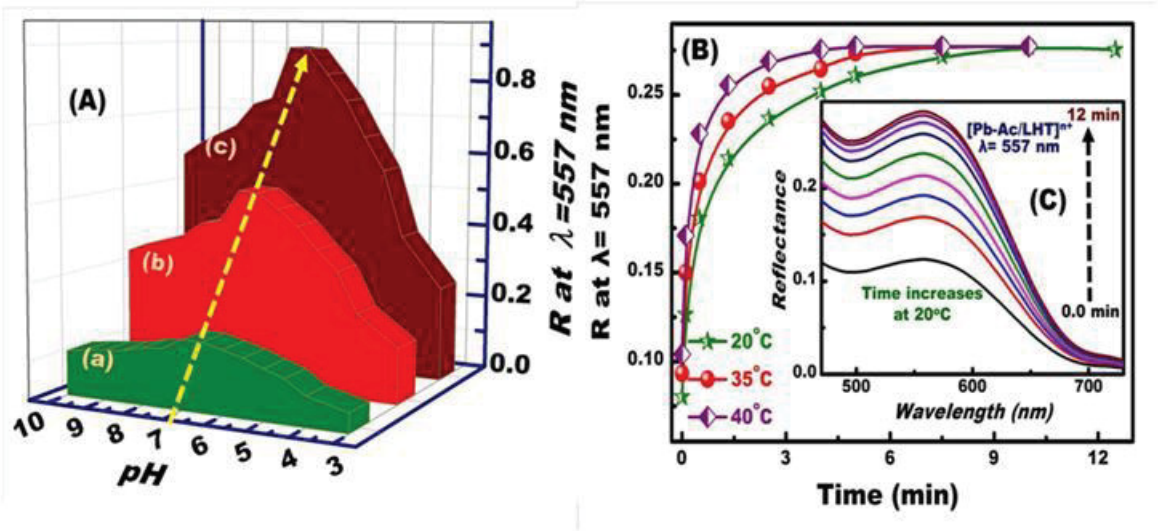

Figure 5.18: (A) The pH-dependent response profile observed for the multi-shelled sensor when individually equilibrated at different pH conditions, with [0.05 ppm] (a), [0.5 ppm] (b), and [2 ppm] (c) Pb^{2+} ions, respectively, at 20 °C with 10 mg amount and $R_t \geq 8$. (B) Study of the temperature-control effect on the kinetic responses of the multi-shelled sensor during the recognition of [200 ppb] Pb^{2+} ions at pH 7, with 10 mg amount and 20 ml volume. (C) Variation in the reflectance signal response with respect to the response time ($R_{t0\rightarrow 12\ min}$) of the multi-shelled sensor during the recognition of [200 ppb] Pb^{2+} ions at pH 7, with 10 mg amount, 20 ml volume, and 20 °C temperature, respectively.

5.3.3. Capture of lead from the blood

The removal of lead from blood was studied as an example of the potential use of our sensor in removing toxic metals (Figure 5.19). The result indicates the medical application of our sensor. The presence of Pb^{2+} ions in blood has numerous adverse effects because of the vital role of RBCs in the storage and transportation of lead ions to other organs. The ability of the sensor to remove Pb^{2+} ions was demonstrated through the inhibition of the specific toxic effects associated with the presence of Pb^{2+} ions in blood. The blood samples were obtained from healthy donors who were nonsmokers, had not received any pharmacological treatment, and were not occupationally exposed to Pb^{2+}. Sodium citrate (3.2%, w/v) was used as an anticoagulant at a whole blood ratio of 1:10. The plasma and buffy coat samples were removed after the centrifugation of blood for 8 min at 600 rpm. The RBC suspensions were washed twice with phosphate-buffered saline (PBS).

5.3.4. Hemolysis assay

An isotonic solution of Pb^{2+} ions in 0.9% NaCl was added to the RBC suspension (1% in

PBS) at a concentration of 3 μM, followed by the addition of 20 μM to 100 μM H_2O_2. A suspension of NS sensor in the PBS was then added. This solution was incubated at 37 °C with gentle shaking for 12 h. The samples were centrifuged for 8 min at 600 rpm. The absorbance of the hemoglobin at 540 nm was measured (iMark microplate reader, Bio–Rad). The hemoglobin was released into the supernatant because of lead-induced RBC hemolysis in the presence of 20 or 100 μM H_2O_2.[104] The results were expressed as a percentage of the total hemolysis, which is given by

$$\% \text{ of Hemolysis} = \frac{\text{Mean absorbance of sample} - \text{Mean absorbance of blank}}{\text{Mean absorbance of} + \text{ve control (H O)} - \text{Mean absorbance of blank}} \text{ X } 100$$

H_2O_2 was used to enhance RBC hemolysis and the oxidative stress induced by the Pb^{2+} ions because of the ultra-trace concentration of Pb^{2+} ions, as previously reported.[104] The hemolysis assay was conducted for 12 h to ensure the complete inhibition of the toxicity induced by Pb^{2+} ions through the 0.02% sensor (Figure 5.20A). The RBC hemolysis was determined by measuring (≥10 times) the absorbance of the released hemoglobin at 540 nm. Each experiment was repeated three times on three different days. A statistical analysis was performed using the Student's t-test (SigmaPlot 11.0 at $P<$ 0.05). RBC hemolysis with hemoglobin release resulting from lead-induced cell toxicity was significantly reduced by our multi-shell sensor, as proven by the phase-contrast microscopic images (Figure 5.20B). These results highlight the potential of our sensor as a new strategy of controlling the toxicity of elevated blood lead levels through the removal of lead ions.

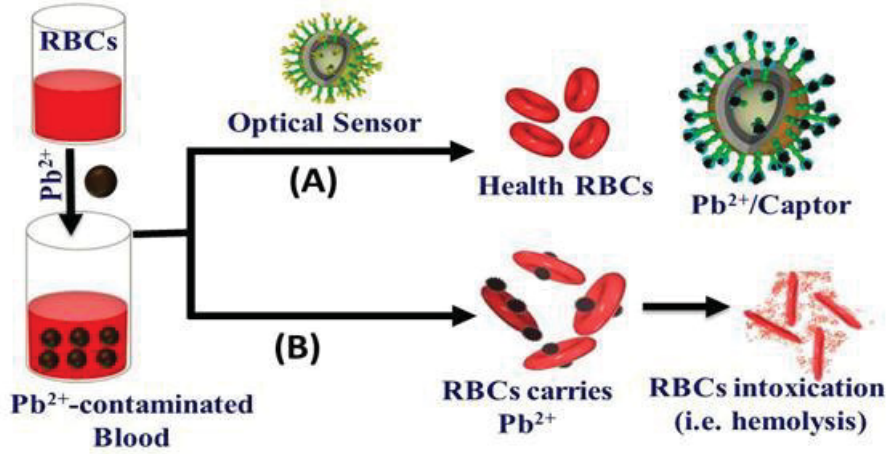

Figure 5.19: Medical applications based on the optical sensor of the shell-by-shell synthesis as a removal strategy for toxic metals such as Pb(II) from human blood.

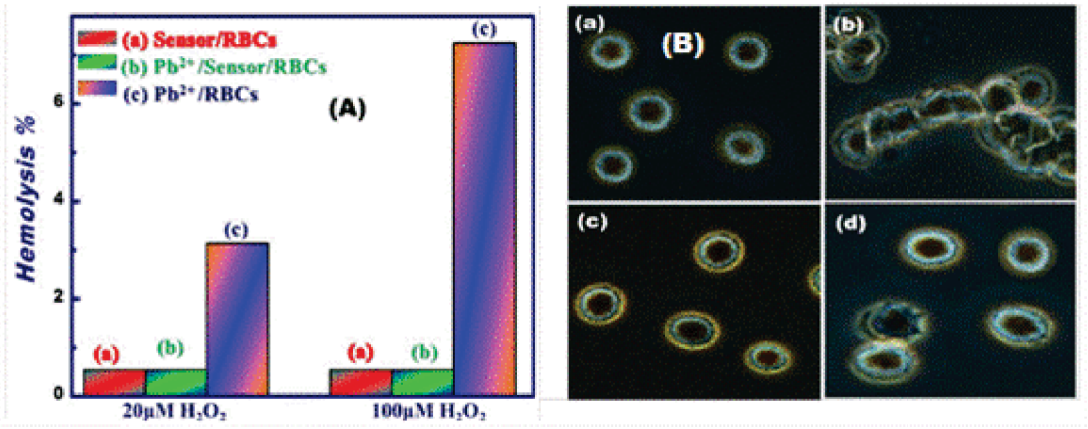

Figure 5.20: (A) Percentage of the lead-induced hemolysis of RBCs in the presence of 20 and 100 μM H_2O_2 and the inhibition of hemolysis because of the removal of Pb^{2+}through the NS sensor. The error bars represent SEM. (B) Phase-contrast microscopic images (100×) showing the RBCs incubated with (B-a) blank (PBS/H_2O_2 only) for 12 h, (B-b) lead-induced hemolysis after a 12 h incubation in PBS/H_2O_2, (B-c) NS sensor addition and inhibition of lead-induced hemolysis after 1 h, and (B-d) sensor addition and inhibition of lead-induced hemolysis after 12 h of hemolysis.

5.3.5. Toxicity control and selective removal of Pb^{2+} ion in water

The remarkable color and ion–spectral responses of the multi-shelled sensor ensured excellent optical isolations of the ultra-trace concentrations of Pb^{2+} analyte, as shown by the limit of detection values (6.6× 10^{-8} mol/dm^3) .[70-73,90-92] The reflectance spectra of the sensor exhibited a bathochromic shift from (λ_{max}) 445 nm to the low-energy side-band at 557 nm with the addition of a wide range of Pb^{2+} concentration ions (4.8 × 10^{-8}–9.6 × 10^{-6} mol/dm^3). These results indicate the formation of a charge–transfer (intense π–π^* transition) complex between the Pb^{2+} ions and the probes with a high stability constant (log K_s) of 8.0 (Figure 5.21).

The effect of the interfered ions on the Pb^{2+} ion-selective sensor was investigated by initially adding the interfered cations and anions with tolerance concentrations of up to 50 and 6000 times greater than those of the Pb^{2+} target ions (Figure 5.21 (C and D)) under ion-sensing/ion-capture conditions (pH 7, 20 °C, and Rt≥ 10 min). The results showed no significant changes in the reflectance spectra of the sensor (blank) at λ_{max} of 557 nm despite the addition of high doses of various cations or anions (i.e., cited in Y–axes), which indicates negative disturbance effects on the Pb^{2+} ion-selective sensor. The

calibration plot (Figure 5.21B, blue curve) of the Pb^{2+}analyte in the presence of these matrix species also proved the significant correlation between the recognition-sensing procedure of the Pb^{2+} ion through the fabricated multi-shelled sensor and the Pb^{2+} ion-sensing data obtained in the presence of a high concentration of active multi-ion matrix species.[112-116] The interference studies were extended by adding these actively interfered species prior to the [0.05, 0.5, and 2 μg/L] Pb^{2+} analyte in these ion-sensing shells. However, the Pb^{2+} ions in real samples are normally encapsulated by a variety of matrix compounds such as cationic and anionic species.[32-37] Given this interfering system, the results also show the efficiency of the Pb^{2+}ion-selective sensor with a high tolerable level of interfering matrix concentrations despite the increase of the interfered ion–spectral signals with the [0.05 μg/L] Pb^{2+} ion system.

High response speed and reliable removal of ultra-trace wide-range (0.010 mg.dm^{-3} to 2.0 mg·dm^{-3}) concentrations of Pb^{2+} ions from naturally occurring environmental samples containing chemically complex matrices (thiourea, CH_3COO^-, and SCN^-) and 10.0 mg dm^{-3} to 300 mg dm^{-3} of alkali and alkaline earth metal ions (including Na^+, K^+, Li^+, Mg^{2+}, and Ca^{2+}) in addition to traces (0.02 mg dm^{-3} to 0.083 mg dm^{-3}) of Mn^{2+} and $Fe^{2+/3+}$ ions and 1 mg dm^{-3} to 5 mg dm^{-3} of inorganic [NO_2^-, NO_3^-, F^-, SO_4^{2-}, CO_3^{2-}, and PO_4^{3-}] anions were achieved at specific sensing conditions (pH 7, 20 °C, time ≥ R_t, 20 ml solution volume) (Figure 5.22 A). The behavior of the multi-shelled sensor with the Pb^{2+}analyte and its matrix environments showed linear removal plots, which indicated two key components:

(1)A wide range of concentrations of Pb^{2+} ions can be removed in a one-step treatment with a high adsorption efficiency of ~93%. The adsorption capacity (q_m) indicated that the practical removal of 1 g of Pb^{2+} ions from an aqueous solution required ~ 2.3 g of the multi-shelled sensor.

(2) The formation of the monolayer coverage of the Pb^{2+} ions in the interior/exterior shells of multi-shelled sensor with these recogination/removal system assays.

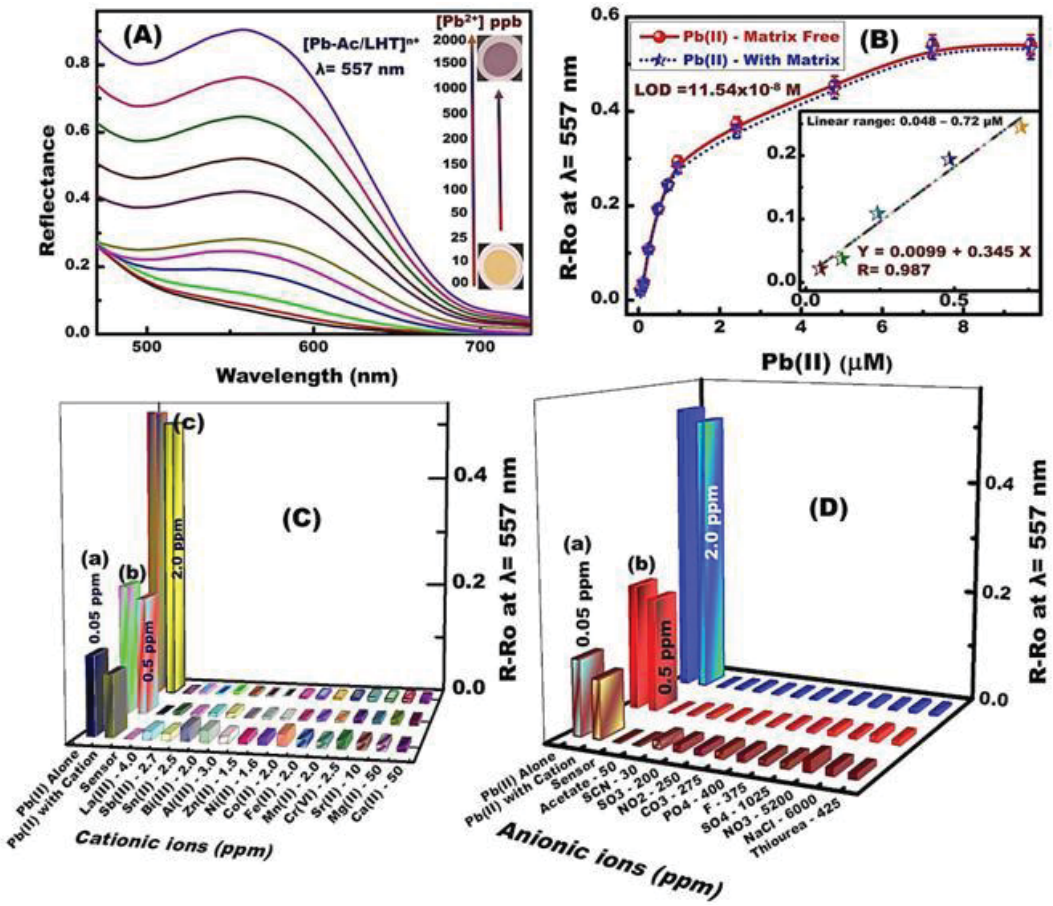

Figure 5.21: (A) Concentration-proportionate color transition map (insert) and reflectance spectra (b) observed for the Pb^{2+} ion sensor with increasing concentrations of Pb^{2+} ions at pH 7, with 8 min Rt, 20 ml total volume, and 20 °C temperature, respectively. (B) Calibration plot for the multi-shelled sensor of the reflectance spectra measured at λ_{557} nm with different Pb^{2+} concentrations. Inset (B): A linear fit line in the linear concentration range before the saturation of the calibration plots for the multi-shelled sensor of the spectral absorbance measured at λ_{557} nm with different Pb^{2+} concentrations. The error bars denote a relative standard deviation > 2.5% for the analytical data of 10 replicate analyses. Sensing signal responses (C, D) for the multi-shelled sensor in the presence of Pb^{2+} concentrations of [0.05], [0.5], and [2.0] ppm, respectively. Sensing signal responses in the presence of other interfered cations (C) and anions (D) at pH 7 after 10 min of contact time at 20 °C, with 10 mg amount and at 20 ml volume, respectively. The graph (C, D) represents the difference in the reflectance spectra of the sensor with (R) and without (Ro, blank) the addition of active matrices at λ_{557} nm, respectively. The selectivity profile of the Pb^{II} ions was obtained by adding the concentrations of the cations (C) and anions (D) to the sensor system beside the ions' notification.

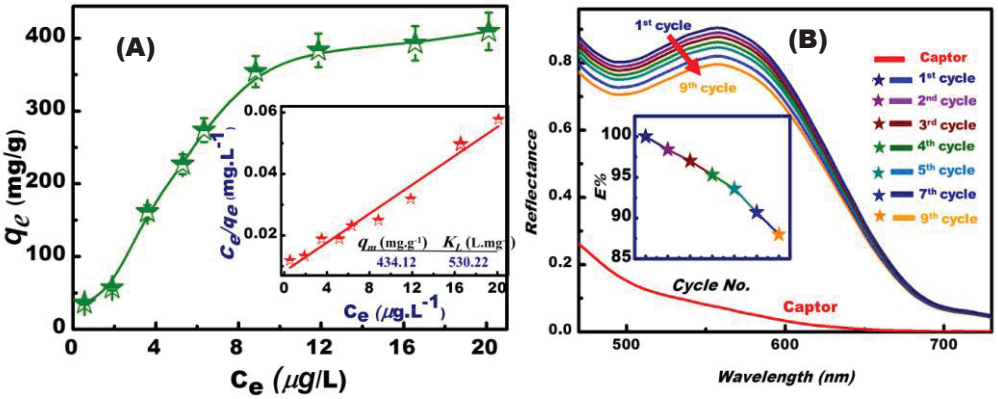

Figure 5.22: A) Langmuir adsorption isotherms and the liner plots (inserts) of the removal processes of Pb^{2+} ions using the multi-shelled sensor at pH 7, and amount 10 mg, at a temperature of 20 °C. B) Multiple reuse cycles of the sensor for Pb^{2+} ions. The signaling spectra of sensor recorded at 557 nm, using 10 mg/L sensor at pH 7.

Toxicity control and collection of the captured Pb^{2+} species with consistent solid sensor fidelity are highly important to reduce the volume of commercial waste.[12-15] One of the key features of the proposed process is that the captured Pb^{2+} ions can be separated from the sensor shells through chemical stripping. For example, a 0.02 mol.L^{-1} concentration of HCl was used as a stripping agent for the extraction and collection of Pb^{2+} ions. The stripping experiments were conducted several times through a liquid-exchange process to release the metal ions and to obtain "metal ion-free" captor surfaces. This simple releasing process concentrated the collected elements, thereby reducing their volume and enabling controlled waste management with 97% efficiency. The ICP–MS analysis of the collected Pb^{2+} ion solution also indicated that 95.1% to 99.4% of the Pb^{2+} ions could be released using this simple chemical treatment. The Pb^{2+} ion-sensor system can be repeatedly recycled (i.e., $\geq$ 9) without damaging the hieratically multi-shelled spheres (Figure 5.15 and Figure 5.22).

5.4.References

[1] S. Sthiannopkao, S. Sreesai, J. Environ. Manage., 90, 2009, 3283–3289.

[2] F. Xiao, J-C. H. Huang, J. Environ. Manage., 90, 2009, 3105–3109.

[3] C. Vulpe, B. Levinson, S. Whitney, S. Packman, J. Gitschier, Nat. Genet., 3, 1993, 7–13.

[4] P.C. Bull, G.R. Thomas, J.M. Rommens, J.R. Forbes, D.W. Cox, Nat. Genet., 5,1993, 327–337.

[5] P.L. Malvankar, V.M. Shinde, Analyst, 116, 1991, 1081–1084.

[6] M. Goyal, V.K. Rattan, D. Aggarwal, R.C. Bansal, Colloid Surface A, 190, 2001, 229–238.

[7] J. Jung, J.A. Kim, J.K. Suh, J.M. Lee, S.K. Ryu, Water Res., 35, 2001, 937–942.

[8] T. Vengris, R. Binkiene, A. Sveikauskaite, Appl. Clay Sci., 18, 2001, 183–190.

[9] H.D. Ozsoy, H. Kumbur. J. Hazard. Mater., 136, 2006, 911–916.

[10] Z. Xu, J. Yoon, D. R. Spring, Chem. Soc. Rev., 39, 2010, 1996–2006;

[11] U.C. Saha, B. Chattopadhyay, K. Dhara, S. Kumar Mandal, S. Sarkar, A. R. Khuda-Bukhsh, M. Mukherjee, M. Helliwell, P. Chattopadhyay, Inorganic Chemistry, 50, 2011, 1213-1219.

[12] S. K. Das, R. Guin, S. K. Saha, Radiochimica Acta, 88, 2000, 107; Nnabuk O. Eddy, Stevens A. Odoemelam, Afr. J. Pure and Appl. Chem. 3, 2009, 145-151; V. Vinod, D. Kailash, C. Suresh, L. Madan, Res. J. Recent. Sci., 2012, 160-165.

[13] D-H. Kima, M-C.Shina, H-D. Choi, C-I. Seob, K. Baek, Desalination, 223, 2008, 283–289; O. Kozák, P. Praus, V. Machovič, Z. Klika, Ceram. Silik., 54, 2010, 78-84.

[14] W. Ngeontae, W. Aeungmaitrepirom, T. Tuntulani, Talanta, 71, 2007, 1075–1082.

[15] G.J. Mohr, Anal. Bioanal. Chem., 386, 2006, 1201–1214.

[16] S. Ng, R. Narayanaswamy, Anal. Bioanal. Chem., 386, 2006, 1235–1244.

[17] B. Lei, B. Li, H. Zhang, S. Lu, Z. Zheng, W. Li, Y. Wang, Adv. Funct. Mater., 16, 2006, 1883– 1891.

[18] M. Koneswaran, R. Narayanaswamy, Sensor Actuat. B-Chem., 139, 2009, 104–109.

[19] G.G. Huang, J. Yang, Anal. Chem., 75, 2003, 2262–2269.

[20] V. Camel, Spectrochim. Acta B, 58, 2003, 1177–1233.

[21] P.K. Jal, S. Patel, B.K. Mishra, Talanta, 62, 2004, 1005–1028.

[22] E. Coronado, J.R. Galán-Mascarós, C. Martí-Gastaldo, E. Palomares, J.R. Durrant, R. Vilar, M. Gratzel, M. K. Nazeeruddin, J. Am. Chem. Soc., 127, 2005, 12351–12356.

[23] S.A. El-Safty, A. Ismail, H. Matsunaga, F. Mizukami, Chem. Eur. J., 13, 2007, 9245–9255.

[24] S.A. El-Safty, D. Prabhakaran, A. Ismail, H. Matsunaga, F. Mizukami, Adv. Funct. Mater., 17, 2007, 3731–3745.

[25] E. Palomares, R. Vilar, J.R. Durrant, Chem. Commun., 10, 2004, 362–362.

[26] P. Buhlmann, E. Pretsch, E. Bakker, Chem. Rev., 98,1998, 1593–1687..

[27] B. Ma, S. Wu, F. Zeng, Sensor Actuat. B-Chem., 145, 2010, 451–456.

[28] B.N. Ahamed, I. Ravikumar, P. Ghosh, New J. Chem., 2009, 33, 1825–1828.

[29] S.A. El-Safty, D. Prabhakaran, Y. Kiyozumi, F. Mizukami, Adv. Funct. Mater., 2008, 18, 1739–1750.

[30] S.A. El-Safty, A. Ismail, H. Matsunaga, F. Mizukami, J. Phys. Chem.,112, 2008, 4825–4835.

[31] S.A. El-Safty, A.A. Ismail, H. Matsunaga, T. Hanaoka, F. Mizukami, Adv. Funct. Mater., 18, 2008, 1485–1500.

[32] S.A. El-Safty, D. Prabhakaran, A.A. Ismail, H. Matsunaga, F Mizukami, Chem. Mater., 20, 2008, 2644–2654.

[33] A.B. Desacalzo, K. Rurack, K.H. Weisshoff, R.M. Manez, M.D. Marcos, P. Amoros, K. Hoffmann, J. Soto, J. Am. Chem. Soc., 127, 2005, 184–200.

[34] D. Dubé, S. Royer, D.T. On, F. Béland, S. Kaliaguine, Micropor. Mesopor. Mater. 79, 2005, 137–144.

[35] Y. Wang, N. Lang, A. Tuel, Micropor. Mesopor. Mater., 93, 2006, 46–54.

[36] A. Corma, S. Iborra, S. Miquel, J. Primo, J. Catal., 161, 1996, 713–719.

[37] M.T. Janicke, C.C. Landry, S.C. Christiansen, S. Birtanlan, G.D. Stucky, B.F. Chmelka, Chem. Mater., 11, 1999, 1342–1351.

[38] Y. Zhang, X. Shi, J.M. Kim, D. Wu, Y. Sun, S. Peng, Catal. Today, 93, 2004, 615–618.

[39] D.L. Trimm, A. Stanislaus, Appl. Catal., 21, 1986, 215–238.

[40] P. Kim, J.B. Joo, H. Kim, W. Kim, Y. Kim, I.K. Song, J. Yi, Catal. Lett., 104, 2005, 181–189.

[41] A.R. Garcia, R.B. de Barros, A. Fidalgo, L.M. Ilharco, Langmuir, 23, 2007, 10164–10175.

[42] J. Cejka, J. Appl. Catal. A, 254, 2003, 327–338.

[43] H. Du, V.V. Terskikh, C.I. Ratcliffe, J.A. Ripmeester, J. Am. Chem. Soc., 124, 2002, 4216–4217.

[44] S.A. El-Safty, A. Shahat, K. Ogawa, T. Hanaoka, Micropor. Mesopor. Mater., 138, 2011, 51–62.

[45] S.A. El-Safty, A.A. Ismail, A. Shahat, Talanta, 83, 2011, 1341–1351; S. A. El-Safty, J. Porous Mater., 15, 2008, 369-387.

[46] M.J. Frisch et al, Gaussian 03, Revision C.02, Gaussian, Inc., Wallingford CT, 2004.

[47] S.A. El-Safty, T. Hanaoka F. Mizukami, Chem. Mater., 17, 2005, 3137–3145.

[48] X. Liu, T. Peng, J. Yao, H. Lv, C. Huang, J. Solid State Chem., 183,2010, 1448–1456.

[49] B.R. White, J.A. Holcombe, Talanta, 71, 2007, 2015–2020.

[50] A. Yari, N. Afshari, Sensor Actuat. B-Chem., 119, 2006, 531–537.

[51] T. Leelasattarathkul, S. Liawruangrath, M. Rayanakorn, B. Liawruangrath,W. Oungpipat, N. Youngvises, Talanta, 72, 2007, 126–131.

[52] S.A. El-Safty, T. Balaji, H. Matsunaga, T. Hanaoka, F. Muzukami, Angew. Chem. Int. Ed., 45, 2006, 7202–7208.

[53] S.J. Lee, S.S. Lee, J.Y. Lee, J.H. Jung, Chem. Mater., 18, 2006, 4713–4715.

[54] F. Yu, W. Zhang, P. Li, Y. Xing, L. Tong, J. Ma, B. Tang, Analyst, 134, 2009, 1826–1833.

[55] W. Yantase, C. Timchalk, G.E. Fryxell, B.P. Dockendorff, Y. Lin, Talanta, 68, 2005, 256–261.

[56] J. Huang, Y. Xu, X. Qian, Dalton Trans., 2009, 1761–1766.

[57] C.F. Chow, M.H.W. Lam, W.Y. Wong, Inorg. Chem., 43, 2004, 8387–8393.

[58] J.V.R. Lis, M.D. Marcos, R.M. Mánez, K. Rurack, J. Soto, Angew. Chem. Int. Ed., 44, 2005, 4405– 4407.

[59] a) H. Y. Lee, D. R. Bae, J.C. Park, H. Song , W. S. Han, J. H. Jung, Angew. Chem. Int. Ed. 121, 2009, 1265–1269; Y-H. Li, Y. Zhu, Y. Zhao, D. Wu, Z. Luan, Diam Relat Mater., 15, 2006, 90 – 94.

[60] Y-H. Li, S. Wang, J. Wei, X. Zhang, C. Xu, Z. Luan, D. Wu, B. Wei, Chem Phys Lett, 357, 2002, 263–266.

[61] F. Oktem, M. K. Arslan, B. Dundar, N. Delibas, M. Gultepe, I. E. Ilhan, Arch Toxicol, 78, 2004, 681-687.

[62] C. Winder, N. G. Carmichael, P. D. Lewis, Trends Neurosci, 5, 1982, 207-209.

[63] D. A. Cory-Selechta, Adv Behav Pharmacol, 4, 1984, 211-255

[64] S. Araki, H. Sato, K. Yokoyama, K. Murata, Am J Ind Med., 37, 2000, 193-204.

[65] Q. He, E. W. Miller, A. P. Wong, C. J. Chang, J. Am. Chem. Soc. 128, 2006, 9316-9317.

[66] M. Vigeh, K. Yokoyama, Z. Seyedaghamiri, A. Shinohara, T. Matsukawa, M. Chiba, M. Yunesian, Occup Environ Med, 68, 2011, 231-234.

[67] H. Gurer, Ercal, N. Biol. Med. 29, 2000, 927-945.

[68] P.Hsu, Y.L Guo, Toxicology, 280, 2002, 22-44.

[69] S. A. El-Safty, M. A. Shenashen, A. A. Ismail, Chem Commun, 48, 2012, 9652-9654.

[70] S. A. El-Safty, D. Prabhakaran. A. A. Ismail, H. Matsunaga, F. Mizukami, Chem Mater, 20, 2008, 2644-2654.

[71] T. Li, E. Wang, S. Dong, Anal Chem, 82, 2010, 1515-1520.

[72] X. Miao, L. Ling, X. Shuai, Chem Comm., 47, 2011, 4192–4194.

[73] Q. Y. Chen, Z. Luo, C. Hills, M. Tyrer, Water Res, 43, 2009, 2605-2614.

[74] H. Ozaki, K. Sharm, Saktaywin, W. Desalination, 144, 2002, 287-294.

[75] L. J. Janssen, L. Koene, Chem Eng J, 85, 2002, 137-146.

[76] M. Y. Vilensky, B. Berrkowitz, A. Warshawsky, Environ Sci Technol, 36, 2002, 1851-1855.

[77] Y.Q. Xing, X.M. Chen, D.H. Wang, Environ Sci Technol, 41, 2007, 1439-1443.

[78] R.S. Juang, R.C. Shiau, J Membr Sci, 165, 2000, 159-167.

[79] L. Wang, Z. Yang, J. Gao, K. Xu, H. Gu, B. Zhang, X. Zhang, B. Xu, J. Am Chem Soc., 128, 2006, 13358-59.

[80] H. Y. Lee, D. R. Bae, J. Park, C.H. Song, W. S. Han, J. H. Jung, Angew Chem Int Ed, 121, 2009, 1265-1269.

[81] M. Sekar, V. Sakthi, S. Rengaraj, J Colloid Interf. Sci. 279, 2004, 307-313.

[82] A. N. A. El-Hendawy, S. E. Samra, B. S. Girgis, Colloid Surf. A, 180, 2001, 209.

[83] C. Liu, P. M. Huang, G. Cosmo, chimica Acta 2003, 67, 1045-1054.

[84] W. C. Leung, H. Chua, W. H. Lo, Appl Biochem Biotechnol, 91, 2001, 171.

[85] B. Biskup, B. Subotic, Sep Sci Technol, 39, 2004, 925-940.

[86] R. Sublet, M.O. Simonnot, A. Boireau, M. Sardin, Water Res, 37, 2003, 4904.

[87] W. Chu, Water Res, 33, 1999, 3019-3025.

[88] X. Zhan, A. Miyazaki, Y. Nakano, . Chem Eng Jpn, 34, 2001, 1204-1210.

[89] Y. Salinas , R. Martínez-Máñez, M. D. Marcos, F. Sancenón, A. M. Costero, M. Parra, S. Gil, Chem Soc Rev. 41, 2012, 1261-1296.

[90] W. S. Han, H. Y. Lee, S. H. Jung, S. J. Lee, J. H. Jung, Chem. Soc. Rev. 38, 2009, 1904-1915.

[91] J. H. Jung, J. H. Lee, S. Shinkai, Chem. Soc. Rev. 40, 2011, 4464–4474.

[92] S. A. El-Safty, A. A. Ismail, H. Matsunaga, T. Hanaoka, F. Mizukami, Adv Funct Mater, 18, 2008, 1485–1500.

[93] S. A. El-Safty, M. A. Shenashen, Trends Anal Chem. 38, 2012, 98-115.

[94] S. A. El-Safty, Shenashen, M. A. Khairy, M. Talanta, 98, 2012, 69–78.

[95] A. Hartwig, M. Asmuss, I. Ehleben, U. Herzer, Kostelac, D. A. Pelzer, T. Schwerdtle, A. Bürkle, Environ Health Perspect, 110, 2002, 797-799.

[96] A. Hartwig, Biometals, 23, 2010, 951-960.

[97] W. Zhao, H. Chen, Y. Li, L. Lang, M. Shi, J. Adv. Funct. Mater.18, 2008, 2780-2788.

[98] W. Zhao, J. Gu, L. Zhang, H. Chen J. Shi, J Am Chem, Soc, 127, 2005, 8916-8917.

[99] A. López-Noriega, E. Ruiz-Hernández, S. M. Stevens, D. Arcos, M. W. Anderson, O. Terasaki, M. Vallet-Regí, Chem Mater, 21, 2009, 18-20.

[100] J. Shen, Y. Zhu, X. Yang, J. Zong, C. Li, Langmuir, 2013, 29, 690−695; W. Schärtl, Nanoscale, 2, 2010, 829-843

[101] H. Wang, L. Sun, Y. Li, X. Fei, M. Sun, C. Zhang, Y. Li, Q. Yang, Langmuir, 2011, 27, 11609-15; J. Wang, X. Qu, Nanoscale, 5, 2013, 3589-3600.

[102] X. Gong, S. Peng, W. Wen, P. Sheng, W. Li, Adv Funct Mater, 19, 2009, 292-297.

[103] M. F. Casado, A. L. Cecchini, A. N. C. Simao, R. D. Oliveira, R. Cecchini, Food Chem Toxicol, 45, 2007, 945-952.

[104] S.A. El-Safty, Trends Anal. Chem., 30, 2011, 447-458.

[105] S.A. El-Safty, A. Shahat, W. Warkocki, M. Ohnuma, Small, 7, 2011, 62-65.

[106] N. D. Hoa, S. A. El-Safty, Chem. Eur. J., 17, 2011, 12896–1290.

[107] S. A. El-Safty, M. A. Shenashen, M. Khairy, M. Ismeal, Chem. Commun., 48, 2012, 6708–6710.

[108] S. A. El-Safty, M. A. Shenashen, M. Khairy, M. Ismeal, Adv Funct Mater, 22, 2012, 3013–3021.

[109] K. Eisele, P. A. Lang, D. S. Kempe, B. A. Klarl, O. Niemöller, T. Wieder, S.M. Huber, C. Duranton, F. Lang, Toxicol Appl Pharm, 210, 2006, 116 – 122.

[110] K-M. Lim, S. Kim, J.-Y. Noh, K. Kim, W-H. Jang, O-N. Bae, S-M. Chung, J-H. Chung, Environ Health Perspect, 118, 2010, 928-935.

[111] X. Guo, C. Wang, Y. Fang, L. Chen, S. Chen, J Mater Chem, 2011, 21, 1124.

[112] X. Zhang, Huang, Chem Commun, 46, 2010, 6042-6044.

[113] W. S. Han, H. Y. Lee, S. Jung, S. Lee, Chem. Soc. Rev., 38, 2009, 1904-1915.

[114] T. Zhang, Z. Cheng, Y. Wang, Z. Li, C. Wang, Y. Li, Y. Fang, Nano Lett, 10, 2010, 4738-4741.

CHAPTER 6

DEVELOPMENT OF PSEUDOCAPACITORS FOR EFFICIENT ENERGY STORAGE DEVICEs

Mohamed Khairy, Sherif A. El-Safty, Superior Pseudocapacitor Mesoporous NiO Nanoarchitectures for Electrochemical Energy Storages. ***Journal of Physical chemistry C,*** 2013, submitted.

6.1.Introduction

The world is facing a critical energy problem characterized by rising energy costs and declining productive capacities for oil and gas. Considerable efforts have been devoted to the development of alternative energy storage/conversion devices in response to supply depletion. Electrochemical capacitors (ECs), also called supercapacitors or ultracapacitors, have become crucial and drawn significant interest in recent years owing to their unique energy buffers, reliable life cycle (10,000 cycles), low internal resistance, fast charge and discharge rates, high power densities, and environment-friendly features.[1,2] ECs are prevailing in uninterruptible power sources in electric/hybrid and fuel cell vehicles, memory back-up equipment, and numerous portable electronics such as cellular phones and entertainment devices.[3] ECs with high power density have been associated with the combined advantages of conventional dielectric capacitors and rechargeable batteries. Emerging as an ideal model, ECs have been touted as a solution to the mismatch between the rapid growth in power required by devices and the inability of batteries in various applications, which require transient but high/peak power pulses for time-dependent usage.

ECs may be classified into two distinctive parts according to charge storage mechanisms: electrochemical double-layer capacitors (EDLCs) and pseudo-capacitors.[2,3] EDLCs are based on the electrostatic charge separation between electrolyte ions and electrodes, whereas pseudocapacitors entail reversible Faradaic redox reactions on the surface of an electroactive material for charge storage. The latter have a value of 10 to 100 times that of EDLCs. Since the 1990s, ECs have introduced in their development with materials mostly used as EDLCs based on carbonaceous materials, such as activated carbon,[4,5] carbide-derived carbon,[6] graphene,[7,8] carbon nanofibers,[9] and carbon nanotubes [10] with a large surface area on which charge can reside. Alternatively, pseudocapacitors exhibit high-rate performance related to capacity, rate capability, and cycling stability attributed to unique hierarchical structures. Such performance improves electron/ion transport, enhances the kinetics of redox reactions, and facilitates facile stress relaxation during cycling. Thus, the rational design and fabrication of high surface area-conductive electrodes with well-defined micro/nanoarchitectures for facile electron/ion transport are required for further enhancing electrochemical properties.

Transition metal oxides, such as RuO_2,[11] MnO_2,[12] Co_3O_4,[13] ZnO,[14] NiO,[15] and

MoO_3,[16] have been widely used for ECs with high power density, taking advantage of their fast redox kinetics. Among these metal oxides, nickel oxide (NiO) is a prosperous material used not only for supercapacitor applications due to its high theoretical specific capacitance (2573 F/g), but also as a catalyst and an electrode material for lithium ion batteries and fuel cells as well as in electrochromic films and dye-sensitized photocathodes.[15, 17–19] NiO is one of the relatively few metal oxides having a well-defined redox behavior with *p*-type semi-conductivity; the material is also affordable, abundant, environmentally friendly, and has a stable band gap.[20] With high specific surface area, short diffusion path, and high transfer rate of electrons and/or ions, porous nanostructures are among the best systems in energy storage fields. Given that surface properties considerably influence the charge storage mechanism, the most active approach in supercapacitor research has been the development of electrode materials with improved surface properties.[21] Gogotsi et al.[22] demonstrated that pore size significantly affects ion adsorption, enhancing the capacitance down to the solvated ion size. Several synthetic strategies are attempted to control the surface area, tunable pore size and morphology, and other physicochemical properties of NiO nanocrystals (NCs) and NiO-based composites.[23–28] These studies revealed that parameters such as surface area and pore size, suitable surface morphology, and synthetic strategy of NiO play a significant role in exhibiting higher pseudocapacitance. Despite the development in fabrication strategies, most processes for the fabrication of electrodes are either too delicate, which makes them less viable for large-scale industrial applications, or require additives, which deteriorates the performance of the electrodes.

Recently, mesoporous NiO nanoplatelet (NPL)- and nanoflower (NF)-like structures were fabricated through direct hydrothermal synthesis.[26,27] However, practical supercapacitor design requires controlled assessment processes, which involve high-performance electron/ion transport into the porous networks. Therefore, the fabrication of the controlled mesopore cavities of NiO-based supercapacitors that are simple, high-performance, and have appropriate dynamic working ranges remains a challenge. Moreover, the factors that control the performance of the supercapacitor remain poorly understood. A microwave-assisted strategy has received considerable attention owing to its ability to accelerate the kinetics of particle formation with uniform dimensions and its capacity to form high-purity products with controlled morphology without producing any thermal gradients. Microwave radiation, a nonionizing electromagnetic radiation with

greater penetration depth, significantly enhances the rate of nucleation, thereby reducing the time required for material fabrication.[21]

6.2.Superior pseudo-capacitor mesoporous NiO nanoarchitectures for electrochemical energy storages.

Developing of synthetic approaches to fabricating mesoporous NiO in nanosized dimensions, large-scale production, and tunable pore sizes with controlled surface morphologies were recently reported. Mesoporous NiO NCs were fabricated through homogeneous precipitation reactions under microwave-reflux conditions. The proposed approaches showed that microwave-assisted synthesis is an ideal strategy for controlling the size, shape, and mesoporosity of NiO NCs in flakes-, slice-, and platelet-like structures, and for manufacturing superior recyclable pesudocapacitors. Our findings reveal that NiO NPLs exhibit high capacitance and better electrochemical reversibility than nanoflakes (NFs) and nanoslices (NSs) or even NiO samples prepared through the hydrothermal method. In fact, the large specific capacitance due to the surface characteristics and nano-sized dimensions might be suggested as new prospects for future low-cost and environmentally sustainable energy storage devices.

6.2.1. Formation mechanism of mesoporous NiO nanostructure.

To demonstrate the formation mechanism of NiO samples, the surface morphology was analyzed using field emission scanning electron microscopy (FE-SEM). Figure 6.1 presents the SEM images showing the formation of NiO NFs. The morphology of the mesoporous NiO NCs has been reported numerous times in the literature.[15] However, the formation mechanism remains poorly understood because of hydrophobic interactions, hydrogen bonding, Van-der Waals forces, crystal face attraction, electrostatic and dipolar fields, intrinsic crystal contraction, and ostwald ripening, which simultaneously contribute to product formation. Rao et al.[21] proposed that NFs were formed under the rapid growth of nanoflakes followed by self-assembly to form ball-like structures with hierarchical porosity. However, our findings showed that the extrinsic modulation of crystal nucleation and growth occurs through an aggregation-based mechanism to generate sphere-like crystal structures. The crystallographic planes in the sphere-like structures arranged and modified the relative order of surface energies to form interweaved flakes and flake-

like structures [Figure 6.1(C)]. In general, the plausible mechanism underlying the formation of NiO nanomaterials involved three stages, namely, nucleation, growth, and dehydroxylation or decomposition. The crystal growth seems to proceed via the aggregation of nickel acetate precursor. The nascent nickel acetate nuclei impinge on the neighboring crystals and assemble along a particular crystal orientation because of the slow and continuous reaction under homogeneous precipitation conditions. The extrinsic crystal growth is modulated to a certain extent through the aggregation of nickel acetate nuclei to decrease the surface energy and form a sphere-like structure. Under microwave irradiation, the sphere-like structure decomposes to ripple surface superstructures (flake-like) of NiO NCs with a high degree of retention even after heat treatment (Figure 6.1).

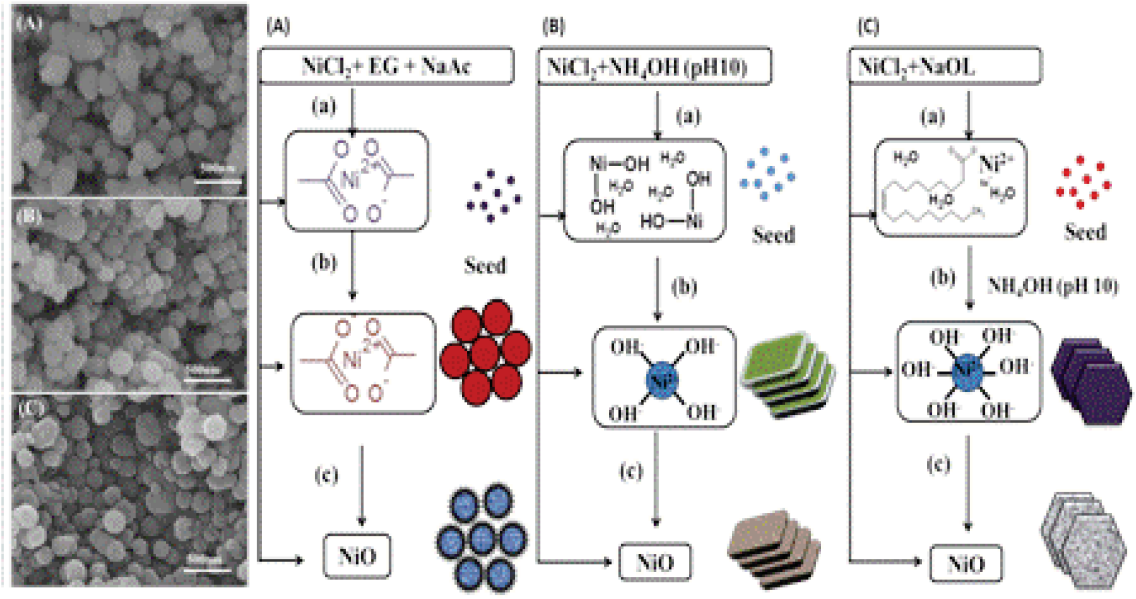

Figure 6.1: Formation mechanism of NiO nanostructured A) mesoporous NiO nanoflakes, B) mesoporous NiO nanoslices, and C) mesoporous NiO nanoplatelets.

6.2.2. Features of mesoporous NiO samples.

The control of the physico-characteristics of mesoporous NiO supercapacitor electrodes was necessary to optimize their performance, stability, and resistivity. Recent reports [21] revealed that surfactant molecules play a significant role in the development of specific morphology and high porosity. However, in this study, we

introduced simple strategies via a microwave-assisted method to control the morphology and mesoporosity with high surface areas. Panel A in Figure 6.2A show the nitrogen adsorption–desorption isotherms and pore size distribution plots of the NiO samples, respectively. The N_2 isotherms of the NiO nanostructure feature type IV isotherms with H_3-type (NFs) hysteresis loop for typical mesoporous materials with different sizes. The desorption branch of the isotherms exhibits stepwise behavior and ends at the limiting pressure of the hysteresis closure. This behavior suggests the non-uniformity of pore openings associated with pore constrictions and/or ink-bottle pores with narrow necks. The BET-specific surface areas of NiO NFs, NiO NSs, and NiO NPLs were 191, 145, and 161 $m^2 g^{-1}$, respectively; the corresponding pore volumes were 0.43, 0.32, and 0.36 $cm^3 g^{-1}$, respectively. For NiO NFs, the generation of flaky structures from sphere-like structures and factors such as inter-particle spacing were the apparent reasons for the bimodal pore size distribution (3.41 nm and 49.09 nm). The decomposition for both rectangular NSs and hexagonal NPLs of $Ni(OH)_2$ also generated the pore network within the NiO nanostructure with morphology retention. The pore distribution sizes were 3.41 nm and 242.7 nm as well as 3.9 nm for NiO NPLs and NiO NSs, respectively. The formation of mesopore type was probably related to the pores inside the NSs and NPLs, which were formed between the primary crystallites. The macroporous type at a relatively high pressure ($0.85 < P/P_o < 1$) in the NiO NPLs was probably associated with textural larger pores that can be formed between secondary platelet particles (Figure 6.2B). This finding demonstrates that our synthesis protocols enabled effective control over the size and shape of the cavity pores. In fact, such mesoporosity can create more convenient channels for hydroxide ions to transport and electrochemically access the active sites for massive charge storage as quickly as possible at large current density. Recently, Simon and Gogotsi reported that the pore size distribution in the range of 2 nm to 5 nm significantly improves energy density and power capability because of unhindered diffusion and accession of solvated hydroxide ions into the 3D pore network matrices.[31]

After mild thermal treatment at 300 °C, the NiO nanostructure pattern showed a broadly resolved scattering peak at approximately q = 1.92, 1.84, and 1.88 nm^{-1}, corresponding to $d_{(spacing)}$ = 3.31, 3.38, and 3.37 nm. Despite the broadening and low resolution in the intense scattering peak, the formation of mesostructures and

retention of the mesopore architectures inside the NiO nanostructure were evident (Figure 6.2, panel C). The wide angle X-ray diffraction (XRD) profiles of the NiO samples showed well-resolved and distinctive diffraction peaks (Figure 6.2D), indicating the formation of single-phase NiO nanostructure with crystalline structures, which is consistent with JCPDS No. 01-089-5881. These diffraction peaks are consistent with face-centered cubic *Fm3m* symmetry with the lattice constant a = 8.35 Å, as revealed in the TEM profiles (see below).

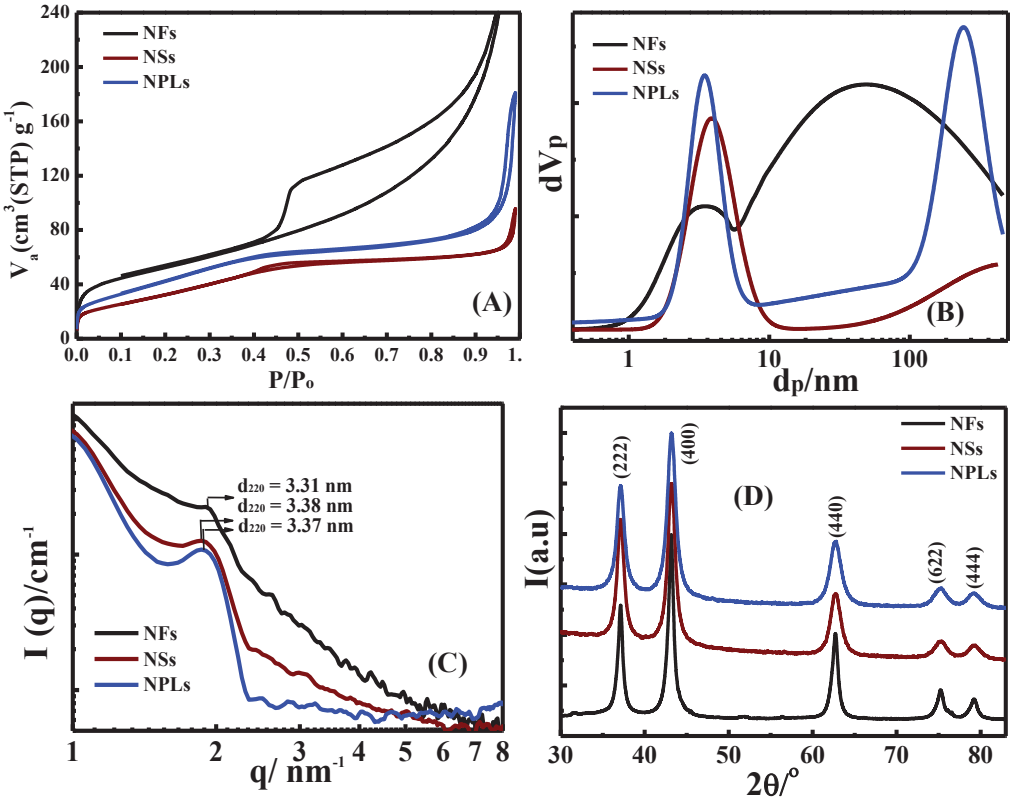

Figure 6.2: Nitrogen adsorption–desorption isotherm (A) pore distribution (B), Small angle X-ray scattering (C) and wide X-ray diffraction (D) of NiO nanoflakes, NiO-nanoslices and NiO nanoplatelets.

A key approach to boosting the specific capacitance of electroactive nickel-based materials is their morphological and/or chemical composition, as well as suitable pore sizes for penetrating the [OH^-] electrolytes into the active site of the 3D network matrix. FE-SEM, HR-TEM, and STEM-EDS mapping were used to analyze NiO characteristics. FE-SEM micrographs revealed the following dimensions of the NiO materials: average diameters ranging from 200 nm to 250 nm for nanoflakes; 300 nm to 350 nm with a thickness of approximately 40 nm for

rectangular slices; and 150 nm to 200 nm with a thickness of approximately 10 nm for hexagonal platelets. Figure 6.3 shows the NiO nanoparticles with uniform sizes and small petals having a smooth, fine surface with an average thickness of 5 nm aligned according to the flake-like structure. In accordance with synthesis conditions, the NiO nanoparticles were arranged in rectangular slices and hexagonal platelets with smooth fine surfaces. The SEM images indicated that NiO NFs, NiO NSs, and NiO NPLs exhibit high degrees of retention even after heat treatment at 300 °C (Figure 6.3). SEM images showed significant evidence of shape- and size-controlled NiO NCs in different morphologies, indicating the versatility of the microwave-assisted method compared with the real control of the NiO nanostructured geometry. Thus, the uniform heating and acceleration of the homogeneous precipitation rate during the microwave-assisted synthesis enhanced the crystal growth and crystallinity of the product, as shown in the XRD and TEM results.

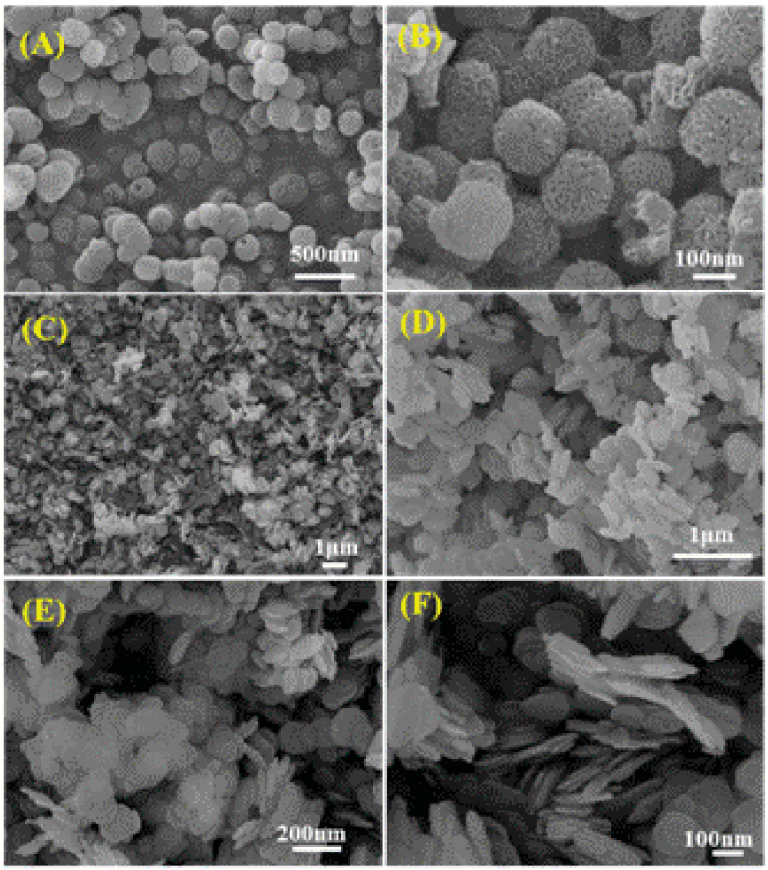

Figure 6.3: FE-SEM images of NiO nanoflakes (A and B), NiO nanoslices (C, and D) and NiO nanoplatelets (E and F).

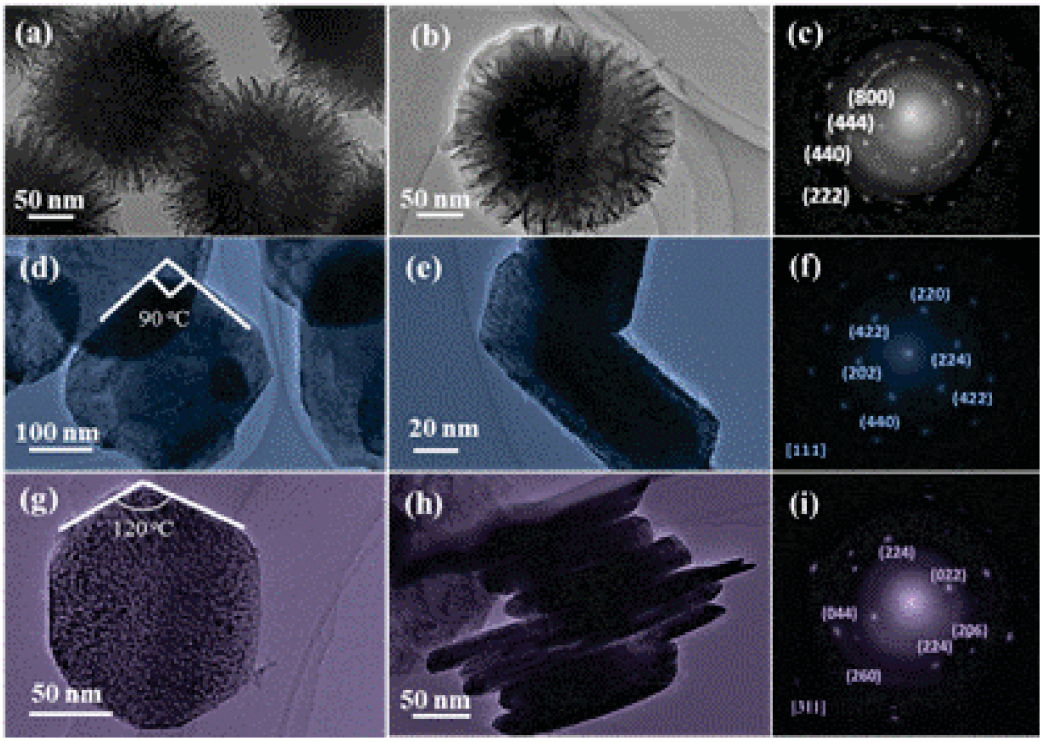

Figure 6.4: HR-TEM images of mesoporous NiO nanostructured (a and b) NiO nanoflakes, (d and e) NiO nanoslices, (g and h) NiO nanoplatelets and (c, f, and i). The corresponding ED patterns of selected areas reveal the high crystallinity of the NiO samples.

The HR-TEM images clearly reveal control over the size and morphology of the NiO samples. Figure 6.4(a and 4) illustrate the formation of a flake-like structure exhibiting smooth and uniform surfaces with an average diameter of 250 nm and a thickness of less than 5 nm. The irregular rectangular slices of NiO NCs have an average size of 350 nm and a thickness of less than 50 nm (Figure 6.4 (d and e)). The addition of oleate ions to the nickel precursor altered the surface energy and crystal orientation to hexagonal platelets with uniform and smooth surfaces (Figure 6.4(g and h)). Meanwhile, oleate prevents the random agglomeration of primary crystals by shielding the OH^- ions and decreases its activity for nascent crystals. Such control of size and morphology draws interest in material science and nanotechnology. Figure 6.4 (g and h) illustrate NiO hexagonal nanoplatelets with an average size of 125 nm and a thickness of less than 10 nm. The adjacent edge angle measures approximately 120°. The TEM micrographs also present the formation of disordered (wormlike) mesopores as suggested by the small angle X-ray scattering

and N_2 adsorption isothermal profiles. The corresponding electron diffraction (ED) patterns of the NiO samples are presented in Figure 6.4 (c, f, and i). The NiO NSs and NPLs exhibit bright spots, indicating a single crystalline NiO nanostructure. However, NiO NFs demonstrate polycrystalline mesoporous nanostructures. The ED pattern matches the cubic NiO crystal structure, which is consistent with the XRD results (Figure 6.2).

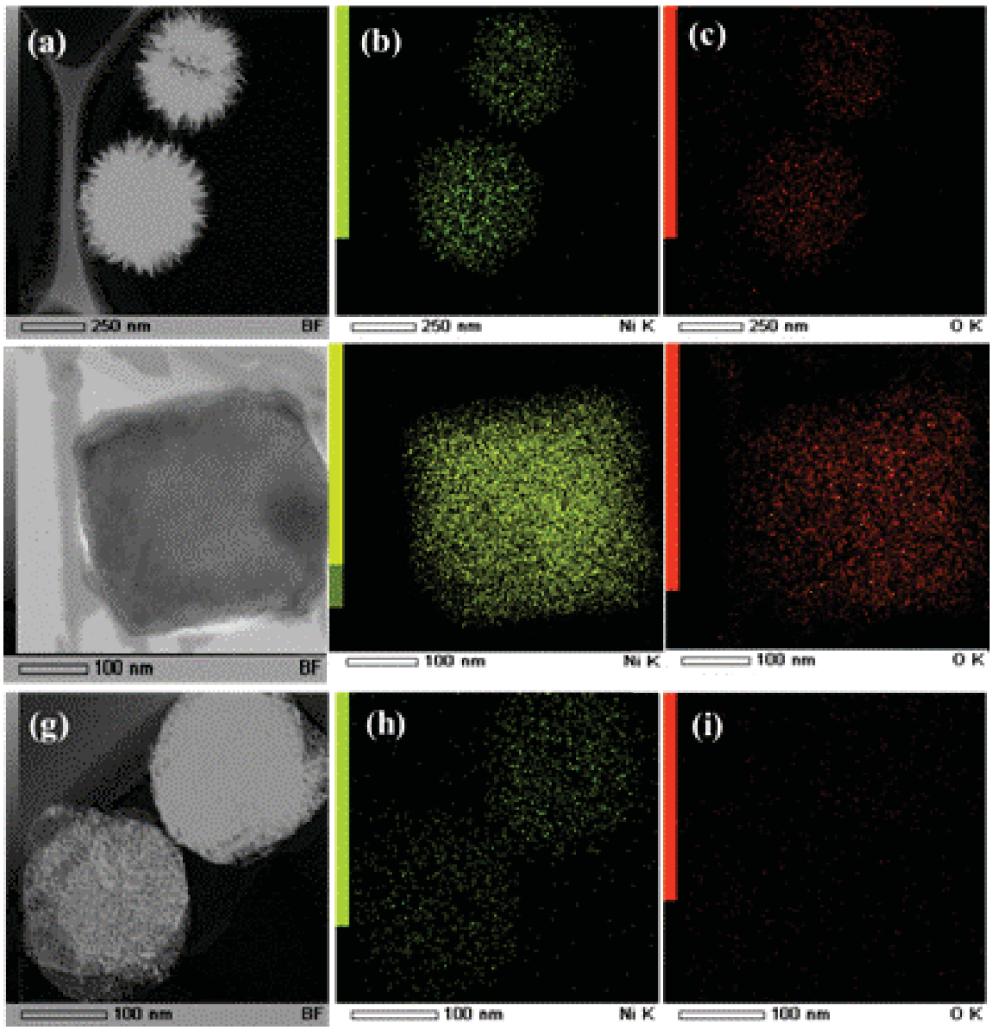

Figure 6.5: STEM-EDS mapping of mesoporous NiO nanostructured (a, d, and g) STEM images, (b, e, and h) Nickel atoms, and (c, f, and i) oxygen atoms of NiO nanoflakes, NiO nanoslices, and NiO nanoplatelets, respectively.

In addition to the TEM images, the elemental composition and surface topology of mesoporous NiO nanostructure were illustrated using STEM-EDS mapping. Figure 6.5 presents the STEM-EDS mapping of mesoporous NiO

nanostructures. Our findings reveal that the maps of Ni and O elements have a contrast area over the whole area of mesoporous NiO nanoparticles. Ni and O elements were observed on the whole surface area of the NiO particles. Elemental analysis of the mesoporous NiO samples indicates the presence of Ni, O, and Cu atoms. The O and Ni atoms were originally found in the mesoporous NiO NCs. The ratio of [O]/[Ni] is slightly higher than unity. These findings reveal that the oxygen atoms were directed to the surface of mesoporous NiO nanoparticles. Hence, the electrochemical characteristics of mesoporous NiO nanostructures and their performance as pesudocapacitors were considered in this study.

6.2.3. Electrochemical measurements

Figure 6.6 illustrates the typical CV curves of mesoporous NiO nanostructures at scan rates from 1 mVs^{-1} to 20 mVs^{-1} in the potential range of 0.0 V to 0.7 V vs. Ag/AgCl (3 M NaCl). The CV patterns showing a pair of redox current peaks reveal that the capacitance characteristic is very different from that of traditional double layer capacitance related to the Faradaic redox process at the electrode surface. The NiO NFs show symmetrical redox peaks, whereas NiO NPLs and NiO NSs illustrate unsymmetrical ones. The unsymmetrical nature of the redox peaks indicates the quasi-reversible redox process of the NiO samples. At scan rate 20 mVs^{-1}, no obvious change in the CV curves is observed. The double layer capacitance also increases with scan rate, particularly with NiO NSs and NiO NPLs. This outcome indicates the good capacitive behavior and high-rate capability of mesoporous NiO samples. Oxidation peaks (E_o) were observed at approximately 0.64 V, 0.61 V, and 0.58 V. Correspondingly, reduction peaks (E_R) were observed at approximately 0.56 V, 0.55 V, and 0.47 V (vs. Ag/AgCl) at scan rate = 1.0 mVs^{-1}. Peak separation (ΔE_p) values were 80 mV, 60 mV, and 110 mV for NiO NFs, NSs, and NPLs, respectively, and increased with the increase in the scan rate (Figure 6.2, panels A to C). Therefore, the Faradaic redox process was related to the quasi-reversible redox process arising from the transition of Ni (II) to Ni (III), and could be represented by the following electrochemical reaction:

$$NiO + OH^- \rightleftharpoons NiOOH + e^-$$

The quasi-reversible process can be ascribed to ohmic and polarization resistance resulting from the diffusion of electrolyte to the active sites within the mesoporous

network mesochannels. The redox currents of the GC/NiO electrode increase as a function of scan rates, which imply a larger electrode pseudocapacitance. The peak current is linearly correlated with the square root of the scan rate, indicating that the electrochemical process is controlled by the diffusion of [OH^-] into the mesopore cavities of NiO NPs. With the increase in scan rates, a positive shift of oxidation peaks in the case of NiO NSs and NiO NPLs, but a negative shift occurs for NiO NFs. The electrocatalytic activity of NiO NPLs is also higher than those of NiO NSs and NiO NFs. The oxidation potential shifts to a lesser value. This behavior is due to the mesoporosity of preferred thickness with the small size and controlled hexagonal shape of NiO NPLs, thus promoting the diffusion of OH^- ions to the active sites of the platelets. The specific capacitance values were calculated by the integration of current vs. time curves according to Equation **(**20). The calculated specific capacitance values at 1 mVs^{-1} were 720 Fg^{-1}, 685 Fg^{-1}, and 1361 Fg^{-1} for NiO NFs, NiO NSs, and NiO NPLs, respectively. Only a 25% loss in specific capacitance values for NiO NPLs is observed compared with the 36% and 54% of NiO NSs and NiO NFs at 20 mVs^{-1}. Although NiO NFs have a higher specific surface area, NiO NPLs have a large specific capacitance. These results indicate that surface composition, small particle size, and hexagonal platelet-like morphology as well as mesoporosity have distinct effects on pseudocapacitor performance. Conversely, the large specific capacitance of NiO NFs is related to the interwoven-shaped mesochannel that enhances the diffusion of OH^- ions. These results also demonstrate the higher current response of NiO NPLs with high applicability even at high scan rates. Based on our results, the portion of pore volume with suitable pore size and the 3D connectivity in the NiO nanostructure are suggested to be more important factors than the surface area.

The most important feature that emphasizes pesudocapacitors over traditional batteries is their much higher power densities. As shown above, the good rate capability of NiO NPLs indicates high power density. The values of power density and energy density were calculated using Eqs. 21 and 22 based on CV measurements at various scan rates. The high power density of NiO NPs was verified by Ragone diagram (Figure 6.6d). The values of energy density were 63.8 Wh/kg, 29.04 Wh/kg, and 22.5 Wh/kg corresponding to power density 13.2 kW/kg, 6.16 kW/kg, and 4.74 kW/kg for NiO NPLs, NiO NSs, and NiO NFs, respectively. Such high energy densities and power densities are better than those of supercapacitor electrodes reported recently.[22] A good electrochemical supercapacitor is expected to provide high energy density or high specific capacitance at a

high scan rate. Our results revealed that the energy density decreased from 92.6 Wh/kg to 63.8 Wh/kg, whereas power density increased from 0.95 kW/kg to 13.2 kW/kg as the scan rate increased from 1 mV/s to 20 mV/s. The mesoporous NiO NPLs showed an excellent reversibility with high specific capacitance and remarkable rate capacitance that highlighted NiO NPLs as superior pseudocapacitor materials for electrochemical energy storage devices.

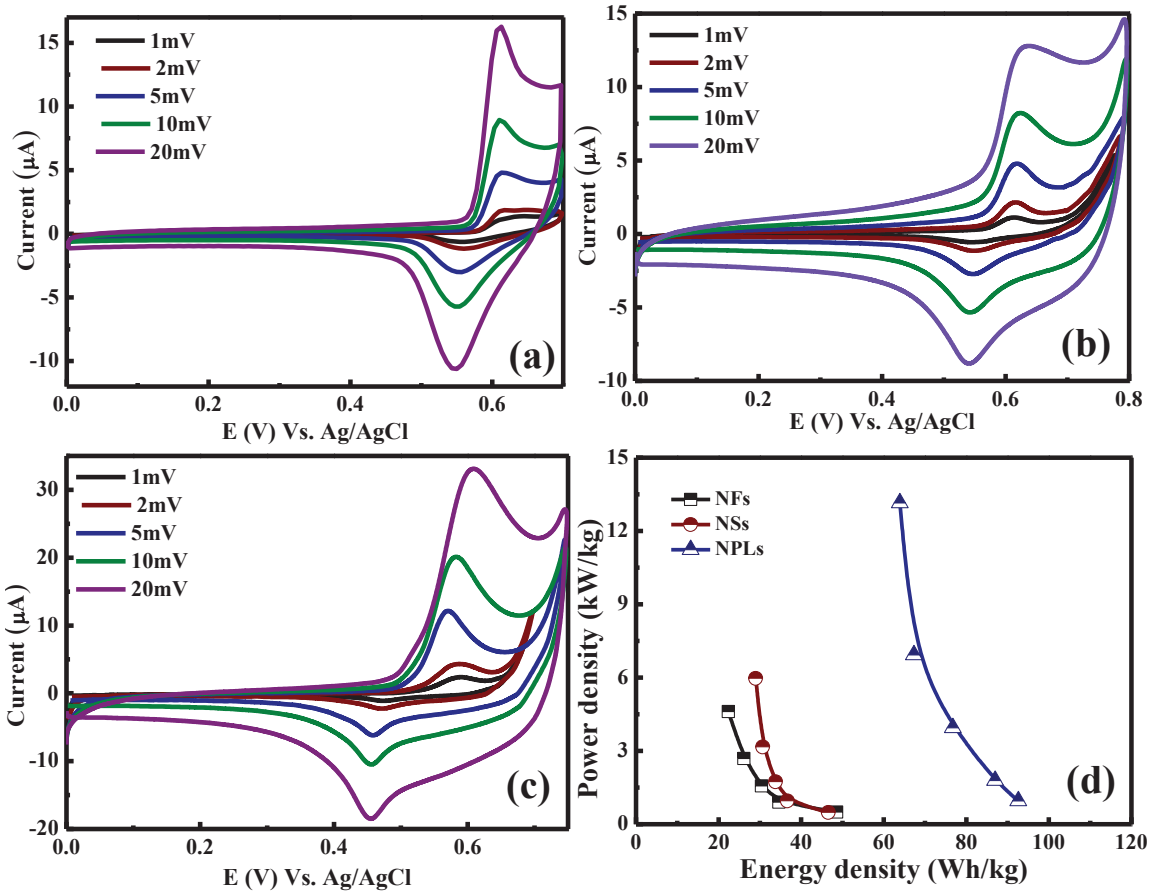

Figure 6.6. Cyclic voltammetric measurements of NiO nanostructured at different scan rates for NiO NFs (a), NiO NSs (b), and NiO NPLs (c); D) Ragone plot of NiO NPs; the specific capacitance values were derived from CV measurements at various scan rates.

Figure 6.7 illustrates the representative galvanostatic discharge curves of mesoporous NiO films at various current densities from approximately 0.65 V to 0.0 V (vs. Ag/AgCl/3M NaCl). Irrespective of the applied current density, the nonlinear discharge curves were observed for all mesoporous NiO NPs. The NiO NPLs exhibit a lower charge plateau and a higher discharge plateau with longer discharge time, indicating that their enhanced electrochemical reactivity with lower polarization was

confirmed by the CV measurements (Figure 6.6). The calculated specific capacitance at various current densities of mesoporous NiO samples according to Eq. 23 is illustrated in Figure 6.7d. As an example, at discharge current of 1.0 Ag^{-1} (7.07 Am^{-2}), the specific capacitance values were 1200 Fg^{-1}, 770 Fg^{-1}, and 600 Fg^{-1} for NiO NPLs, NiO NFs, and NiO NSs, respectively. Noticeably, the specific capacitance remained as high as 750 F/g, 420 F/g, and 346 F/g for NiO NPLs, NFs, and NSs, respectively, even when the discharge current density was increased to 4 A/g (28.28 Am^{-2}). These results showed satisfactory cycling stability in addition to high specific capacitance and rate capacitance. These findings indicated that the NiO NPLs have an excellent capability rate compared with NiO NFs or NiO NSs due to the well-connected mesochannel nanostructures in controlled particle size and closed pore distribution. Such mesoporous structures subsequently increased the active material usage because of the reduction in the diffusion path and acted as an OH^- ion reservoir, which led to sufficient Faradaic reactions at high current densities for energy storage devices.

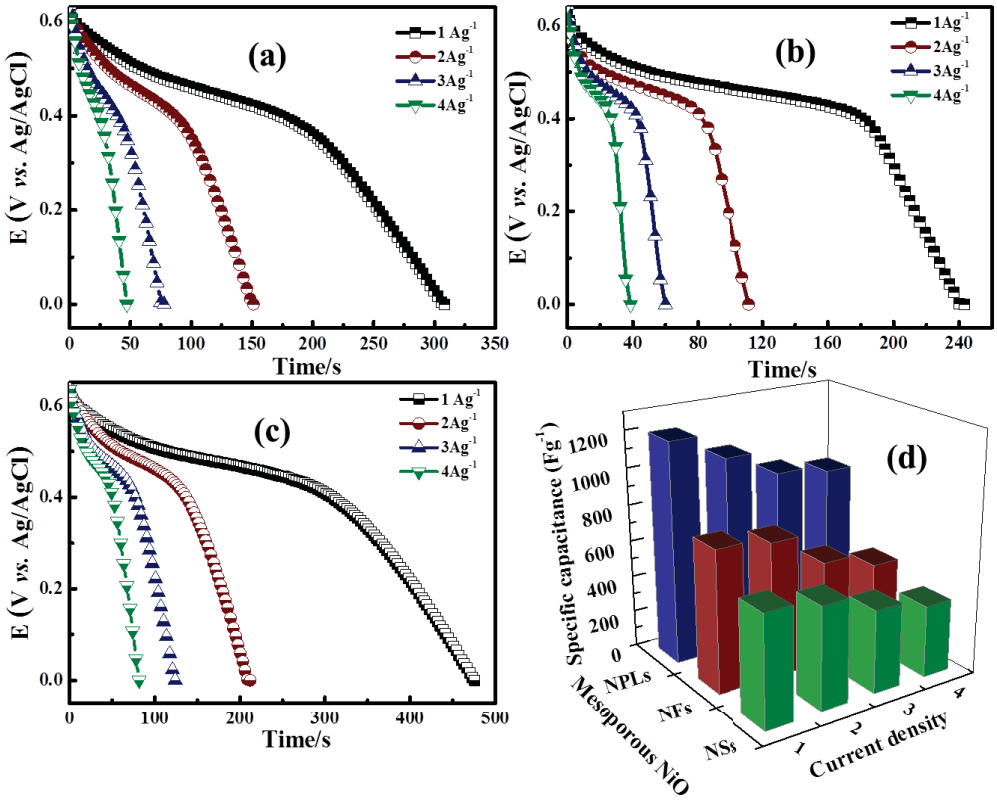

Figure 6.7: Galvanostatic discharge curves at different discharge currents for (a) NiO NFs, (b) NiO NSs, and (c) NiO NPLs. (d) The calculated specific capacitance of NiO NFs, NSs, and NPLs at different current densities.

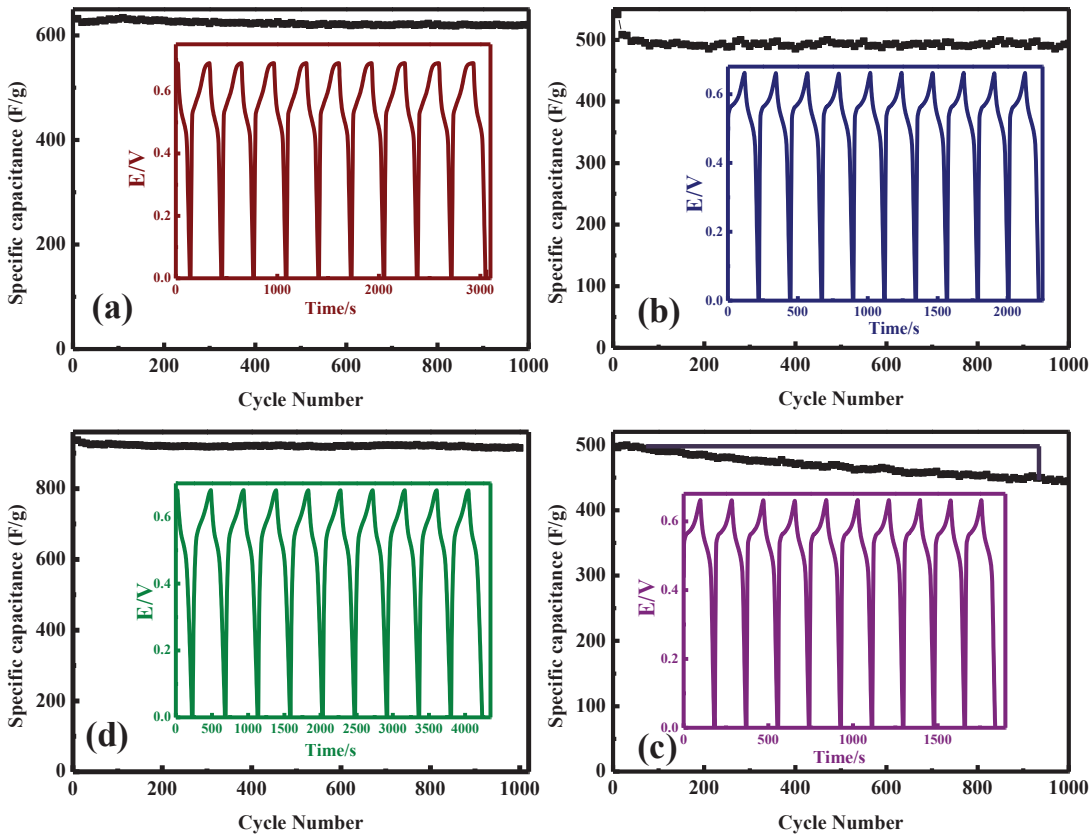

Figure 6.8: Applicability and cycling performance of mesoporous NiO nanostructured in 2 M NaOH at 2 Ag^{-1} prepared through microwave-assisted synthesis (a) NiO NFs, (b) NiO NSs, (c) NiO NPLs, and NiO-NPLs prepared through the hydrothermal method.[34]

The major advantages of pseudocapacitor electrodes for their practical applications are reversibility and long-term cycling. Figure 6.8 illustrates a continuous galvanostatic charge/discharge cycling at constant current density of 2.0 Ag^{-1} over 1000 cycles in representative voltage profile from 0.65 V to 0.0 V. The specific capacitance of NiO NFs gradually increased to 635 Fg^{-1} in an initial course of 100 cycles and decreased to 620 Fg^{-1} at the end of the test. The mesoporous NiO NPLs and NiO NSs displayed long-term cycling stability; almost 1.5% was lost in the first 100 cycles, and then no further change was observed over the following 900 cycles. Our results also revealed that NiO NFs need approximately 3 h to fully activate to provide high capacitance. Conversely, the mesoporous NiO NPLs and NiO NSs are fully activated from the first cycle to store high specific capacitance at 940 Fg^{-1} and 495 Fg^{-1} with good stability up to 1000 cycles. To our knowledge, such superior pseudocapacitive performance is rarely observed in electroactive NiO electrodes, which may be attributed to the structure, size, morphology, and mesoporosity of the present electrode. Further investigation of the applicability of NiO NPLs reveals that the specific capacitance is comparable to those of other unique

NiO structures recently reported, such as flower-like NiO hollow nanospheres,[25,33] nanocolumns,[22] nanoplates[26,34] (Figure 6.8d), or even NiO composites.[35,36] The specific capacitance of NiO NPLs is higher than those of MnO_2,[37] Fe_3O_4,[38,39] Co_3O_4[13], and ZnO.[40] Fine tuning the mesoporous NiO nanostructure of these electrode materials can ultimately optimize performance in terms of energy, power capabilities, and cyclability (Table 6.1).

Table 6.1: Comparison of the capacity of the our mesoporous NiO NPs and other materials in literatures

Material	Specific capacitance	Energy density	Power density	Reference
NiO nanoplatelets	1361 Fg^{-1} at 1 mVs^{-1}	63.8 Wh/kg	13.2 kW/kg	In this work
NiO nanoflakes	720 at 1 mV/s	22.5 Wh/kg	6.16 kW/kg	In this work
NiO Nanoslices	685 at 1 mVs	29.04 Wh/kg	4.74 kW/kg	In this work
NiO nanocolumns	390 F/g at 5A/g 686 F/g at 1A/g	---	---	(25)
NiO nanoslices	176 F/g at 5A/g	---	---	(25)
NiO nanoplates	285 F/g at 5A/g	---	---	(25)
NiO platelets	286.7 F/g at 1A/g	---	---	(34)
NiO flower	381 F/g at 1A/g	---	---	(21b)
NiO slices	86 F/g at 1A/g	---	---	(21b)
NiO nanoparticles	235 F/g at 1A/g	---	---	(21b)
C@NiO	988.7 F/g at 0.5 A/g	---	---	(36)
$Ni(OH)_2$	755 F/g at 1A/g			(20)
NiO/Ni Nanocomposites	905 F/g at 1A/g	60 Wh/kg	10 kW/kg	(28)
NiO Flower	370 F/g at 2A/g	50 Wh/kg	4.4 kW/kg	(21)
Au/MnO_2	1,145 F/g at 50mV/s	---	---	(2)
Au/MnO_2 Core/Shell	1020 F/g at 5 mV/s	---	---	(37b)

The EIS measurements were carried out to fully understand the effect of pore architectures and morphology of mesoporous NiO NPs on their electrochemical performance. Figure 6.9 presents the Nyquist and bode plots of mesoporous NiO NPs after the 20th cycles. As shown in the inset in Figure 6.8a, in high frequency region, all

mesoporous NiO NPs showed an obvious semicircle, which indicates the charge transfer resistance (R_{ct}) between the electroactive material and electrolyte interface, followed by an inclined straight line in low frequency region presenting Warburg behavior. The straight line is nearly close to the vertical line along the imaginary axis due to the accumulation of electrolyte ions at the bottom of the pores, which reveals the ideal capacitive behavior of the electrode. The numerical values of the semicircle diameter provide the approximate induction of R_{ct}. In the bode diagrams (Figure 6.9b), the absolute values of impedance |Z| strongly depend on the frequency, thus indicating the capacitive behavior of mesoporous NiO NPs. These results support the CV measurement data and reflect the diffusion process. The slight increase in R_{ct} is due to the absence of carbon materials at the electrode. The EIS data for NiO NPs can be fitted by an equivalent circuit consisting of a bulk solution resistance R_s, charge-transfer R_{ct}, pseudo capacitive element C from the redox process, and Warburg impedance to determine the diffusion of ions to the electrode surface. The calculated parameters of the equivalent circuit are consistent with the CV and galvanostatic charge/discharge measurements. These findings implied that the mesoporous NiO NPLs with controlled shape, size, and pore architectures could reduce the diffusion length of ions within the pseudo capacitive phase, ensuring a high utilization of the active materials.

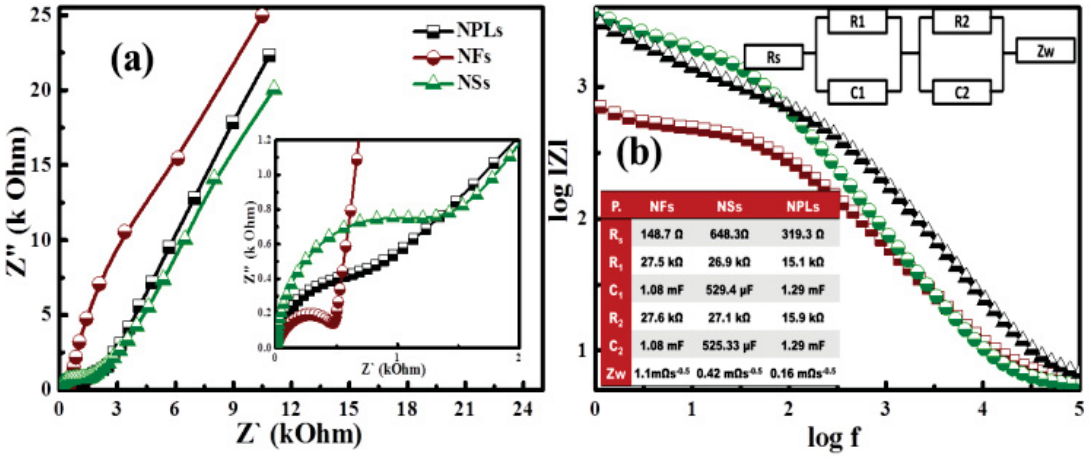

Figure 6.9: Nyquist and bode plots of mesoporous NiO NPs in the frequency range between 100 kHz and 10m Hz; the excitation voltage was 5 mV (inset, the equivalent circuit model and calculated parameters that describe the electrochemical process).

In the pseudo-capacitor fabrication, metal oxide is usually mixed with the conductive materials to enhance metal oxide conductivity and the efficiency as supercapacitor.[37,41] In this process, the NiO NPs are directly used as carbon-free

electrodes. A comparable high energy and power density, as well as satisfactory reversibility without carbon materials, have been obtained using a microwave-assisted control. Thus, we can avoid the poor electrical conductivity between the carbon and NiO nanomaterials that allow higher volume/mass specific energy density. In previous reports,[25,34] NiO nanoplates, nanosheets, and column-structured nanosheet assembly only showed capacitance less than 400 Fg^{-1}. High specific capacitance, high power density, and cycling stability may be attributed to the thinning nanoplatelet morphology, good crystallinity, and stable chemical bonding of the NiO nanoplatelets on the GCE substrate. The NiO NPLs showed a narrow pore size distribution with uniform nanosized architectures as represented by the TEM measurements (Figure 6.4). The thickness of the nanoflake's patel is 5 nm, less than 10 nm for platelet and approximately 50 nm for slices. Hu et al.[42] reported that the maximal proton diffusion distance is approximately 20 nm, which is greater than the thickness of our patels and platelets of mesoporous NiO. In addition, protons and hydroxyl ions have similar superconductivity due to the Grotthuss mechanism. The mesoporous NiO NPLs and NFs act as worm-like sieve or superhighways for hydroxide ions, reducing the diffusion distance to penetrate or transport during electrochemical reaction. Nanosized particles with controlling morphology also maximize the active surface sites accessible to fast Faradaic, demonstrating better rate capability and great potential as electrode materials for supercapacitors. In addition, the oleate might be altering the surface functional groups of NiO, which assist the diffusion of the electrolyte by increasing the surface hydrophility (Figure 6.10)

As shown in Figure 6.8, the microwave-assisted synthesis of NiO NPs showed a good cycling stability compared with that prepared through the hydrothermal method, which indicates the good crystallinity of NiO NPs. The electrochemical impedance spectroscopy measurements also suggested a strong chemical bond formed between the NiO NPs and GCE due to the easy transport of electrons from the NiO NPs and the GCE.

Based on our results, we could cite the following possible reasons for the performance enhancement of NiO pseudocapacitors:

I. The thickness and size of the nanoparticles. The specific capacitance of NiO NPLs is three times that of NiO NSs; however, the capacitance of NiO NFs is close to that of NiO NPLs.

II. The controlled morphology of NiO NPs enhances the diffusion of electrolytes to the active sites.

III. Narrow pore distribution with a high degree of pore connectivity in the 3D mesoporous network enhances the mass transport and increases the material lifetime in energy storage applications.

IV. Strong chemical bonding and hydrophility between NiO NPs and substrate enhance the electrochemical process.

V. The good crystallinity of NiO NPs is an important factor that improves the cycling stability. In the previous report,[43] the increase in annealing temperature induced high crystallinity. However, we fabricated highly crystalline NiO NPs using a simple and green microwave-assisted method.

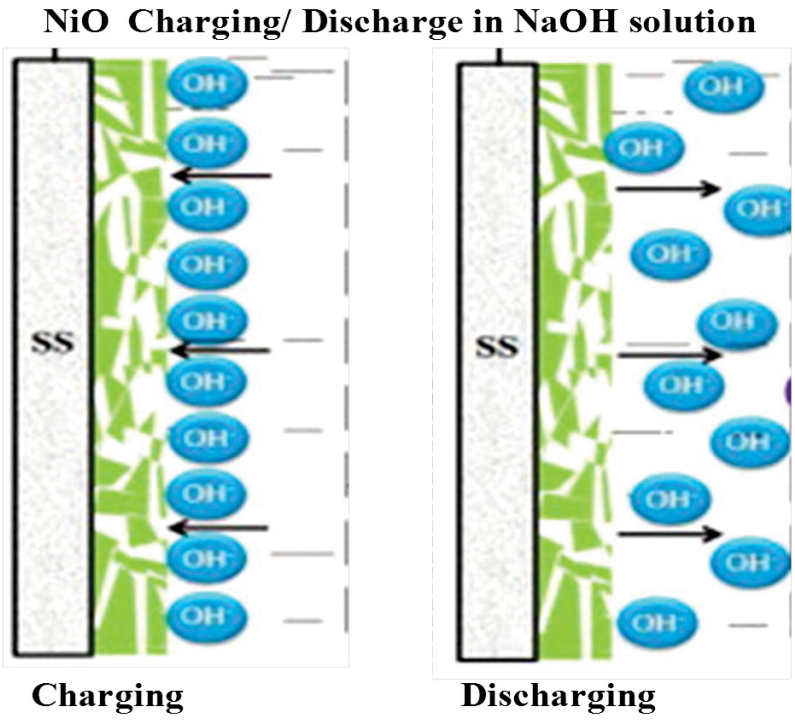

Figure 6.10: Charge discharge mechanism of NiO NPs in NaOH solution

6.3.References

[1] B. Guo , X. Wang, P. F. Fulvio, M. Chi, S. M. Mahurin, X.-G. Sun, S. Dai, Adv. Mater. 23, 2011, 4661–4666.

[2] X. Lang, A. Hirata, T. Fujita, M. Chen, NAT. Nanotechnol. 6, 2011, 232-236.

[3] V. L. Pushparaj, M. M. Shaijumon, A. Kumar, S. Murugesan, L. Ci, R. Vajtai, R. J. Linhardt, O. Nalamasu, P. M. Ajayan, PNAS, 104, 2007, 13574 –13577.

[4] L. Demarconnay, E. Raymundo-Pinero and F. Béguin, Electrochem. Commun., 12, 2010, 1275; K. Xia, Q. Gao, J. Jiang and J. Hu, Carbon, 46, 2008, 1718.

[5] A. Balducci, R. Dugas, P. L. Taberna, P. Simon, D. Plée, M. Mastragostino , S. Passerini, J. Power Sources, 165, 2007, 922.

[6] E. Iyyamperumal, S. Wang, L. Dai, ACS NANO, 6, 2012, 5259–5265; M. Rose, Y. Korenblit , E. Kockrick , L. Borchardt , M. Oschatz , S. Kaskel , G. Yushin, Small, 7, 2011, 1108–1117; L. Zhang, F. Zhang, X. Yang, K. Leng, Y. Huang, Y. Chen, Small, 9, 2013, 1342–1347

[7] Z. Chen, W. Ren, L. Gao, B. Liu, S. Pei, H.-M. Cheng, Nat. Mater., 10, 2011, 424.

[8] J. R. Miller, R. Outlaw, B. Holloway, Science, 329, 2010, 1637.

[9] L.-F. Chen, X.-D. Zhang, H.-W. Liang, M. Kong, Q.-F. Guan, P. Chen, Z.-Y. Wu, S.-H. Yu, ACS Nano, 6, 2012, 7092–7102.

[10] P. C. Chen, G. Shen, Y. Shi, H. Chen, C. Zhou, ACS Nano, 4, 2010, 4403;

[11] K. Naoi, P. Simon, the Electrochem. Soc. Interface, 17, 2008, 34–37.

[12] D. Q. Liu, Q. Wang, L. Qiao, F. Li, D. S. Wang, Z. B. Yang, D. Y. He, J. Mater. Chem., 22, 2012, 483.

[13] a) S. K. Meher, G. R. Rao, J. Phys. Chem. C, 115, 2011, 15646.

[14] Z. L. Wang, R. Guo, G. R. Li, L. X. Ding, Y. N. Qu, Y. X. Tong, RSC Adv., 1, 2011, 48.

[15] J. T. Li, W. Zhao, F. Q Huang, A. Manivannan, N. Q. Wu, Nanoscale, 3, 2011, 5103.

[16] R. L. Liang, H. Q. Cao, D. Qian, Chem. Commun., 47, 2011, 10305.

[17] Y.J. Mai, J. P. Tu, C.D. Gu, X. L. Wang, J. Power Sources, 209, 2012, 1–6.

[18] X.H. Xia, J.P. Tu, J. Zhang, X.L. Wang, W.K. Zhang, H. Huang, Sol. Energy Mater. Sol. Cells, 92, 2008, 628–633.

[19] A. Nattestad, M. Ferguson, R. Kerr, Y.-B. Cheng, U. Bach, Nanotechnology 19, 2008, 295304.

[20] P. Lu, F. Liu, D. Xue, H. Yang, Y. Liu, Electrochimica Acta, 78, 2012, 1– 10.

[21] S. K. Meher, P. Justin, G. R. Rao, ACS Appl. Mater. Interfaces, 2011, 3, 2063–2073.

[22] C. Largeot, C. Portet, J. Chmiola, P.-L. Taberna, Y. Gogotsi, P. Simon, J. Am. Chem. Soc., 130, 2008, 2730.

[23] M. Ghosh, K. Biswas, A. Sundaresan, C. N. R. Rao, J. Mater. Chem., 16, 2006, 106–111.

[24] D. Wang, R. Xu, X. Wang, Y. Li, Nanotechnology, 17, 2006, 979–983.

[25] X. Zhang, W. Shi, J. Zhu, W. Zhao, J. Ma, S. Mhaisalkar, T. L. Maria, Y. Yang, H. Zhang, H. H. Hng, Q. Yan, Nano Res. 3, 2010, 643–652

[26] S. A. El-Safty, M. Khairy, M. Ismael, H. Kawarada, Appl. Catal., B, 123, 2012, 162-173.

[27] M. Khairy, S. A. El-Safty, , M. Ismael, H. Kawarada, Appl. Catal., B, 127, 2012, 1-10.

[28] Q. Lu, M. W. Lattanzi, Y. Chen, X. Kou, W. Li, X. Fan, K. M. Unruh, J. G. Chen, J. Q. Xiao, Angew. Chem. Int. Ed. 50,2011, 6847–685

[29] B. P. Bastakoti, H.-S. Huang, L.-C. Chen, K. C.-W. Wu, Y. Yamauchi, Chem. Commun., 48, 2012, 9150-9152.

[30] A. Fihri, R. Sougrat, R. B. Rakhi, R. Rahal, D. Cha, M. N. Hedhili, M. Bouhrara, H. N. Alshareef, V. Polshettiwar, Chem.Sus.Chem., 5, 2012, 1241– 1248.

[31] P. Simon, Y. Gogotsi, Nat. Mater. 7, 2008, 845–854.

[32] S.K. Meher, G. R. Rao, J. Phys. Chem. C, 115, 2011, 25543–25556.

[33] C.-Y. Cao, W. Guo, Z.-M. Cui, W.-G. Song, W. Cai, J. Mater. Chem., 21, 2011, 3204-3209.

[34] Z, Zhu, J. Ping, X. Huang, J. Hu, Q. Chen, X. Ji, C. E. Banks, J Mater Sci, 47, 2012, 503–507.

[35] Y.-Y. Yang, Z.-A. Hu, Z.-Y. Zhang, F.-H. Zhang, Y.-J. Zhang, P.-J. Liang, H.-Y. Zhang, H.-Y. Wu, Mater. Chem. Phys., 133, 2012, 363– 368.

[36] L. Fan, L. Tang, H. Gong, Z. Yao, R. Guo, J. Mater. Chem., 22, 2012, 16376

[37] a) J. Zhu, W. Shi, N. Xiao, X. Rui, H. Tan, X. Lu, H. Hng, J. Ma, Q. Yan, ACS Appl. Mater. Interfaces, 4, 2012, 2769−2774.

[38] P. M. Hallam, M. G.-Mingot, D. K. Kampouris, C. E. Banks, RSC Adv., 2, 2012, 6672–6679.

[39] M. Zhu, Y. Wang, D. Meng, X. Qin, G. Diao, J. Phys. Chem. C, 116, 2012, 16276−16285.

[40] X. Dong, Y. Cao, J Wang, M. B. Chan-Park, L. Wang, W. Huang, P. Chen, RSC

Adv., 2, 2012, 4364–4369.

[41] H. L. Wang, H. S. Casalongue, Y. Y. Liang, H. J. Dai, J. Am. Chem. Soc., 132, 2010, 7472–7477.

[42] C.-C. Hu, K.-H. Chang, M.-C. Lin, Y. - T. Wu, Nano Lett. 6, 2006, 2690-2695.

[43] J. H. Kim, K. Zhu, Y. F. Yan, C. L. Perkins, A. J. Frank, Nano Lett. 10, 2010, 4099–4104.

CHAPTER 7

GENERAL CONCLUSION

The increase in the global contamination of environment with industrial and natural chemical compounds is one of the key problems facing the world today. We developed a simple, large-scale, low-cost manufacturing and feasible method for the design of mesoporous NiO NPs with platelet-, flower- and sphere-like morphology without using hard or soft templates. The morphology and chemical reactivity of NiO NPs with controlled morphology are highly promising candidates in the catalytic transformation of organic pollutants particularly phenolic compounds such as *o*-aminophenol and *o*-aminothiophenol. The new approach features of multidirectional porous NiO NPs fabrication are the significant factor in enhancement of the coverage surfaces and in the intra-particle diffusion on the network surfaces and into the pore architecture. The results revealed that the catalytic activity of NiO nanoplatelets is higher than NiO nanoflower and NiO nanosphere or even Fe_3O_4. The control of the size and shape of the NiO nanoplatelets in condensed orientation "tesserae blocks" leads to the formation of hexagonal NiO platelet-like mosaics enhanced accessibility and the interaction affinity of the phenolic pollutants for functional active sites of the NiO surfaces with Ni site deficiencies are intrinsic properties of NiO NPLs. However, the NiO nanoflowers are capable of the high-gradient magnetic separation of organic contaminants from aquatic life with excellent reusability even after several cycles, which may help in wastewater management and supply. Moreover, the magnetic property of NiO nanoflowers does not affect the catalytic reaction pathway. To understand the proposed chemical oxidation mechanism of phenolic pollutants, the energy profiles and charge distribution of reactants, intermediates, and products were calculated using the DFT. A major advantage of NiO nanocatalysts is their retained texture, morphology, and magnetic characteristics in terms of reactivity with fast chemical transformation even after multiple cycles. We expect these mesoporous NiO NPs to be a promising development for nanoscale devices. Moreover, this study may provide guidelines for NiO nanoparticles optimization for use in effective chemical and biochemical processing applications, particularly in the field of catalysis and environmental clean-up systems, for the transformation and removal of organic pollutants from wastewater.

Fabrication of selective protein adsorption that didn't impede by the physical shape of the protein, its three-dimensional hydrodynamic dimensions, clogging effect with high retention, and uniformly-sized pore of adsorbents is a key requirement in successful protein encapsulation. A novel nanomagnet-selective supercaptor approach in the

encapsulation of hemoprotein from mammalian cells using mesoporous metal oxide nanoparticles was studied. Different morphologies of mesoporous NiO and Fe_3O_4 nanoparticles were fabricated. Among these nanoadsorbents, NiO nanoflower had higher loading capacity of hemoprotein than NiO nanospheres and nanoplatelets, or even superparamagnetic Fe_3O_4 nanoparticles. The key finding of this study was that mesoporous NiO nanomagnet supercaptors show exceptional encapsulation and selective separation of high-concentration Hb from human blood. In this induced-fit separation model, in addition to the heme group distributions and protein-carrier binding energy, the morphology and magnetic properties of NiO NPs had a key function in broadening the controlled immobilization affinity and selectivity of hemoproteins. Guidelines for optimization of selective adsorption of biomolecules using magnetic nanoparticles must be developed to use this technology effectively in biochemical processing applications.

The tailored sensor design based on the direct immobilization of hydrophobic ligands into ordered pore-based monoliths enabled easy generation and transduction of optical colour signals as a response to M-to-ligand binding events, even at ultra-trace concentrations (10^{-9} mol.dm^{-3}) of toxic metal ions in drinking water, without the need for sophisticated instruments. In solid-state ion-sensing and capture systems, the physical features of the mesocaptors such as the large surface area-to-volume ratios of functional chromophores and the uniform mesocage pores enabled the creation of a multiparticulate capture system for the optical separation/extraction and monitoring/detection of metal ions even at trace concentration levels without a preconcentration process. Our mesocaptors show significant adsorption efficiency (~96% to 99%) over commercial adsorbents, which require intensive design and experimental conditions during the adsorption and assessment monitoring of Cu(II) and Zn(II) ions. A major advantage of the mesocaptors is their ability to create selective extracting systems of Cu(II) and Zn(II) ion, thus preventing hindrance from actively interfering components, particularly competitive element ions. This finding indicates that the ion-capture model enables the development of simple and effective technique for effective wastewater treatment and management.

Moreover, the colorimetric approach to Pb^{2+} ion recognition and removal using cross-responsive shells that contain a chemically responsive AC–LHT dye were developed. The design of the multi-shelled sensor was created through sufficiently physisorbed interactions between the interior/exterior silanol and APMS groups of the core/double-shell silica nanospheres and the heteroatoms of AC–LHT. The remarkable

ion–spectral response of the hierarchical multi-shell sensor ensures excellent optical isolation for ultra-trace concentrations of Pb^{2+} ions, where the color transitions are at a frequency detectable by the human eye. The pH and kinetic contact time are key control factors in the selective and sensitive detection or removal of Pb^{2+} ions from water or blood using the multi-shelled sensor. A wide range of Pb^{2+} ion concentrations can be removed from aqueous water in a one-step treatment with a high adsorption efficiency of ~93%. An example of the potential use of the sensor in medical applications is the removal of Pb^{2+} ions as demonstrated through the inhibition of specific toxic effects associated with the presence of Pb^{2+} ions in blood. This hierarchal sensor can revolutionize the inhibition of the health risks associated with elevated blood lead levels such as anemia.

The development of flexible, sustainable, and efficient energy storage has recently attracted considerable attention to satisfy the demand for huge energy and power density and meet future societal and environmental needs. Consequently, numerous studies have focused on the design/development of nanomaterials based on mesoporous architectures to improve energy and power densities. The large-scale production, low-cost manufacturing, and high-performance of supercapacitors based on the microwave-assisted synthesis of mesoporous nickel oxide nanocrystals (NCs) were presented. Mesoporous NiO in various morphologies, including nanoflakes (NFs), nanoslices (NSs), and nanoplatelets (NPLs), were synthesized. The superior electrochemical performance of mesoporous NiO NPLs is significantly related to their unique morphology, size, and pore size distribution, which enhance the diffusion of electrolyte through porous network "superhighways". These characteristics induce the high capacitance and excellent recyclability of NiO NPLs more than NiO NFs and NiO NSs. Microwave synthesis enhanced charge storage and stability compared with those prepared through the hydrothermal approach. This approach demonstrates the potential of free-standing NiO NPL electrodes for developing high-performance pseudocapacitors.

Further, the results cited the following possible reasons for the performance enhancement of NiO pseudocapacitors:

1. The size of the nanoparticles. The specific capacitance of NiO NPLs is three times that of NiO NSs; however, the capacitance of NiO NFs is close to that of NiO NPLs.

2. The controlled morphology of NiO NPs enhances the diffusion of electrolytes to the active sites.
3. Narrow pore distribution with a high degree of pore connectivity in the 3D mesoporous network enhances the mass transport and increases the material lifetime in energy storage applications.
4. Strong chemical bonding and hydrophility between NiO NPs and substrate enhance the electrochemical process.
5. The good crystallinity of NiO NPs is an important factor that improves the cycling stability. The increase in annealing temperature induced high crystallinity. However, we fabricated highly crystalline NiO NPs using a simple and green microwave-assisted method.

SUMMARY

This dissertation research work focused on simple and eco-friendly fabrication approaches of various mesoporous metal oxides targeting environmental remediation based monitoring, sensing, and decontamination, in addition to possible applications in the energy storage. Detailed studies revealed the potential applications of mesoporous metal oxides, as follows;

- The development of a sustainable catalyst could potentially provide a long-term solution to industrial health-risk processes, especially in the environmental cleanup systems from organic contaminants. The nickel (II) oxide catalysts with a controlled platelet, flower, and sphere morphologies have been reported. The NiO nanoparticles having three dimensional 0.5 nm micro- and 4 nm mesopores within the platelets, and 270 nm macropores between platelets, has been produced via a one-pot method using ethylene glycol to control particle morphology. These platelets, which form a mosaic arrangement, exhibit higher activity for the decomposition of phenyl-containing pollutants than NiO nanoflower and/or nanospheres However, The NiO nanoflowers show superior capability in magnetic separation of organic contaminants from aquatic life which may help in wastewater management and supply. This study may provide guidelines for mesoporous NiO nanoparticles optimization as an effective catalyst for the transformation and removal of organic contaminants from wastewater.
- The clogging pores with large-molecular-weight proteins, particularly at high feed concentration, during the size-selective encapsulation assays still remain challenge. Therefore, the fabrication of selective protein supercaptors that didn't impede by the physical shape of the protein, its 3D hydrodynamic dimensions, clogging effect with high retentate, and uniformly-sized pore of adsorbents is a key requirement in successful protein encapsulation and uptake. Therefore, the adsorption of proteins onto magnetic mesoporous NiO and Fe_3O_4 nanoparticles was studied. Interestingly, the mesoporous NiO and Fe_3O_4 nanoparticles can act as nanomagnet-selective adsorbent of hemo-proteins, particularly haemoglobin, among various biological molecules. It was found that, the morphology, crystal sizes and shapes, and magnetic properties of mesoporous NiO and Fe_3O_4 nanoparticles, in addition to the heme group distributions, and protein-carrier binding energy play a key role in broadening the controlled immobilization affinity and selectivity of hemo-proteins. In real application, such approach opens a new avenue of magnetic separation of single proteins regardless size- and shape of proteins which is impressive in biochemical processing applications.

- The efficient sequestering and detection of toxic metal ions form environment using mesoporous metal oxides is discussed. Simple, inexpensive, rapid responsive and portable sensors are highly recommended for monitoring of toxic metal ions. The mesoporous alumina and aluminosilica composites used as selective optical sensing system due to the use of "low-tech" spectroscopic instrumentation to detect relevant metal ions such as lead, mercury, copper, zinc and cadmium ions in environment. In order to apply the developed nanosensors in medical applications, a novel optical multi-shell nanosphere sensor was fabricated. This sensor enables selective recognition, unrestrained accessibility, monitoring, and removal of lead ions (Pb^{2+}) from human blood. A unique feature of the core/double-shell sensor design is the capacious hollow cage shell structure that can encapsulate numerous different types of functional groups and protect the immobilized probe to maintain electron acceptor and donor strength. Indeed, such optical sensors offer a possibility of simultaneous detection and sequestering of toxic ions with a minimum sample manipulation, reasonable selectivity and improved sensitivity of Pb^{2+} ions from blood without using any reference devices.
- The Development of pseudocapacitors for efficient energy storage devices were presented. The mesoporous NiO nanoparticles with controlled morphologies, including nanoflakes, nanoslices, and nanoplatelets, were synthesized in a large-scale production, and low-cost manufacturing via microwave-assisted synthesis approach. The mesoporous NiO platelets showed superior electrochemical performance due to their unique morphology, size, and mesopore size distribution that enhance the diffusion of electrolyte through porous network “i.e. superhighways”. This approach demonstrates the potential of free-standing NiO NPL electrodes for developing high-performance pseudocapacitors.

Finally, the research guidelines show evidence of the applicability of developed metal oxides as key components in the future development of high-grade environmental chemistry and energy.